Analysis and monitoring of single HaCaT cells using volumetric Raman mapping and machine learning

Michael James Greenop

This thesis is submitted for the degree of Doctor of Philosophy

Lancaster University – School of Engineering

September 2023

Abstract

No explorer reached a pole without a map, no chef served a meal without tasting, and no surgeon implants untested devices. Higher accuracy maps, more sensitive taste buds, and more rigorous tests increase confidence in positive outcomes. Biomedical manufacturing necessitates rigour, whether developing drugs or creating bioengineered tissues [1]–[4]. By designing a dynamic environment that supports mammalian cells during experiments within a Raman spectroscope, this project provides a platform that more closely replicates *in vivo* conditions. The platform also adds the opportunity to automate the adaptation of the cell culture environment, alongside spectral monitoring of cells with machine learning and three-dimensional Raman mapping, called volumetric Raman mapping (VRM). Previous research highlighted key areas for refinement, like a structured approach for shading Raman maps [5], [6], and the collection of VRM [7]. Refining VRM shading and collection was the initial focus, k-means directed shading for vibrational spectroscopy map shading was developed in Chapter 3 and exploration of depth distortion and VRM calibration (Chapter 4). “Cage” scaffolds, designed using the findings from Chapter 4 were then utilised to influence cell behaviour by varying the number of cage beams to change the scaffold porosity. Altering the porosity facilitated spectroscopy investigation into previously observed changes in cell biology alteration in response to porous scaffolds [8]. VRM visualised changed single human keratinocyte (HaCaT) cell morphology, providing a complementary technique for machine learning classification. Increased technical rigour justified progression onto *in-situ* flow chamber for Raman spectroscopy development in Chapter 6, using a Psoriasis (dithranol-HaCaT) model on unfixed cells. K-means-directed shading and principal component analysis (PCA) revealed HaCaT cell adaptations aligning with previous publications [5] and earlier thesis sections. The k-means-directed Raman maps and PCA score plots verified the drug-supplying capacity of the flow chamber, justifying future investigation into VRM and machine learning for monitoring single cells within the flow chamber.

Acknowledgements

Writing this thesis provided a unique learning and development experience, made impossible without the opportunity, guidance, and support I received through the project. I am forever indebted to all who contributed, not only during the doctorate but the years prior encompassing housemates, coursemates, colleagues, lecturers, teammates, and the Nottingham lot.

Specifically, I thank my supervisors, Prof. Rehman, and Dr. Ashton whose research and guidance helped shape this project. I am incredibly fortunate to have had both of you as my supervisors and have your continued support. Prof. Rehman, who brought me into the Bioengineering research group, who I thank for their advice, training, and friendship. Whilst in the group I completed my MSc dissertation, resulting in this Lancaster University School of Engineering funded PhD opportunity. I acknowledge the support of the School of Engineering, both financially and in providing a world-leading engineering environment to develop skills, knowledge, and resilience.

The incredible support, phenomenal experiences, and tolerance provided by my family are the foundation for any successes I have. Thanking my parents and sister for their help and my childhood is therefore critical. To Mitch, I am grateful for the friendship and distraction of watching the Garibaldi Reds. Finally, but significantly, Ellie, first defence against stress, forgiver of my quirks and geographical distance, and enabler of my dreams, I thank you for everything.

Declaration

This thesis and the results in it are all my own work, have not been submitted for any other higher degree, and the word count is below the maximum allowed.

Michael Greenop

Contents

List of abbreviations

ANN ..... Artificial Neural Network

CA ..... Collection Area

DLW ..... Direct Laser Writing

DPBS ..... Dubeccos Buffered Saline

DR ..... Depth Reolution

HaCaT ..... Immortalised Human Keratinocyte

HEZ ..... Heat Effected Zone

hMSC ..... Human Mesnchymal Stem Cell

LDA ..... Linear Discriminant Analysis

LgSq ..... Large Square

lsqr ..... Least Square Solution

MdSq ..... Medium Square

PAT ..... Process Analytical Technology

PCA ..... Principal Component Analysis

PEG ..... Polyetylene Glycol

PETA ..... Pentaerythritol Tetraacrylate

PFA ..... Parefomaldehyde

RBF ..... Radial Base Function

SEM ..... Scanning Electron Microscope

SmSq ..... Small Square

svd ..... Singular Value Decomposition

SVM ..... Support Vector Machine

TPA ..... Two-Photon Absorption

VRM ..... Volumetric Raman mapping

List of figures

Chapter 1 - Introduction

1.1. Introduction

Autologous or allogeneic transplants are the gold standard methods for replacing damaged or ineffective organs and tissues such as the heart, skin, or kidneys [9]–[11]. Autologous transplantation, using the patient tissue, provides immunologically matching tissue but frequently does not provide enough tissue and increases patient morbidity [12], [13]. In cases where a donor cannot be found (blocking allogeneic transplant), tissue engineering can provide an alternative by producing tissues from patient cells. However, the formation of tissues is a complex process, with numerous biochemical and physical cues [14]. Determining and prioritising the best combination of signals during the culturing of cells into tissues is a key issue for advancing tissue engineering. A potential method of monitoring cells as they are exposed to different stimuli is Raman spectroscopy (section 1.2.1), which can provide non-destructive, label-free, aqueous spectral analysis and mapping. Larger scale pharmaceutical applications of Raman spectroscopy including Process Analytical Technology (PAT) of monitor cell cultures [15], without the use of mapping. Raman mapping has been used in research to assess bioengineered bone [16] and tissue-engineered cartilage [17], with Raman spectroscopy, also used to monitor tissue-engineered skin [18] and single cells [19]. The two have not yet been combined into a single platform to monitor cell cultures using combined Raman spectral and mapping analysis.

To understand the cellular processes underlying the formation of tissue-engineered contracts, a mixture of morphological, physical, and molecular information must be gathered. Cell response to scaffolds can be monitored non-destructively using fluorescence microscopy, and destructively using scanning electron microscopy, atomic force microscopy, etc. Microscopy is widely used for the collection of

morphological information, providing easily interpretable, high-resolution images. The limitation of microscopy introduction of large dye molecules into the cell when visualising the cells internal structures [20] potentially disrupting the process the researcher is trying to observe. The number of distinguishable colours is also a limitation, to make target molecules distinct, microscopy images are limited to three or four molecules relies on labelling. Vibrational spectroscopy by comparison collects a range of wavelengths, typically a range with 1000 wavenumbers, providing a greater depth of molecular data [21]. Raman and infrared spectroscopies can provide complementary quantitative and qualitative data from a wide range of biological molecules, alongside molecular and morphological insights in a single process.

Raman maps are produced by collecting an array of spectra at discrete XY coordinates over a plane a set distance from the lens (the focal distance), which are the map pixels. Collecting each pixel individually can make Raman maps unintuitive to interpret compared to microscope images, especially when optical conditions vary over the mapped area. Microscopes focus a lens onto the subject, collecting photons from a focal depth in the same way a human eye does, forming a comparable image where observers intuitively understand the relative positions of other sections of the sample relative to the focused region of the image. An image produced by focusing a microscope is therefore intuitively understood, with out-of-focus regions interpreted instinctively as separate from the focal region (seen as unfocused). A danger of Raman maps is the expectation, or assumption, that all detected Raman photons originate in the laser beams focal position, allowing their interpretation in the same way as microscope image. However, previous research has shown that not all detected photons do originate in the laser focus, with such “out-of-focus” contamination potentially resulting spurious images/conclusion. The visual similarity of Raman maps to microscope images can therefore result in overconfidence in the images produced. Varied optical conditions are especially acute during volumetric Raman mapping (VRM) production, see section 1.2.2), which involves sub-surface analysis. A challenge for this thesis is there to explore a VRM calibration method, moving towards a standardised approach to the production of VRM.

Another factor in Raman mapping requiring standardisation is determining and presenting shading parameters, as highlighted by Ashton et al [5]. Raman mapping can require the allocation of colour to physical features of unknown dimension and/or is transparent to the human eye, e.g., organelles like the nucleus. Where labelling is used in microscopy to colour target regions of images, Raman maps plot the Raman intensity for each pixel. Transparency settings allow Raman maps to be layered, called low-feature Raman mapping in this thesis, as the number of features (wavenumbers) visualised using this method are typically below four to maintain an interpretable image. The colour, colour intensity, and transparency of the different layers are typically determined by the researcher, resulting in the potential for subjective or arbitrary shading [5]. The aim of this thesis is therefore to determine an objective and repeatable method of determining and presenting Raman map shading parameters, ideally linked to Raman spectrum features (spectrally justified). Another common method of producing Raman maps is hyperspectral imaging, where chemometric/machine learning methods such as principal component analysis (PCA) [22] or clustering [23] are used to determine features that are then visualised over the mapped area. An area of research will be linking low-feature and hyperspectral imaging methods to combine their advantages to counter their limitations and outline a solution to the issues raised by Ashton et al [5].

Each voxel/pixel in Raman maps is a spectrum, making chemometric algorithms available, and providing a wide range of features for machine learning analysis. Deep learning algorithms have provided medical diagnoses using images [24], [25], however, the substantial number of observations required for such a model makes such an undertaking impractical for many studies. Deep learning models are also less interpretable when compared to less complex models, providing sample classification but limited information about which molecules/features resulted in the separation. The reduced interpretability makes drawing clear conclusions about the underlying biological process complex. The wavenumbers and molecules (features) highlighted from the analysis of Raman maps are easier to comprehend and compare to comparative studies than the abstract features determined by machine vision algorithms. The challenge for this thesis is to explore approaches to improve

the repeatability of Raman spectroscopy machine learning, where the high number of features increases the risk of algorithm overfitting; where the model overfits to the data, rather than discerns insights. Once the technical aspects of collecting data from single cells (shading, VRM production, & machine learning methods) have been refined for the monitoring of single cells, the final phase of the thesis will explore their combination. Tissue-engineered products are designed to be implanted into a dynamic environment. A platform to explore the capacity of the methods developed in Chapters 3-5 will therefore aim to replicate in vivo conditions as closely as possible, leading to unfixed and eventual live cell (section 1.2.3) Raman platform.

1.2. Raman spectroscopy theoretical background

Raman spectroscopy is a form of vibrational spectroscopy, which alongside infrared spectroscopy detects altered vibrational states in chemical bonds [21]. Six basic vibrations occur in three symmetries/directions within bonds constituting molecules including latitudinal rocking & scissoring, longitudinal wagging & twisting, and radial symmetric or antisymmetric stretching [26], with more complex combinations of vibrations occurring in increasingly complex molecules. If a change occurs in a biological or chemical system that alters the molecular composition of the system, the kinds of bonds and their corresponding vibrations are changed. Vibrational spectroscopy detects the altered vibrations within samples to provide qualitative and quantitative data describing the changed state in the system.

A spectrometer detects the changes over a pre-selected spectral range [21], [27] based on bonds relating to the research question and available equipment. Changes in the spectrum produced relating to the molecular composition of the samples are shown using a line plot known as a spectrograph, referred to as a spectrum in this thesis. Peaks in the spectrum indicate an increased bond detection relative to the other areas of the spectral range. The relative heights and shapes of spectral peaks

identify the material alongside some material properties, like sharp peaks relating to crystalline structures and rounded peaks indicating amorphous materials.

Infrared and Raman spectroscopies are complementary analyses due to their respective selection criteria [27]. Infrared spectroscopy requires a bond to have a change in dipole moment (occurring most frequently in bonds with high polarity). Conversely, Raman scattering occurs most frequently in bonds with low polarity. Therefore, the two conditions cover the bonds that occur within a molecule, and analysis with both techniques provides information on bonds with both a low and high polarity. The polarity of bonds links to a key advantage of Raman spectroscopy for the aqueous analysis of living biological samples. A limitation of infrared spectroscopy is masking, where the high polarity of the H_2O molecule results in the masking of key biological signals when analysed in water. As this project aims to detect changes in living HaCaT cells, experiments will use Raman spectroscopy.

1.2.1. Raman theory

Raman spectroscopy is named after C. V. Raman who discovered the principle governing its spectral patterns, Raman scattering. Raman scattering is the inelastic scattering of an incident photon after interaction with an atomic bond [21]. Photons collide with molecules, and as they do, they briefly disrupt the electron field around the molecule atoms in a virtual state [28]. The interaction is typically so brief that the relatively quick electrons are pulled into a new arrangement before the nucleus has time to adapt its position to an equilibrium geometry the negative and positive charge, polarizing the bond [28]. Normally the bond returns to its previous state and in these cases, the scattered photon leaves with the same energy as it arrived with (elastic, Rayleigh scattering) [21], [28]. In some rare (~1 in 10^8) [21], [29] cases, the bond is left in a higher or lower energy state, resulting in the difference being added or subtracted from the scattered photon; known as inelastic, Raman scattering [21], [28].

The altered energy level of the Raman scattered photon changes its frequency [21]. The frequency of the photon may be reduced, known as a Stokes shift, where the bond is in a higher vibrational level post scattering. Conversely, if the bond starts in a higher vibrational level than the ground state, the scattered photon may have a higher frequency than the incident, with the molecular vibration left in a lower vibrational level, known as an anti-Stokes shift [21]. The confirmation of the constituent atoms is unique in each bond, the energy required for each bond to make an energy state jump is indicative of that bond [21]. The rarity of Raman scattering results in a balance being required between collection speed, collection time, laser power, and spectral quality [21]. Balancing practical limitations against maximised signal-to-noise is especially critical in biological samples where fluorescence and sample damage are key considerations [21].

Raman spectrometers utilise monochromatic light emitted by a laser [21], a filter, and a detector. The laser wavelength is a key consideration when determining a methodology involving Raman spectroscopy. The wavelength (λ) affects the kind of material that can be analysed, for example, a higher energy wavelength may damage samples [21]. The spatial resolution is also dependent on wavelength as the smaller λ, the smaller the diffraction limit [30]. The diffraction limit determines the spatial resolution alongside the numerical aperture of the objective used [7].

The laser beam is transmitted onto the sample, the Raman scattered photons are then allowed to pass through the filter, which removes the incident photon frequency [16]. The inelastically scattered light then travels through a slit into the detector onto the grating [21]. The grating deflects the different wavelengths with groves that split them into the spectrum [21]. A charged-couple devices (CCD) camera, a multichannel array consisting of thousands of pixels, then collects the scattered photons [21]. The CCD detector produces a charge proportional to the detected Raman scattering intensity, which is read out of the detector chip and plotted as a function of the wavelengths [21].

The advantages of Raman include high molecular specificity producing qualitative and quantitative data [21]. Raman can analyse unprocessed biological samples and

is a non-invasive, label-free method [21], [29]. Three-dimensional mapping through the depth of the sample (VRM) is possible with confocal Raman spectroscopy [6] as well as live-cell Raman [20]. A disadvantage of Raman is the possibility of photo-bleaching and fluorescence [6]. The limitation of confocal Raman spectroscopy is the reduced collection area compared to Fourier transform infrared spectroscopy (FTIR) due to restriction to the microscope field of view, making FTIR advantageous for larger 2D maps.

1.2.2. Volumetric Raman mapping (VRM)

Volumetric Raman maps (VRMs) are produced by collecting two-dimensional Raman maps through a sample, typically using conventional (lateral) mapping, where every map is known as a slice in the VRM context. The information provided to the system (Renishaw WiRE^{TM}/WiRE^{TM} system throughout the thesis) is the number and distance between coordinates in the X dimension, and Y dimensions, determining the number of pixels (spectra) to be used to map a given area (resolution) of the slices. The number of slices and distance between them (z-step) then determines the intended depth of the map. A consideration for VRM is the increase temperature resulting from focusing a laser onto a localised position repeatedly, as happens as the laser focus is moved along an axis. In their study Slipets et al developed a novel Raman spectroscope to counter the increased temperature resulting from VRM [31]. The spectroscope collects the Raman spectra at coordinates spaced apart, avoiding high temperature localisations, then returning to previous sections when they have cooled [31]. By limiting temperature build up in this way, a large VRM of a Direct laser written (DLW) printed capsule, made of the epoxy-based negative photoresist SU-8^{TM}, can be collected to show the drug distribution within (Figure 1.1) [31]. Finding a method of cooling samples using a spectroscope available on the market is an aim of this project, alongside investigating other technical challenges relating to the production of VRM and shading of Raman maps.

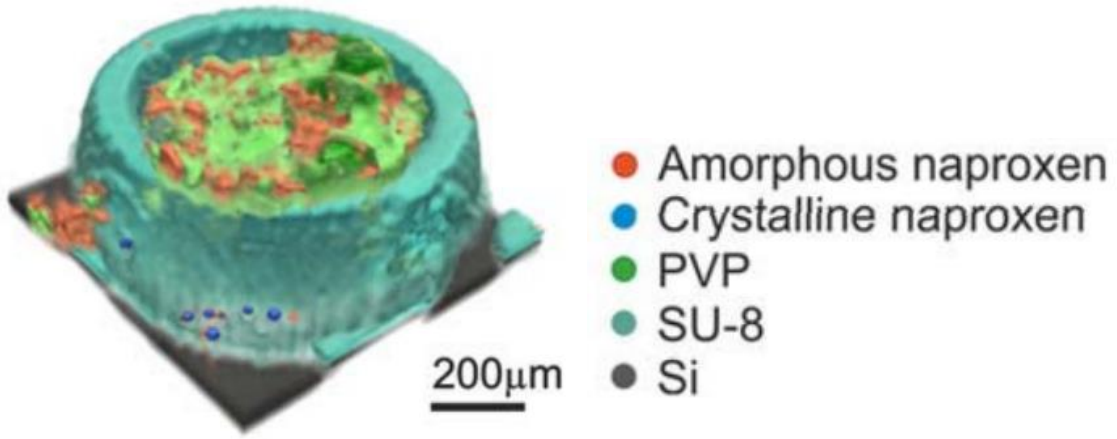

Figure 1.1 – VRM of SU-8^{TM} Capsule: *Three-dimensional Raman map showing the location of amorphous (red) and crystalline (blue) naproxen, alongside PVP (green) loaded into a SU-8^{TM} (turquoise) DLW capsule on a silicon (black) surface* [31].

Figure 1.2 uses VRM to compare human Mesenchymal stem cells (hMSCs) cultured in inert (left) polyethylene glycol (PEG) and functionalised PEG (right) using matrix metalloproteinase (MMP) degradable and arginylglycylaspartic acid (RGD) peptides. The MMPs-RGD functionalised PEG showing the altered cell morphology resulting from the hydrogel functionalisation [34]. Vertex component analysis was used by Kallepitis et al [32] to "unpack" the hyperspectral dataset into endmembers, allowing quantitative analysis of different molecules to be carried out alongside 3D visualisation of the cell. The endmembers were linked to different sub-cellular regions, allowing for spectral peaks unique to specific regions to be identified and used to visualise the different regions distinctly. The PEG network was associated with the 847 cm^{-1} band (C–O–C or C–C stretching), the cytoplasm (blue) relates to phenylalanine (1008 cm^{-1}), and red indicates the nucleic acids O-P-O band (789 cm^{-1}).

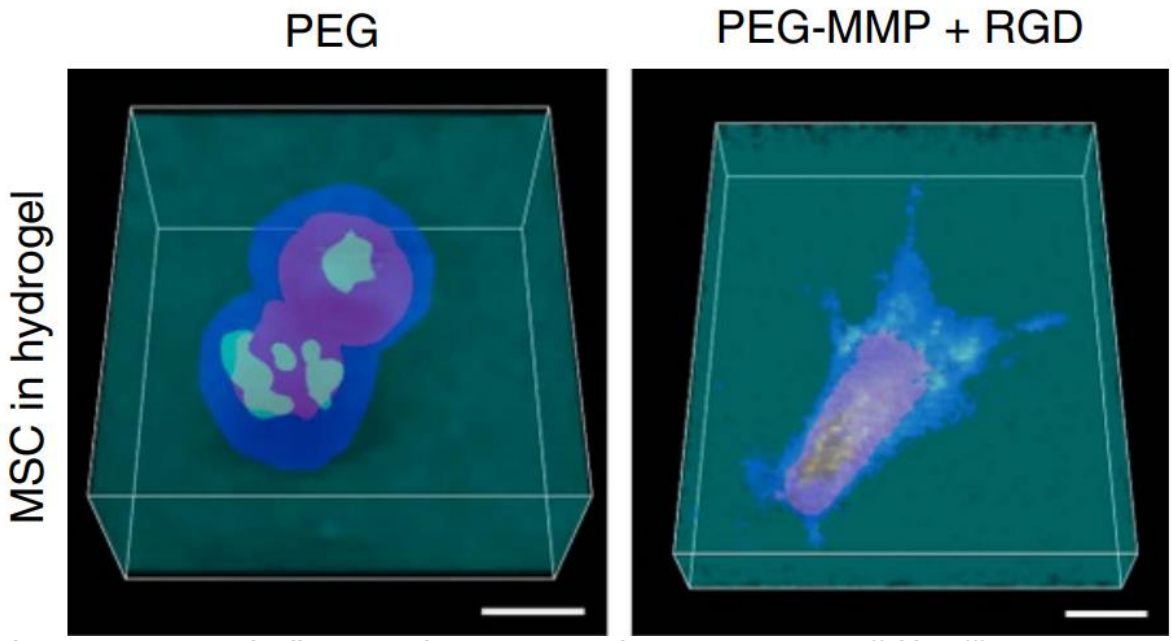

Figure 1.2 – Compared cell response between PEG and PEG+MMP+RDG scaffolds: *Different components such as cytoplasm (blue), nucleus (red), TAGs (green) and PLPs (orange) illustrate the difference between inert (left) and functionalised (right) scaffold materials with VRM* [32]*, scale bar = 10 µm.*

The hMSC in the inert hydrogel retains a spherical morphology, with a more natural morphology observed in the PEG-MMP+RGD environment [32]. Observing the cells in three dimensions provides the researcher with greater detail and an image that can be rotated to show different angles, providing a more thorough inspection. The additional perspective provided by the VRM comes at increased complexity due to the optical considerations described in section 1.3. Figure 1.3 shows MCF-7 cell mitosis using a VRM with collections over a 1× 1×1 µm array, including the 1 µm steps along the z-axis [33]. The trans and gauche (A) conformations are visualised with the methyl peak, associated with the 2870 cm^{-1} peak for the gauche conformation (B) shown in green, and blue intensity for the trans conformation (C) related to the 2850 cm^{-1} intensity, and the 2870/2850 cm^{-1} ratio (where a large ratio relates to ordered lipids) to visualise in red (D). The ordered lipids within the cell located primarily within the nucleus, and suggested as colocalising with the chromatin [33].

An advantage of VRM was demonstrated, with the ordered lipids (red) in relation to the green gauche conformation (E) [33]. However, a potential limitation is also highlighted, with the association of the ordered lipids to the nucleus, even during mitosis, exclusively shown in the nucleus region of the VRM. References highlighting the increased viscosity of lipids ratios with a lower gauche conformation (figure 1.3 F) [34] might result in the conclusion that the nucleus is comprised of only a high viscosity, ordered lipids, where it can only be concluded that they are present or most common in the nucleus. The VRMs of unordered lipids (B and C) impede the view of the nuclear region, potentially resulting in confusion, where the reader might only associate ordered lipids with the nucleus. Clarification is provided in the text, and Ramamurthy *et al* do show unordered lipids inside the nucleus in an earlier figure, potentially providing lower viscosity regions to aid nuclear separation during mitosis.

If presented alone, figure 1.3 highlights the care required when presenting a VRM and selecting shading parameters [5,6]. The reduced image resolution (figure 1.3 B-E) in the publication [33] makes it difficult to know the dimensions/scale of the mapped area. However, both methods shown in Figures 1.2 and 1.3 distinguish the nucleus from the cytoplasm, assigning spectral insight to physical locations within the cells. The advantages described can be reinforced by the publication of VRM resolution justification, shading parameters [5], transparency, and opaqueness settings used in the VRM production for a systematic, repeatable method to be available to subsequent VRM research.

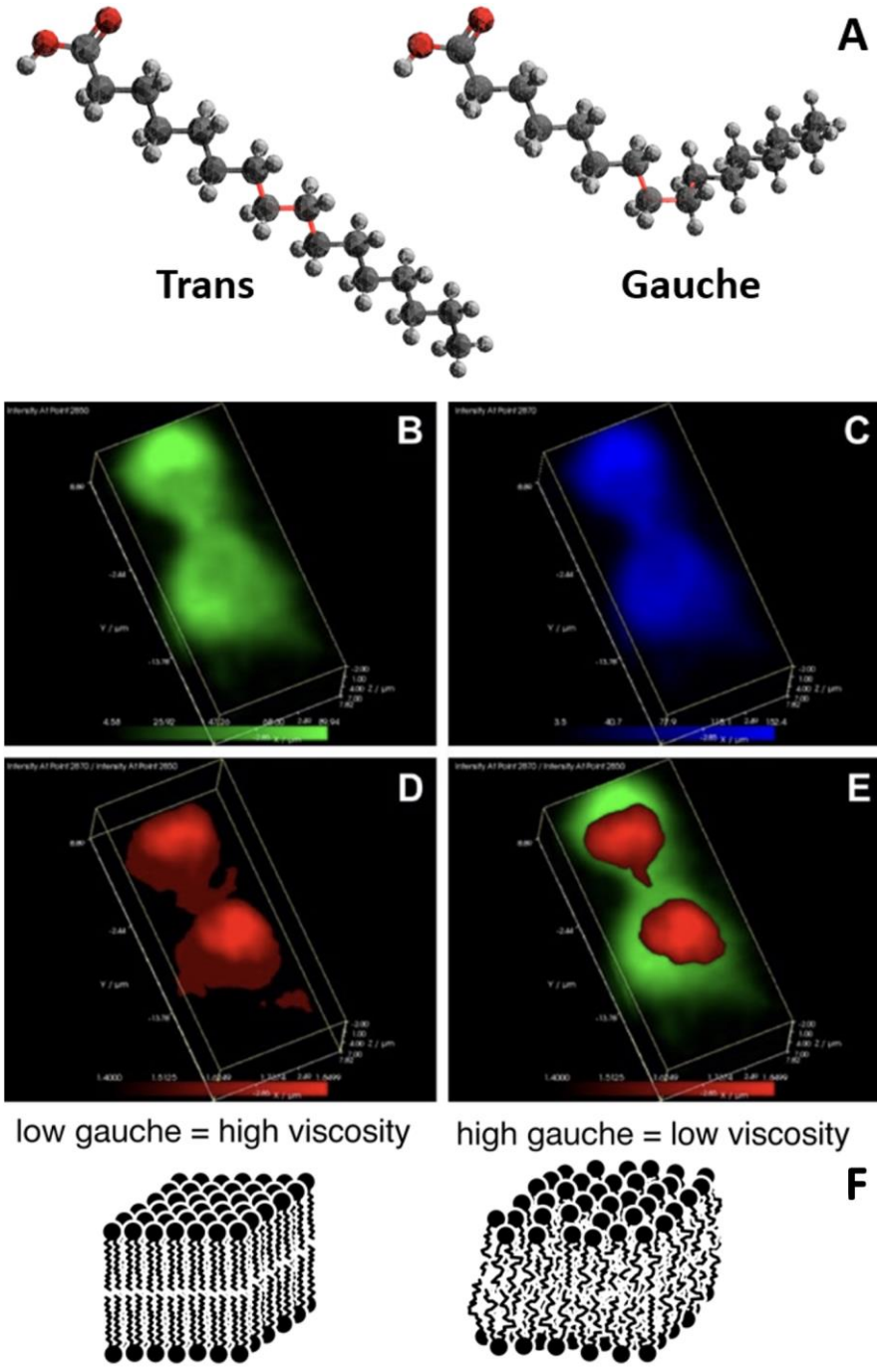

Figure 1.3 – 3D Raman of mitosis: *A) Molecular structure of the trans and gauche conformations* [34]*. B) 2850 cm^{-1} lipid methyl in gauche conformation (green), 2870 cm^{-1} lipid methyl in the trans conformation (blue), C) 2870/2850 cm^{-1} ordered lipids (red), E) 2870/2850 cm^{-1} overlapping 2850 cm^{-1} lipid methyl peak (green)* [33]*, F) High and low viscosity trans/gauche ratios, relating to the low and high gauche respectively* [34].

1.2.3. Live-cell Raman

Live-cell Raman analysis has found application in immunology [35], and cancer research [36]–[38] and is preferable over fixed cell analysis whenever practical. Biological samples are typically fixed or preserved with formalin, allowing the samples to be more easily transported and analysed at the will of the researcher, removing the risk of a sample becoming unviable. The disadvantage of fixed or preserved samples during vibrational spectroscopy analysis is that the samples are dead and therefore incapable of responding to further stimulation. Observing an individual cell before and after a biochemical or physical event removes the possibility of inter-sample variance. In vibrational spectroscopy, ethanol, methanol, paraformaldehyde, formalin, and formaldehyde have all been shown to degrade Raman signals for biological molecules within the nucleic acid and protein regions [39]. Live cell Raman avoids these contaminants, as well as unfixed cell analysis. Unfixed Raman analysis is defined as the analysis of cells that are not fixed and technically alive at the time of analysis, but are not fully supported with the correct temperature, nutrients, and CO_2 concentration, which is also advantageous when a fully live cell is unavailable.

During live-cell Raman, the cells are maintained in conditions close to an incubator, with controlled temperature (typically 37 °C) and CO_2 concentration (5%) in an incubation chamber that fits around the objective. The drawbacks of fixed cell analysis are therefore avoided, at the cost of simplicity, allowing individual cells to be monitored during fluctuations in their biochemical state. Changes in the molecular composition of a cell may be due to cell cycle, biochemical, or physical stimulation. Cells can be analysed in phosphate buffered solution or cell culture media, where a low protein content culture media is preferable to minimise protein spectral peak contamination. Live-cell Raman should be distinguished from unfixed-cell Raman analysis, where Raman spectra are collected from living cells without any provision for their capacity to proliferate (temperature and CO_2 levels). In unfixed Raman spectroscopy, cells are not dead yet but collections from cells under distress erode the benefit of analysing living cells.

The collection time is a key variable in live-cell Raman analysis, as cells are free to migrate away from the collection (especially for Raman mapping), incentivising optimised experimental variables to maximise the Raman signal and minimise collection time. Studies have compared different experimental variables such as substrates [37], cell culture media, and data acquisition methods (point vs. line) [37]. Different lasers (488 vs. 785 nm) were compared and the extent of photodamage was observed using ratios of spectral peaks (2870/2850 cm^{-1}), with the 785 nm producing less photodamage [37]. Different collection methods, point, line, and map were also compared, finding ten-point line collections to be as accurate as a map [37]. However, maps do provide increased morphological insight and are possible for live-cell Raman [35], [37], demonstrating the potential for the possibility of live-cell VRM, despite the probable necessity for a reduced resolution to minimise collection time [37]. VRM inherently takes longer than a Raman map of the same dimensions. But by analysing sections of a cell, rather than a whole cell, potentially the collection time may be brought down enough for live-cell VRM.

1.3. Confocal Raman optics theoretical background

The purpose of a Raman map is to assign a Raman signal to a position within an area, allowing changes in Raman intensity to be observed over the area (or through a volume for VRM). The more accurately the signal is assigned to each location, the higher confidence researchers can have in conclusions drawn from the map. Three optical factors that affect the apparent origin location of a detected photon are diffraction [40], [41], refraction [7], [41], and out-of-focus contributions [30], [42], which must therefore be considered when carrying out Raman mapping in two and three dimensions. Diffraction is the most widely understood and accounted for in microscopy and spectroscopy, through the calculation of a point-spread function and the convention of spacing Raman spectra a minimum of 0.5 the diameter of the Airy disk for lateral Raman mapping. Equation 1 was though to indicate the axial

resolution for confocal Raman systems [40], [41], where n is the refractive index of the material, λ is the irradiating laser wavelength, and NA is the numerical aperture of the objective. However, for sub-surface analysis, it has previously been shown that this convention is insufficient [20], [41].

Equation 1 [40]: $Diffraction\ limit\ (DL) = \frac{4n\lambda}{NA^2}$

1.3.1. Confocal systems

In Figure 1.4 (A), an idealised diagram shows the Raman systems focusing lens, located in the objective, focusing a laser beam to its maximum intensity, a volume of L length, and d_o diameter. L and d_o describe the collection area and the volume of maximum focus for the given equipment (laser & objective) being used. The length from the objective that the collection area is (the depth-of-focus) is calculated as shown in section 1.3.2. Confocal systems aim to exclude photons originating outside the collection area, improving the confidence a spectroscopist has that a Raman signal originated in the expected location (the collection area). Figure 1.4 B shows photon paths after Raman scattered photons are randomly scattered from the molecular bonds, some of which align with a path leading through the confocal aperture (C - green), which is the position closest to the centre of the collection area. In theory, photons from positions outside the collection area (A – red & B – blue) are excluded from passing through the aperture onto the detector.

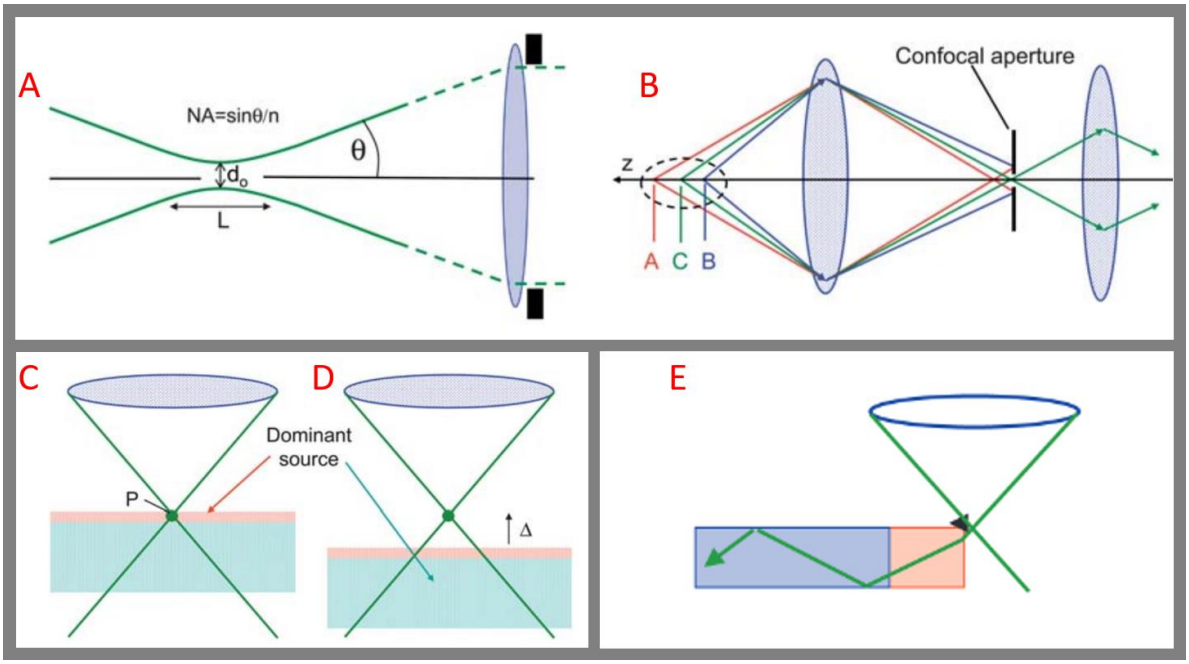

Figure 1.4 – Confocal systems and limitations: *A) Laser focus through a lens to a minimum diameter (d_o) and length (L). B) The confocal aperture blocking photons from outside the intended focal depth (A & B), whilst allowing the intended photons (C) through. C) Photons from two different materials are detected from the focal point P, showing the limitations of confocal systems. D) Shows the detection of photons when the focus is off the sample. E) Material 1 (blue) is seen in a spectrum when the laser is focused to the side, through material 2 (red), resulting from photon migration through the materials.* [42]

In practice, photons have been shown to reach the detector from outside the collection area, known as out-of-focus contributions. In C & D, two examples demonstrated by Everall [42] of Raman scattered photons from below the collection area are shown, with the focus on a thin layer (C) resulting in spectral peaks being produced from the substrate in C, and spectral peaks being produced when the laser focus is above the sample altogether in D. The out-of-focus contributions originating below the collection area seem reasonable, as their original position may happen to align with the confocal aperture. In E, Everall [42] showed a case where photons travel through samples. Polyethylene terephthalate (blue) contributed to spectra as well as the polyethylene (red) that the laser was focused on, showing that out-of-focus contributions can occur laterally from the collection area as well as axially. The inclusion of photons from outside the collection area is reduced by the confocal system. However, the confocal aperture cannot be assumed to remove all out-of-focus contributions, increasing VRM complexity further, alongside depth distortion,

and the non-trivial shading process required even with conventional (lateral 2D) Raman maps [5].

1.3.2. Refraction

Depth distortion results from several factors during sub-surface Raman analysis. One limitation is the collection areas link to the diffraction limit, resulting in a collection area typically three or more times larger in the z-axis that x or y [41]. Another collection area distortion occurs if the refractive index changes between the objective immersion fluid (air, water, media, etc.) as it is stretched increasingly with depth as discussed by Neil Everall previously [7] Figure 1.5 shows how the laser focus is altered at the sample surface (A) relating to the change in refractive index between the immersion media (n_1) and the sample (n_2). The increase in the depth resolution (DR) is shown in Figure 1.5 B and C, where the size of DR increases from DR_1 to DR_2 as the laser is focused on an increased depth position. Depth distortion results when the asymmetry between the lateral and axial diffraction limits and the change in DR are not accounted for. A solution proposed for the mismatched refractive indices was oil immersion objectives (Figure 1.6), where refractive index matching oil (B) can be used to significantly improve depth collection when compared to the uncorrected axial Raman map in A [7]. Oil immersion minimises depth distortion [7] but is inappropriate for live-cell Raman analysis, providing a need for a solution to depth distortion in live-cell Raman z-axis analysis.

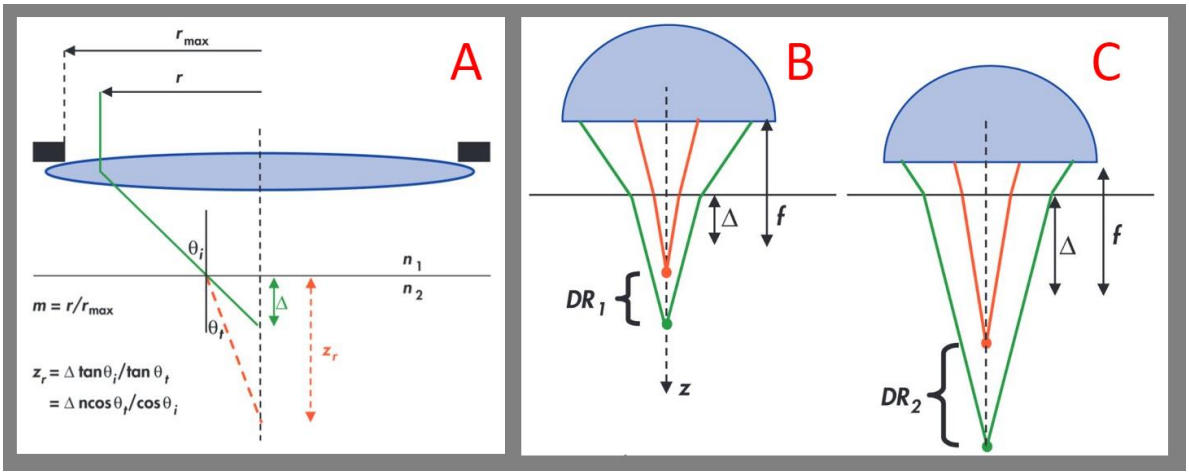

Figure 1.5 – Laser focus refraction: *A) Showing the altered angle (red line) and depth (Z_r) of compared to the expected focus (green line) and depth (Δ). B-C) The increasing change in depth resolution (DR) as the focal depth (Δ) increases.* [30]

The importance of accounting for depth distortion was demonstrated by Lambert et al [43]. Lambert et al demonstrated how depth distortion is calculated before Raman analysis through an experiment carried out on multi-layer paint for the automotive industry [43]. The investigation aimed to determine the best method of analysing a basecoat layer of paint through a transparent clearcoat, without the clearcoat altering the spectra [43]. A range of equipment options including different factors that could alter the Raman analysis was compared including equipment, settings, and sample preparation [43]. The equipment options included laser mode (edge or streamline), laser wavelength (488 nm, 514 nm, 633 nm, and 785 nm), and objective (5×, 20×, 50× and 100×) were analysed [43]. The settings balanced were the accumulations (1 or 5) and exposure time (10 or 50 seconds) [43]. Sample preparations considered were support material (aluminium or glass), pigment type (varnish of metallic), and sample preparation (microtome) [43]. Statistical analysis found that the only factor with statistical significance was the sample preparation, with a p-value of 0.0485, leading to an investigation into the effects of surface finish and depth [43].

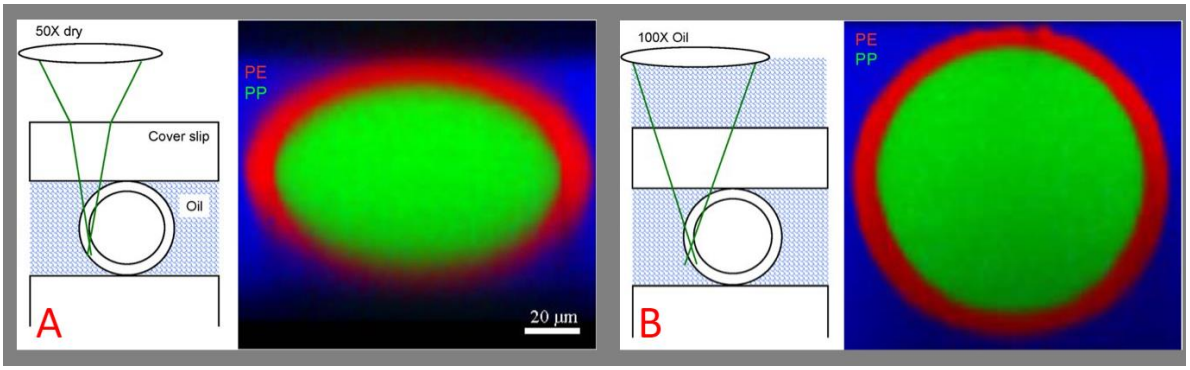

Figure 1.6 – Refractive index matching: *A) The compressed view of a polymer thread cross-section (compared to known diameter) collected using an air-immersion objective. B) A cross-section image of the same polymer thread where refractive index-matching oil is used to avoid depth distortion.*[7]

Different materials require tailored experimental designs, for example, the use of a 532 nm laser is applicable for OrmoComp™ but a 785 nm must be used for IP-Dip [6]. Factors not found to be of significance for a material may similarly have an effect in a different situation. The individual considerations of individual materials demonstrate the importance of applying the findings of Neil Everall, who published equation 2.

Equation 2 [7]: $Depth\ resolution\ (DR)\ = \Delta\left[\left[\frac{NA^2(n^2-1)}{1-NA^2}+n^2\right]^{1/2}-\ n\right]$

In the depth study, a 785 nm laser was used to reduce fluorescence alongside a 100× objective [43]. Equation 2 calculated the true acquisition range for the material. The values for the variable are numerical aperture (NA) = 0.85, the refractive index of the material (n) = 1.6, and the intended acquisition depth (Δ) altering, and the result is graphed with the intended acquisition depth and the actual acquisition range from the lower limit (nΔ) to the higher limit (DR + nΔ) [43]. The conditions in Lambert et al resulted in a -20 µm intended acquisition depth resulting in a collection range of -32 µm to -51 µm [43]. Carrying out pre-calculations allowed the use of an acquisition depth of -25 µm, avoiding clearcoat contamination of the sample [83]. Clearcoat contamination would have occurred had the depth resolution calculation not been carried out, with significant spectral contamination resulting [43]. Although

biological samples provide increased complexity, mixed refractive indices are not directly comparable to paint where surfaces can be polished. The principle can be applied to biological studies and has in the case of melanoma [44].

Chapter 2 - Literature review and methods

2.1. Introduction

Vibrational spectroscopy can produce spatially resolved quantitative chemical information. The quantity of a molecule within a sample is directly proportional to the amount of Raman scattering within that location [21]. Unfortunately, Raman scattering is not exclusively affected by molecular concentration within a sample. The range of factors influence Raman intensity can be broken into three main considerations, the laser [45], [46], the confocal system [40], [41] and the sample [7], [20]. Pre-processing of collected data prior to analysis and calibration of the results typically focuses on the differing laser conditions. Laser wavelength selection aims to balance fluorescence, photo-degradation and signal-to-noise ratios depending on the sample [21]. Rectifying spectral distortions that result from fluorescence, temperature/moisture variation and laser intensity fluctuation over time is carried out with normalisation, baseline correction, smoothing and scaling [47]. For quantitative measurement, partial least squares has calibrated quantitative Raman pharmaceutical measurements [45], [46]. The influence of the confocal system and sample are rarely considered, even in volumetric Raman mapping (VRM), where the laser and corresponding Raman intensities can fluctuate drastically within a single sample [7], [20], [40], [41] .

The purpose of this thesis is to first demonstrate the effect that confocality, confocal variables (microscope objective, pinhole size etc.) and the samples optical properties have on Raman measurement. An approach of maximising quantitative accuracy through the utilisation of micro-engineered cell scaffolds as a means of calibrating VRM collection is then presented. This chapter begins by providing a foundation in general confocal and Raman specific optics, informing the techniques applied through this thesis. The theory underpinning direct laser writing (DLW) is

then described alongside the materials and application of previous DLW scaffolds for cell behaviour, influencing the design of scaffolds in later chapters. Finally, the theory of chemometric techniques used for calibration and false-colour shading of VRM produced will provide context for false-colour shading.

2.2. Literature review (Part A: Cells and scaffolds)

2.2.1. Direct laser writing

Direct laser writing is a two-photon polymerisation printing process, where the energy to initiate free-radical polymerisation is provided by the simultaneous absorption by a bond of two photons [48]. The amount of energy required to excite the initiator into producing free radicals is a distinct amount known as the band gap, bridgeable by a single photon during linear absorption [49]. Absorption excites the molecule, resulting in a heat effected zone (HEZ) that induces free radical polymerisation within a confined focal region, known as a voxel [49]. The resolution for linear polymerisation is the diffraction limit, with the smallest resolvable distance given by 0.5λ/NA, where λ is laser wavelength and NA is numerical aperture. To increase the resolution past the diffraction limit, two-photon absorption is required [48].

Direct laser writing (DLW) therefore uses simultaneous two-photon absorption (TPA) predicted by Göeppert-Mayer in her 1931 doctoral dissertation [48], winning her a Nobel prize. The simultaneous TPA process requires two photons to hit the bond at the same time, hence known as simultaneous [48]. During the simultaneous TPA process, two photons of half the band gap energy combine to bridge the gap through an imaginary excitation level [48]. In two-photon polymerisation, band gap bridging is used to produce a voxel of energy that results in local free-radical polymerisation [48]. The voxel is moved in a layered fashion to build the 3D structure with an

accuracy that can be reduced to below 100 nm when femtosecond (10^{-15}) lasers are used, such as in the Nanoscribe™ system [49].

Femtosecond lasers provide short (10^{-15} second) laser pulses, critical to improving the resolution of the printing [49]. Reducing pulse width of the laser bursts alters the thermal diffusion l_d, which for a pulse within the femtosecond range is faster than the electron-photon coupling time in laser-matter interactions (approximately 1-100ps), under these conditions l_d is calculated with equation 3 [49].

Equation 3 [49]: $l_d = [\frac{128}{\pi}]^{\frac{1}{8}} [\frac{DC_i}{T_{im}\Lambda^2 C_e'}]^{\frac{1}{4}}$

D is the heat conductivity, C_i is the lattice heat capacity, T_{um} is the melting point, Λ is the electron-photon coupling instant and C_e' is calculated with equation 4.

Equation 4 [49]: $C_e' = \frac{C_e}{T_e}$

In equation 4, C_e is the electron heat capacity and T_e is the electron temperature [43]. Under the conditions, l_d = 329 nm for copper, where T_{im} = 1356K. A laser pulse of greater length than the electron-photon coupling results in the calculation of l_d being carried out with equation 5, where κ is the thermal diffusivity [49]. Calculating with equation 5 results in l_d = 1.5 μm for copper when τ = 10 ns, clearly shows the difference in the diffusion length, reducing the HEZ. The piezo setting produces the option for highly accurate printing with Nanoscribe™, dependent on the material.

Equation 5 [49]: $l_d = \sqrt{K\tau}$

Material selection also affects the resolution of DLW printing, which must be balanced against a range of other factors including biocompatibility and suitable refractive index [6], [7]. Biocompatibility is a diverse term which in this project will be defined as; non-toxic to the cells during the culture time frame, adhesive to the cells directly or capable of protein coating and non-reactive to culture media. The material must be a photoinitiated whilst being providing a suitable surface for cell culture, have a defined refractive index (Chapter 1, section 1.3), and be a Raman scattering material. A key feature that a material used for low-feature Raman mapping cells on scaffolds should have a bio-distinct region, allowing separation of the scaffold from biological samples within the map. A range of IP resists are available from Nanoscribe^{TM}, including IP-Dip, IP-S and IP-L that have been used widely in biological studies [50]–[52], with refractive indices of ~1.54-1.57. IP-Dip is a low viscosity, high accuracy material previously used in a study exploring the effect of different groves, on cell migration speed [50]. OrmoComp^{TM} by comparison suffers from post-printing shrinkage, reducing accuracy, but has previously been mapped with cells using VRM [6], using the bio-distinct 1715-1750 cm^{-1} region. Fibronectin was selected for cell adhesion, having previously been used to functionalise DLW scaffolds [6], [53].

2.2.2. Directing cells using substrate surfaces

Section 2.2.1 outlined DLWs capacity to fabricate nano-tolerance substrates and scaffolds, but how can this help discern changes in cell behaviour? HaCaT PEG and co-polymerised pentaerythritol tetraacrylate-PEG (PETA-PEG) in Figure 2.1 [54], where PEG resists protein coating, impeding cell attachment to regions outside of pre-defined square blocks. As the percentage of PETA in the co-polymerisation rises, the protein coating allows increasing motility to the cells [54]. The experiment not only demonstrated the ability of the substrate material to encourage or impede cell migration, but the ability to influence cell morphology, with the cells forming a square morphology in the 0 and 4.8% PETA percentages in a, b, e & f.

Material choice and coatings are not the only way to influence cell migration using substrates. Nano-pores produced in SU-8™ photoresist used to increase the migration and neurite outgrowth, having overcome SU-8™ leaching cytotoxic contaminants into cell cultures previously [55]. The nanopores were compared to poly-L-lysine (PLL) coated surfaces and uncoated flat surfaces, producing similar migration and neurite outgrowth to the PLL coating (24.3%) an improvement on the 1.1% seen on the bare surface [55]. The effect of the nanopores was further demonstrated by the migration of neurons to a nanoporous area of a plate when a region was kept flat, where in Figure 2.2) it can be seen to determine the region covered by the cells [55]. The change in cell behaviour raises the question into how the change in morphology (Figure 2.1) and migration (Figures 2.1 & 2.2) are regulated by the cells.

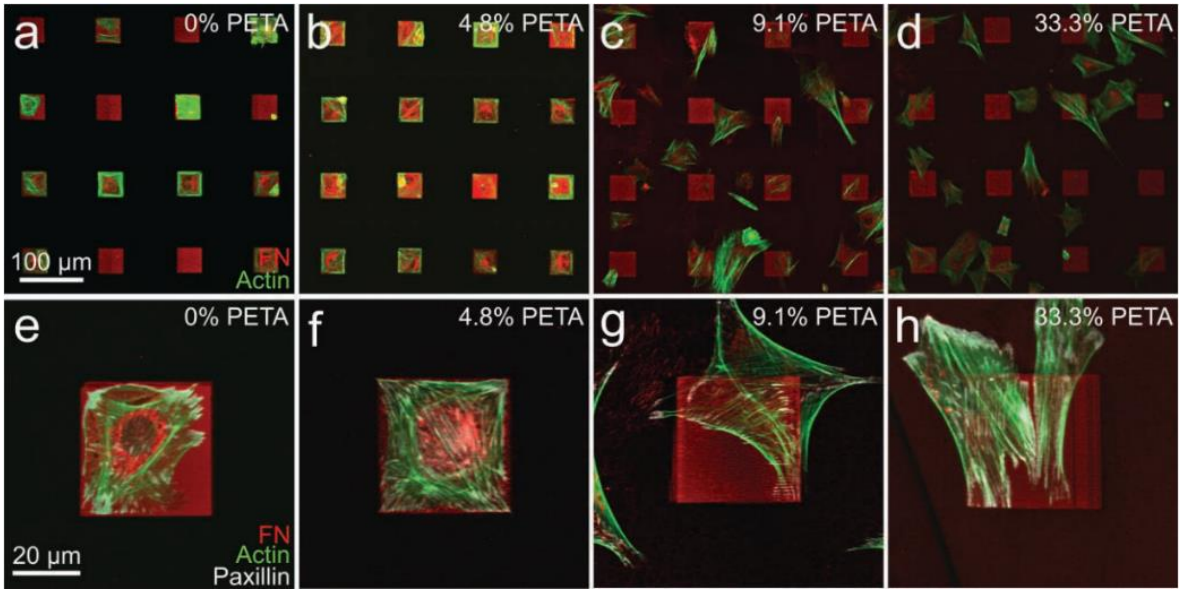

Figure 2.1 – PEG/PETA cell adhesion comparison: *The increased cell motility correlating to larger PETA percentage (0, 4.8, 9.1 and 33.3%) in PEG-PETA composite demonstrating PETA cell adhesion* [54].

D. Cheng *et al* demonstrated DLWs capacity for producing surfaces for migration studies and IP-Dips suitability for the purpose [50]. The combination of DLW and gene inhibition with NSC23766 was used to investigate the influence of the Rac1 on neuronal cell migration over wave patterns of square, triangle and sine on cell migration [50]. Initially, the different wave geometries were compared, finding that

the square wave was found to produce the fastest migration, followed by the triangle and the sine wave producing the slowest migration [50]. Rac1 gene inhibited cells were found to have increased directional migration on flat surface whilst reducing it on the sine waves [50]. The reason for the change in behaviour was determined to be Rac1 repressing directional behaviour on flat surfaces whilst being important for topography-induced directional migration [50]. The ability to demonstrate how a gene influences cell migration over different surfaces, alongside how different substrate geometries influence cell behaviour like migration, raises questions about how three-dimensional cell scaffolds can direct cell behaviour. Including a depth dimension to the substrate using different grove geometries incentivises the investigation of two- and three-dimensional environments as part of the thesis investigation. Asking whether difference between substrate/scaffold geometry and dimensions can be detected using Raman spectroscopy.

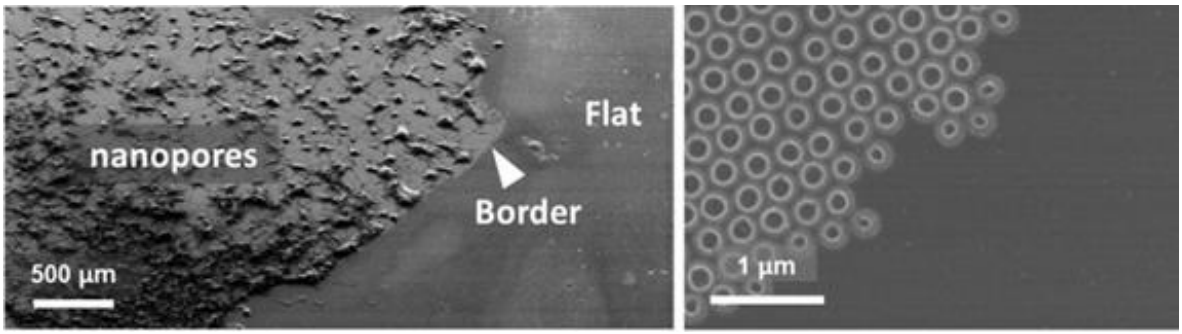

Figure 2.2 – SU-8™ Nanopores: *Demonstrating the nanopore capacity of SU-8™, with the scale shown (right) and their effect on cellular behaviour (left) where cellular expansion is constrained within the nanopores border highlighted* [55].

2.2.3. Cell response to 3D scaffolds

Three-dimensional scaffolds, fabricated in OrmoComp™ using DLW have been applied to directing pluripotent stem cell derived neuronal cell behaviour [56]. The OrmoComp™, an inorganic (Si-O-Si)-organic hybrid polymer (refractive index ~1.51-1.53 [57]), with previous applications for Raman investigation of cells [6], [53], [58] was laminin coated [56] to aid cell attachment (Figure 2.3). The advantage of repeatability provided by DLW was clearly demonstrated through repeat

experiments. For example, four copies of the scaffold were printed, aiding the verification of findings. The paper reported cells appearing to migrate towards the structures with promising neurite guidance. Figure 2.3 showing neurite stained green (MAP-2) travelling along the scaffold channel, suggesting the possibility for DLW printed scaffold directing of neurite growth [56].

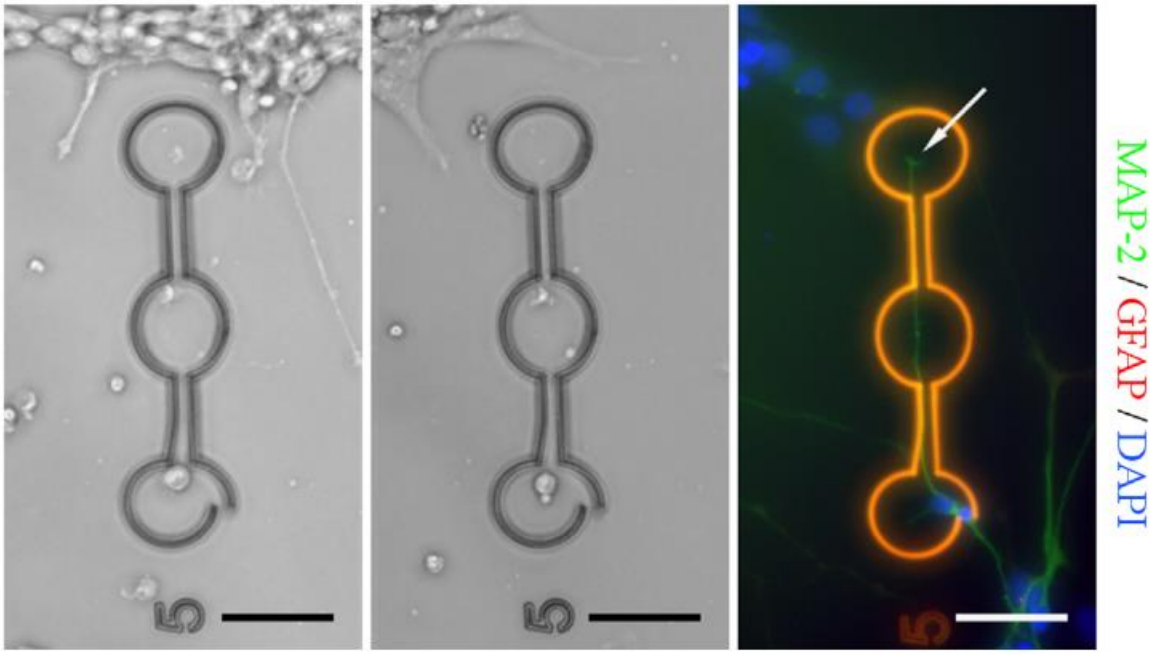

Figure 2.3 – Neuron direction: *Neuronal cell directed by OrmoComp™ scaffold and stained for markers MAP-2 (green), GFAP (red), and DAPI (blue) for nuclei* [56], [59]*, scale bars relate to 50 µm*

More recently, the same group took the DLW printed scaffold process further, printing towers to study more complex 3D structures and their effect of neuronal culture [59]. Figure 2.4 shows the scanning electron microscope (SEM) image and confocal image stacks, immunocytochemically stained for neuronal markers MAP-2 (green), β-tubulin III (red), and DAPI (blue) for nuclei [59]. The neurons clearly produce neurite “bridges” extending from the towers and crossing to other towers, demonstrating DLWs capacity for true 3D culture of cells [59]. The use of SEM and confocal allows different aspects of the study to be interrogated, SEM providing high resolution and the confocal (and staining) providing molecular data [59]. The

combining of spatial and chemical information would clearly be an advantage, allowing information to be determined in a single process.

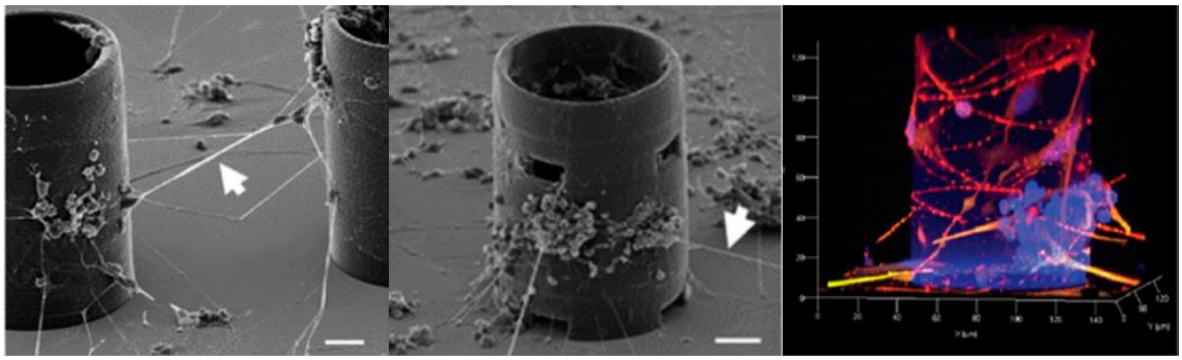

Figure 2.4 – Neuron towers: *3D culture on towers to monitor neurite development and stained for neuronal markers MAP-2 (green), β-tubulin III (red), and DAPI (blue) for nuclei* [56], [59]*, scale bars relate to 20 µm*

2.2.4. 3D scaffolds used to test cell behaviour.

Three-dimensional scaffolds provided support for a wider and directed range of neuronal cell growth in section 2.2.3 when compared to the flat surfaces in Figure 2.5. An area of interest in this thesis is exploring how DLW printed scaffolds can be used to determine differences in cell behaviour. A study exploring the metastatic potential of different cell lines [60] (MCF-10A, MCF-7 and MDA-MB-231) used DLW cages, printed from IP-L (refractive index ~1.51-1.53) [57]. The migration of the sub-type through the cage was used as a means of gauging the metastatic potential of each sub-type [60]. The higher the metastatic potential, the greater its capacity to spread from the primary site, through the vasculature system and initiating secondary tumours. The more metastatic tumours spreading through the cage demonstrated the capacity of DLW to target specific biological characteristics, such as the metastatic potential of a biopsy [60]. The application of vibrational spectroscopy could increase the diagnostic power of a scaffold invasion assay. Vibrational spectroscopy distinguishes tumour sub-types and grades [61], providing

the biomolecular composition providing key information alongside the physical invasion of the scaffold. The advantages of IP-resists must be balanced against the fluorescence induced by laser wavelengths such as 532nm [6] and a limitation in properties that could be manipulated with a self-produced resist.

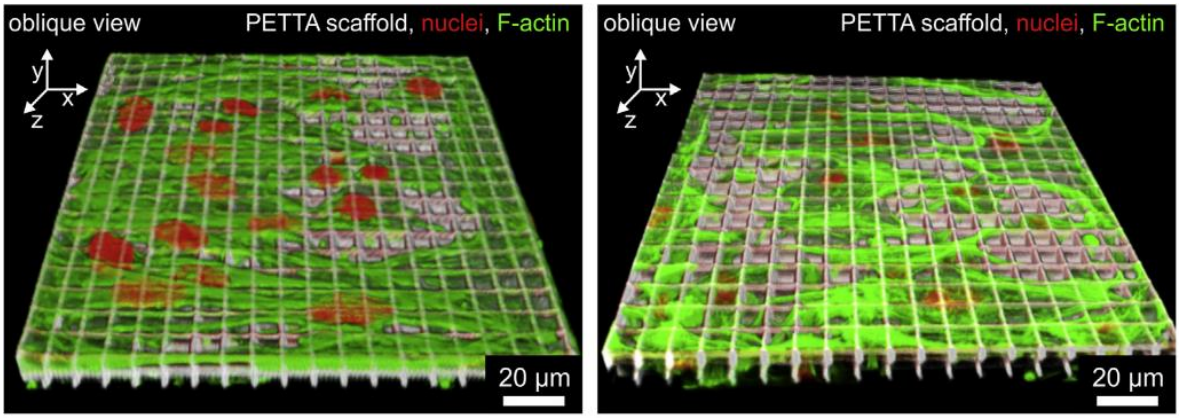

Figure 2.5 – Invasion of log stack scaffold: *Cytoplasm (green) of mouse embryonic fibroblasts (MEF) is shown in both images but nucleus (red) is submerged in Lamin A gene knock out (left), illustrating Lamin A/C effect on nuclear stiffness* [62].

In another study, genetic changes for 3D scaffolds as was seen in section 2.2.2 for Cheng *et al* and the effect of the Rac1 gene [50]. Pentaerythritol tetra acrylates (PETAs) use alongside Irgacure® 379 photoinitiator (Ciba®) during fabrication of an invasion scaffold for A549 cells (human lung carcinoma cells), Wildtype mouse embryonic fibroblasts (MEF WT) and Lamina A gene knocked out (lmna-/-) MEFs (MEF lmna KO) [62]. A range of log stack scaffolds were produced with 2×2 µm, 5×5 µm & 10×10 µm meshes to allow changes in invasiveness of the scaffold to be monitored over different pore sizes [62]. Demonstrating the effect the scaffold surface and geometrical environment has on the cells of the same type. The Lamin A gene were then knocked out because it is responsible for expressing the Lamin A/C intermediate fibrils [62]. Lamin A/C was shown to be responsible for nuclear stiffness through measurement of the nucleus through atomic force microscopy [62]. The reduction in nuclear stiffness is shown to increase invasiveness in MEF lmna KO cells (Figure 2.5 right), then the MEF WT cells (Figure 2.5 left) [62]. The MEF WT cells clearly sitting on the scaffold surface, leaving more nuclei (red) sitting on top of

the scaffold. Greiner et al clearly demonstrated the ability of one variable (mesh size) to provide conclusions on the physical effect of a single gene (Lamin A) [62]. The cell adhesion property PETAs demonstrates its suitability for cell behaviour analysis platforms.

In a second stage to their experiment Greiner et al printed a second scaffold onto a porous membrane, resting it upon chemoattractant to determine its effect on driving invasion [62]. The inclusion of chemoattractant resulted in the A549 cells being found to be more invasive when a chemoattractant was used but no significant difference was reported in the MEF cells compared to the previous stage of the experiment [62]. The two-stage experiment demonstrated the benefit of high tolerance printing. The production of repeatable conditions that allowed the influence of a single variable (pore size) to be compared to others such as nuclear stiffness or a chemoattractant.

Greiner et al and the other studies discussed through sections 2.2.3 and 2.2.4 demonstrate the wide range of investigations that demonstrate the advantage of nano-tolerance printing. The varied experiments were all limited to external imaging of the constructs with staining used to highlight key biochemical features, making sub-surface analysis an area of progress within the field. One technique capable of providing increased information is Raman spectroscopy. Confocal Raman microscopy produces chemical maps that combine spatial resolution with chemical composition [6], potentially in live cells [20]. The use of confocal Raman can bridge the gap, allowing researchers to monitor internal interactions between the cell and scaffold both spatially and chemically.

2.2.5. VRM of cells on DLW scaffolds

The previous studies discuss in section 2.2.4, justifies the exploration of VRM as a method of combining the spectral analysis used for molecular investigation (distinguishing Lamin A/C +/-), with the 3D microscopy mapping. The use of VRM allows for a 3D image to be produced that projects molecular features determined using spectral inspection through the volume. In their study, Baldock et al showed the capacity of VRM to map cell on DLW printed scaffolds [6]. A log stack scaffold

was printed from OrmoComp™ and seeded with a CaCo2 cell [6]. A clear advantage of using OrmoComp™ for cell-scaffold VRM was shown in Figure 2.6, with the bio-distinct spectral band allowing the nucleus (blue), cytoplasm (green) and scaffold (yellow) to be viewed in isolation, highlighting the interaction between the cell and the scaffold [6]. The reference highlighted the increased difficulty in selecting shading parameters, alongside the optical considerations discussed in Chapter 1. Having demonstrated the uses of DLW printed scaffolds and the application of VRM to map cells on them, an overview of the different chemometric/machine learning techniques that can be used to interrogate the spectral dataset further will be provided next.

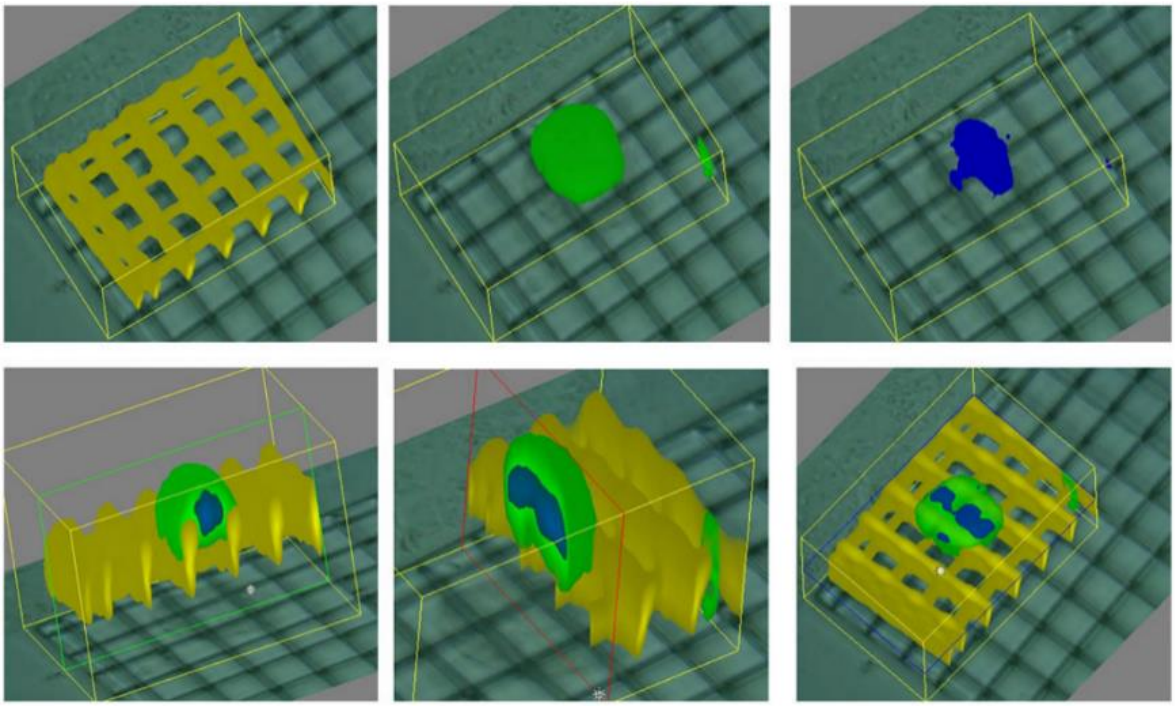

Figure 2.6 – Cell-scaffold complex: *3D Raman mapping of a CaCo2 cell seeded onto an Ormocomp™ scaffold printed by direct laser writing. Demonstrating the capacity of Raman to highlight the nucleus (blue), cytoplasm (green) and scaffold (yellow) with the correct scaffold material selection* [6]*, map dimensions are 65 × 43 × 44 µm*

2.3. Literature review (Part B: Dimension reduction and machine learning)

Sections 2.2.3 and 2.2.4 showed substrates and scaffolds influencing or directing cell behaviours like migration and invasiveness and verified the physical impact on cells relating to the Rac1 [50] or Lamina A genes [62]. Raman spectroscopy was highlighted as a method of combining three-dimensional imaging/mapping (VRM) with spectral analysis in section 2.2.5. The findings from section 2.2 inform a hypothesis for the thesis that Raman spectroscopy can be used to monitor cellular response to scaffold geometry. A future application would be the use of Raman spectroscopy to monitor the production of bioengineered constructs. Technical challenges in producing VRM like the one shown in section 2.2.5, were discussed in Chapter 1 (section 1.3), the use of spectral analysis is typically complemented with the use of chemometrics, the topic of Part B of the literature review.

It is common to prior to comparison of two Raman spectra, or inspection of a single spectrum, to carry out some pre-processing. The most common types of processing that are caried out before inspection or comparison are smoothing, baseline correction, and normalisation, although other kinds of pre-processing are available. Smoothing is used to remove random noise. Baseline correction remove baselines typically caused by fluorescence. Normalisation or scaling are used to minimise differences in spectra resulting from fluctuations in collection conditions, like detector temperature, or laser differences in laser focus between different collections. The pre-processing in through this thesis (see methods section 2.4.4.) was kept consistent with the aim of maximising comparability of results, with some exceptions resulting from Covid-19 induced unavailability to software. The kinds of chemometric analysis used through the thesis will now be described and compared to alternatives, providing a background and justification for their use.

2.3.1. Principle component analysis

Principle component analysis (PCA) is an unsupervised (chemometric or dimension reduction) technique. Chemometrics is a term that describes statistical methods for the analysis of chemical systems, which PCA is when applied to vibrational spectroscopy. PCA is a dimension reduction method as it transforms the data, allowing insights to be determined from fewer dimensions (features in data science and wavenumbers in spectroscopy), reducing complexity and computational costs from larger datasets [63], [64]. Being unsupervised and interpretable makes PCA ideal as an initial analysis, as unsupervised methods do not use sample labels, increasing objectivity during the data exploration stage of the analysis. In spectroscopy, the data set is collected into an n×m matrix (X), where n is the number of observations (points analysed in a scan) and m is the measurements (spectra of that point) [64]. The definition of Principle component analysis is the Eigen decomposition of X multiplied by X transpose (X^T) [64]. Eigen decomposition produces two matrices, the first (W) provides eigenvectors in each column [64].

The eigenvectors, known as the principal components (PCs) become the new axis [64]. The PCs are ranked largest to smallest, maximising the variance accounted for with the smallest number of PCs [64]. Variance is a measure of the spread of the data, it is calculating by squaring the distance each point is from the mean of the data set and dividing the result by the number of points being analysed [65]. By plotting the PCs in virtual space, the maximum information is retained whilst observable on a two- or three-dimensional plane (score plot). Producing a score plot that provides insights by forming clusters relating to the covariance between wavenumbers. The covariance reveals the interdependence of one wavenumber to another, indicating how they affect each other within the complex system. The second matrix provides eigenvalues (λ) that quantify the load (statistical importance) of each column (wavenumber) [64]. The column is given a value between 0 and +/- 1, the further from zero, the greater the wavenumber influences the PCs maximised variance [63]. By providing an indication of the wavenumbers responsible for the PC variance, the highly loaded wavenumbers can be investigated for links to a physical phenomenon, providing interpretability to PCA analysis.

PCAs limitation also relates to it being an unsupervised technique. Being unsupervised means that there is no input into the calculation to direct it towards the specific research question being asked. PCA finds new axes (dimensions) within the dataset based on maximised variance, this means that features within the dataset that may be unrelated to the experiment will be prioritised (have a higher loading) than subtler features that may be of greater interest to the researcher. The subsequent of different unsupervised and/or supervised methods may be required to focus the analysis once PCA has provided initial results. Relationships indicated by PCA add strength to any further conclusions, as they are present without any directing of the analysis. Variations/extensions of PCA include sparse-PCA [66] and kernel-PCA [67]. Sparse PCA highlights the most impactful features, wavelengths in a spectroscopy context, frequently to one or two key regions of the spectrum. Sparse PCA can, therefore, simplify interpretation but can oversimplify the results for biological analysis (where many molecules/peaks may need to be considered/balanced. Kernel-PCA provides non-linear dimension reduction [67], extending the kinds of relationships discernible through PCA (a linear technique) through the addition of a kernel (similar to support vector machines; section 2.3.5).

2.3.2. Cluster analysis

Cluster analysis assigns samples to groups (clusters), typically visualising the clusters in two- or three-dimensional plots using different colours for each cluster. The assignment of a spectrum to a cluster means that clustering can be used for qualitative shading of Raman/vibrational spectroscopy maps [68]. Forms of clustering used in vibrational spectroscopy are k-means clustering, hierarchical cluster analysis (HCA), and fuzzy C-clustering (also called soft k-means). Fuzzy C-clustering can assign probabilities of cluster membership to each point or pixel, essentially providing the capacity to describe the points (samples) relation to two or more clusters [69]. Assigning probabilities to each point provides the capacity to reveal a level of uncertainty when allocating labels to samples and potentially highlights regions of maps for further investigation. Uncertainty increases the

complexity in the context of mapping, the main application of clustering for this thesis. As a result of the limitation of fuzzy c-clustering, this thesis will focus on k-means clustering and HCA.

In k-means clustering, a researcher selects a k number of centroids [68], [70], suitable for the research question, or selected with the aid of an elbow plot. The features (wavenumbers) for each observation or element (spectrum) are then assigned to the centroid has the traditionally Euclidean, minimum distance from, forming a cluster [70]. The mean is calculated for each cluster and the distance between the means and each observation calculated, with each point then assigned / reassigned to the closest mean position [68], [70]. The new clusters that are produced have a mean calculated and the process is repeated until the clusters remain consistent [68], [70]. The entire process is then repeated iteratively N time, where N is determined by the researcher selects, with a thorough approach being to increasing N until the clusters remain consistent [70]. The clusters produced minimise variance within each cluster, whilst maximising the difference between clusters [70].

In Hierarchical cluster analysis (HCA), Euclidean distance is again commonly used, alongside other distance measures. Clusters are formed based on the distance between observations, either divisive clustering, where a single cluster is produced and then broken into incrementally smaller clusters, or more commonly agglomerative clustering, where the number of clusters starts as the number of observations and increasing numbers of clusters are formed as samples are grouped based on how similar they are. Dendrograms can be used to visualise how the samples have been split into the different clusters.

2.3.3. Machine learning assessment and validation methods

Sections 2.3.1 and 2.3.2 discussed unsupervised PCA and clustering methods, where assessing the separation of clusters is carried out using score plots (PCA), elbow plots (k-means), and dendrogram (HCA). The remaining algorithms are supervised methods, meaning that the class labels are used in the classification

calculations. Supervised learning methods have some general advantages, such as the easily saved models that can then be used to make predictions about new, unknown (unlabelled) samples. Another advantage of supervised learning is the researchers influence over the focus of the analysis through the labelling of the samples, meaning that the analysis can be focused directly onto a specific research question. The general disadvantage for supervised learning is that the researcher input through the labelling process increases the subjectivity of the analysis. Another problem is that the labels may be assumed to be 100% accurate, which may not be the case. Any error in the labelling would be carried forward, distorting learning, and reducing the accuracy of predictions made by the trained model. To counter the increased risk of subjective analysis, a range of verification methods are available.

Regression and classification have different metrics, with regression metrics including R2, and mean squared error, and many others [71]. The supervised learning carried out in this thesis focuses on classification, where many metrics relate to the four quadrants of a confusion matrix (see Figure 2.7). A key distinction to make is the specific meaning of accuracy in a machine learning context, where it is defined as the number of correct predictions divided by the total number of predictions, giving a decimal percentage accuracy (0 = 0% & 1 = 100%); as opposed to a general “accuracy” statement relating to any high metric score. A range of plots are available to assess model validity and the effect of parameter change on different metrics including receiver operating characteristic–area under curve (ROC-AUC) plots [72] and learning curves. Exploring learning curves, which plot changes in a metric against a varied variable such as dataset size or hyperparameter, is a key focus for this project; with the aim of exploring the repeatability of vibrational spectroscopy machine learning.

Data class	Classified as *pos*	Classified as *neg*
pos	true positive (*tp*)	false negative (*fn*)
neg	false positive (*fp*)	true negative (*tn*)

$$\begin{bmatrix} tp & fn \\ fp & tn \end{bmatrix}$$

Metric	Formula
Accuracy	$\frac{tp+tn}{tp+fn+fp+tn}$
Precision	$\frac{tp}{tp+fp}$
Recall (Sensitivity)	$\frac{tp}{tp+fn}$
F1-Score	$\frac{tp}{tp+0.5(fp+fn)}$
Specificity	$\frac{tn}{fp+tn}$

Figure 2.7 – Confusion matrix and classification metrics: *Example confusion matrix showing the actual positive (pos) and negative (neg), against the classified pos and neg, resulting in true positive (tp), true negative (tn), false positive (fp), and false negative (fn). Highlighting the formula for accuracy, precision, recall, specificity* [72]*, and f1-score* [73]

2.3.4. Linear discriminant analysis

Linear discriminant analysis (LDA) is a supervised method that aims to minimises within class variance alongside maximising variance between classes. LDA components can be plotted in a similar manner the principal component score plots, reducing the dimensionality of the data to make visualisation of clusters within the data possible. Discrimination rules such as maximum likelihood, Fisher's linear discriminant rule, and Baye's discriminant rule are used to classify the samples, with Baye's rule being used most to produce a probability field. Samples are then assigned to the class based on largest probability. In the python package Scikit-learn 1.1.1, the solver is a hyperparameter that can be optimised. Solvers available are the singular value decomposition (svd), least square solution (lsqr), and eigenvalue decomposition (eigen). The svd solver is the default option in and is used for all LDA

analysis through the thesis to maintain consistency through the analyses. Limitations of LDA relate to the assumptions, LDA assumes features have a Gaussian distribution and can be linearly distinguished [74]. It is also advised that the classes are of similar sizes (the dataset is balanced). If a non-linear classification is required, quadratic discriminant analysis is an alternative.

2.3.5. Support vector machines

Support vector machines (SVMs) produce decision boundaries (support vectors) around hyperplanes determined using functions known as kernels. The availability of different kernels, hyperparameter tuning, binary and multi-class analysis [75], and classification and regression capability makes SVM highly adaptable to different research questions and datasets. The hyperparameters that can be optimised include C and gamma depending on the kernel, with different kernels another variable to be selected depending on the dataset being analysed, e.g., linear kernel for linear data and polynomial kernel form non-linear data [75]. The most used kernels, which are the kernels compared in this thesis, are the linear, polynomial, and radial basis function (RBF) kernels [76]. The kind of kernel determines required the hyperparameter tuning, C is tuned for the linear, C and gamma (γ) for the RBF, and γ, a constant (r), and the polynomial degree (d) for the polynomial kernel. C influences the decision boundary by penalising misclassified samples, reducing the support vectors as C increases to lower the probability of misclassification [75]. For the kernels that use γ, it reduces a samples area of influence, increasing the area of influence as gamma reduces [77].

The range of options (kernels & hyperparameters) available to researchers means that SVMs can be tailored for a wide range of applications, focusing on a higher sensitivity or specificity, or optimised for any metric. However, the higher range of potential models comes at the cost of an increased risk of finding a model that fits the data by random chance, rather than learning key features; especially when paired with the large number of features (and relatively low number of observations/spectra) available in vibrational spectroscopy datasets. The increased

risk of overfitting must be countered with a raised burden of proof when assessing the validity of SVM models.

2.3.6. Logistic regression

Logistic regression classification uses a sigmoid function to provide a probability of a sample being in a class between 0 and 1, with samples assigned to the class closest to their probability e.g. sample < 0.5 (assigned to 0) and sample > 0.5 assigned too 1. Logistic regression has advantages including efficient classification of new samples (when data is linearly separable), providing binary (binomial) and multi- (multinomial) classification, and interpretability through evaluation of the feature coefficients. A limitation of logistic regression for vibrational spectroscopy is the high number of observations (spectra) required per feature (wavenumber). The approximately 10 observations recommended per feature typically necessitates dimension reduction, as a 1000 wavenumber spectrum could need 10,000 spectra to be effective [77].The sigmoid function used in logistic regression is also used as activation functions in artificial neuronal networks (ANNs), where the value of each feature is assessed in a process known as back propagation. ANNs can outperform logistic regression, with the disadvantage of increasing the algorithm complexity and can be further developed into increasingly advanced deep learning depending on the application. The increased complexity comes at the cost of increasingly large datasets and reduced interpretability. The disadvantages make higher complexity algorithms unsuitable for early-stage studies such as those carried out through this thesis, however, an advantage for large datasets have been seen using a convolutional neural network, where the need for pre-processing was avoided [78].

2.3.7. Decision trees and random forests

Decision trees are simple algorithms that divide and subdivide the dataset into separate branches based in order of the feature that provides the greatest separability at the points where the branches split; known as nodes [79]. A key advantage of decision trees is therefore the capacity for feature selection, ordering

the features using splitting algorithm such as gini impurity to inform the user of which features sperate the classes most efficiently. It is an objective of this study to explore the use of decision trees as a method of streamlining feature selection, for applications such as identifying principal components the distinguish classes most clearly. Another benefit of decision trees is their simplicity and robustness, being able to handle missing data, not requiring scaling, and capable of using categorical or continuous data [79]. For vibrational spectroscopy studies, features are typically continuous, e.g., wavenumbers or chemometric features such as principal components [77]. The branches can keep subdividing the data until each sample is cleanly placed into a class, however, this will probably result in the decision trees key disadvantage, overfitting [79]. One way to reduce the risk of overfitting is to tune the decision tree depth, accepting some misclassifications in the training dataset by limiting the number of nodes. Another way of limiting overfitting is to use a Random Forest. Random Forests are ensemble algorithms, produced by combining decision trees to counter overfitting [80], [81] and similarly limiting the algorithm size through a process known as pruning.

2.4. Methods

2.4.1. Scaffold computer aided design (CAD) & fabrication

Design aims are described in the individual chapters/sections. Constructs are modelled using the computer-aided design package Solidworks RX 2018 and converted into STL. file format and uploaded to the DeScribe™ software that produces a script for the Nanoscribe™ 3D printer. Indium TIN Oxide (ITO) coated glass coverslips 70-100 Ω2, No 1.5 (Diamond coatings, UK) were used. The coverslip is wiped on both sides with 2-3 ml acetone, then isopropanol (2-3 ml) and dried with dry nitrogen. The top is determined by measuring the resistance of each surface with a multi-meter, either more or less 4.000, with the top being the higher resistance. The slip is glued onto the holder top up, left to dry for 5 minutes, and checked to ensure the glue has not spread into the centre of the slip. The commercially available resist, OrmoComp™, is drop cast onto the coverslip and the holder is loaded into the Nanoscribe™ GmbH, which is equipped with 100-fs–pulsed 780-nm laser. The laser was focused with either a micro-scale ×63 (NA 1.4) or a mesoscale times 25 (NA 0.8) laser objective directly into the material. The printed scaffolds are developed by immersing the scaffold, with remaining unused resist removed. OrmoComp™ immersed in acetone 50% / isopropanol 50% for 5 min, then isopropanol for 5 min and dried with nitrogen.

2.4.2. Cell culture

Cell culture was carried out on ITO coated glass coverslips to facilitate DLW printing of scaffolds and maintain consistency of analysis. The coverslips were sterilised through immersion in 70% ethanol and left to dry in a 35 ml cell-culture dish. Fibronectin solution was applied to the scaffold and/or slide surface, left to dry, and washed three times with Dulbecco's phosphate buffered saline (DPBS). A concentration of ~1 × 105 cells were then seeded onto the scaffolds and slide surfaces in 2 ml of fresh complete media and incubated overnight to attach. In

experiments where the cells were fixed, 4% paraformaldehyde (PFA) in DPBS and incubated at room temperature. The PFA is removed prior to Raman analysis, the cells washed, and the cells stored and analysed in DPBS to avoid dehydration. In Chapter 6, dithranol exposure is carried out prior to fixing (if fixed) through the inclusion of the descried concentration. For unfixed cell analysis, the dithranol is provided in the quoted concentration during analysis (see chapter).

2.4.3. Microscopy

White light images of HaCaT cells were collected in the Confocal Raman system (inVia^{TM}, Renishaw plc, Wotton-under Edge, UK) using a 60 × NA = 1.00 water immersion objective (LUMPLFLN60XW Olympus). Scanning electron microscope (SEM) images collected under vacuum by Scanning Electron Microscopy (JEOL JSM-7800F - JEOL Ltd., Tokyo, Japan) after gold coating. The fluorescence microscopy verification (Zeiss LSM880) in Chapter 3 used DAPI staining was used to image the nucleus after the HaCaT cells were incubated for 1-5 minutes in a 300 nM DAPI solution. The cell body (proteins) were imaged using wheat germ agglutinin (WGA), the cells being incubated for 10 minutes in a WGA solution of 5 µg / mL concentration. Cropping, colour, and scale bars were added to the microscopy images using ImageJ Fiji 2.9.0 software.

2.4.4. Raman spectroscopy, mapping (2 & 3D) & pre-processing

Renishaw spectroscope Confocal Raman system (inVia^{TM}, Renishaw plc, Wotton-under Edge, UK) with a 532 nm laser (~10 mW). Two- and three-dimensional mapping was carried out using WiRE^{TM} 4.0 software (Renishaw plc, Wotton-under Edge, UK), alongside depth profiles (Chapter 4) were collected by selecting the number of collections and distances between them along the z-axis. Raman maps were produced by selecting the number and distance between X and Y spectral collection coordinates (2D mapping & 3D slices) and then specifying the number and distance (z-step) between the collection of slices along the z-axis for 3D maps, with

"WiRE™ produced" VRM were generated in Volume Viewer. K-means directed shading was carried out using an approach developed for conventional Raman mapping in Chapter 3 and expanded for shading VRM slices in Chapter 4. Pre-processing was carried out in WiRE™ 4.0, with a standardised process of cosmic ray removal, noise filter smoothing, baseline correction, and linearly scaled between 0 and 1 for chemometric analysis and cosmic ray removal, noise filter smoothing, & baseline correction for mapping. Asymmetric least squares baseline correction is used in Chapter 3, using a script written in python. An alteration resulting from Covid-19 restrictions on lab and software availability.

2.4.5. Spectral and chemometric analysis

After pre-processing and Raman mapping carried out in Renishaw WiRE™ 4.0 and volume viewer software, subsequent analysis was carried out using open source or in house software facilitated by the Python 3.6 programming language. Data manipulation was carried out using the NumPy 1.19.1 and Pandas 1.1.4 Python 3.10 packages, data visualisation used the matplotlib 3.5.2 library, and chemometric and machine learning models used Scikit-learn 1.1.1 for cluster analysis, and SciPy 1.8.1. Example code for the k-means directed shading method described through Chapter 3 is provided in a GitHub repository [82], alongside the python modules used within the example [83].

Chapter 3 - Raman mapping and shading

3.1. Introduction

A monitoring method for bioengineered constructs requires a repeatable method of analysis, that provides the broadest understanding of the biological system possible. Currently, shading parameters are not published enough [5] and the information that is published is insufficient to replicate Raman maps exactly when two or more wavenumbers are mapped simultaneously and overlapped. For example, if two researchers produced Raman maps, using the same map data showing a cell, with consistent software, pre-processing, and colour allocation, the lack of published transparency and colour intensity parameter choices would inevitably result in different images being published. Any technique being designed for research or manufacturing environments requires complete repeatability, where different labs following all published information produce the same results. Publishing transparency settings alongside colour intensity ranges [5], would produce repeatable results, but does not provide a method of linking spectral insights to regions of a Raman map. The aim of this chapter is to present a method for producing Raman maps with reproducible map boundaries that can be justified by comparison to a Raman spectrum.

3.1.1. Raman mapping

Raman maps are produced by collecting Raman spectra over a plane and assigning colours relating to the relative intensity of a spectral region, peak, or chemometric feature, such as a principal component (PC). Raman maps combine the high chemical specificity of Raman spectroscopy alongside greater context and morphological insight, increasingly in three dimensions. Univariate, multispectral, and hyperspectral [84]–[95] methods are all used to produce Raman spectroscopy

maps. In vibrational spectroscopy mapping, univariate mapping plots the distribution of a single wavelength or spectral feature (e.g., spectral peak or molecule), producing easily interpreted images [95]. Univariate maps are frequently presented alongside clustering or hyperspectral maps [85]–[94], providing verification/clarification of conclusions drawn from the less interpretable hyperspectral maps.

Multispectral and hyperspectral techniques determine features from five or more wavelengths [96], as opposed to the single spectral features used in univariate analysis. The number of wavelengths analysed can also distinguish multi- from hyperspectral imaging, where 5-12 wavelengths, or spectral bands (depending on the application) are used for multispectral [96]. Hyperspectral techniques use far more wavelengths (hundreds to thousands) [96]. However, it is not uncommon for hyperspectral datasets to have multispectral techniques applied to them [85], [87]–[89], [91]–[93]. As all datasets are within the hyperspectral range in this chapter, all statistical shading methods will be referred to as hyperspectral.

Examples of hyperspectral imaging include dimension reduction and clustering. Dimension reduction includes principal component analysis (PCA), which rotates the data onto new axes that maximises variance, providing an objective method of imaging key features. Clustering algorithms such as k-means clustering [97] or hierarchical cluster analysis (section 2.3.2.) cluster the Raman maps constituent spectra, providing a method of distinguishing groups within the image. The key advantage of hyperspectral imaging is the capacity to visualise spectral features that have been determined using the entire spectral range. Hyperspectral imaging therefore increases the information used in the image production, at the cost of complexity during map production and interpretation.

Both the univariate and hyperspectral Raman mapping then use false-colour shading to reveal the intensity of the Raman peak, molecule, or hyperspectral feature being visualised. False-colour shading [5], [6], [98], [99], sometimes called pseudo-colour shading [100], refers to the assignment of a colour to a molecule or statistical feature that has no relation to the actual colour of the object or substance being

imaged. Terms can vary when discussing vibrational spectroscopy imaging methods. Differences can occur due to their development or earlier application in different, frequently overlapping research fields. For example, variables (statistics), features (data science), and dimensions (linear algebra) can all refer to wavelengths (spectroscopy). Similarly, variate (e.g., uni/multivariate) is the statistical term for techniques once applied to spectral mapping that can be called spectral (e.g., multi or hyperspectral). Spectral terms are prioritised in this chapter unless the naming convention within spectroscopy/chemometrics has retained the general term (e.g., univariate) or when the term is part of a non-spectroscopy context.

The Raman mapping method used will depend on the research question. As highlighted by Ashton et al [5], [6], low-feature analysis is widely used for the mapping of cells, including processes such as monitoring drug uptake. Selecting a Raman peak associated with a drug allows its location within the cell to be mapped [5], where the signal may be too subtle for hyperspectral methods to discern. However, the limitation of low-feature mapping is the inherently reduced information provided by a small number of (commonly one) features, making judgements about the shading parameters currently subjective [5]. The difficulty of objectively determining accurate shading parameters is further complicated when mapping is carried out in three dimensions [6], with a range of complicating factors explored further in Chapter 4. To minimise complicating factors and to make the solution as clear as possible before moving on to distortion factors, this chapter will focus on conventional two-dimensional Raman mapping.

In some cases, univariate shading is layered through the manipulation of shading parameters like transparency, opaqueness, and colour intensity [5], [6]. The layering of univariate Raman maps allows the distribution of two or more wavelengths to be visualised simultaneously, which in a single cell context, can visualise different regions of the cell like the nucleus and cytoplasm, showing cell-scaffold interaction [6]. A small number of wavelengths or spectral features can be visualised using this method if the final image is to remain clear and interpretable. The layering of univariate Raman maps will therefore be referred to as low-feature Raman mapping through the remainder of the chapter and thesis.

Unfortunately, the information provided by Raman maps is degraded when shading is applied arbitrarily and reproducibility is hindered when parameters are published opaquely, if at all [1]. Ashton et al previously showed that a single Raman map can be presented showing varied intensities for different selected molecular signals to highlight the necessity of careful shading with transparent shading parameters [5]. The use of a distribution plot was recommended approach to reduce shading parameter ambiguity [5], [6]. In Raman mapping, comparing machine learning-generated images to labelled microscopy provides a method of determining the morphological accuracy of a completed map [37]. However, no current approach provides a method of systematically verifying the shading parameters selected during the production of Raman (or vibrational spectroscopy in general) maps revealing a current gap in the research.

3.1.2. Repeatability in Raman mapping

One solution previously published was to present the shading range used alongside a distribution plot to aid reproducibility [5]. Care is required during low-feature mapping, where the current protocol is to produce a map for each feature being visualised using pseudo/false-colour shading, then determining shading boundaries to allow the key regions of each map to be layered to distinguish key sections of the map; different sub-cellular regions when analysing single cells. The non-arbitrary nature of choosing/justifying the boundaries between key features has been previously published [5]. The complexity of boundary choice can be especially acute in biological samples, where the spectral features (Raman peaks) used to define each morphological feature can be present in both features. For example, proteins are detected in both the cytoplasm and nucleus. K-means clustering compares the entire spectrum to determine groups (clusters) within the data, providing objective shading of the Raman map that clearly distinguishes different sub-sections within a single cell, e.g., the nucleus and cytoplasm. The limitation of clustering is the blocked (qualitative) shading it provides, with each cluster assigned a single colour providing

no capacity to relate colour intensity to molecular intensity. The number of clusters used is also a source of subjectivity.

This chapter presents a novel application of k-means clustering to colour map regions of interest (the cell nucleus, cytoplasm, etc.) or disinterest (the map background, a scaffold material, etc.) based on clusters verified through spectral inspection. Known as k-means directed shading, this approach provides the quantitative and interpretability of low-feature shading, alongside the objectivity and increased spectral input of unsupervised hyperspectral imaging. A secondary aim of this chapter is to demonstrate K-means directed shadings capacity for image background removal, where spectra associated with the map background are replaced with arrays filled only with zeros (a zero array), the same length of the spectrum. By removing the background, a range for low-feature shading can be more simply defined as the range within the cell, the entire range within a single morphological feature. The use of spectral substitution can also reduce the influence of highly Raman scattering scaffold materials within an analysis, which distracts from biological targets during cell-scaffold analysis (continued in Chapter 4). Unsupervised clustering methods (k-means and hierarchical clustering) are compared to determine the most effective solution. Feature selection is carried out with PCA for verification of the number of clusters and to aid the assignment of molecules and corresponding colours to them through comparison with the low-feature maps produced after background removal.

Chapter aims:

1) To provide a method of justifying cellular subsections in Raman maps by comparing spectral features.
2) To provide a repeatable method of combining two or more low-feature Raman maps.
3) To demonstrate K-means directed shadings ability to select or remove regions of interest and disinterest respectively from Raman maps.

3.3. Methods

See Chapter 2, section 2.4. for all methods including the cell culture (section 2.4.2), microscopy (2.4.3), Raman map collection (2.4.4), and Raman map production/analysis (2.4.5)

3.4. Results and discussion (section 1)

Raman mapping provides a label-free and non-destructive method of mapping the molecular composition of single cells, where the colour intensity indicates molecular concentration. As the map represents the intensity of inelastically scattered photons instead of labels, a wide number of molecules including nucleic acids, proteins, lipids, carbohydrates, and polysaccharides are analysed simultaneously. Molecular distributions can then be visualised individually or together by layering the individual Raman maps of different molecules [6], such as proteins and nucleic acids, as shown in Figure 3.1. Raman mapping reveals the morphology of the cell and its nucleus, like microscopy methods, which can be key indicators of cell function and behaviour [6], with additional molecular pathological biomarkers and concentration. Layered Raman maps can save space and make the relationship between different cell structures clearer [6]. Target molecules are regularly present throughout cells, proteins for example are found in both the nucleus and cytoplasm. Contamination of Raman spectra and unwanted collections outside the cell can also reduce the clarity of Raman maps. To counter these issues and provide flexibility when producing Raman maps, shading parameters in Raman mapping software such as Renishaw WiRE^{TM} are easily adaptable.

3.4.1. Challenges of shading single cells

Figure 3.1 shows how parameters such as shading range and transparency can drastically alter the presented image. Figure 3.1 (A-D) shows the 1330-1350 cm^{-1} protein intensity map, where the shade of green indicates the intensity of proteins. Figure 3.1 (A) includes 95-5% of the range, showing most of the analysed area as bright green. The intensity and apparently high concentration of proteins that it represents is then reduced through Figure 3.1 B-C, fading away as the mapped intensity is reduced. There is no change in the underlying data in the adaption of the maps, only the range of Raman intensity included. In Figure 3.1 E-H, the intensity of the 775-800 cm^{-1} nucleic acid region of the spectrum is mapped and overlaid over the protein map by making lower-intensity regions transparent. In the highest intensity map, Figure 3.1 (E) blocks the protein map below as 100% of the range is included with no transparency. Figure 3.1 (E) demonstrates that nucleic acids have been detected throughout the cell, although these settings make layering ineffective as the protein map is obscured. As the nucleic acid intensity is reduced through Figure 3.1 (E-H), the protein shading is revealed below.

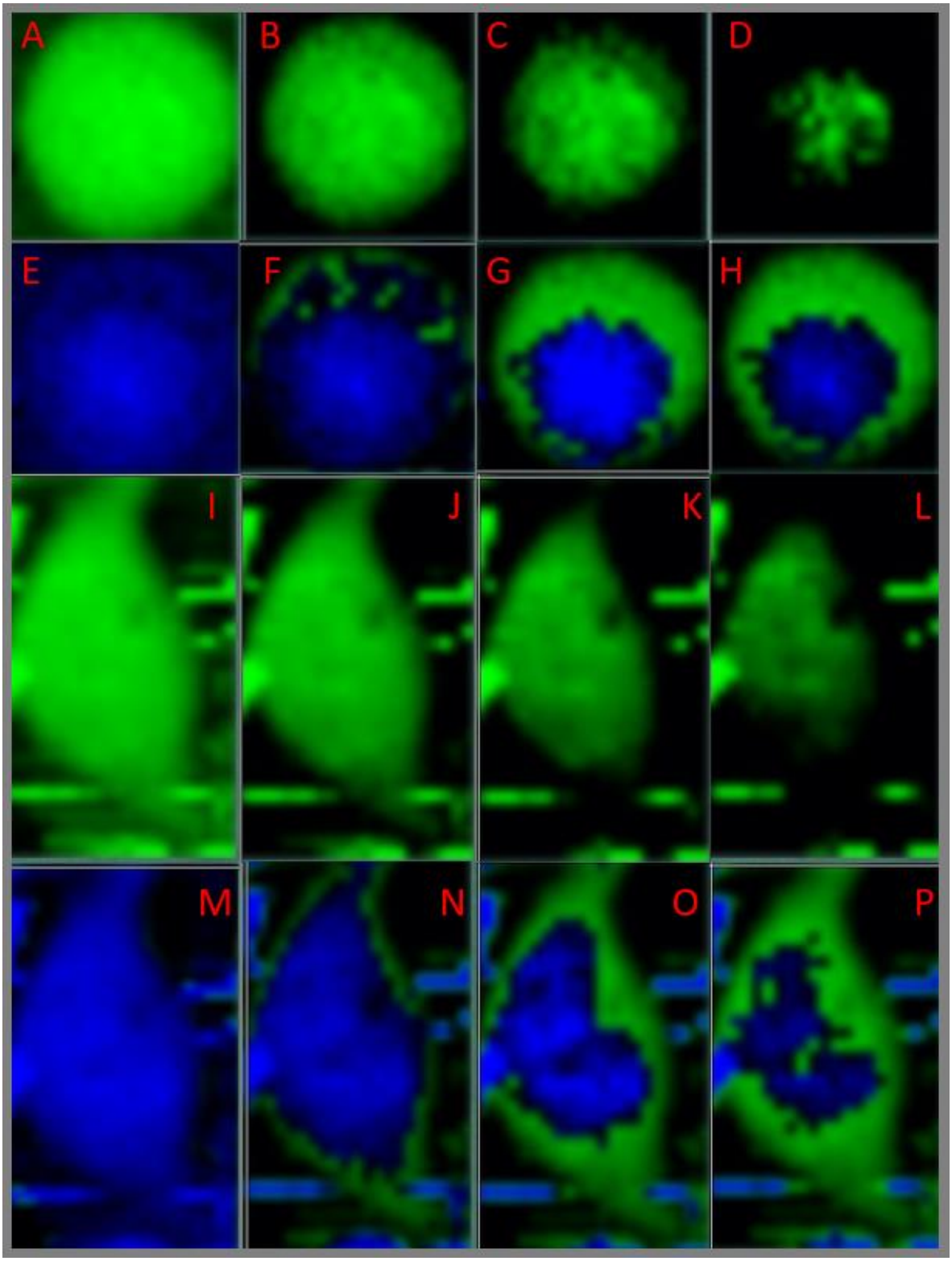

Figure 3.1 – Low-feature shading variability: *See text for discussion on shading parameters, such as colour intensity and transparency setting used. A-D) Reducing intensities of the 1330-1350 cm^{-1} intensities associated with proteins for the HaCaT Cell 1 (mapped area = 21 × 22 µm). E-F) Reducing intensities of the 775-800 cm^{-1} intensities associated with nucleic acids for the HaCaT Cell 1. I-L) Reducing 1330-1350 cm^{-1} intensities for the HaCaT Cell 2. M-) Reducing 775-800 cm^{-1}intensities for the HaCaT Cell 2 (mapped area = 21 × 33 µm).*

The choice of shading parameter is hidden in Figure 3.1, removing the capacity of the reader to make a judgement on the parameters used. Providing the shading parameters is critical due to the significant effect on the morphological information provided by the map and altered apparent molecular concentration, especially when different parameters are used for the different molecules. The same process is carried out through Figure 3.1 (I-P), except for mapping a cell (HaCaT Cell 2), where the most noticeable difference is lines that are across the map; probably resulting from the dragging of the objective over the analysed area, missing the cell except for a small section on the left of the cell. The distorting effect the contamination has on the map and any further analysis can result in the discarding of otherwise valuable data. To counter these issues, a method of substituting the Raman spectra for zero intensity spectra (spectra where every intensity is zero) and objectively determining subsections within the cell, and their constituent molecules. Ready to apply this approach to more complex volumetric Raman mapping in further chapters.

3.4.2. Background removal with clustering/intensity levels

In Figure 3.2, the microscope view of the cells (HaCaT Cell 1 & HaCaT Cell 2) before Raman mapping is shown in (A) and (D). Five initial clusters determined using the k-means clustering algorithm are shown in (B) and (E), with bold colours used to easily distinguish the different clusters. By comparison with the microscope maps in (A) and (D), it is observed in (B) that clusters zero (blue), one (red), two (blue), and three (yellow) are associated with the background of HaCaT Cell 2. Similarly, it can be seen for HaCaT Cell 1 in (E) that clusters zero (blue), one (red), three (yellow), and four (turquoise) are linked to the background. In Figure 3.2 (C) and (F), substituting the spectra of the highlighted clusters with an array of the same length that contains only zeros (a zero array), a new cluster for the background is produced (coloured black). As the new background is represented by spectra where all wavenumbers are zero, the differences determined by the k-means clustering are focused exclusively on the cell. The number of clusters for background removal requires that the total cell morphology, as determined by the microscope image

(Figure 3.2 A & D), is captured (the external clusters then being substituted with zero arrays). The number of sub-cellular clusters is then verified through spectral and hyperspectral investigation (next sections). The advantages of substituting background spectra for zero arrays are shown in Figure 3.2 (C) and (F). Figures 3.2 (C) and (F) provide details within the cell, as opposed to being distracted by the background. The same effect can be obtained by increasing the number of clusters, however, increasing the number of clusters can result in a cluttered image and convolute further analysis. A homogeneous background also removes distracting artefacts from the image, providing clarity and increased contrast between the background and the subject of the image. Removing the background makes the image easier to understand for observers and focuses any further statistical analysis on the cell.

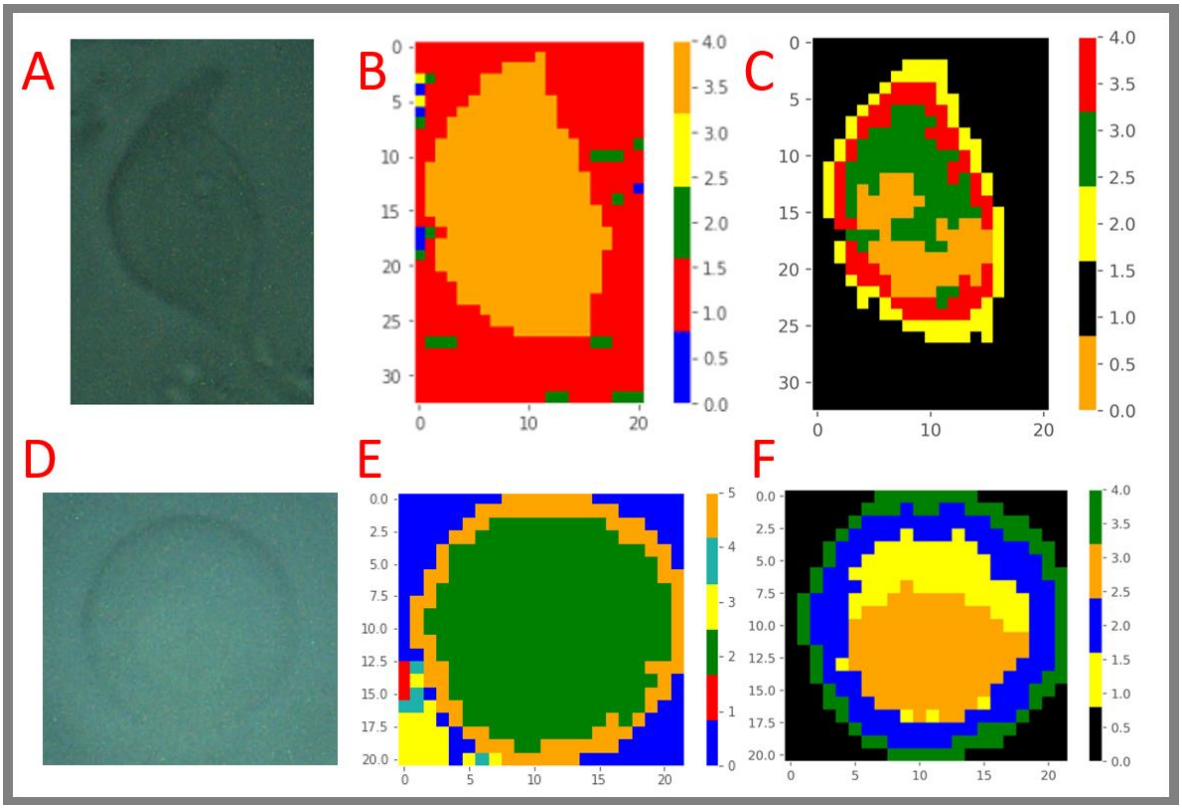

Figure 3.2 – Cluster shading: *A) Microscope image of HaCaT Cell 2, B) K-means clustering used to capture HaCaT Cell 2 background, C) Zero array substituted background k-means image of HaCaT Cell 2, D) Microscope image of HaCaT Cell 1, E) K-means clustering used to capture HaCaT Cell 1 background and F) Zero array substituted background k-means image of HaCaT Cell 1. Pixel counts (x and y axis) in B, C, E, & F, are in µm*

3.4.3. Clustering comparison

To ensure the most accurate method is being used to remove the background and determine regions of interest within the cell, hierarchical cluster analysis (HCA) was carried out for comparison to the k-means clustering method using the HaCaT Cell 1 cell Raman map. To verify the accuracy of the clustering algorithms, false-colour Raman maps were produced of the 693-713 cm^{-1} lipid (C – purple), and the 775-800 cm^{-1} nucleic acid (D – blue) [5], [6] regions of the spectrum. A custom shading range was coded in Python 3.7.6, using the Matplotlib 3.1.3 library. The shading indicated the background in black, with dark colour indicating low Raman intensity and increasing colour intensity/brightness relating to a higher Raman intensity. Black was chosen for the background to highlight the cell and conform to the shading convention used throughout the chapter. By comparing the maps of molecular regions of the spectrum, conclusions about the accuracy of the clustering can be determined, verifying the clustering.

In Figure 3.3, the largest feature within the cell shown within the false-colour maps is the nucleus (D), which appears as a high-intensity region in the nucleic acid (775-790 cm^{-1}) map and a low-intensity region in the lipid (693-713 cm^{-1}) map (C). Figure 3.3. E & F visualise the nucleus [101] in blue and proteins (WGA) in green, with the DAPI-stained nuclei showing the presence of DNA. The expected size of the nucleus (E-F) aligns most closely with cluster 3 (orange) for the k-means algorithm, whereas the HCA image produces a larger orange cluster (number 0). Another region of interest in the false colour maps is the inner cell body above the nucleus (yellow), cluster 1 in the k-means, and cluster 4 in the HCA image, probably relating to the endoplasmic reticulum (ER) [102], [103]. The ER shows low nucleic acid intensity (D), with the lipids (C), maps indicating higher intensities. The third region of interest is the outer cell body, shown as a ring around the nucleus and the inner cell body (blue), cluster 2 in the k-means image and cluster 1 in the HCA. The outer cell body is shown as a ring in the nucleic acid map (D) but is undistinguishable in the lipid map (C). The final feature in the clustering images on the edge of the cell (green), is shown as cluster 4 in the k-means image and 2 in the HCA. The defining factor of all

molecular maps within this region is a low concentration, potentially indicating a reduction in cell thickness.

Differences are present in Figure 3.3 between the k-means (A) and HCA (B) images, including the size of the nucleus and the inner and outer cell bodies. The HCA image groups the nucleus and part of the outer cell body, reflecting the ring of nucleic acids shown around the ER in the nuclear acid map. The ER (yellow) is shown as larger in the k-means image, more closely matching the low-intensity region in the nucleic acid map (D). The nucleus, defined by the high-intensity region in (D) the nucleic acid map (verified in E & F), and the low-intensity region in the lipid map (C) is more accurately depicted by the k-means clustering image. The use of k-means as a method of shading further clustering images will therefore be carried forward for the remained of the project. The colours assigned to the clusters in this section were designed to increase contrast, without the assignment of molecules to those colours. The next section will be focused on assigning the appropriate false-colour shading to each cluster so that a reader can determine what molecule defines that cluster, distinguishing it from the others / maximised the variance between them.

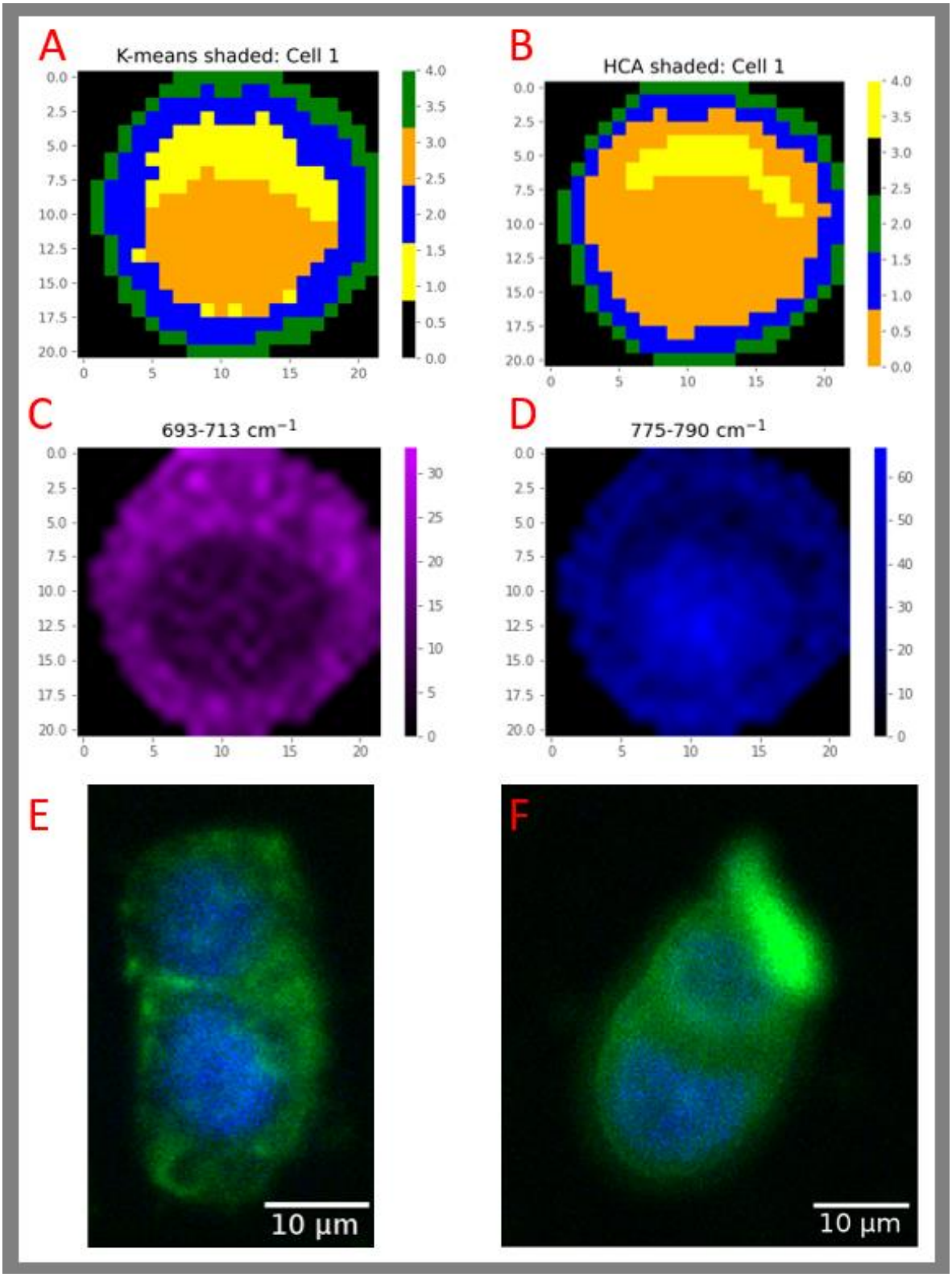

Figure 3.3 – Microscopy verification of clustering: *A) K-means clustering image of HaCaT Cell 1 (5 clusters). B) HCA image of HaCaT Cell 1 (5 clusters). C) Univariate Raman map of HaCaT Cell 1 shaded to the 693-713 cm^{-1} (lipid) spectral peak (purple). D) Univariate Raman map of HaCaT Cell 1 shaded to the 775-800 cm^{-1} (nucleic acid) spectral peak (blue). E & F) HaCaT cells imaged using fluorescence microscopy, labelled using DAPI (blue) to visualise DNA, and WBA (green) to visualise proteins. Pixel counts (x and y axis) in A-D, are in µm*

3.4.4. Single-cell map segmentation comparison

Some Raman peaks and regions are only associated with a single class of molecule, in section 3.4.3, the regions, 693-713 cm^{-1} (lipids) [5], 775-800 cm^{-1} (nucleic acids), and 1330-1350 cm^{-1} (proteins) [6] were chosen for this reason. Other Raman peaks do not provide such a simple interpretation, where the vibration (or a similar vibration) responsible for the peak can be found in more than one molecule, an example is lipids and proteins that share regions of the spectrum. In such cases, determining the exact combination of molecules responsible for the Raman peak can become complex, making the assignment of colours to those regions non-trivial, with the reward of potentially increased insight. Raman mapping provides a method of visualising disputed target peaks, which once compared to known (single) molecular region maps allow for conclusions to be drawn as to the contributor or contributors to the peak and the assignment of a colour to reflect these conclusions. The purpose of a rigorous approach to assigning colours to subsections of Raman maps is to minimise subjectivity when deciding on morphological boundaries within a cell, which may indicate altered behaviour [104]–[107]. The use of unsupervised learning is therefore justified when identifying boundaries and selecting target spectral regions for their verification.

PCA is a commonly used technique in vibrational spectroscopy, as an unsupervised method of determining new axes (components) that account for the maximum variance within the dataset (as described in Chapter 2, section 2.3.1) The columns of the loadings matrix produce the loadings plot, which describes the “importance” of each feature (wavenumber). Greater importance is defined as the wavenumbers contribution towards maximising the variance within that dimension (axis) and indicated by the loadings distance from zero (the greater the more important). PCA therefore provides the advantage of objectively highlighting wavenumbers or spectral regions for further analysis. As each spectrum within a PCA data matrix, is a pixel in a Raman map (assuming the correct order is retained), once the data has been rotated onto new axes, the PC provides a score for each spectrum which can then be rearranged into an image. PCA can objectively indicate key constituents of

each region of the cell, which can then be used to aid verification of cluster colour assignments in the next section. By false colour shading the maps to regions indicated by the PCA loadings plot, the distribution of these factors can be observed. Factors that indicate morphological features are then selected for the next section of the chapter and maps that do not show anything of interest can be discarded.

Shading using PCA is a hyperspectral imaging method, as a larger number of features (wavenumbers) are used to produce the image. Each PC images the feature or features that maximises the variance within the dimension, therefore producing images that incorporate the different features whilst minimising subjectivity. The limitation of objective methods, like PCA, is that any known subject of an investigation (to the researcher), may be disregarded if it does not maximise variance [108]. An example is dithranol absorption by a cell, visualised by shading to a spectral peak intensity [5] may be disregarded due to PCA's purpose of determining axes relating to variance rather than clusters within the data [109]. For example, the shading of drug absorption. PCA hyperspectral images are therefore hypothesised as providing an additional method of combining Raman maps, where the loading plot can be used to determine the features that have maximised the variance to produce the image. Testing the ability of PCA to aid cluster assignment to sub-cellular regions, can be tested by mapping the PC by plotting the PC loading plot, and false-colour shading target spectral regions indicated by the loading plot. By using the loading plot determined false-colour maps and hyperspectral images to identify regions within the cell, PCA will have reduced subjectivity in the selection of molecules used to assign clusters to sub-cellular regions.

3.4.5. HaCaT Cell 2 principal component 3

In Figure 3.4 (A), a threshold of 0.06 was used on the loading plot for PC3. The 0.06 threshold was determined through inspection of maps above the threshold and is used to identify the highest intensity loadings using the find_peaks function provided in the python SciPy 1.8.1 signal library, which is labelled. A hyperspectral image of the third PC (PC3) is shown with the selected molecular maps to aid molecular

assignments through comparison. PC3 was selected as its image (I) reproduced the spectrally verified k-means image. The positive and negative loadings for PC3 also reinforce the molecular assignments relating to the nucleus and cell body regions of the cell. Positive loading peaks in the 784 cm^{-1}, 1000 cm^{-1}, 1095 cm^{-1}, 1489 cm^{-1}, and 1575 cm^{-1} mainly indicate the positive loadings relate to nucleic acids [37], [110]–[112]. Only the 1000 cm^{-1} phenylalanine loading peak [37], [110] relates to protein but does not provide morphological detail and will not be used in further stages. The maps were shaded blue to visualise their distribution in Figure 3.4 (B-E), where the overlapping regions of the highest intensity overlap reinforcing the assigned molecule. It can therefore be said that the high positive intensity regions of the PC3 hyperspectral image relate to nucleic acids.

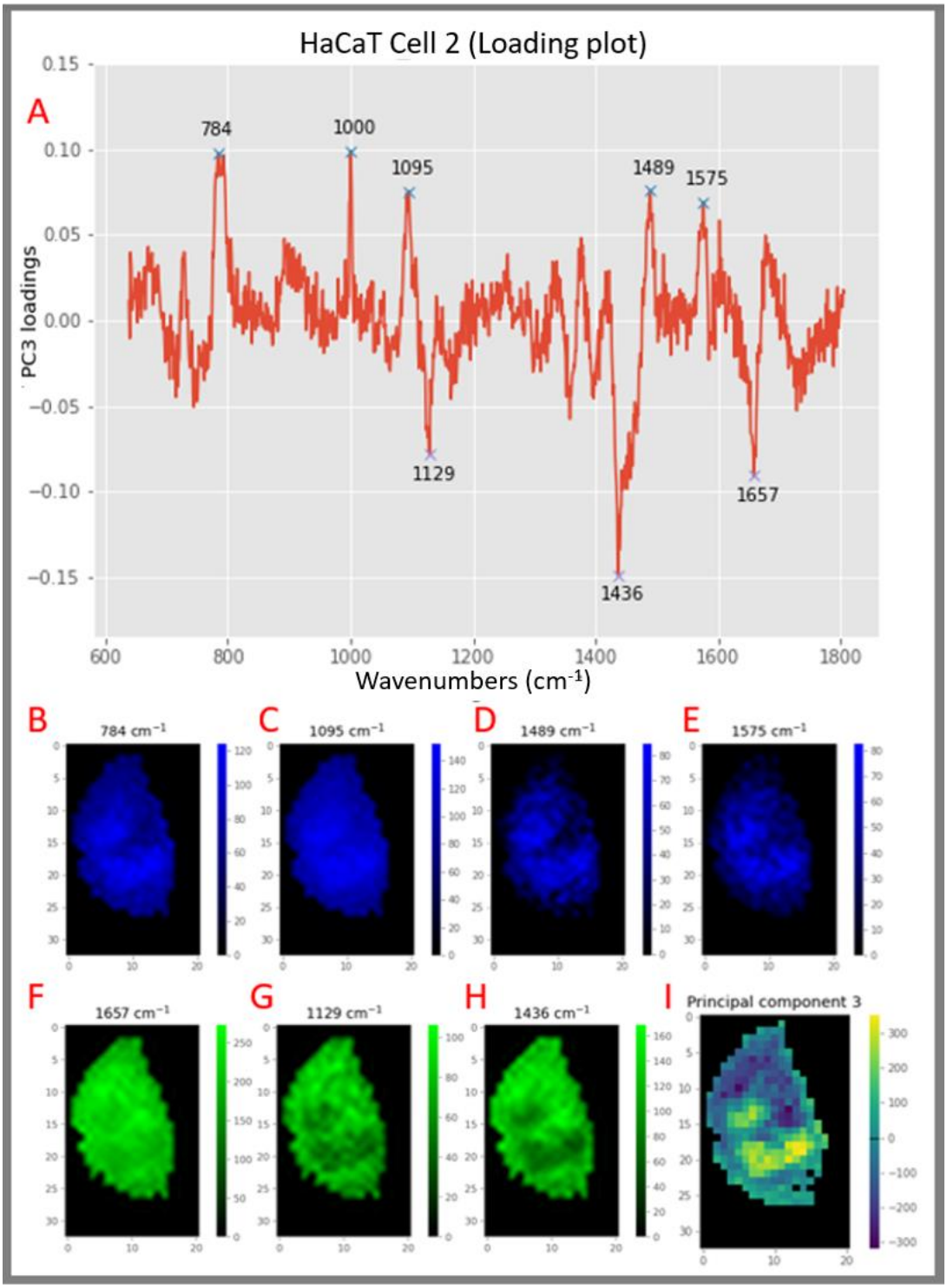

Figure 3.4 – HaCaT cell 2 PC3: *A) Loading plot of HaCaT Cell 2 (PC2), highlighting the 784, 1095, 1489 and 1575 cm^{-1} loading peaks when a 0.06 threshold was applied to the positive loading peaks and 1129, 1436 and 1675 cm^{-1} when a 0.06 threshold was applied to the negative loadings. B-H) Univariate Raman maps of, B) 784 cm^{-1} (nucleic acids), C) 1095 cm^{-1} (nucleic acids), D) 1489 cm^{-1} (nucleic acids), E) 1575 cm^{-1} (nucleic acids), F) 1129 cm^{-1} (proteins), G) 1436 cm^{-1} (proteins), & H) 1675 cm^{-1} (proteins). I) Hyperspectral image of PC3. Pixel counts (x and y axis) in B-I, are in µm*

Negative loading peaks under a -0.06 threshold include lipids or proteins (1129 cm^{-1}, 1436 cm^{-1}, and 1657 cm^{-1}) [110], where the highest intensity regions surround the nucleus region of the map. The intensities drop slightly within the nucleus, suggesting a small contribution of lipids as proteins would not drop within the nucleus, whereas lipids would be expected to drop significantly, as shown in section 3.4.3. The 1129 cm^{-1}, 1436 cm^{-1}, and 1657 cm^{-1} relate primarily to proteins, resulting in a green shading in Figure 3.4 (F-H), with a small lipid contribution that cannot be clearly visualised but must be acknowledged. In cases where a PC is only focused on a single feature such as nucleic acids, there would be no additional benefit to using PCA to shade the image. In this case, the negative loadings focus primarily on proteins, allowing the different molecules to be shaded in Figure 3.4 (I) simultaneously and providing a shading gradient that does not require a transparency setting to shade multiple features within the cell.

3.4.6. HaCaT Cell 1 principal component 2

In Figure 3.5 (A) the HaCaT Cell 1 PC2 loadings plot, the negative loadings with a 0.05 threshold highlighted the 1128 cm^{-1} loading peak of lipids [21] and carbohydrates [112], 1302 cm^{-1} lipids [3], nucleic acids and proteins 1341 cm^{-1} [110], 1448 cm^{-1} proteins and lipids [21] or lipids [111] and 1652 cm^{-1} (proteins and lipids) [21], [37]). The positive loadings do not provide morphological insight when assigning clusters to sub-cellular regions, so 1000, 1155, 1507, 1600, and 1341 cm^{-1} are excluded from the morphological analysis alongside the 1341 cm^{-1} negatively loaded peak. The high-intensity region for HaCaT Cell 1s PC2 is associated with the inner cell body with a high protein and lipids concentration, Figure 3.5 (B).

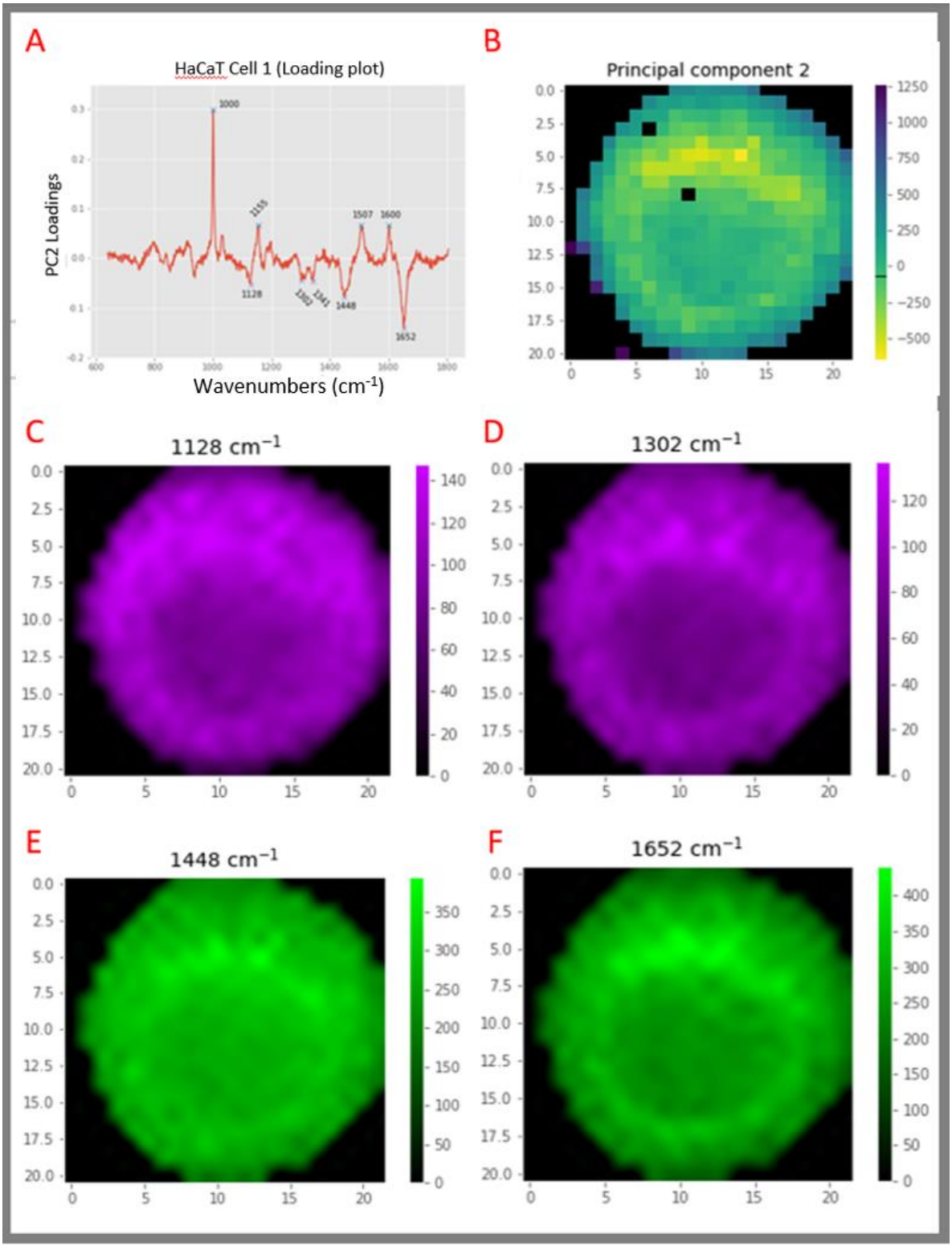

Figure 3.5 – HaCaT cell 1 PC2: *A) Loading plot of HaCaT Cell 1 (PC2), highlighting the 1000, 1155, 15007 and 1600 cm^{-1} loading peaks when a 0.06 threshold was applied to the positive peaks and 1128, 1302, 1448 and 1652 cm^{-1} when a 0.06 threshold was applied to the negative loadings. B) Hyperspectral image of PC2. C-F) Univariate Raman maps of, C) 1128 cm^{-1} (lipids), D) 1032 cm^{-1} (lipids), E) 1448 cm^{-1} (proteins), F) 1652 cm^{-1} (proteins). Pixel counts (x and y axis) in B-F, are in µm*

The reversed colour bar for the PC2 hyperspectral image provides a clearer image, as the loadings responsible for the shading are negative. The shaded molecules shown in Figure 3.5 (C-F) reflect this, with the highest intensity map (1652 cm^{-1}) being assigned to proteins, the most abundant molecule in the cell. Proteins are also assigned to 1448 cm^{-1}, which alongside 1652 cm^{-1} does not have a significant drop in intensity in the region of the cell associated with the nucleus when compared to the protein and lipid maps in section 3.4.5. Green is therefore assigned to 1448 cm^{-1} and 1652 cm^{-1} maps.

The 1302 cm^{-1} map has lower intensities than the protein map and has a large difference between the nucleus and cell body, as would be expected for lipids. The 1128 cm^{-1} map has the lowest intensities from the selected wavenumbers, with the higher intensities in the cell body. In section 3.4.5, 1129 cm^{-1} is green for proteins as the highest contributor to the spectral peak. The lower intensity of the 1128 cm^{-1} maps, combined with the low-intensity region associated with the nucleus suggests a higher relative lipid concentration for the 1128 cm^{-1} map, resulting in purple shading. The reduction in the nucleus region of the map is not as significant as in the 1302 cm^{-1} map; therefore, lipids (purple) are assigned to the map, with the expectation of some protein contribution.

3.4.7. HaCaT Cell 1 principal component 3

For HaCaT Cell 1 PC3, the positive loadings in Figure 3.6 (A) relate primarily to the nucleus, with loadings over a 0.06 threshold of 784 cm^{-1} (nucleic acids) [21], [37], 1095 cm^{-1} (DNA) [21], 1488 cm^{-1} (DNA) [21] and 1678 cm^{-1} relating to proteins [21], [37]. 1095 cm^{-1} provided no morphological information and was removed. The nucleic acid maps (784 cm^{-1} and 1488 cm^{-1}), in Figure 3.6 (C and D) have high intensities in the nucleus region of the maps, with rings associated with the cluster 2 region surrounding the inner cell body of high lipids and proteins determined in section 3.4.6. The 1678 cm^{-1} map in Figure 3.6 (E) could have been related to lipids

also, but the high-intensity regions are focused on the nucleus, indicating that they are proteins.

Negatively loaded peaks included 748 cm^{-1} (nucleic acids or protein) [21] or proteins and lipids (1433 cm^{-1} 1586 cm^{-1}) [21], [37], [112]. The 1586 cm^{-1} map shows a ring of proteins and lipids, where the intensity is the lowest from the negative loadings, suggesting lipids. The 1586 cm^{-1} map in Figure 3.6 (G) has a very low intensity in the nuclear region of the cell, with slightly higher intensity within the inner cell body, resulting in lipids being assigned to this map, with purple shading. The 748 cm^{-1} map (F) has a high-intensity region in the cluster 2 section of the cell, similar to a ring of nucleic acids seen in the 784 cm^{-1} and 1488 cm^{-1} nucleic acid map (Figure 3.6 (C and D)). The 748 cm^{-1} Raman peak can be assigned to nucleic acids or proteins, although there is no high-intensity region where the nucleus is, resulting in an assiginment of proteins and green shading for the 748 cm^{-1} map. The map for 1433 cm^{-1} in Figure 3.6 (E) shows a drop in intensity, similar to the 693-713 cm^{-1} lipid region in Figure 3.3. However, the 1433 cm^{-1} intensity is the highest of all the map, suggesting a large protein constituent of the peak that incentivises a green shade.

The hyperspectral map of HaCaT cell 1 PC 3 in Figure 3.6 (B) reflects the shading of the highlighted spectral regions, except for the outer ring of nucleic acids, proteins, and lipids. The combination of all the factors being visualised in PC2 to distinguish the nucleus, and the cell body, the positive intensity shading the nucleus and the lower and negative intensities shading the cell body. The only spectral peak to isolate the nucleus similarly is the 1678 cm^{-1} protein peak (seen in E). The distinction between the nucleus and cell body is difficult to determine with the 1678 cm^{-1} map, highlighting the advantage of hyperspectral imaging for some applications.

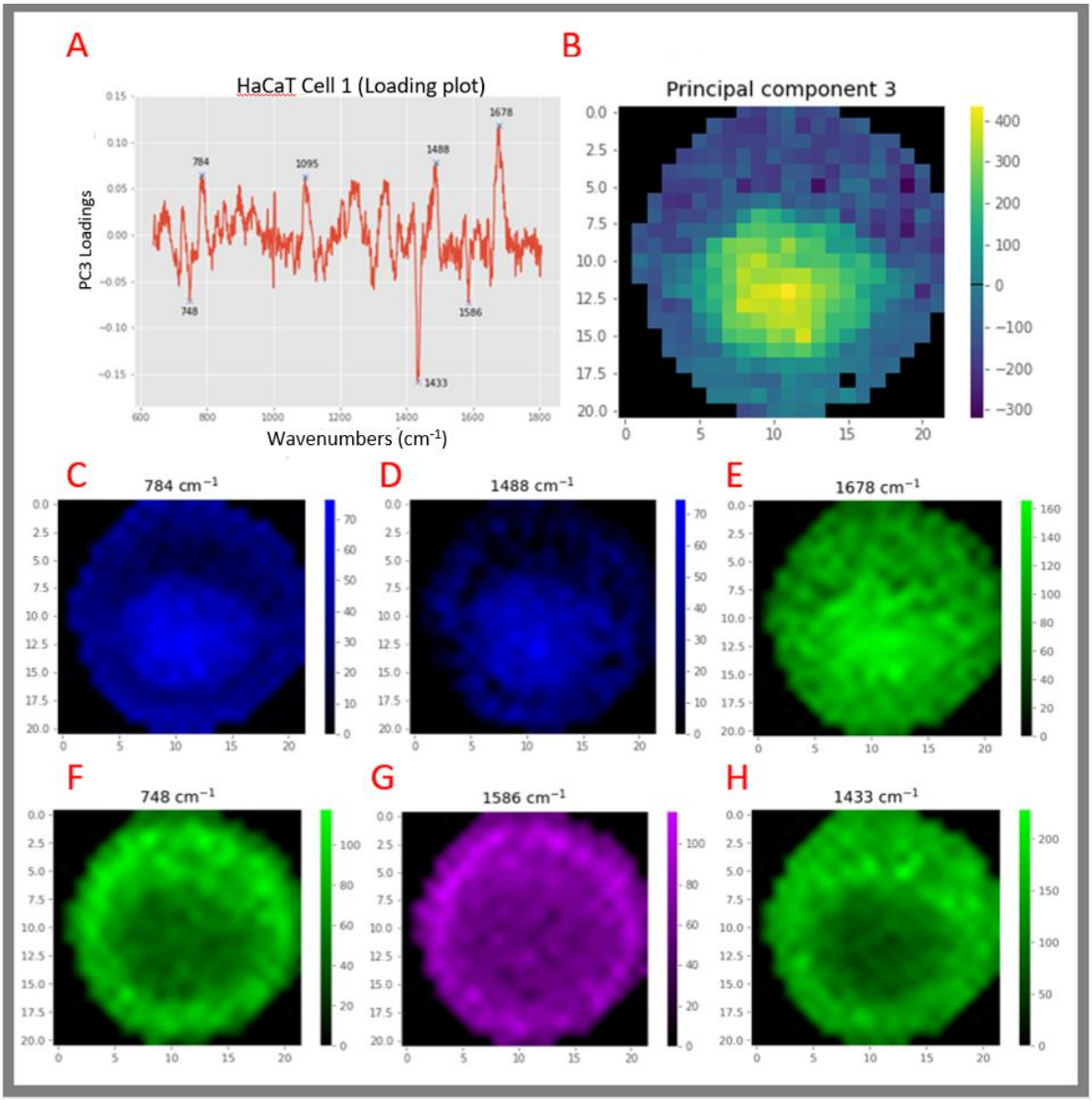

Figure 3.6 – HaCaT cell 1 PC3: *A) Loading plot of HaCaT Cell 1 (PC3), highlighting the 1000, 1155, 15007 and 1600 cm^{-1} loading peaks when a 0.06 threshold was applied to the positive loading peaks and 1128, 1302, 1448 and 1652 cm^{-1} when a 0.06 threshold was applied to the negative loadings. B) Hyperspectral image of PC3. C-H) Univariate Raman maps of, C) 784 cm^{-1} (nucleic acids), D) 1488 cm^{-1} (nucleic acids), E) 1678 cm^{-1} (proteins), F) 748 cm^{-1} (proteins), G) 1586 cm^{-1} (lipids), & H) 1433 cm^{-1} (protein). Pixel counts (x and y axis) in B-H, are in µm*

3.5. Results and discussion (seciton 2)

In section 3.4, PCA indicated regions of the spectrum that resulted in the maximum variance within the dataset that constitute the Raman maps. The indicated regions of the Raman spectrum can now be compared to the k-means cluster image Figure 3.7 (F) to verify the number of clusters and assign colours to the clusters that represent that primary molecular constituent. By associating the high-intensity regions of a molecule to locations within the cell, it is hoped that the primary molecules that define clusters can be isolated, linking biological insights to physical locations in the cells. The advantage of using hyperspectral methods to determine regions within the cell and determine key biological features within them is their inherent objectivity and capacity to balance each wavelength in the Raman spectrum whilst reducing the number of dimensions.

3.5.1. Assigning colours to the different HaCaT Cell 2 k-means clusters

Figure 3.7 shows the full range spectrum (A) with the spectral peaks selected in section 3.4. highlighted with colour shading, alongside focused sections in (B). The green lines/shading are associated with proteins and blue for nucleic acids. Plotting the average spectrum for each sub-cellular cluster allows the average molecular information to be compared when assigning the cluster to a region of the cell (e.g., cell body vs. nucleus). For example, it can be seen in Figure 3.7 (C) that the 784 cm^{-1} Raman peak, assigned nucleic acids, has approximately 25% higher intensity in cluster 4. Whereas the map of 1436 cm^{-1} (D) and 1657 cm^{-1} (E) intensities show darkening (reduced Raman intensity) in the region of cluster 4, most clearly seen in (D). The gradient in proteins is reflected in the spectra, where the protein intensities are highest for cluster 2, lowest for cluster 3, and in between for cluster 1 for the highlighted protein regions, dividing the cell body into outer, inner, and edge. Cluster 3 shows the lowest intensities, potentially because of reduced sample thickness near the edge of the cell, as all Raman peaks are shown to be reduced compared to the other clusters, justifying grey to show the reduced molecular content.

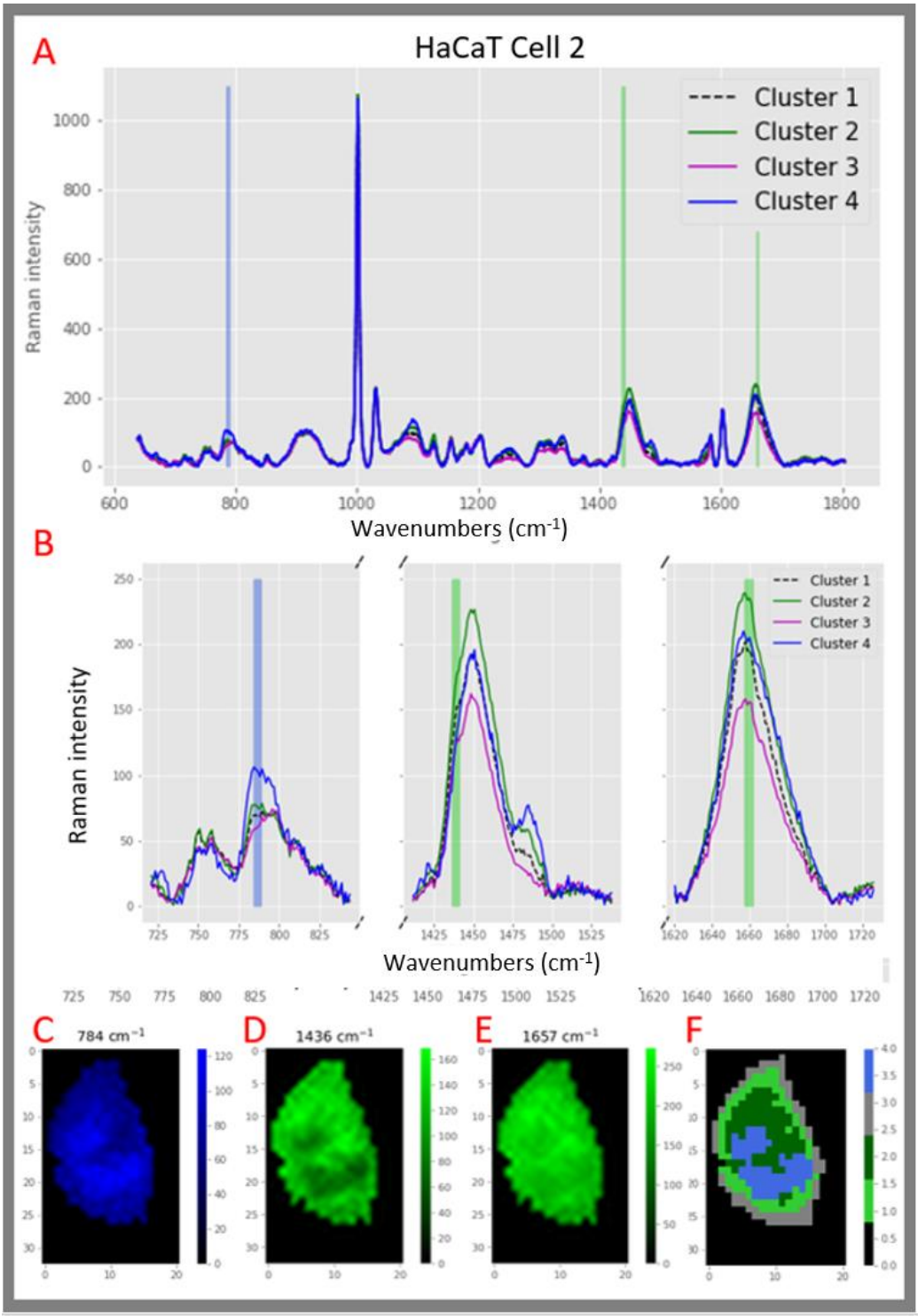

Figure 3.7 – HaCaT cell 2 cluster assignment: *A) HaCaT Cell 2 Cluster average spectra (full). B) HaCaT Cell 2 Cluster average spectra (focused). C-E) Inivariate Raman maps of, C) 784 cm^{-1} (nucleic acids), D) 1436 cm^{-1} (proteins), & E) 1657 cm^{-1} (proteins). F) K-means cluster image using 5 clusters. Pixel counts (x and y axis) in C-F, are in µm*

3.5.2. Assigning colours to the different HaCaT Cell 1 clusters

Figure 3.8 repeats the analysis from Figure 3.7 for HaCaT cell 1, linking (colouring) the clusters (E) to different regions of the cell (nucleus vs. cell body). The assignments are based on spectral regions highlighted through PCA shown behind the spectra on both the full spectrum (A) and the focused spectral regions (B). The background is captured by cluster 1, which is not included in the spectral comparison due to the zero-array substitution and subsequent elimination, the background is then shaded black concurring with the shading convention. The distinct nucleic acids (748 cm^{-1}) and proteins (1678 cm^{-1} - G) define the cluster 4 average spectrum, with the higher nucleic acid 784 cm^{-1} spectral peak allowing the cluster to be shaded blue, as previously nucleus regions have been coloured. The 748 cm^{-1} protein (F), 1433 cm^{-1} protein (H), and 1586 cm^{-1} lipid (C) maps justify the distinction of cluster 0 as a molecularly distinct region of the cell, also highlighted in the 784 cm^{-1} nucleic acid (D) map. As clusters 0 and 3 are shown to have the highest protein contents through inspection of the cluster average spectra in Figure 3.8 (B). The assignment of different shades of green to both cluster 0 and 3 is therefore justified, showing proteins are the primary constituent of both, with the use of different shades highlighting the intensity difference. The average spectrum of cluster 2 has the lowest intensities in all regions of the spectrum except for the 775-800 cm^{-1} nucleic acid region, where it has slightly higher intensities than cluster 3, although this is more due to the reduced nucleic acid levels in the inner cell body as shown in the 784 cm^{-1} map. Cluster 2 can also be assigned the colour grey to indicate the low intensity detected from the edge of the cell.

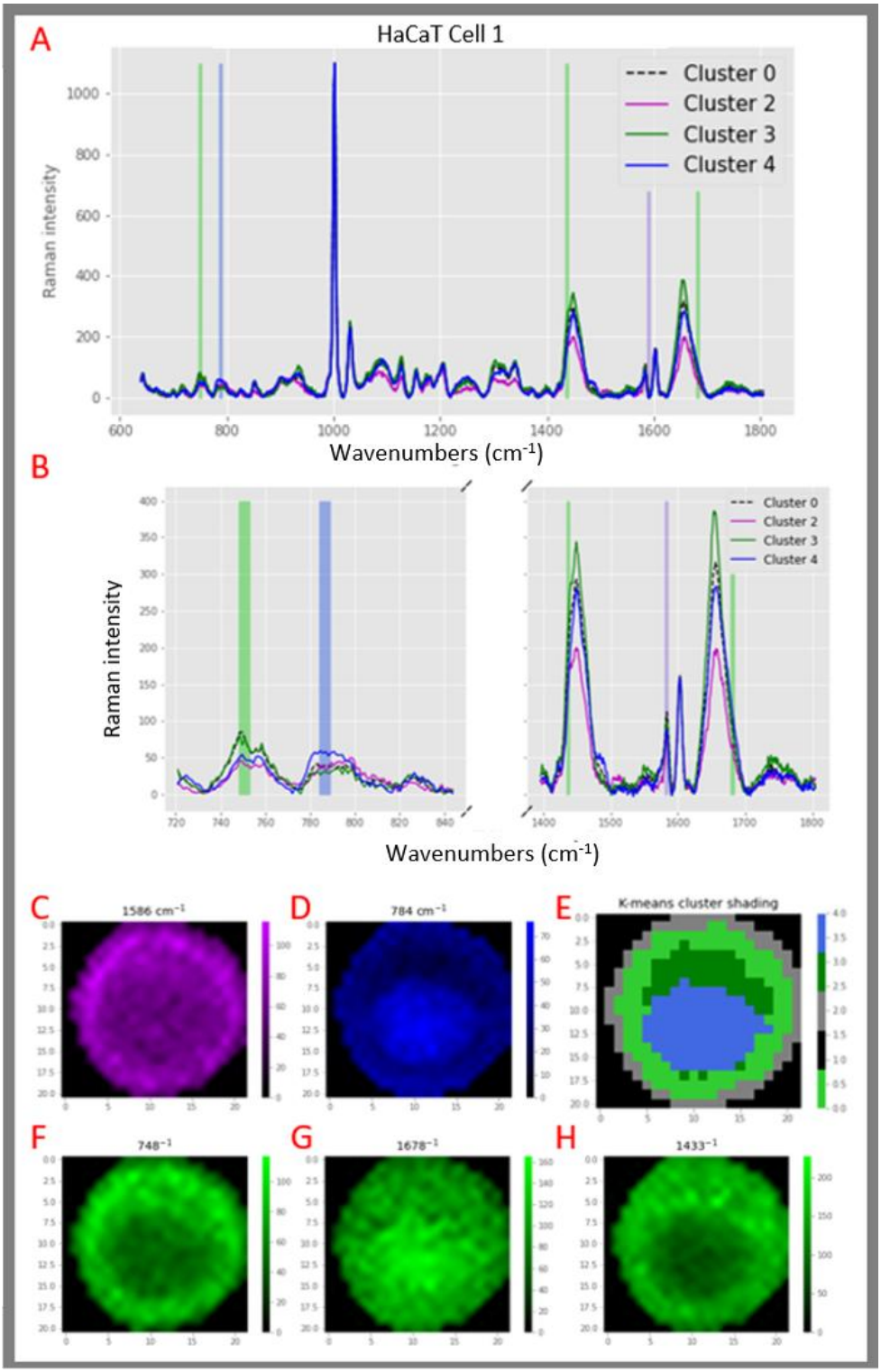

Figure 3.8 – HaCaT cell 1 cluster assignment: *A) HaCaT Cell 1 Cluster average spectra (full). B) HaCaT Cell 1 Cluster average spectra (focused). C & D/F-H) Univariate Raman maps of, C) 1586 cm^{-1} (lipids), D) 784 cm^{-1} (nucleic acids), F) 748 cm^{-1} (proteins), G) 1678 cm^{-1} (proteins), & H) 1433 cm^{-1} (proteins). E) K-means cluster image using 5 clusters. Pixel counts (x and y axis) in C-H, are in µm*

3.5.3. Complete k-means-directed shading maps

Having assigned clusters to different sub-cellular regions in section 3.4, k-means directed shading provides the capacity to shade the combined areas indicated by the clusters with a colour associated with the morphological feature. In keeping with previous conventions, the 1330-1350 cm^{-1} (proteins) and 775-790 cm^{-1} (nucleic acids) spectral regions were associated with the cell body and nucleus respectively [6], providing relatively homogeneous regions of the spectrum. Figure 3.9 (B-G) reiterates the variable shading that can be produced using WiRE™ (from section 2.4.4), for HaCaT cell 1 (B-D) and HaCaT cell 2 (E-G). The final k-means directed maps for HaCaT cell 1 and HaCaT cell 2 are shown in Figure 3.9 (H) and (I) respectively, where the shading range for each region is the entire range within the identified area, shown on the colour bars. Background removal increased the clarity most for HaCaT cell 2 (I), focusing the image onto the cell. K-means-directed shading is shown to provide clarity similar to that achieved by fluorescence microscopy (Figure 3.9 A). K-means-directed false-colour shading, therefore, retains the increased molecular information provided by spectroscopy, whilst gaining objectively determined boundaries between features such as the nucleus through unsupervised learning, which are verifiable through spectral inspection. Removal of the background also improved the contrast between the cell and background for HaCaT cell 1. The main benefit of k-means directed shading is the increased confidence when visualising boundaries between features such as the cytoplasm and nucleus, whereas shading previously relied on incremental alterations (Figure 3.1) and researcher judgement, the sub-cellular regions in the k-means directed shading are determined using unsupervised k-means clustering and assigned through spectral and hyperspectral (PCA) analysis.

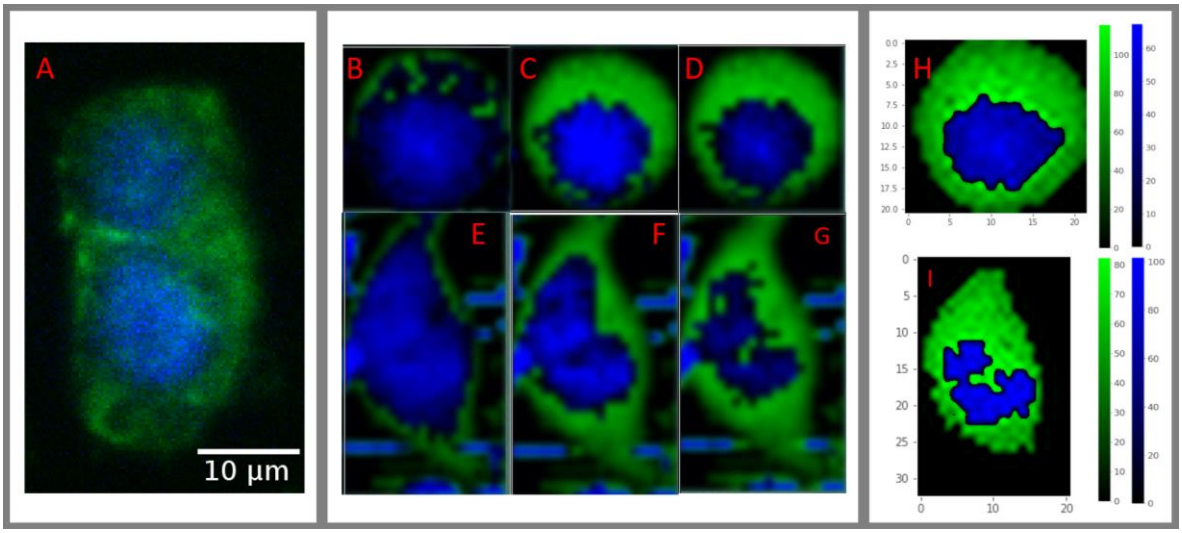

Figure 3.9 - Cell visualisation comparison: *A) Fluorescence microscopy, providing a comparative imaging technique, staining the nucleus blue with a stain for DNA (DAPI) and the cell body / cytoplasm green for proteins (WBA). (B-C) showing the incremental shading of the 775-790 cm^{-1} nucleic acid Raman peak (blue) for HaCaT cell 1 (mapped area = 21 × 22 µm), and HaCaT cell 2 (mapped area = 21 × 33 µm) (E-F), with consistent shading for the 1330-1350 cm^{-1} protein region (green), which can be similarly varied. H) The k-means directed false-colour shading of HaCaT cell 1, showing the objectively derived and spectrally verified boundaries for the nucleus (blue) and the cell body (green). Colour bars indicate the Raman intensity for the proteins (green) and nucleic acids (blue) to the right of the map; with the same shown for HaCaT cell 2 in (I). Pixel counts (x and y axis) in H and I, are in µm*

3.6. Conclusions

K-means directed shading is a method that provides increased objectivity, compared to the subjective shading described by Ashton et al [5] and demonstrated in Figure 3.1. Plotting the averaged spectrum for clusters provides the capacity to justify molecular allocations to the cluster, fulfilling the first aim of the chapter. The second aim of the chapter, providing a repeatable method that reduced shading subjectivity, was provided by combining a hyperspectral method (k-means clustering) with low-feature Raman. The interpretability of low-feature Raman is maintained, whilst gaining repeatability through the publication of the number of clusters and molecular assignment justification. Breaking Raman maps into distinct regions determined by unsupervised clustering took advantage of hyperspectral techniques, which discern insights from the entire Raman spectrum. Using the clusters to define boundaries within the maps for the application of low-feature mapping then retained the

interpretability that can be lost through the abstraction of many features into reduced dimensions or clusters. The challenge was then to objectively assign the different regions to target morphological features, Ashton et al discussed the desire to determine suitable shading parameters for each molecule that can then be overlapped [5]. Combining the two techniques addressed the second aim of the chapter, providing a repeatable and spectrally justifiable method.

Focusing on the repeatability of Raman map production in this chapter allows the approach to be applied to subsequent chapters looking at further challenges and studies towards an automated method of cell culture and monitoring. For studies aiming to understand a cellular response with greater objectivity and depth before developing a cell culture monitoring method, a deeper investigation into the molecules being mapped or used as biomarkers for cell behaviour can be carried out using PCA. PCA provides an objective method of selecting the molecules to be mapped during the verification and assignment of colours (molecules) to clusters. The automation of the analysis steps using Python scripts and Jupyter 7.0 Notebook [82], [83] makes the analysis accessible for future researchers. Investigating two commonly used clustering algorithms (k-means and hierarchical) provided an opportunity to verify the clustering by comparison to false-colour shaded maps of the same cell and fluorescence microscopy DAPI stained cells. K-means clustering was found to not only be quicker but produce clusters that more closely matched the false-colour shaded maps.

The third aim of the chapter was to explore the use of k-means to exclude or select Raman map regions. Removing the backgrounds by zero-array substitution allowed clearer, more easily interpreted images to be produced (Figure 3.2). Substituting zero-arrays also provides a method of removing high Raman scattering regions, such as those associated with scaffold materials, in future studies and the next chapter. The process of exploring different regions of the Raman map facilities the development of tools to quantify different aspects of the cell being mapped. Creating a map exclusively of the nucleus, or cell body is carried out technically by creating a data feature relating only to that cellular region. Carrying out standard statistical analyses of Raman intensity (min, man, averages, standard deviation, etc.) on

specific regions within the map is therefore simplified. As the area of a pixel is known during Raman mapping, it is easy to determine the area of a cellular feature, say the nucleus, through the multiplication of the pixel area by the count of spectra in the nucleus data feature. Measuring the area of target map features through the multiplication of selected pixels is not available in standard Raman map visualisation software, to the best knowledge of the authors. Having established a protocol for and demonstrated the application of k-means directed shading using conventional two-dimensional Raman mapping, expanding the process for analysis of three-dimensional VRM can be carried out in Chapter 4, where depth-associated challenges will be addressed.

Chapter 4 - Raman mapping of single cell scaffolds

4.1 Introduction

Confocal Raman analyses and visualises the bulk chemical / molecular composition of samples by focusing a laser beneath the sample surface and detecting the Raman scattered photons from that location [6], [7]. Applications include determining paint layer thickness [43], mapping pharmaceutical drug particle coatings [113], locating surface enhanced Raman spectroscopy nanoparticle cellular uptake [114], visualising extracellular vesicles in cells [115], microplastic analysis [116], and monitoring drug release from polymer capsules in three dimensions [31]. By collecting Raman maps (slices) through a sample at regular z-axis intervals (z-steps), 3D Raman mapping, or volumetric Raman Mapping (VRM) [31], [32], non-destructively visualises molecular distributions through a sample [6], [7], [32]. However, mapping along the Z-axis increases sample thermal damage [31] and makes axial morphological verification complex. Conventional Raman mapping (across a single XY plane) is commonly verified through comparison to stained [117], [118] or labelled [37] microscope images, as was carried out in chapter 3. For VRM, Raman mapping along the z-axis increases experimental complexity [6], [7]. Complicating factors for VRM include physical properties of light like diffraction [41], refraction [7], [40], and a range of practical considerations specific to each Raman system. Practical considerations include manufacturing tolerances, system calibration, maintenance, and confocality have a greater influence on VRM than conventional Raman mapping, resulting in the detection of photons from outside the collection area (out-of-focus contributions) [30], [42]. Verification of axial VRM details is not currently available within VRM-producing software. Chapter 4 investigates the hypothesis that calibrating z-steps for a specific Raman system to counter z-axis incurred abortions, will increase confidence in morphological conclusions drawn

from VRM. The VRM axial dimensions are verified through comparison to electron microscopy images.

4.1.1. Resolution

The starting point for VRM calibration is understanding image resolution and acknowledging the resolution asymmetry between the axial and lateral axes. The resolution of an image determines the detail it can visualise, measured in pixels. A pixel contains a colour for a given area of the image. In Raman mapping, the colour can indicate quantitative data through shade intensity relating to Raman intensity [5], or chemometric features such as principal component score [21]. Chemometrics can also provide shading to qualitative data such as association to a cluster [37]. Higher-resolution images contain more pixels per image area, revealing greater detail. Higher resolution in Raman mapping, where every pixel relates to a Raman spectrum, increases resolution by reducing the distance between collections. Increased resolution improves both the molecular and morphological insight provided by the map [21], with the image detail increased alongside the reduced distance between measurements of any molecular fluctuation [21]. Calculating the diffraction-limited Airy disk indicates confocal microscope resolutions (lateral and axial), defining the minimum distance between two collections to avoid sampling the same area twice (oversampling) [21] for conventional (lateral) Raman mapping. Calibration of the laser focus before experiments can produce a laser focus approaching the diffraction limit, with high-quality equipment and calibration for lateral mapping.

Resolution is a key factor in Raman mapping, where every pixel is collected individually, so increased detail must be balanced against increased data collection times. One of the chapters aims is to show the effect of map resolution on the capacity of the map to show the size of a physical feature. Figure 4.1 (A-D) shows Raman maps produced using k-means clustering of the same HaCaT cell produced with different resolutions. The colours relate to sub-cellular regions and the map background (black), where the loss in detail can be seen as the resolution reduces.

(A) shows the clearest 44×40-pixel map, in (B) the map shown in 17×17-pixel resolution requires less memory with a small detrimental effect on map detail. By (C), an 8×8-pixel map, the information is provided in 27.5 times fewer pixels, but the image detail is significantly diminished and by (D) a 4×4-pixel map of the cell, it is difficult to know what the map focus is of without prior knowledge of the image subject. By altering the level of detail, resolution affects the apparent sample dimensions. To demonstrate this, a 20×20 µm OrmoComp™ direct laser written (DLW) block is shown in Figure 4.1 (E-G) mapped using four different pixel sizes, with qualitative shading of the construct (yellow) and the background (black). (A) shows 0.5×0.5 µm pixels, where the edges of the scaffold appear rounded and undefined, explained by the rounded corners observed in the SEM image of a comparable block in (D). The apparent dimensions and shape of the block vary due to the different resolutions used in (B) 2×2 µm pixels, and (C) 10×10 µm pixels. The altered dimensions are clear for constructs of known size, but potentially misleading for samples of an unknown size such as the multi-resolution HaCaT cell shown above it in the figure.

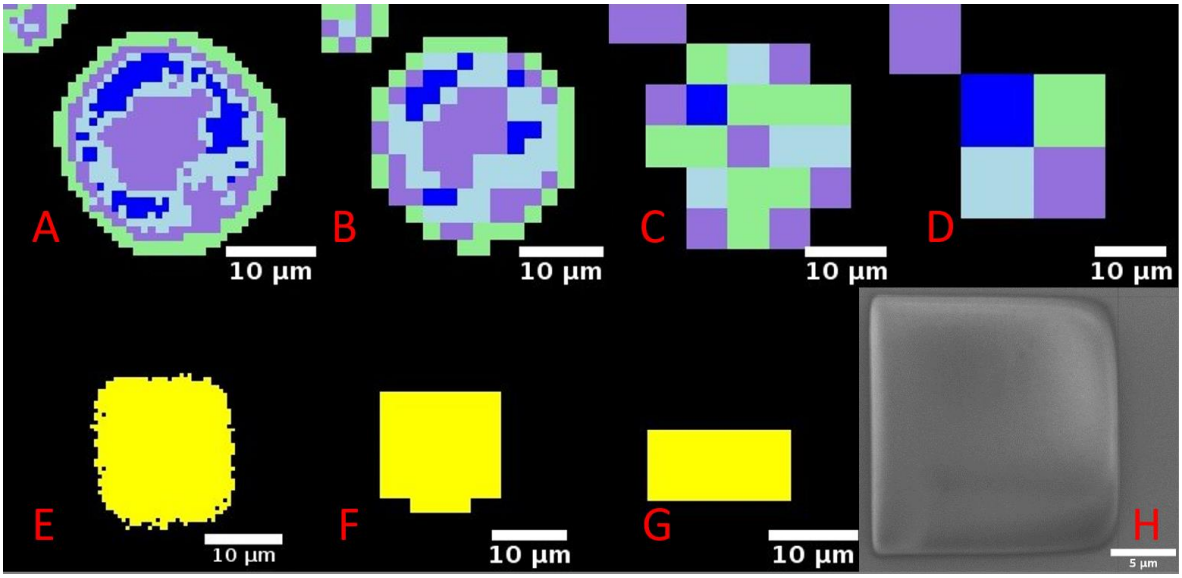

Figure 4.1 – Multi-resolution image of HaCaT cell: *A-D) HaCaT cell (dithranol 3 hours) Raman mapped using 5 k-means clusters and different resolutions. A) 0.8 µm² pixels (44×40-pixel map), B), 2 µm² pixels (17×17-pixel map), C), 5 µm² pixels (7×7-pixel map), D) a 10 µm² pixels (4×4-pixel map). E-G) Mapping 20×20 µm DLW printed OrmoComp™ pillar, with SEM print accuracy verification (H). E) 0.5 µm² pixel map, F) 2 µm² pixel map, & G) 10 µm² pixels.*

4.1.2. VRM resolution and distortion

In VRM, the calculation of lateral and axial dimensions for three-dimensional pixels (voxels) is similarly indicated using the diffraction limit. The lateral resolution remains the same for VRM as conventional Raman mapping for the same laser and objective. A different equation is used to calculate the diffraction limit along the optical axis (z-axis for VRM) than the lateral diffraction limit [40], [41]. The diffraction limit equations describe an inherent laser focal asymmetry, where focal depth is larger than focal width [119], [120]. Measurement of a confocal Raman lasers depth of focus is carried out by measuring the full width half maximum for the depth profile of a silicon wafer, plotting the 520 cm^{-1} spectral peak intensity [40], [41]. Different studies may desire oversampling to increase Raman map contrast [121], under sampling to speed analysis, or a balance between speed and accuracy. However, determining which is occurring during analysis is critical to obtaining the highest accuracy conclusions in a study. The axial collection area (CA) dimension will not match the dimensions calculated by the diffraction limit formulae if there is a difference between the refractive indices of the sample and the immersion media (air, oil, or water) [7], [40], [41]. The diffraction limit calculations assume the laser is focused in the immersion media, whereas in reality, the CA is distorting from that ideal, immediately once focused into the sample (if the sample has a different refractive index from the immersion media). Refraction, alongside further aberrations, result in the axial CA dept, and corresponding VRM resolution, rarely achieve anything near the diffraction limit laser focus of conventional Raman mapping. The influence of refraction and out-of-focus contributions increase the collection area axial depth, resulting in the collection of photons from a larger volume than expected incentivising increased z-steps to counter oversampling or a required acknowledgement if oversampling is used. Although the diffraction limit does provide a starting point when selecting a z-step, a benchmark that calibration can distinguish further distortion from when aiming to maximise the accuracy when mapping a samples height.

The resulting disparity between the actual and expected collection area location and volume results in the assignment of Raman scattered photons to the incorrect region of a VRM reduces confidence a spectroscopist could place in the assignment of coordinates to a Raman signal [7], [40], [41]. Initial research into depth distortion focused on depth profiles analysing the thickness of polymer layers [30], [40]–[42] and the development of mathematical models to correct results showing shallower layers than expected [40], [41]. Depth distortion reveals the sample thickness at which confidence that a Raman signal assigned to a position originated within an expected volume is lost. VRM collected at axial depths dominated by depth distortion are corrupted, resulting in VRM distortion, eroding the morphological insight provided by mapping the z-axis. In 2000, the calculation of depth resolution was published, quantifying depth distortion [40], [41]. Everall [40], [41] demonstrated the distorting effect of depth distortion on VRM and then used refractive index matching oil-immersion objectives to avoid the distortion [40], [41]. Depth distortion makes determining a samples true axial dimension highly complex, with accurate sub-surface analysis previously described as impossible with mismatched refractive indices [40], [41]. Refractive index matching biological studies is possible using phosphate-buffered saline solution, which has a similar refractive index to cells [122], [123]. Matching refractive indexes and the mathematical corrections developed for correcting depth profiles becomes prohibitively complex for multi-material samples used in some pharmacological and bioengineering applications [6], [31], especially for potential adopters of VRM.

4.1.3. Hypotheses

A potential solution is to determine a range and z-steps, calibrated using a method suggested for calibrating the false-colour shading of VRM by Baldock et al [6]. Baldock et al described constructs DLW to known dimensions, where comparison provides a verification method for shading parameters [6], where a hypothesis to be tested is; z-steps can be determined that minimise VRM distortions. Constructs are distinguished from scaffolds as DLW printed articles unused for cell growth support. Another hypothesis to test a chapter aim of developing a calibration method for VRM

z-steps; that the z-step calibration can be verified. Verification of the z-steps can be tested using scanning electron microscopy of calibration blocks and scaffolds, to determine the accuracy of spatial information provided by the VRMs. The z-step that most accurately reproduce the known dimensions of the calibration block have then been calibrated as the most accurate for the system. Finding the smallest z-step that avoids oversampling therefore provides a target resolution for this chapter / project. A range of heights will be tested, aiming to determine out-of-focus contaminated slices outside the known calibration block, which are then reduced by increasing the z-step. Having determined constraints around the upper and lower bounds of the collection area which account for diffraction, refraction, and the unique features of the system being used, the only remaining factor to be considered is the increased heat exposure to the sample, which is discussed in Chapter 6. The findings from the calibration block experiments will be used to explore the aims of VRM mapping a cell on a scaffold (with the hypothesis that k-means directed shading can be used to shade a cell-scaffold VRM, building on the previously applied k-means shading for 3D Raman [124], [125]). The final aim of the chapter will be to use the calibration block findings to design further scaffolds that account for depth distortion.

Chapter aims:

1) To establish that image resolution relates to the confidence in spatial/morphological insights determined using Raman mapping.
2) Develop a calibration method for volumetric Raman mapping (VRM) to increase the confidence researchers have in VRM spatial measurements.
3) Verify the ability of z-step calibrated VRMs to map a cell on scaffolds prior to further application of the technique in subsequent chapters.
4) Use the VRM calibration findings to develop improved scaffold design for the production of Raman maps of cells in three-dimensional morphologies, whilst minimising depth related distortions.

4.2. Chapter specific methods

Methods for the VRM, cell culture, and DLM are found in Chapter 2 (materials and methods), which contains experimental details of methods employed in multiple chapters.

4.2.1. Calibration block design

Constructs are modelled using the computer-aided design package Solidworks RX™ 2018 and converted into STL. file format and uploaded to the DeScribe™ software that produces a script for the Nanoscribe™ 3D printer. Calculating the axial diffraction limit (DL) for the system being used provides a starting point when investigating the axial resolution for that system, calculated with equation 1,

Equation 1 [126]: $DL = \frac{4n\lambda}{NA^2}$

where n is the ratio of refractive indices between the refractive index of the material being analysed $n(m)$ and immersion media $n(i)$, λ is the lasers wavelength and NA is the objectives numerical aperture. As λ = 532 nm, NA = 1, and n = 1.52/1.33 = 1.14 when a water immersion objective is used, the diffraction limit is 2.4 µm. As described in the introduction, Depth resolution (DR), determines the depth at which assigning a coordinate to a Raman signal becomes impractical. DR is calculated using equation 2, where Δ is the intended depth of analysis provides a method of determining the extent to which the collection areas axial depth has changed in response to refraction. The aim of the calibration block is to determine a consistent CA depth and corresponding z-step, where distortion of the collection area is minimised to minimise out-of-focus contributions being detected. By substituting DR for the known value of DL (2.4 µm) and rearranging for Δ, the depth at which DR exceeds DL can be determined and used to define the depth at which refraction degrades a VRM:

Equation 2 [7]: $DR = \Delta\left[\left[\frac{NA^2(n^2-1)}{1-NA^2}+n^2\right]^{1/2} - n\right]$

For an NA = 1 objective, the denominator in equation 2 ($1 - NA^2$) becomes $1 - 1^2 = 0$, resulting in a division of zero. Graph 4.1 shows the depth when DR = DL for different increments of NA as NA approaches one. The closer NA gets to one, the closer the depth DR = DL gets to zero. The calibration block was therefore designed to be a similar depth to the diffraction limit for the water immersion objective Where NA = 1 and a 532 nm laser.

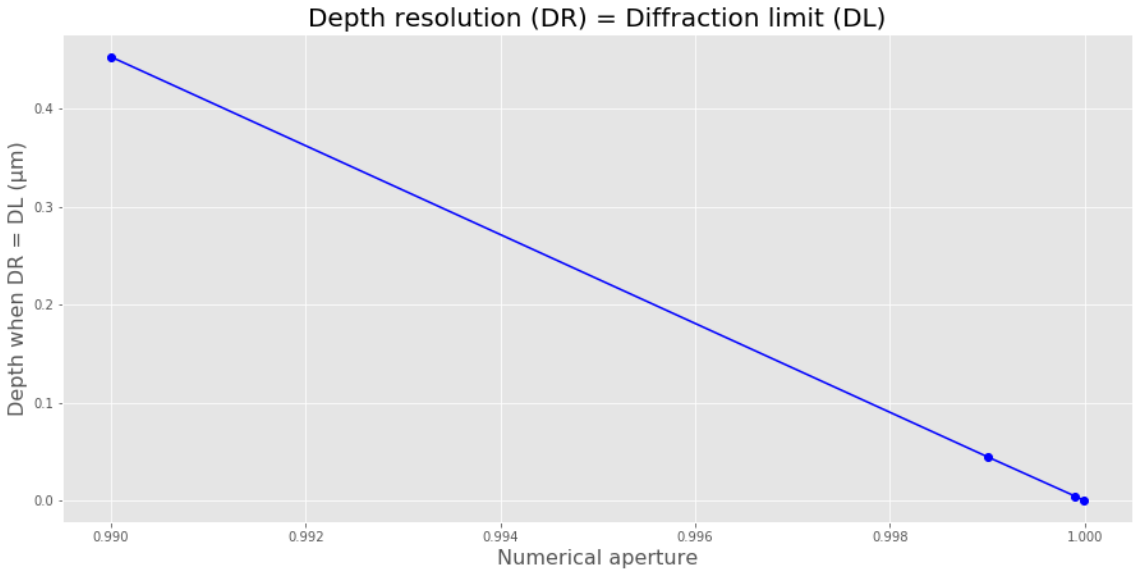

Graph 4.1 - DL vs. DR: *The depth when the diffraction limit (DL) equals the depth resolution (DR), plotted against numerical apertures approaching one, showing the trend for the depth where DL = DR to approach zero as NA tends to one.*

4.2.3. Median shading

Once the calibration block is fabricated, using it to determine a z-step that achieves research aim 1 for aim 2 is the next step. A definition of image resolution is the capacity of an image to distinguish two points. In this study, an aim is to produce images of cells that are resolved along the axial dimension. Producing resolved VRM

requires proof that the chosen z-step produces slices independent of each other, defined as supplying slices that are not oversampled (providing the same information twice). This chapter aims to determine the smallest z-step that avoids oversampling, to provide the highest accuracy VRM when compared to SEM measurements, a previously applied method of verifying VRM accuracy [127]. A further goal is to produce VRM z-steps that do not miss sections of the sample (under sampling), distorting the VRM (see Figure 4.3). Median shading is a shading method where shading parameters relate to a multiple of the median Raman intensity for the slice. As each slice is multiplied by the same multiple, a proportional shading is applied through the VRM, whilst favouring slices showing features with intensity distributions above the slice mean for that wavenumber.

A region containing high Raman intensities appears on histograms and violin plots as Raman peaks higher along the scale and is also noticeable when comparing the difference between the slice mean and median. The difference between the mean and median grows in slices with a high-intensity region, as occurs when mapping polymer constructs. The difference between the mean and median results from the way the two averages are calculated. The mean is the summed Raman intensities divided by the number of slice collections. As the mean accounts for all Raman intensities, regions of higher intensity (such as the construct) increase the mean. The median is the middle value in the range of slice Raman intensities and is therefore unaffected by the regions of higher intensity remaining lower in those slices. Determining shading parameters such as a lower range to exclude using the median, therefore hypothesised as an opportunity to exclude out-of-focus contributions. Median shading exclusion of out-of-focus contributions from VRM would then facilitate the smallest resolvable distance between VRM slices, maximising the resolving power for a given Raman system.

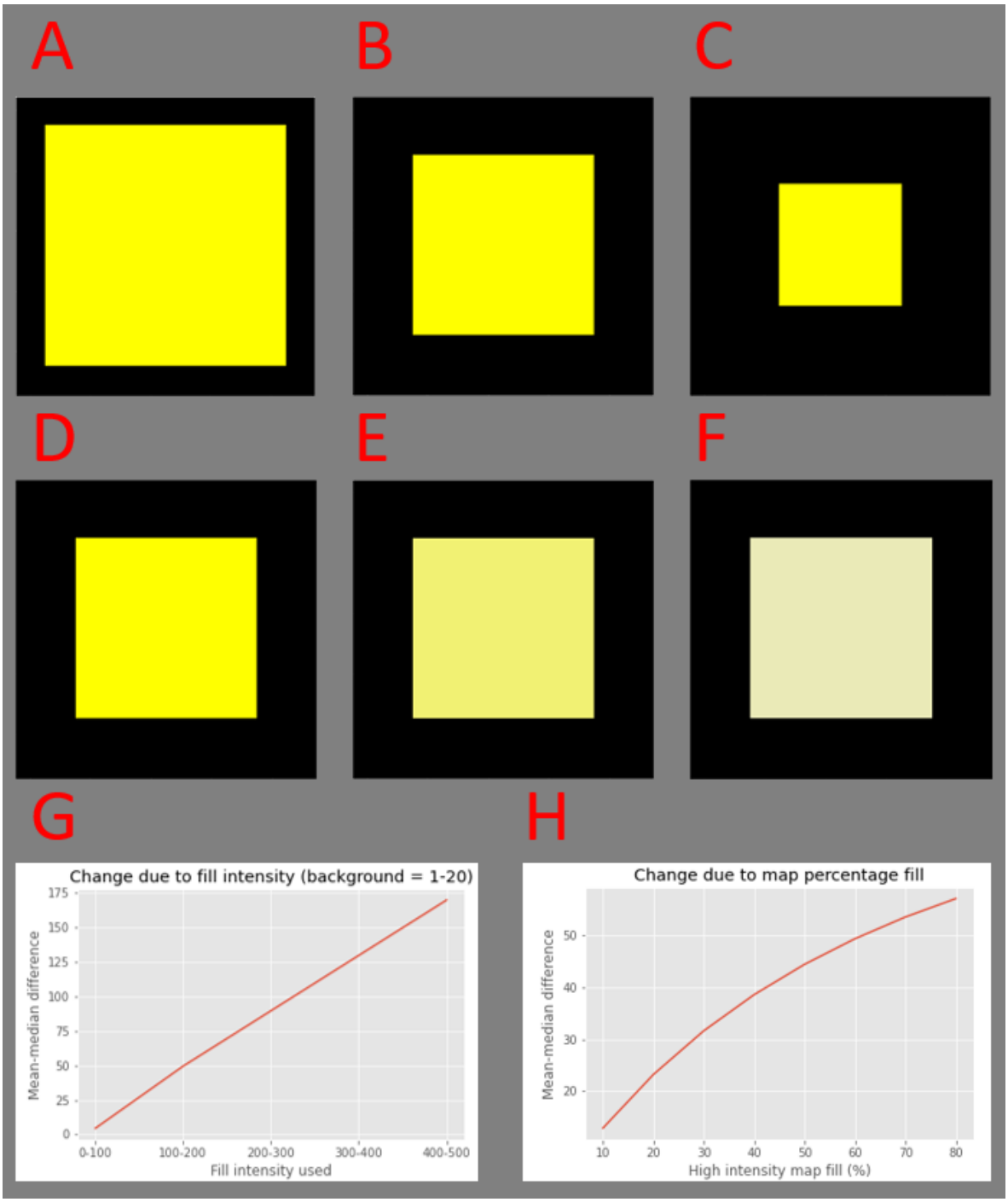

Figure 4.2 – Percentage fill vs. Fill intensity: *A-C) Varied percentage fill from 81% (A), to 36% (B), and 16% (C), consistent colour intensity. D-F) Fill intensity change, starting at a colour intensity of 100% (D), to 70% (E), and 30% (F), with the percentage fill kept consistent. G) Graphing the relationship between map mean and median difference (y-axis) and the intensity fill (x-axis). H) Graphing the relationship between map mean and median difference (y-axis) and percentage fill (x-axis).*

Figure 4.2 demonstrates two considerations when designing a construct to calibrate z-steps using median shading. Both considerations relate to factors that influence the difference between the slice mean and median. Datasets of 200,000 simulated 30×30-pixel slices per sample type were produced by looking at two variables, the percentage of a slice the scaffold fills (percentage fill) and the intensity difference between the scaffold and the background (fill intensity). Figure 4.2 top (A-C) shows the difference in fill intensity, where the colour intensity drops from A to C, indicating a reduction in fill intensity. The simulated slices for fill intensity kept the percentage fill (36%) and background intensity range (1-20) consistent, using a random number generator for the background and fill values. The fill values were then increased within ranges between 100-200, 200-300, 300-400, and 400-500, to simulate incrementally increasing Raman intensities within the scaffold. The mean and median of each simulated slice were calculated and averaged. The 200,000 slices were chosen as the number at which the averages became consistent to within three decimal places when repeated five times. The average for each range was then calculated over the five repeats and the difference between the means and medians plotted in Figure 4.2 (G), producing a linear trend being produced showing the increasing difference between the mean and median as the fill intensity increases relative to the background intensity.

The percentage fill of the slice is the percentage of the slice that the construct or sample fills, as demonstrated by Figure 4.2 (D-F), where the fill intensity (colour intensity) remains consistent, but the percentage of the slice filled by the construct reduces between D and F. Figure 4.2 (H) shows the plot calculated using the same method, except keeping the fill intensity consistent and varying the percentage fill at 10% intervals between 10 and 90%. A similar trend can be seen, although the rate is not as consistent, that the mean-median difference increases with the percentage fill. Both the percentage fill and the fill intensity affecting the mean-median difference make a consistent lateral dimension critical for a calibration block, as this keeps the percentage fill consistent (assuming each slice has the same lateral dimensions), focusing the difference on the fill intensity.

4.3. Results and discussion

4.3.1. Arbitrary z-steps and subjective shading

Figure 4.3 reveals the non-trivial nature of producing VRM, with scanning electron microscope images (A-C) of a book construct showing Lancaster University crest book, printed in OrmoComp^{TM}. Figure 4.3 (A) shows the lateral view of the scaffold and the (B) shows the construct tipped at a 40° angle. The SEM images verify the print quality for the lateral (VRM top view), with some rounding occurring at the edges and shallow sections of the print shown in the tipped image. The axial depth of the construct can be measured using the SEM of the construct whilst tipped, by measuring the distance from the top and bottom of the side of the construct, 1.67 µm, and dividing by $\sin(40)$, equalling 2.59 µm. The measurement is not exact, due to the rounding of the top edge of the construct, however, the axial depth of the construct being below 5 µm can be asserted with confidence. The drastically increased effect of the z-step on apparent sample dimensions is demonstrated by comparing the four VRMs produced of the same construct. The book is mapped using staggered z-steps 2, 6, & 12 µm, the VRM lateral resolutions shown in Figure 4.3 (D, F, & H), and the axial views shown in (E, G, &, I). The shading parameters used were chosen to produce the best reproduction of the construct lateral resolution, which stays relatively consistent compared to the axial dimensions. The resulting axial views are drastically changed when shading parameters are chosen to keep the lateral view consistent, where improving the axial dimension degrades the lateral.

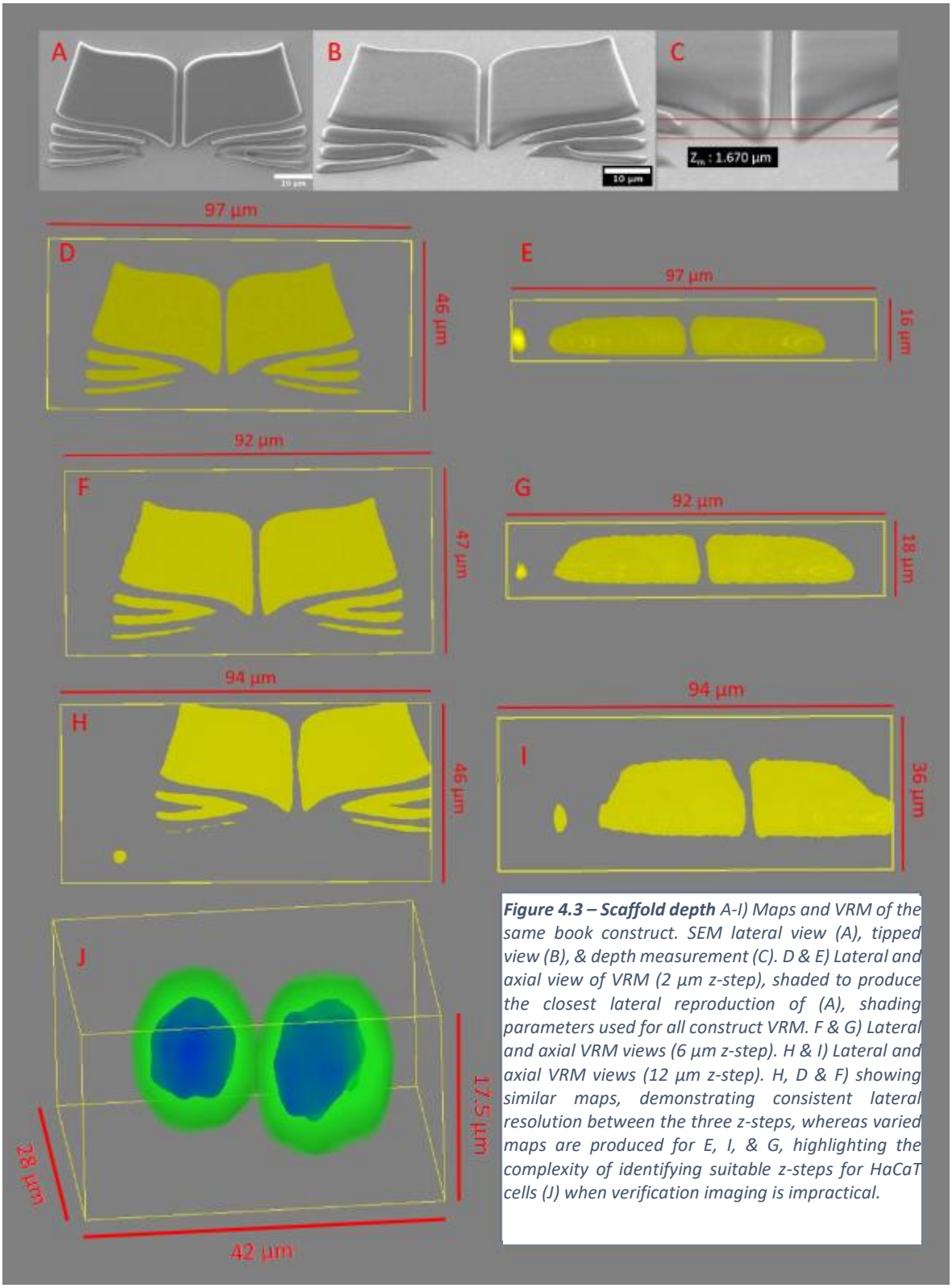

Figure 4.3 – Scaffold depth *A-I) Maps and VRM of the same book construct. SEM lateral view (A), tipped view (B), & depth measurement (C). D & E) Lateral and axial view of VRM (2 µm z-step), shaded to produce the closest lateral reproduction of (A), shading parameters used for all construct VRM. F & G) Lateral and axial VRM views (6 µm z-step). H & I) Lateral and axial VRM views (12 µm z-step). H, D & F) showing similar maps, demonstrating consistent lateral resolution between the three z-steps, whereas varied maps are produced for E, I, & G, highlighting the complexity of identifying suitable z-steps for HaCaT cells (J) when verification imaging is impractical.*

It can be seen from Figure 4.3 that the choice of z-step can drastically alter the apparent size of a sample at this scale. The altered apparent height of the construct is comparable to the increased interface depth previously described by Neil Everall [40], [41]. Under-sampling changing the book constructs axial dimension of the construct in the same way the lateral dimensions were changed for the cell and construct in Figure 4.1. In cases where the size is known, this can be corrected or acknowledged in publications. Axial inaccuracy is a greater challenge when studying samples of unknown depth, as verifying the axial accuracy (side view) requires the sample to be tipped, which is unavailable in typical Raman spectroscopy. The dually complex nature of axial distortions previously described by Everall [7], [40], [41] where sample interfaces grow, and deeper samples shrink as a result of depth distortion. Depth distortion occurs as refraction increases the actual depth of the collection area, resulting in it passing through the sample in fewer slices, producing a VRM showing a shallower sample than expected [7]. In Figure 4.3, the construct is too shallow for depth distortion, with the same axial depth as the calculated collection area. Refraction cannot increase the depth of the collection area to deeper sections of the sample, instead, refraction pushes it past the sample. An increased VRM constructs depth occurs because the collection area is focused onto the sample more than once, resulting in more than one slice mapping the construct. The slices above the scaffold are contaminated through oversampling, increasing the apparent height of the construct.

4.3.2. Depth profiles showing out-of-focus contributions.

The apparent construct/sample shape or size is not only influenced by over or under-sampling. In an ideal confocal Raman system, Raman scattered photons originating outside the diffraction-limited collection area would be excluded from the analysis. Even when the axial depth of the collection area is considered there are several other causes of distortion in VRM including, photon migration [30], [42], and equipment engineering tolerances such as imperfect confocality. The combination

of these effects results in the detection of Raman scattered photons from outside the collection area, which will collectively be referred to as out-of-focus contributions, as they are detected photons that originated outside the laser focus (collection area). Out-of-focus contributions have been reported in conventional Raman mapping [30], [42], where the intensity is typically low enough not to distort a conventional Raman spectrum/map. For mapping along the z-axis, out-of-focus contributions are more significant and must be addressed.

Figure 4.4 indicates the effect of out-of-focus contributions with three depth profiles collected at the same XY coordinate of a 6 µm deep direct laser written construct. The plots show the intensity at regular positions along the optical axis (1 µm - green, 3 µm – blue, and 6 µm - red). An ideal Raman system would only detect Raman scattered photons when focused onto the sample, producing a depth profile peak relating to the sample axial depth. A researcher setting the axial 0 µm position on the slide surface to analyse a sample resting on the slide surface would expect the peak to extend from around the 0 µm position. The depth profile peak would persist through the sample axial depth, reducing as it rises above the sample (and the corresponding Raman signal). Signal detected from positions outside the anticipated axial depth would therefore suggest either a larger sample than expected, a poorly set zero position, or out-of-focus contributions.

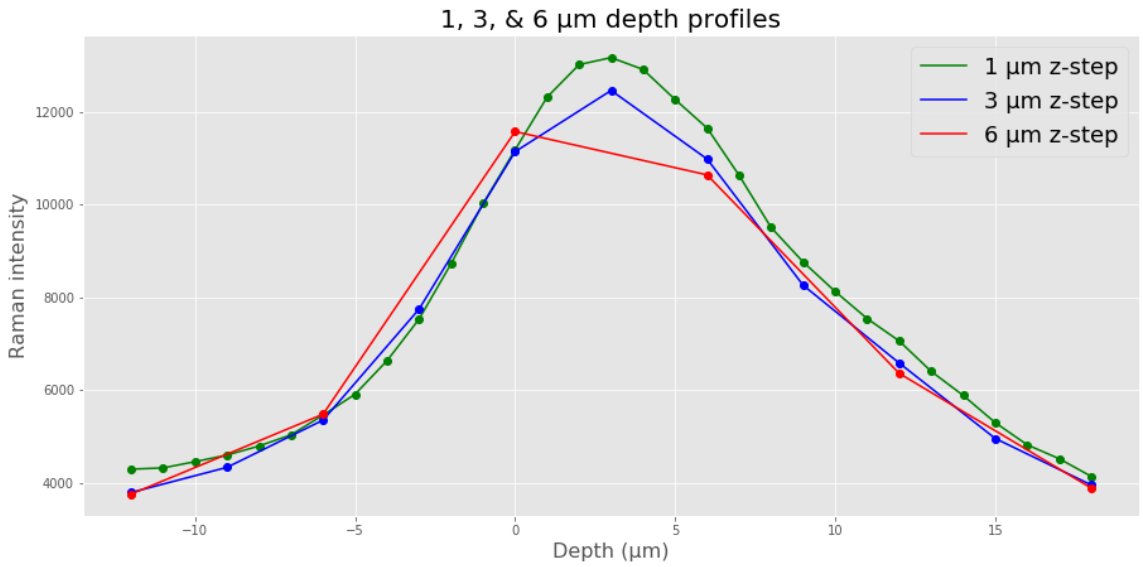

Figure 4.4 – Z-step depth profiles: *Depth profiles of the same XY position on a 6 µm deep construct using 1 µm (green), 3 µm (blue), and 6 µm (red) z-steps, where dots = collection depths.*

Figure 4.4 shows a rising profile peak from around -10 µm, rising steeply until the 0 µm position, and dropping steeply from the 6 µm position (depending on the z-step) until it reaches the 16 µm position. An additional range equally spaced 10 µm either side of the 0-6 µm expected axial depth suggests that the zero position and construct height are correct, and the Raman signal detected outside the 0-6 µm range has an increased probability of being out-of-focus contributions. The three z-steps produce the closest agreement between the -10 to 0 µm and 6 to 16 µm regions, diverging once interacting more closely with the construct. The 1 µm z-step plot (green) is the smoothest because the difference between the Raman intensities is small. A small difference between the highest-intensity collections shows how the same information is captured multiple times when the collections are too close. The lines between the 3 µm z-step collections have a sharper change in gradient between collections than the 1 µm z-step, showing an increased difference between collections. The different z-step depth profiles have similar Raman intensities at each collection (dots), as the same position is analysed.

The steepest gradient occurs between the collections using a 6 µm z-step, indicating that a VRM collected using this z-step would have distinct slices and corresponding lowest levels of out-of-focus contributions. However, the disadvantage of increasing

the z-step length is the potential under-sampling, where sections of the sample are not exposed to the collection area, risking the loss of key features. The choice of z-step is therefore determined by the goals of the study, balancing accuracy, cost, and the use of oversampling to increase signal. If the status of the collection is understood and reported. The goal of this study is to maximise axial accuracy, defined as collecting the tightest z-steps, whilst avoiding oversampling. The depth profiles, therefore, suggest a z-step in the 3-6 µm range would meet these goals, with further investigation required in the next sections to determine z-steps that maximising the Raman signal without duplicating information through oversampling.

4.3.3. Staggered tube constructs

Having demonstrated the necessity of calibrating VRM z-steps in section 4.3.2, a starting point is to explore z-steps intended to match the collection area depth. The diffraction limit provides an initial z-steps, with its conventional link to resolution. A guide for the maximum depth for a given construct is identified by calculating the depth at which the depth resolution exceeds the axial diffraction limit aiming to minimise the influence of depth distortion. To increase the analysis depth without tailoring the construct material refractive index, analysis of cells sitting on a pore (section 4.3.5). Cells can also be analysed on the scaffold side, or the scaffolds designed for shallow axial depth (Chapter 5). By pairing construct height with a z-step that reproduces the correct construct height, the capacity of median shading to exclude out-of-focus contributions can be explored. DLW fabricated constructs were mapped using a 0.75 NA air immersion objective with a 532 nm laser, producing a diffraction-limited minimum depth of 5.75 µm. A 6 µm z-step (rounding to the nearest µm) was used to analyse tube constructs with a maximum height to avoid significant depth distortion at 6, 12, and 18 µm heights. Mapping the 6 µm construct in a single slice, the 12 µm in two, and the 18 µm in three slices would indicate the median shadings capacity to remove out-of-focus contributions or indicate the need for increasing z-steps to reduce out-of-focus contributions.

In Figure 4.5 – C, distribution plots show the higher Raman intensities measured as the laser is focused within the construct produce pixels with an above-median Raman intensity for the slice (section 4.2.3.). The pixels with greater intensity than the median in slice 3 increase the mean for the slice, causing a gap between the averages. As the median is the middle value for the slice in question, the external slices (1, 2, and 4), above and below the construct inevitably contain pixels with above-median values. As the VRM and construct lateral dimensions remain consistent, the smaller difference between averages occurs because the detection of Raman scattered photons in external slices are out-of-focus contributions (section 4.2.3.), which are less predictably distributed over the slice. The difference in Raman intensity between contaminated and uncontaminated (external slice) pixels is also smaller than between internal and external pixels for slices visualising the construct. As the pixel intensities relating to the construct are higher above the median than the out-of-focus contributions, applying shading parameters based on the median discriminates the external slices.

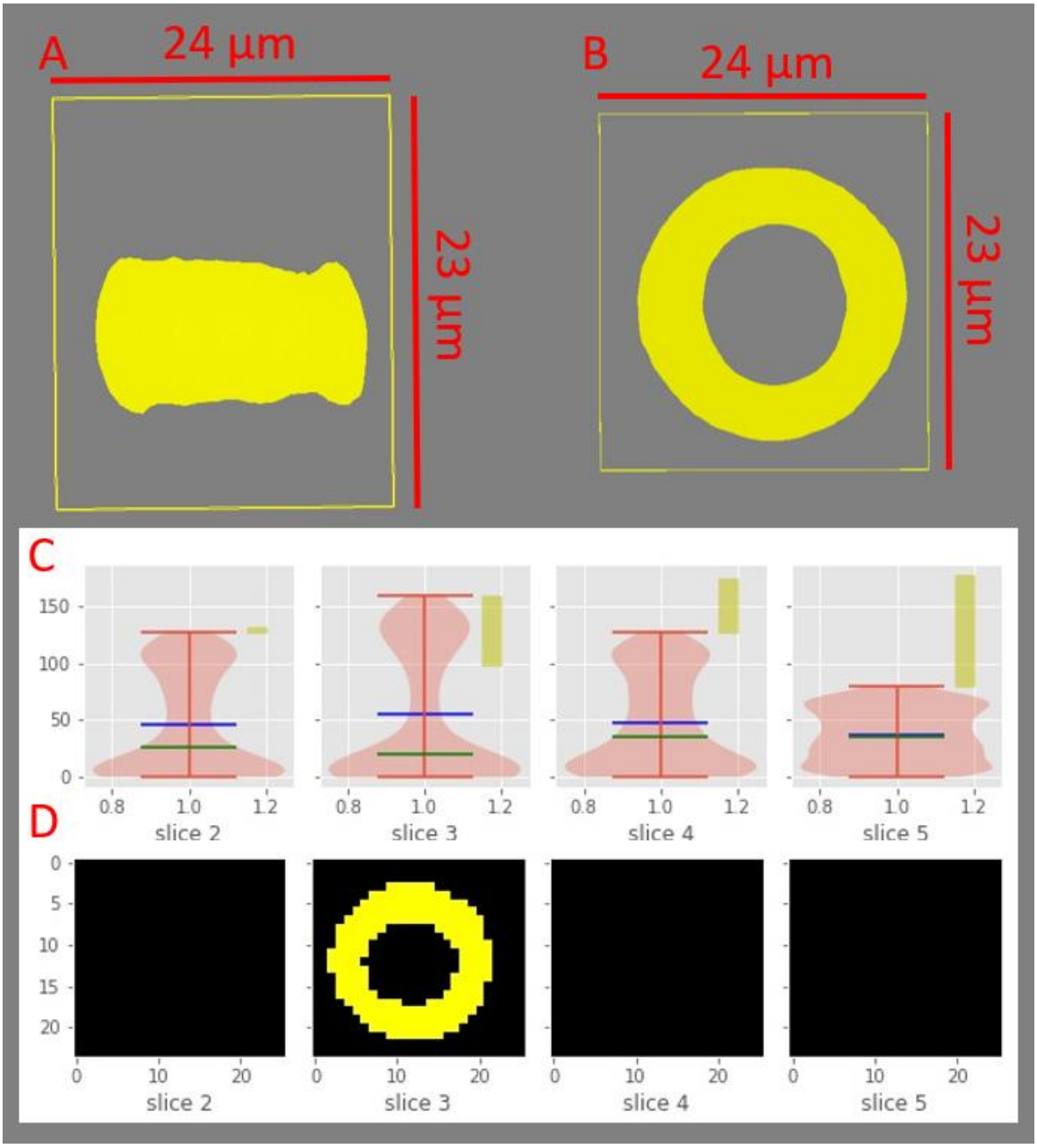

Figure 4.5 – 6 µm Deep tube: *A & B) The side (A) and top (B) views of a VRM of a 6 µm deep OrmoComp™ construct produced using a 6 µm z-step. Violin plots (C) show the Raman intensity (y) against the intensity frequency (x), with the slice mean (green) and median (blue) directly above their corresponding z-stack slice (D). Slice 3 (D) is isolated when intensities below 5 × median for each slice is applied, producing the expected lateral 10 µm inside diameter (ID) - 20 µm outside diameter (OD) and axial (6 µm) dimensions of the tube. Pixel counts (x and y axis) in D, are in µm*

Figure 4.5 shows the side (A) and top (B) views of the WiRE^{TM} VRM, the combination of matching z-step and construct depth producing VRM dimensions that appear to closely match the expected construct dimensions. Analysis of the individual slices provides the opportunity to calculate the exact sample cross-sectional area by multiplying the number of pixels representing the sample by the area of each pixel. steps that avoid out-of-focus contributions (Figure 4.5 - D) show allow the tube thickness to be estimated when the z-steps are large enough to avoid out-of-focus contributions. By including intensities above 5 times the median, the third slice showed a ring cross-section of the tube between 3-7 pixels (each 1 μm^2), where the outer wall of the tube was designed with a 5 µm larger radius than the inner wall. A small amount of contamination in slice 2 indicates that the z-step might need to be slightly larger to exclude all out-of-focus contributions. Showing that a 6 µm construct (with measurable dimensions) can be isolated in a single slice using 6 µm z-steps provides evidence that the method of calculating diffraction and refractive distortions can increase the axial accuracy of VRM. Validating VRM z-steps also increases the strength of conclusions drawn from VRM analysing the morphology of larger biological samples where the optical properties allow deeper analysis, but the morphological dimensions cannot be checked as easily. Further evidence is provided by visualising any distortion incurred when mapping deeper into a sample depth.

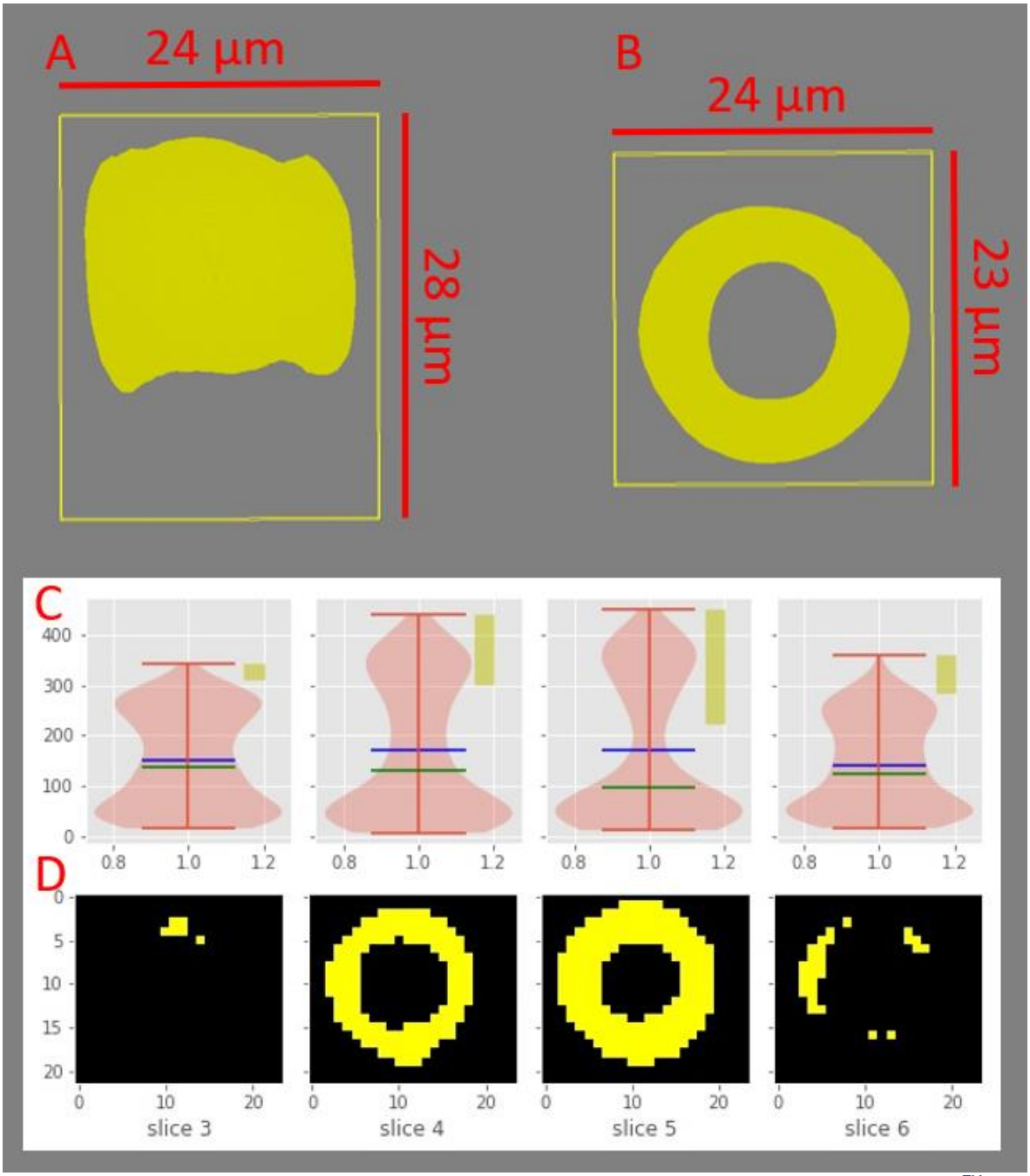

Figure 4.6 – 12 µm Deep tube: *A and B) The side (A) and top (B) view of a 12 µm high OrmoComp™ tube construct mapped using 6 µm z-steps. Shading parameters for (A) and (B) determined as previously by ensuring the lateral dimensions correlated with the expected dimensions aiming for a 5 µm wall thickness in (B). Distribution plots (C) show violin plots, with the Raman intensity (y) against the intensity frequency (x), the slice mean (green) and median (blue) above their corresponding z-stack slice in (D). Slices 4 and 5 were shaded using a 2.3 × median shading parameter (D) to produce the nearest lateral (10 µm ID & 20 µm OD) and axial 12 µm, with the shading range shown in C as a yellow bar. Pixel counts (x and y axis) in D, are in µm*

Analysis of the 12 µm construct (Figure 4.6 – C & D) highlighted two slices (4 and 5), which had the greatest slice mean-median difference. Two slices excluded pixels below 2.3 times the median, with some contamination above and below the construct. A 2-3 µm difference in tube radius may have resulted from the tube bulging around the centre, the VRM (A-B) shows a bulge in the lateral VRM (A), although microscopy verification is required for verification. To determine if the method works for the 6-18 µm range an 18 µm construct was printed and mapped in WiRE^{TM} 3D Volume Viewer (Figure 4.7 – A & B). The difference between the means and medians on the violin plot (B) indicated the fifth, sixth, and seventh slices, with each slice representing the 6 µm below it. The difference between the means and medians was not as clearly distinct as in Figures 4.5 and 4.6, possibly indicating the approach of the VRM depth limit for this refractive index difference, as predicted when the maximum height was set at 18 µm. Pixels with an intensity above 1.8 times the median indicated three slices (D). Slice 6 shows a 2-4 µm larger radius than slices 5 and 7, and contamination above and below the construct. Basing the z-step (6 µm) on the calculation of the axial diffraction limit provided a6method of isolating 1, 2, and 3 slices for the 6, 12, and 18 µm high tube construct respectively, within a maximum range indicated by depth resolution. The disparity between lateral dimensions that increased with depth may have resulted in a deviation from the construct design during printing, or a potential limitation of the system used for VRM of deeper, complex structures, reinforcing the necessity for a microscopy-verified method of calibrating Raman systems for VRM. The ability to link the number of slices, with corresponding z-steps, indicates that the first hypothesis is correct, that z-steps can be identified to minimise depth distortion (within a range), justifying further investigation.

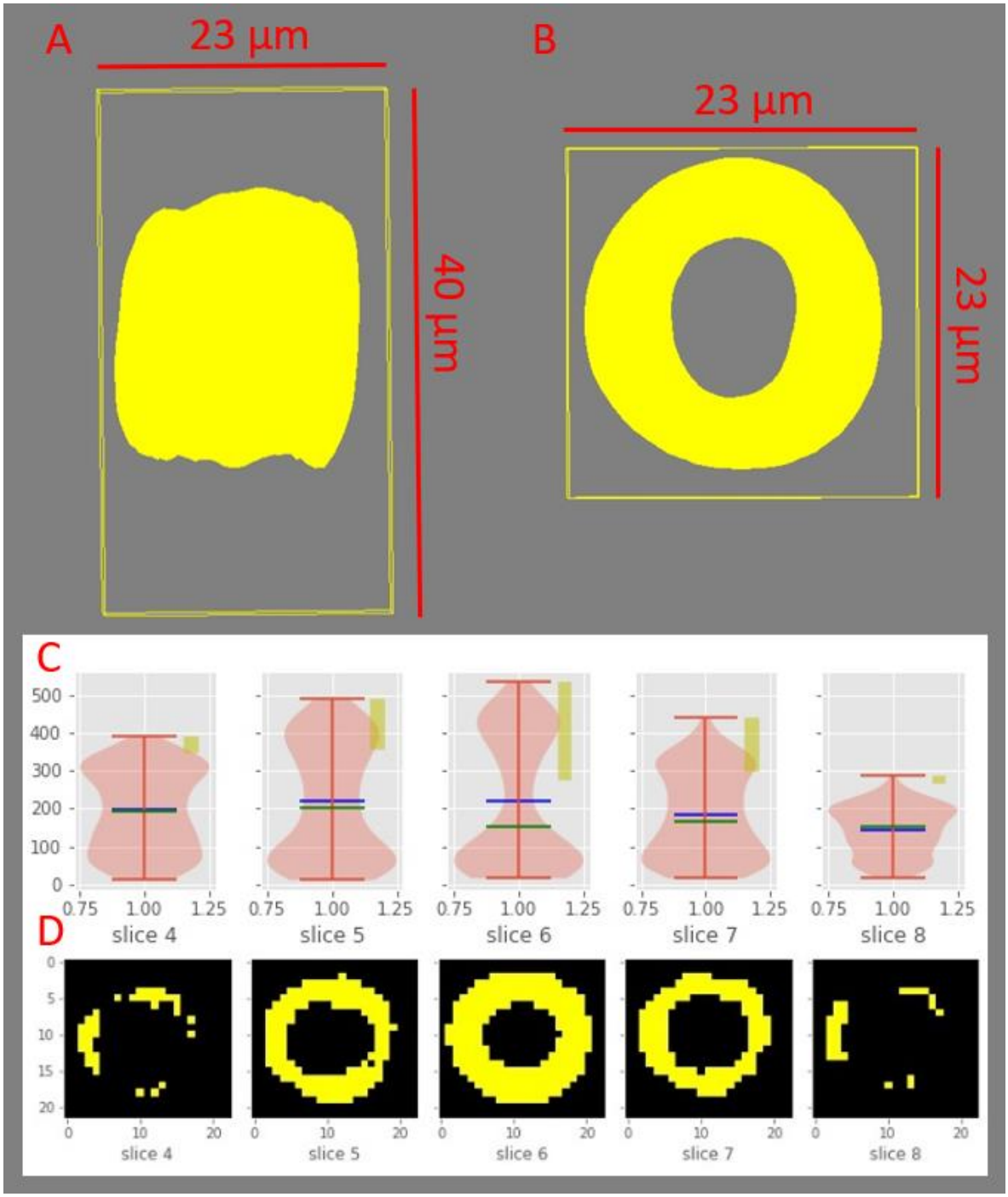

Figure 4.7 – 18 µm Deep tube: *Figure 4.7: The side (A) and top (B) views of a VRM of an 18 µm high tube construct produced using 6 µm z-steps. Violin plots (C) show the Raman intensity (y) against the intensity frequency (x), the slice mean (green) and median (blue) above their corresponding z-stack slice in (D). Slices 5-7 were shaded using a 1.8 × median shading parameter (D) to produce the nearest lateral (10 µm ID & 20 µm OD) and axial 18 µm, with the shading range shown in C as a yellow bar. Pixel counts (x and y axis) in D, are in µm*

4.3.4. VRM z-step calibration

The previous section (4.3.3) demonstrated the capacity of a 0.75 NA objective and 532 nm laser to map three different construct heights. For a system to analyse cell-scaffold complexes, the objective must be a water immersion objective for the cell to stay hydrated. The benchmark set in the previous section is next developed using square pillar constructs of specific dimensions for testing z-steps. Pillars are square to allow lateral accuracy to be easily determined. In section 4.3.3, limited contamination was observed, with the correct number of slices, and the correct distance apart, isolated for the different height constructs. Differences in the 12 and 18 µm high tube diameter in different slices were observed, incentivising the use of scanning electron microscopy to verify the construct dimensions in the next section of the experiment. The experiment was carried out over two stages. The first proof-of-concept stage made sure that the correct number of slices could be isolated whilst retaining the lateral accuracy by comparing the slice of a 20×20×3 µm construct to measurements made using scanning electron microscopy in Figure 4.8. The second repeated experiment used constructs with a 15×15 µm lateral dimension and staggered axial depth, verifying the inability of VRM to visualise features smaller than the CA accurately.

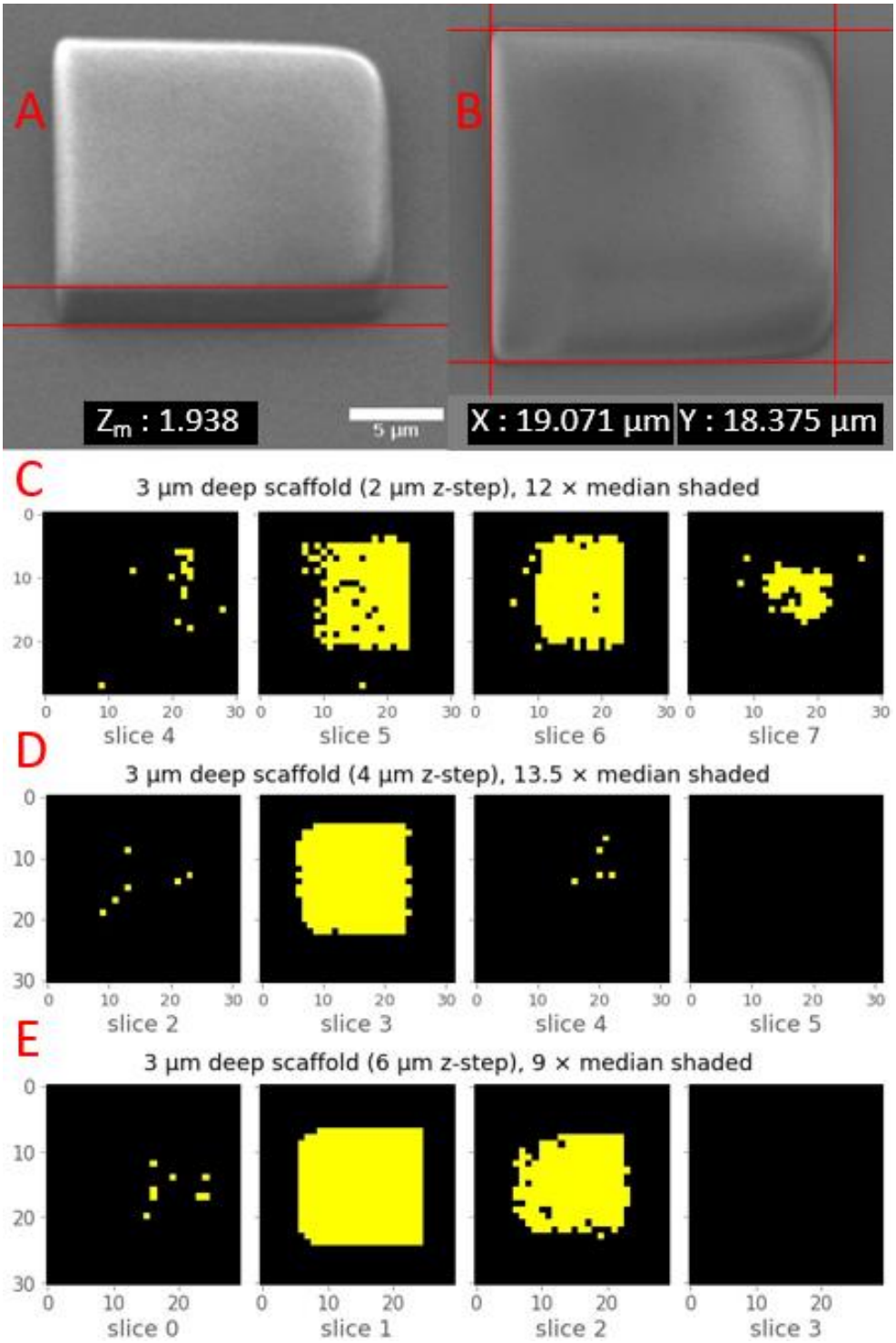

Figure 4.8 – SEM verification of calibration: *A) SEM of a 20×20×3 calibration block tipped 40°, measuring the distance between the top and bottom edge of the block side (1.938 µm) to calculate block depth (3.015 µm). Block lateral (B), measured with X (width) at 19.071 µm and Y (height) 18.375 µm; approximately 1-2 µm smaller than designed. Corner rounding is seen in (A) and (B). C-E) All use a 1 µm² lateral pixels (pixel count along axes). C) VRM z-stack (2 µm z-steps), shaded to 12 × median D) VRM z-stack (3 µm z-steps) with 13.5 × median shading. E) VRM z-stack (6 µm z-step), failing to isolate a single slice. Pixel counts (x and y axis) in C-E, are in µm*

A 20×20×3 μm pillar was used for comparison to scanning electron microscopy (SEM) images to verify the true dimensions of the construct. Figure 4.8 (B) shows the X and Y dimensions of the pillar are 20×20 μm. Two corners have become rounded through shrinkage. The height of the pillar was determined by tipping the scaffold 40 degrees and measuring the distance between the construct observable side top and bottom corners (when observed from above), shown in Figure 4.9 (A). Trigonometry then determined the height of the construct (z-dimension) was 3.015 μm, using the method described in section 4.3.1. In Figure 4.8 (C-E), the slices for the different z-steps used, 2, 4, and 6 μm are shown, with the multiple of the median used for each slice and the z-step used highlighted. In alignment with the previous section, the 4 μm z-step produces the closest agreement with the measured dimensions. The 4 μm distance between slices is within 1 μm of the measured construct height. The rounded corners and edges are shown in the SEM image distorting the edges of the construct. The SEM provides the second hypothesis, that VRM z-steps can be verified, providing information such as showing the reduced thickness at the edges of the constructs, which may produce missing pixels.

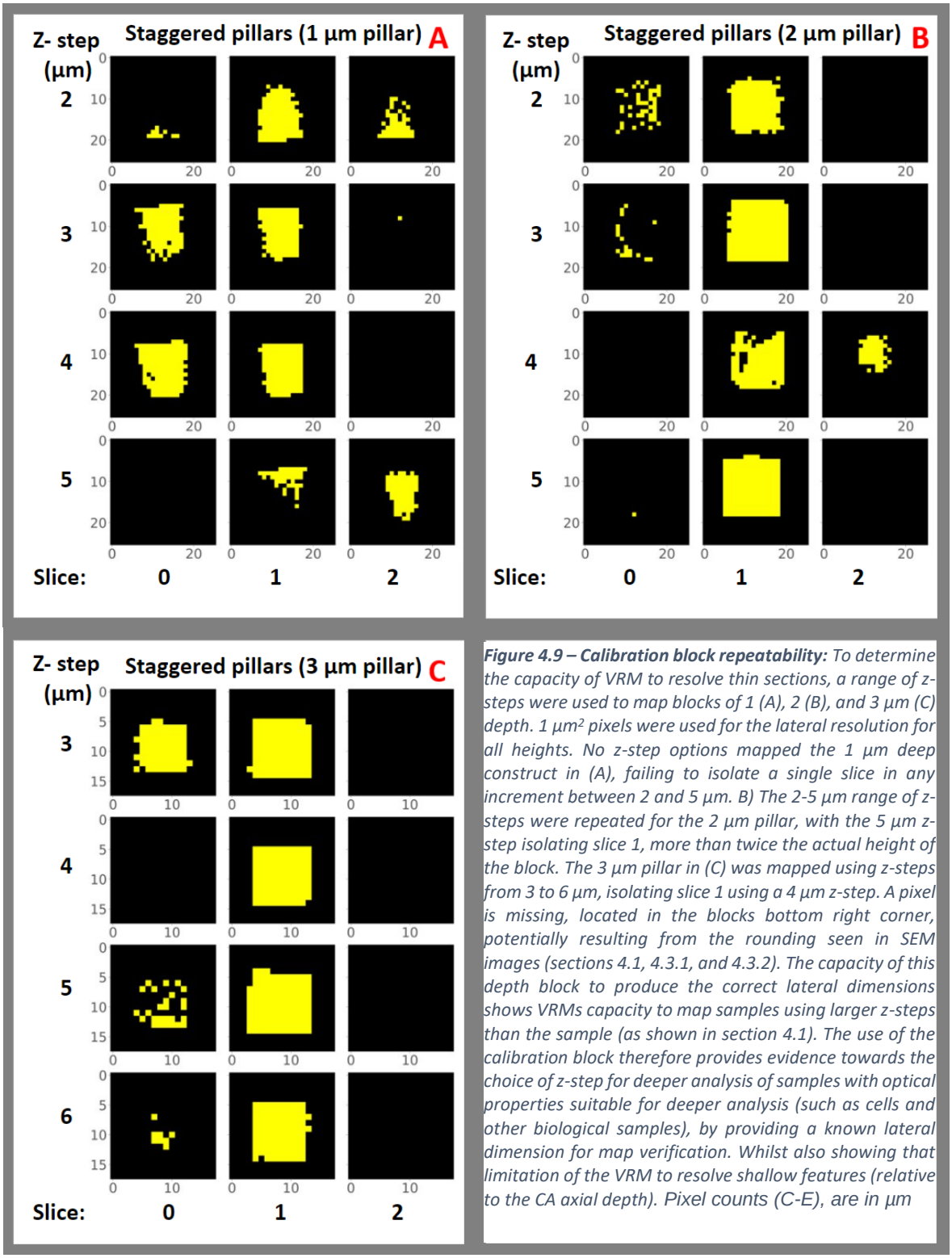

Figure 4.9 – Calibration block repeatability: *To determine the capacity of VRM to resolve thin sections, a range of z-steps were used to map blocks of 1 (A), 2 (B), and 3 µm (C) depth. 1 µm² pixels were used for the lateral resolution for all heights. No z-step options mapped the 1 µm deep construct in (A), failing to isolate a single slice in any increment between 2 and 5 µm. B) The 2-5 µm range of z-steps were repeated for the 2 µm pillar, with the 5 µm z-step isolating slice 1, more than twice the actual height of the block. The 3 µm pillar in (C) was mapped using z-steps from 3 to 6 µm, isolating slice 1 using a 4 µm z-step. A pixel is missing, located in the blocks bottom right corner, potentially resulting from the rounding seen in SEM images (sections 4.1, 4.3.1, and 4.3.2). The capacity of this depth block to produce the correct lateral dimensions shows VRMs capacity to map samples using larger z-steps than the sample (as shown in section 4.1). The use of the calibration block therefore provides evidence towards the choice of z-step for deeper analysis of samples with optical properties suitable for deeper analysis (such as cells and other biological samples), by providing a known lateral dimension for map verification. Whilst also showing that limitation of the VRM to resolve shallow features (relative to the CA axial depth). Pixel counts (C-E), are in µm*

The next stage used constructs with 15×15 µm lateral dimension, looking at constructs of different heights. The focus of the analysis was the repeatability of determining the z-steps and ensuring features shallower than the calculated collection area depth could not be isolated. Constructs deeper than 3 µm were not mapped, as the increased depth would result in depth distortion, which was outside the scope of the experiment. Of the 1 and 2 µm pillar z-steps, only the 5 µm z-step isolated a single slice showing the correct lateral dimensions (Figure 4.9 B). The constructs that were shallower than the collection area axial depth are difficult to isolate because once the z-step is big enough for the slices to be distinguishable, there is not enough material interacting with the collection area to produce significant Raman scattering. The 5 µm z-step maintaining the correct dimensions for the 2 µm pillar fits with this theory, as the z-step is large enough to distinguish slices, with less than ten pixels missing from the high-intensity slice and contaminating the external slice. A single slice showing the correct lateral resolution was isolated using 4 µm for the 3 µm pillar. One pixel is missing from the high-intensity slice, incentivising the use of scanning electron microscopy to verify the construct dimensions and surface finish, as suggested in section 4.3.1.

4.3.5. K-means directed shading of a cell-scaffold.

Section 4.3.4 produced a calibrated z-step, using staggered pillars to determine a z-step range of 3-5 µm, potentially fluctuating in response to laser alignment and power variation on different days. The next chapter aim (3) could therefore be addressed, whether the calibrated z-steps could be applied to the focus of the study, single cells and single cells on scaffolds. A 5 µm z-step was used when analysing a cell attached to the surface of a porous scaffold comparable to the porous construct in Baldock et al [6] (Figure 4.10) to produce the typical collection area depth.

If the map subject is a cell, water-polymer refraction index mismatch-induced depth distortion can be avoided if the cell is above or next to the scaffold. In Figure 4.10, the cell sits on a deep scaffold, in a pore, meaning that the depth distortion occurs below the cell, with only a thin beam supporting the cell (Figure 4.10). Mapping a cell

and scaffold together requires the shading of multiple molecules simultaneously, incentivising the application of the k-means-directed shading to shade 2D Raman maps in Chapter 3. The production of this VRM shows deeper constructs can be used as scaffolds, as long as the cell being mapped has attached to the side or top of the construct, where spectral contamination and depth distortion will be avoided. It also verifies the capacity of calibrated z-steps to map cells and scaffolds, the third aim of this chapter. The production of a VRM of a cell on a scaffold also confirms that calibrated z-steps can be used for cell-scaffold mapping, meeting the goal outlined in chapter aim 3.

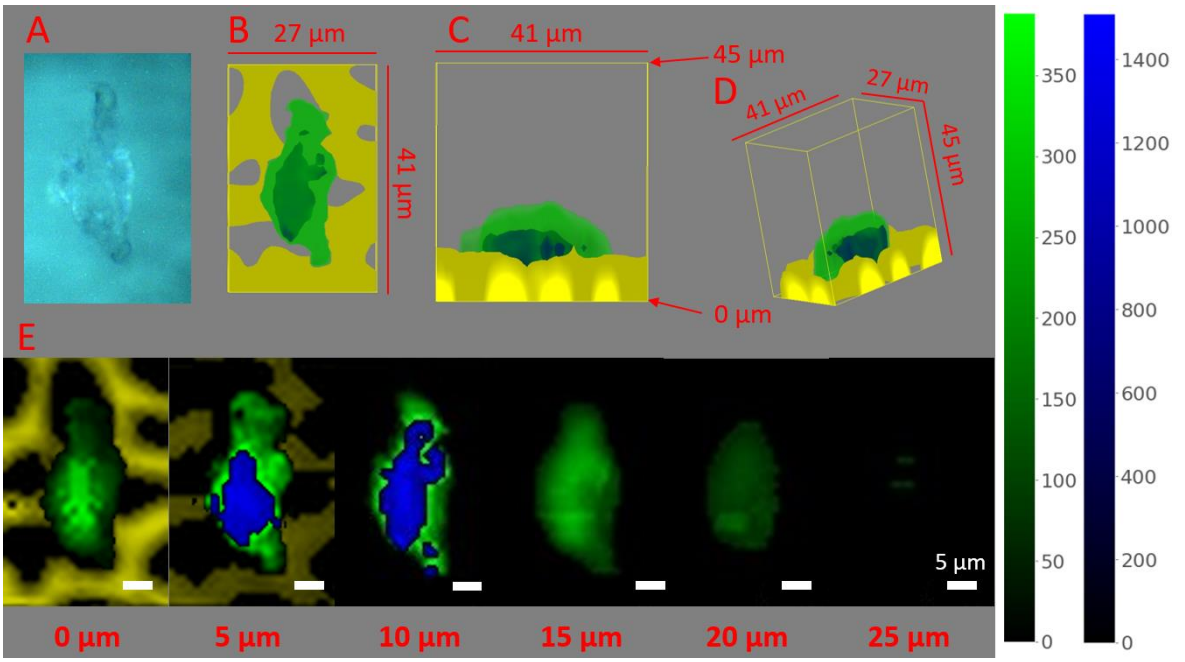

Figure 4.10 – HaCaT cell & porous scaffold: *A) Microscope image of HaCaT cell on porous scaffold. B) Top view of a HaCaT cell on a porous scaffold, mapped using 5 µm z-steps and 1 µm^2 lateral pixels. The same VRM is shown in (C), showing the side view, and (D) and angled view, with the same shading parameters used for (A), (B), and (C). E) The individual VRM slices relating to the cell (slices collected above the cell discarded). Shading ranges in E for proteins 1330-1350 cm^{-1} (green), and nucleic acids 775-790 cm^{-1} (blue), are shown to the right of the feature. The colour relating to the Raman scattering intensity range within the highlighted region, effectively scaling the shading to the region associated with the biomolecule; proteins showing the cell body and nucleic acids the probable nucleus location. Ormocomp^{TM} 1705-1750 cm^{-1} is shaded yellow, with no shading range, as the scaffold location is a qualitative question for this study (present, or not).*

Figure 4.10 compares a WiRE^{TM} VRM and k-means directed shading of cell-scaffold complex (Chapter 3) produced using z-steps determined using the calibration blocks (5 µm). The elongated cell morphology can be seen in a simple microscope image

in Figure 4.10 (A), with the VRM providing additional perspective with depth in Figure 4.10 (B). In Figure 4.10 (C), the cell is supported by the shape of the scaffold, with a beam crossing the pore underneath the cell. The cell position encourages a three-dimensional morphology, with the sides of the pore supporting the cell. In the slices of the VRM (Figure 4.10 - D), starting at the lowest on the left, the scaffold surrounding the cell at the lowest point. In the second slice, the top of the scaffold, with a lower paler shade of the yellow colour linked to the OrmoComp™ reveals a smaller concentration of the material within the analysed voxel (collection area). Removal of background and scaffold spectra was unnecessary as the height of the scaffold avoided spectral contamination from the slide surface.

The value of directing the shading with k-means clustering is highlighted in Figure 4.10 by the difference in nucleus area between the WiRE™-produced (Figure 4.10 - B-D) and k-means-directed shading of the z-stack slices (Figure 4.10 - E). Being able to observe the individual slices provides a more precise view of how the nucleus and cell body change over distances (z-steps) through the cell-scaffold depth. Previous applications of z-stacking shaded with k-means [124], [125] were built upon by providing spectral justification of maps combining the advantages of univariate and cluster shading. The WiRE™-produced VRM indicates the nucleus position, but the k-means directed shading (E) indicates the nucleus sits lower in the cell than the WiRE™-produced map suggests. The nucleus can be seen to match the morphology of the cell body, which in turn is directed by the pore shape. The cell body is a similar size in the maps produced using the different methods, resulting from researcher judgment of the cell body boundaries. It is therefore recommended that shading using WiRE™ (or similar software) be accompanied by some clustering if specific conclusions about the size of the nucleus or cell body are to be drawn.

4.3.6. Mapping a cell on a porous cage scaffold

A wide range of single-cell Raman spectroscopy studies will never need to analyse a greater depth than the cell, as it is a single cell. The mapping method outlined in section 4.3.5 is therefore sufficient for many single-cell studies. However, experiments looking to monitor the cellular response to a bioengineered construct may find the visualisation of the cell invading the construct surface useful. The question of how such a study could use DLW and single-cell analysis under the optical conditions outlined in this chapter should therefore be addressed. As calculated in section 4.3.4, the maximum depth of analysis for the water-immersed OrmoComp™ that can be mapped in three dimensions before depth distortion lowers the confidence in the positional accuracy of the spectral measurement is between 3 and 5 μm. Section 4.3.5 showed that a cell on top of a scaffold could be mapped using VRM, as the depth distortion occurs below the cell (in situations where deeper sections of the scaffold are not the focus of the research). Figure 4.11 shows a simple, novel, solution. By designing a scaffold created from beams that are at an angle (angled beams), the depth of the scaffold is increased, whilst the depth of the material remains within a suitable range to avoid depth distortion for this system.

Figure 4.11 (A) shows the white light microscopy image of HaCaT cells attached to a hexagonal scaffold designed to form a cage from beams angled (angled beams) to meet at a point in the centre of the hexagon, forming pores on each side of the hexagon. The red square in Figure 4.11 (A) is the mapping area for a VRM, where the z-stack through the cell-scaffold complex, showing the constituent slices in their relative positions through the VRM is shown in Figure 4.11 (B). A reduced region of the cell-scaffold complex is analysed in Figure 4.11 (B), reducing the analysed area provides a method of speeding collection, whilst retaining the maximum morphological information. There are two main advantages of speeding the collection time by mapping a region through the centre of the cell. The first is that the collection of VRM when analysing living cells may become possible if the collection time is reduced, as cell movement currently makes live-cell VRM unlikely. A reduced collection time is the other advantage, as angled beams (such as the

ones used in the cage scaffold) diminish interpolation, especially when z-steps are increased to match the collection area depth to avoid oversampling.

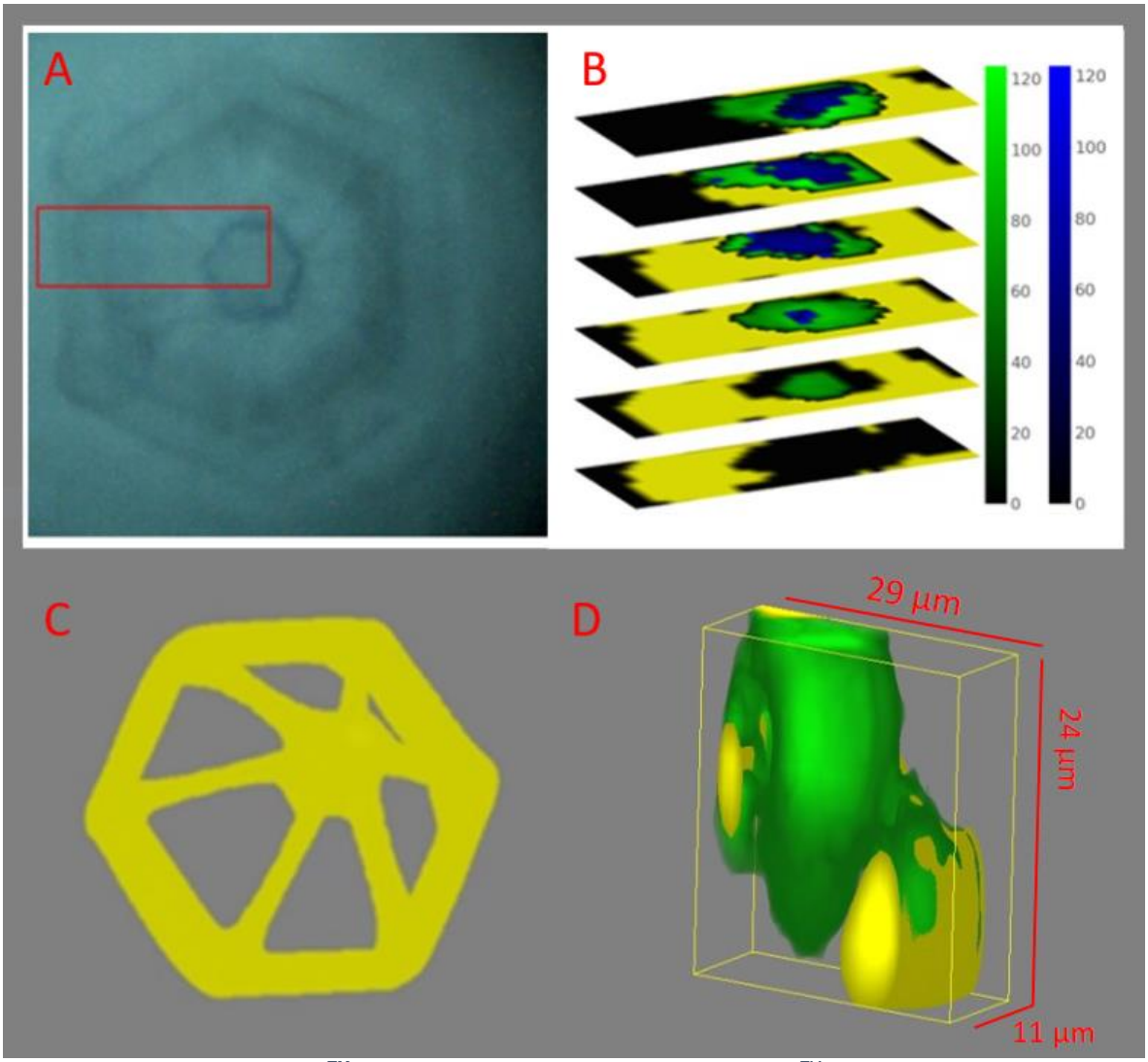

Figure 4.11 – Renishaw WiRE™ VRM and slices of cell-scaffold: *A) WiRE™ VRM of a similar cage scaffold, shaded to the 1705-1757 cm^{-1} OrmoComp™ region and shaded yellow, B) Slices 0 –4 of cell-scaffold 3 VRM, placed in z-stack, C) Analysed region of cell-scaffold 3 & D) WiRE™ VRM of cell-scaffold 3, showing proteins in green (1330-1350 cm^{-1}) and OrmoComp™ in yellow (1705-1757 cm^{-1}).*

As VRMs produced in WiRE™ is not quantitative, a solution is to increase the number of slices, reducing the z-step and then excluding any inappropriate slices if a z-stack is produced. The additional slices increase the collection time, therefore incentivising a method to produce meaningful information with a reduced analysis

volume. The z-stack slices (figure 4.11 B) had their backgrounds removed and were shaded using k-means directed shading. The k-means associated molecules with the cell body (green) and nucleus (blue) using 1330-1350 cm^{-1} and 775-790 cm^{-1} regions of the spectrum respectively based. The colour bars at the side of the z-stack indicate the cluster Raman intensity range, relating to the It has previously been shown that nuclear elasticity affects the capacity of cells to migrate through pores [53]. The nucleic acid region of the map is primarily in the top slice, showing that the more elastic cytoplasm progresses through the pore. It cannot be said with 100% certainty in which direction the cell is travelling. However, as the cell has landed on top of the scaffold, that Figure 4.11 (B) probably shows the nucleus as being the last part of the cell to move through the pore when the z-stack is inspected, as was the case for Greiner et al [53].

Figure 4.11 (C) shows the cage scaffold in isolation, the simplified map, and showing the consistent beam thickness without the cell blocking or distracting the view. To avoid depth distortion in the scaffold, the cells, which have a matching refractive index to the phosphate-buffered saline (PBS) immersion media, allow the cells to be mapped the full scaffold depth. Figure 4.11 (D) shows an intuitive WiRE^{TM}-produced version of the VRM from Figure 4.11 (B). The cell is shown in green, using the 1330-1350 cm^{-1} protein intensity. The cell and scaffold were made visible using WiRE^{TM} transparency settings to remove lower-intensity regions, based on the expected size of the cell in relation to the scaffold/scaffold pore. The cell is seen travelling through the pore, as would be expected looking at Figure 4.11 (B). A big difference is the poor visualisation of the nucleus, with the cell densely packed and through the pore. Choosing transparency and opaqueness settings to visualise the cell body from the scaffold OrmoComp^{TM} (1715-1750 cm^{-1}) yellow and the nucleic acids (775-790 cm^{-1}) blue produced only unsatisfactory results.

As a proof-of-concept study, the cage was designed with a 25 μm radius hexagon, with a 10 mm deep base, to ensure the structure remained stable whilst the capacity of angled beams to avoid depth distortion was established; for a Raman spectroscope using a 532 nm laser, a NA=1 objective, and PBS immersion to map through 25 μm of cell and scaffold. Demonstrated in Figure 4.11 as providing a more

than 6× improvement on the previous 3 μm scaffold depth limit. The clear limitation of the deeper base is depth distortion in the base, which is not the focus of this study (like the deeper sections of the porous scaffold in section 4.3.5), but the aim will be to avoid this distortion also. Design refinements for the next chapter will include producing larger cages, with shallower bases that avoid depth distortion. Another development for the next phase of the project will be varied pore sizes. If the radius of the outer ring is kept consistent, the size of the pores around the edge of the scaffold can be altered by varying the number of beams, potentially stimulating the cells cultured on the scaffold. An aim for the next chapter would be to establish whether Raman spectroscopy could detect molecular changes resulting from any altered cellular response to the cell and to determine whether such an approach is suitable for monitoring cells on bioengineered constructs.

4.4. Conclusions

Using Raman spectroscopy to map molecules through three-dimensional spaces (VRM) takes advantage of the aqueous and non-destructive capabilities provided by detecting Raman scattering. Humans visualise the world in three dimensions and providing researchers with a three-dimensional map not only provides greater context to a map (the fore and backgrounds) but an easier image to interpret, understand, and communicate to non-experts. The advantages supplied by VRM have led to its increased application to biological studies, without a thorough consideration of previous research developed for the analysis of materials [7], [30], [40]–[42].

The first aim of the chapter was to explore the capacity of a map to show the size of an object and explore how resolution affects the accuracy of any conclusion drawn from an image. Figure 4.1 showed how the dimensions of a HaCaT cell and DLW printed construct were altered when the lateral resolution. Similarly, the depth of a

book scaffold was altered in Figure 4.3, when the lateral map typically used to verify shading parameters, remained consistent.

Experiments highlighted a contradiction, where the desire to optimise accuracy through the tightest possible distancing of z-steps has led to oversampling. In section 4.3.5 it was shown that z-steps larger than the minimum (z-steps of 3-5 µm), provided comparable information whilst lowering the number of slices collected, reducing collection time. The hypothesis stating that z-steps can be identified that minimise VRM distortion was tested in section 4.3.3, showing different depths of tube constructs. The tube constructs (Figures 4.5 - 4.7) showed that out-of-focus contributions can be minimised when z-steps correspond to the collection area depth.

The second aim of the chapter was to develop a method of calibrating z-steps to minimise distortions in VRM, relating to the hypothesis raised in the introduction; calibration of z-steps can be verified. The hypothesis was shown to be true in Figure 4.8, with SEM used to check the accuracy of the print and effectiveness of the calibration. The experimentally determined z-step range of 3-6 µm was shown to be larger than the diffraction-limited optimum of 2.4 µm, with contamination of slices above and below the expected range of the construct. Contamination of slices and ambiguity as to the true dimensions of the constructs incentivised an experiment to determine z-steps for the specific Raman system being used, verified against scanning electron microscopy images.

Having verified VRM z-steps using SEM, which provided nanometre resolution in section 4.3.4, Figure 4.10 achieved the third aim of the chapter, using calibrated z-steps to map a cell on a scaffold. Figure 4.10 shows a cell on a porous scaffold inspired by a conventional Raman map by Baldock et al [6]. Collecting a VRM of a cell on a scaffold also provided an opportunity to test the hypothesis that k-means-directed shading can be adapted for VRM. The findings from section 4.3.4 inform subsequent scaffold design, completing the fourth aim of the chapter for greater depth scaffolds with the design and testing of cage scaffolds in Figure 4.11. Comparison of the slices to the WiRE^{TM} VRM demonstrated the value of both

methods and their presentation together. The WiRE^{TM}-produced VRM provides an intuitive image with greater visual context and the slice provides greater morphological accuracy and objectivity. Observing changes in cell morphology using the calibrated z-step method justifies Chapter 5 exploring the relationship between scaffold design and cell morphology on the molecular composition of the cells.

Chapter 5 – Raman spectroscopy of cells on varied scaffolds

5.1. Introduction

Raman spectroscopy is increasingly being used for monitoring cellular responses to the millions of bioengineered products that extend and enhance lives worldwide [128]–[131]. Joint replacements and immunologically matched transplant organs [132]–[134] require 3D cell culture to match the in vivo environment. Raman spectroscopy has previous monitoring applications for tissue engineering including skin [18], [135], cartilage [136], cells [137], and the extracellular matrix [138]. The limitations of 2D cell culture [139]–[141] incentivise an investigation of the capacity of Raman spectroscopy to distinguish cells cultured on different dimension substrates. By exploring the capacity of Raman spectroscopy to distinguish substrate geometries, the findings can inform studies monitoring bioengineered constructs such as bone [142], skin [143]–[145], cartilage [146]–[148], and others [135], [149]–[151]. A key advantage of Raman spectroscopy is the capacity to link machine learning classification with 3D mapping [152], [153], a benefit previously unexploited in single cell analysis. PCA and VRM/3D Raman have previously been shown as complementary [84], [154], [155], no previous study monitoring cells have linked VRM with machine learning classification of Raman spectra. The VRM method developed over the previous two chapters to visualise cellular morphology will therefore be presented alongside machine learning algorithms, providing complementary analysis to visualise morphology alongside corresponding substrate-influenced molecular alterations.

Having found that scaffolds designed with angled beams avoid depth distortion in Chapter 4, with the increased scaffold depth making more intricate designs available, an experiment was designed to take advantage of the more complex scaffolds. The

cages formed by the angled beams (cage scaffolds) provide varied pore dimensions, providing different support to the simple scaffolds. The same analysis, VRM visualisation of cell morphology, PCA data exploration, and supervised learning analysis will be carried out to test the repeatability of the method. A final analysis will then explore the ability of Raman spectroscopy to distinguish cells grown on different 3D morphologies. The cage design provides an opportunity to test the hypothesis that pore dimension influences cell morphology and molecular composition, with the experiment, also repeated with a different pore design (small, medium, and large square pores).

Having optimised k-means directed shading in Chapter 3 and z-step calibration in Chapter 4 for single-cell analysis, one of the aims of this chapter is to determine the adaptability of methods to different scaffold types. To investigate the ability of Raman spectroscopy to distinguish cells cultured on flat 2D surfaces from those supported in a 3D morphology, the direct laser writing (DLW) method described in Chapter 2 provides cell scale constructs (scaffolds). The scaffold designs will initially be simple, simple being defined as straight-edged and having an axial depth greater than the cell. Once cells have attached to the side of the scaffolds, maintaining a 3D morphology, k-means-directed shading of VRM z-stacks can be carried out to ensure the cell has formed a three-dimensional form. The spectra from the volume maps can then be used in datasets aimed at distinguishing the 3D cells from those cultured on a flat surface. Due to the greater cost in time and complexity of the k-means directed shading of z-stacks, a secondary area of investigation for this chapter is comparing them to WiRE^{TM}-produced VRM. The two VRM types will be used to map the different scaffold types and a key research question asking how well the z-step calibrated WiRE^{TM} VRM compares to k-means directed shading when applied to different scaffold types.

Once the capability of VRM to visualise differences between cells grown on and off scaffolds has been determined, a dataset can be collected of cells on and off scaffolds. Collecting the dataset allows the research question; can Raman spectroscopy distinguish cells with a three-dimensional morphology from cells cultured on a flat surface? Providing evidence towards Raman spectroscopy being

used to monitor tissue engineering and the development of cells grown on the three-dimensional scaffolds used in bioengineered constructs [6], [156]–[158]. The analysis will be carried out over two stages, to explore whether principal component analysis can identify molecular changes between the two groups. PCA provides unsupervised and relatively interpretable results, which provide the greater biological understanding required to describe the process being monitored. The initial investigation of the dataset being unsupervised increases confidence in relationships found as potential user biases are avoided before moving on to labelled data. The next stage of the analysis will focus on the aim of determining whether supervised learning can repeatedly distinguish cells grown on different scaffolds.

The repeatability of the supervised learning section must be established as strongly as possible at this stage of development, as any approach aiming to monitor anything over time must provide stable classifications. Assessing the classification confidence for the supervised learning techniques is therefore a key research aim for this chapter. The approaches used to assess the repeatability of the analysis will look at three factors.

1. The first is repeatability over different experiments, explored through the analysis of different scaffold types throughout the chapter, the ability to separate cells over consistent situations, such as on and off scaffolds, or both on scaffolds, increasing the confidence that similar results are producible on different days and using different equipment.
2. The second aspect of repeatability tested is repeatability within a single dataset, aiming to show that an ideal subset of test samples is not chosen by random using 5-fold cross-validation and learning curves.
3. The third aspect of repeatability is testing using different algorithms, testing the performance of three different algorithms to establish consistent classification using different algorithms.

Hypotheses:

1) VRM be used to visualise scaffold-influenced changes in HaCaT cell morphology.
2) Dimension reduction can distinguish Raman spectra collected from cells on two- and three-dimensional substrates.
3) Machine learning algorithms can be trained to classify cells grown on two- and three-dimensional substrates.

5.2. Methods and materials

K-means directed shading (method described in Chapters 3 and 4) was used to shade slices where descried. A standardised colouring convention through the chapter to match previous chapters and references [6], selected for their link to a specific molecule. Standardised colouring through the chapter therefore relates yellow to OrmoComp^{TM} (1715-1750 cm^{-1}) for all scaffold material (all scaffolds being DLW printed OrmoComp^{TM}), cell bodies (green) for the 1330-1350 cm^{-1} protein Raman peak, and nucleic acids (775-790 cm^{-1}) blue. Qualitative shading was used for the OrmoComp^{TM} scaffold regions, as their position (there vs. not) is a qualitative question, with no benefit gained from a quantitative shading range for the research questions posed. No shading ranges are provided for the WiRE^{TM}-produced VRM, as the technique is used for an initial investigation of the map, with k-means directed shading of VRM z-stacks applied (and advised for future applications) to thorough exploration of Raman maps. All other methods are descried in Chapter 2.

5.3. Results and discussion (Part 1: Simple scaffolds)

To establish the capacity of Raman spectroscopy to monitor bioengineered constructs, a proof-of-concept study will first establish the influence of environment geometry on the cells. The VRM method outlined in Chapter 4 and the shading method described in Chapter 3 will be applied to visualise any morphological difference resulting from the geometry of the culture substrate. Gargotti et al compared HaCaT cells cultured on two- and three-dimensional membranes to explore the difference [159]. The aim was to investigate previous assertions that 3D cultures improved viability and reduced toxicity in cell cultures, finding no evidence that they were but 3D cultures do provide a method of altering the cell cycle [159]. 3D cell culture systems influencing the cell cycle [159] reveal potential changes in molecular composition that can be detected using Raman spectroscopy [160] to distinguish cells grown on two- and three-dimensional structures. Changes in HaCaT cell and nucleus morphology have been induced using electrospun scaffolds [161] and in primary keratinocytes [162] using varied substrate designs.

PCA will initially be employed to investigate relatable changes produced through DLW-fabricated scaffolds. PCA provides the dual advantages of objectively indicating class separation (scaffold vs. flat surface), alongside reducing the dimensionality of the data for further analysis. Reducing the dataset dimensions provides the advantage of avoiding the collection of a large dataset (thousands or hundreds of samples) to avoid model overfitting when testing machine learning algorithms to distinguish cells grown on different substrates. The collection of a large dataset is outside the timeframe allocated to this chapter. The training of models from smaller (tens of samples) datasets justifies the collection of larger datasets in future studies, addressing research questions potentially looking at multi-stimuli systems.

5.3.1. Mapping cell morphology on 3D scaffolds

The key advantage provided by volumetric Raman mapping over conventional (two-dimensional) Raman mapping is the increased morphological insight provided by the extra dimension. In Figure 5.1, three versions of the same three-dimensional Raman map showing a cell grown on a scaffold, are produced in Renishaw WiRE™ software. Figure 5.1 (A) shows the VRM before parameter alteration, with the OrmoComp™ (1715-1750 cm^{-1}) region selected and without parameter alteration blocks the other spectral regions, leaving yellow. In (B), the transparency settings are used to remove lower intensity regions of the OrmoComp™ from the VRM, allowing the proteins (1330-1350 cm^{-1}) to be viewed and shaped in green. Any region of the spectrum can be mapped using this method, proteins were selected as the next logical step to view the entire cell, due to the protein region 1330-1350 cm^{-1} region previously being linked to the cell body [6].

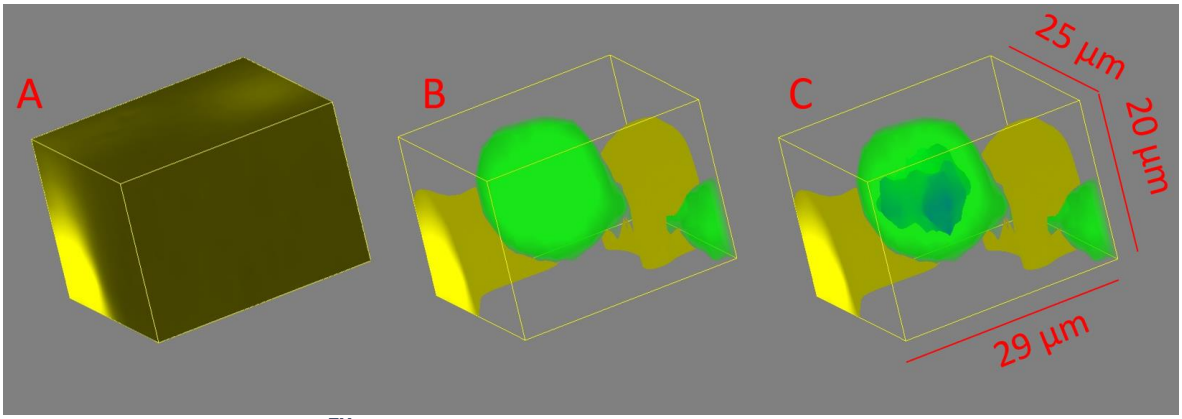

Figure 5.1 – Renishaw WiRE™ VRM of cell-scaffold 1: Using standardised colouring (see methods): *A - C) The gradual removal of lower intensity regions of the VRM, allowing the focuses of the image (cell and scaffold) observable. Starting by imaging the OrmoComp™ 1715-1750 cm^{-1} Raman peak (yellow), imaging the entire range (A), then removing the lower intensities for the OrmoComp™, proteins shown in green (1330-1350 cm^{-1}), and finally using the opaqueness settings to show the nucleic acid (775-790 cm^{-1}) high intensity region within the cell (C).*

Subcellular features can be highlighted through the use of opaqueness settings, applied in Figure 5.1 (C) to highlight in blue prominent nucleic acid (775-790 cm^{-1}) regions within the cell; possibly indicating the location of the nucleus. Opaqueness settings, therefore, aid the production of more complex maps, making the

relationship between the cell, nucleus, and scaffold easier to interpret. However, the cell body opaqueness and the obscured nucleus alter their colour intensities, stopping robust conclusions from being drawn from the colour shade, and reducing Raman mapping advantage. The nucleus can be presented in a single feature map, showing either the nucleic acid intensity throughout the entire cell or on its own by removing lower intensity regions with transparency settings.

No standard or calibration method is enforced (or available) in the WiRE^{TM} software. Researchers are forced to choose colour intensity, transparency, and opaqueness settings based on fluorescence microscopy images, making shading objective and impossible to exactly duplicate. In Figure 5.2. C, the individual slices of the VRM (Figure 5.2 D) of a cell (white light image – B) that are shaded using the method outlined in Chapter 3, where the background and scaffold spectra were removed from the analysis. K-means clustering combines different spectral features when determining boundaries within the hyperspectral image, increasing the strength of the analysis. However, the clustering of different regions within the image results in a single shade being used for the entire cluster, removing the varied shade and corresponding molecular information.

K-means directed shading produces images with the morphological precision of k-means clustering, alongside the molecular insight of low-feature shading. The use of z-stacking or looking at the slices individually also avoids transparency and opaqueness settings. Slices reveal greater morphological accuracy as pixels are a set distance apart. If a systematic approach is taken (see Chapter 3), counting the number of pixels is a method of determining the size of a feature, such as a nucleus. The z-step (distance between slices) is a more precise way of understanding that slices combine the molecular composition of the sample between the slices. Interpolation can then be used in 3D Raman mapping software, bridging the gap to produce more intuitive images if appropriate.

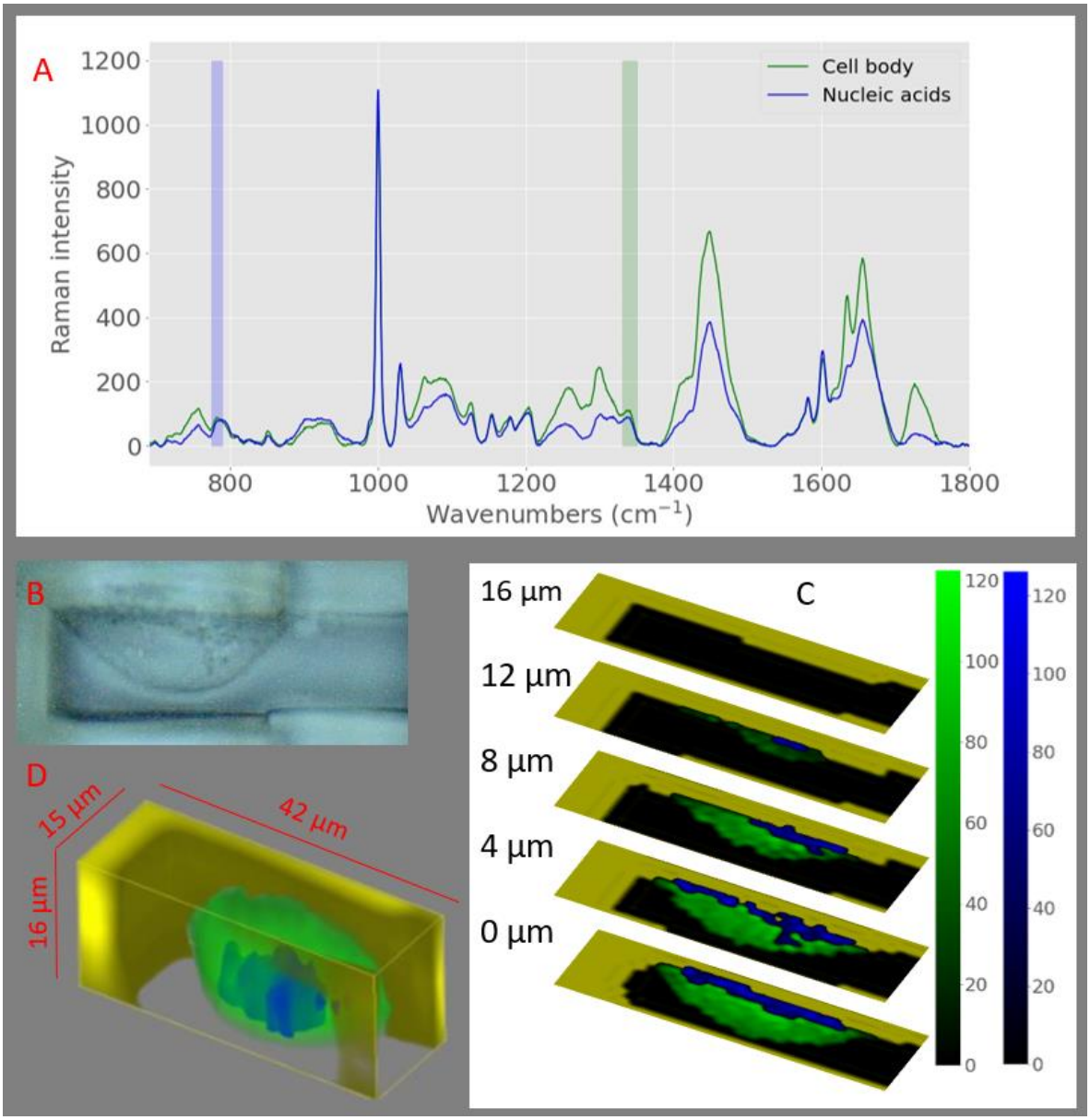

Figure 5.2 – Renishaw WiRE™ VRM and slices of cell-scaffold 2: *Using standardised colouring (see methods), A) WiRE™ VRM of cell-scaffold, B) Microscope image of the cell-scaffold, C) Slices 0 – 2 of cell-scaffold VRM, shading boundaries determined by K-means directed shading, with shading ranges for the nucleic acids and proteins enlarged to the right of (A).*

Figure 5.2 (A) shows the average spectrum for each cluster, with the 775-790 cm^{-1} region indicated with a blue highlight and 1330-1350 cm^{-1} indicated with the green highlight. Providing the average spectrum for the clusters associated with the different cellular regions provides a spectral justification for the association. For example, the 1330-1350 cm^{-1} region of the spectrum is slightly higher for the cell body (green line), than the nucleus (blue line). Spectral peak in the 1715-1750 cm^{-1}

region for the cell body spectrum may indicate some OrmoComp™ contamination of the spectra assigned to the cell body. Contamination by a scaffold material could be expected when mapping a cell attached to the scaffold. Observing the contamination in the averaged spectrum for a map region shows the value of producing the regions average spectrum. By seeing the contamination in a spectrum, the contamination is detected and removed from future analysis. The cluster associated with the nucleus does not have a clearly higher nucleic acid (775-790 cm^{-1}) region, however, when the lower baseline of the spectral peak is considered, the area under the spectral peak is larger, with lower intensities for other key regions such as the 1420-1470 cm^{-1} proteins & lipids region [151].

An intuitive assessment of the maps indicates the cell is supported in a three-dimensional morphology by the scaffolds with a centrally located nucleus. The use of WiRE™ software to draw these conclusions would therefore be justified for applications aiming to determine the general location and morphology of the cell body, alongside the approximate position of the nucleus within the cell. However, more detailed conclusions are unadvisable when using WiRE™ produced VRM, due to the inconstant nature of the shading parameters used to remove obscuring lower intensity regions (Figure 5.1 A-D) [6]. Colour bars were not included for the WiRE™ maps, as the shading parameters cannot be added for each colour and the shade does not relate to a molecular concentration. Difficulty in accurately associating Raman peak and colour intensities is a key Renishaw WiRE™ limitation compared to k-means-directed shading of VRM slices.

5.3.2. Distinguishing cells on and off “simple” scaffolds

Visualising the cell attached to the side of a simple scaffold using VRM (Figure 5.2) showed the 3D morphology of the cell. The 3D dimensions of the VRM give a rotatable view of the cell morphology, resulting in a clearer understanding of the cell attachment to the scaffold than a conventional Raman map. Having observed the cell attachment to the scaffold and the resulting 3D morphology, the question of

whether a 3D morphology supported by a scaffold changes the molecular composition of the cell. To answer this question, a dataset was collected consisting of 5 maps collected from cells attached to scaffold sides (3D) and cells off the scaffolds, on the surface of the slide (Off). Raman maps were collected to capture spectra from different sections of the cells, to avoid the accidental distinction of subcellular regions.

K-means mapping was used to identify regions of the map associated with the cell to avoid the inclusion of spectra associated with the background or the scaffold material. The removal of the scaffold material was a key target, to avoid the separation of the classes based on OrmoComp^{TM} contamination. Five Raman spectra from each map were included. Two spectra were randomly selected using the random module in python 3.6 from the subset associated with the cell with k-means mapping [163]. A third spectrum was an averaged spectrum of the entire cellular subset (minus the two previously selected), and the final two were averaged spectra from two randomly selected subcellular K-means clusters. The aim of this selection method was to maximise the randomness of spectra in each class (the two randomly selected spectra and clusters), whilst averaging out random fluctuations within any given subset, either relating to the cell or an individual subcellular region.

5.3.3. Unsupervised learning: Data exploration

VRM provides the capacity to observe the changes in the cell and nuclear morphology reported in previous studies [162]. Providing the context of morphological insight, such as comparing the spherical cell and nucleus in Figure 5.1 and the elongated morphology in Figure 5.2. The differences between cells cultured into different substrate-influenced morphologies have resulted in altered actin filaments and producing elongated nuclei [161]. Changes in the protein regions of the Raman spectrum are therefore a target region of the spectrum. Actin is also responsible for structures adjusting the nucleus morphology in response to the substrate geometry [164]. Nucleic acid regions of the spectrum are also key spectral regions, with changed nuclear morphology providing a link between the observable

change seen in VRM with altered phenotype, as nuclear morphology is hypothesised as influencing genome function [164].

Chemometric analysis using dimension reduction (PCA) and machine learning (section 2.3) provides approaches for the identification of features between classes, in the case of Figure 5.3, the classes “3D” cells and cells “Off” the scaffold. The first stage of analysis is data exploration, with PCA selected as a technique capable of analysing datasets with more features (wavenumbers) than observations (spectra), which is the case for this dataset. PCA also provides the advantage of being unsupervised, therefore indicating whether class separation is possible without the potentially biasing influence of class labels. In Figure 5.3, the scores plots (A, C, & F) are shown for PC1, PC2, and PC3, which represent 91% of the variance in the dataset, as shown in the explained variance plot (B). The loadings plots for PC1 (D), PC2 (E), and PC3 (G) indicate the features (wavenumbers) that are responsible for the variance in each principal component. In the loadings plots, the positions (peaks) furthest from zero indicate a greater influence on the increased variance.

In Figure 5.3 (A), PC1 is plotted against PC2, with the cells in a 3D morphology indicated in blue and the cells cultured off the scaffolds shown as red. PC1 provides the greatest distinction between the two groups, with the 3D morphology cells being found predominantly in the negative scores. The loading plot for PC1 (D) indicates that both the positive and negative loadings are mainly associated with proteins, potentially linked to the changed actin in 3D morphology cells [161], [164]. The large positive loading peak at 1606 cm^{-1} relates to C=O stretching in the amide I (proteins) [165], [166]. The negatively loaded peak at 1124 cm^{-1} is either the C-N bond in proteins [167]–[169] or C-C stretching mode in lipids [168], [169]. The negative 1447 cm^{-1} loading peak relates to protein and lipid CH_2 bending mode [170] and can be used as a marker for protein concentration due to CH_2 deformation [166]. The 1654 cm^{-1} loading peak relating to C=C [169], [171], [172]. PC2 is also highly linked to proteins, with the positively loaded peak for PC2 (E), the 1161 cm^{-1} peak, which is in the region for 1158 cm^{-1} and 1160 cm^{-1} C-C/C-N stretching proteins [MG5-38]. The negatively loaded PC2 peak (1648 cm^{-1}) is with the 1640-1680 cm^{-1} region C=C and amide I absorption [171], or lipid (C-C stretch) [169].

Figure 5.3 (C) plots PC1 against PC3, where PC3 is primarily associated with nucleic acids, potentially relating to molecular alterations in the nucleus of 3D cells [164]. PC3 loading plot (G) has positive peaks at 809, 1509, and 1726 cm^{-1}. The 809 cm^{-1} peak is located near the 813 cm^{-1} nucleic acid peak [110], which can also be an indicator of RNA [166]. 1509 cm^{-1} is linked to DNA [166]. The final peak indicated in the positive loadings (1726 cm^{-1}) is assigned to C=O (lipids) [172], the same as in Chapter 3. The negatively loaded peaks for PC3 seem associated with proteins, as the 1127 cm^{-1} peak can be linked to the C-N in proteins [167]–[169], or the C-C stretching mode in lipids [168], [169] and [169] 1585 cm^{-1} can relate to amino acids [167], [172]–[174]. For this dataset, the principal components associated with the greatest amounts of variance within the dataset are primarily linked to the regions predicted through literature research [161], [164]. PC1 provides the greater distinction, suggesting cellular adaptations predominantly relate to proteins, possibly actin directing the morphological response to the substrate in the cell body and nucleus.

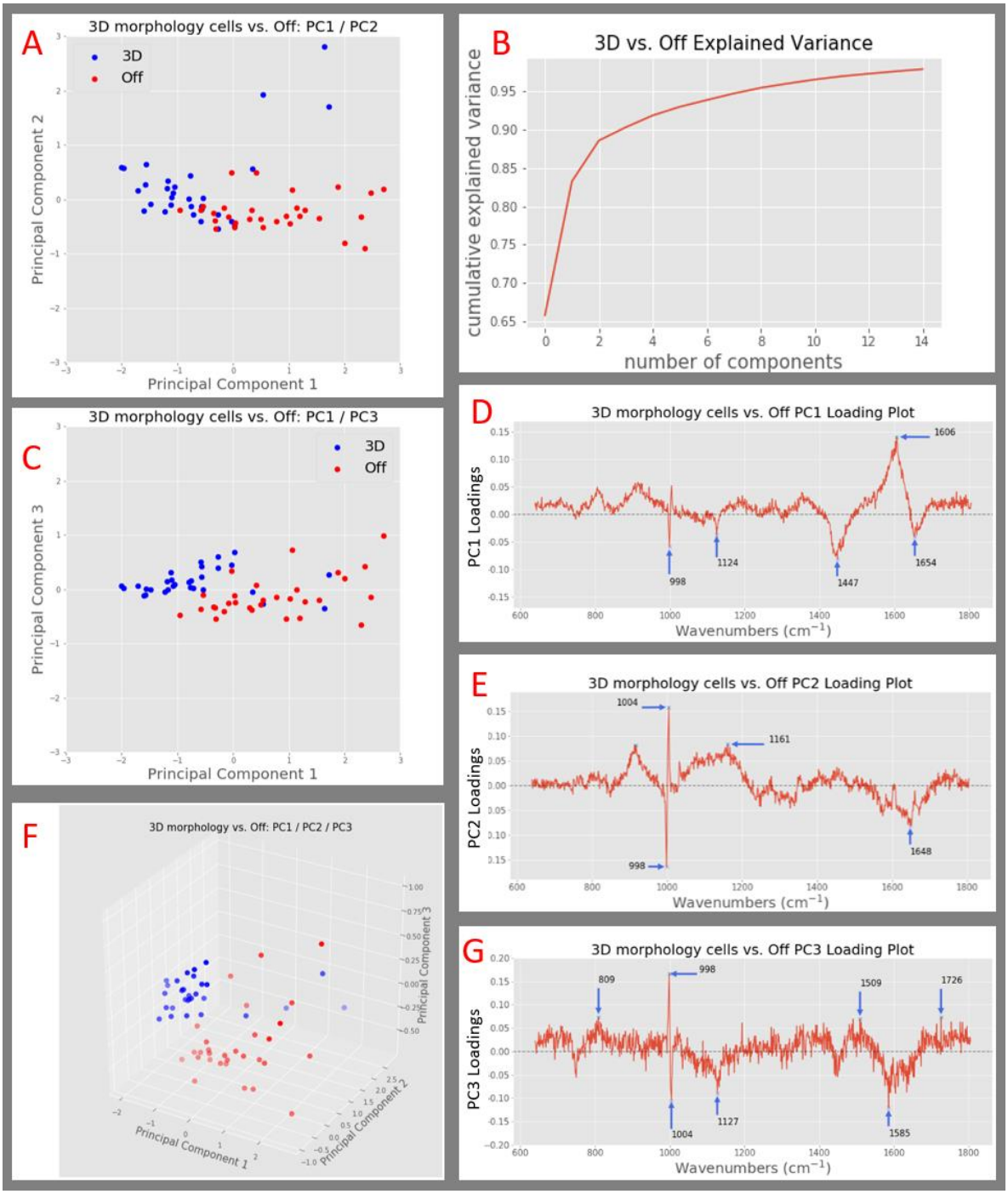

Figure 5.3 - PCA analysis of cells cultured in 3D morphologies supported by 18 µm deep scaffolds: *In all score plots blue = 5-beamed cage (5BC) and red = cells cultured off the scaffold (Off). Score plots for PC1 vs. PC2 (A), PC1 vs. PC3 (C), & PC1 vs. PC2 vs. PC3 (F). B) The explained variance plot, accumulated variance (y-axis) for the number of principal components (x-axis). Loading plots show highly loaded peaks for PC1 (D), PC2 (E), and PC3 (G).*

5.3.4. Supervised learning: Classification

Data exploration with PCA (section 5.3.2.) showed the Raman spectra collected from cells on 3D scaffolds and flat slide surfaces can be separated without the class labels influencing the analysis. The reduced dataset allowed for the assessment of supervised learning algorithms using learning curves. Learning curves can either be used to visualise the effect of a hyperparameter (C, gamma, etc.) by plotting the change in a metric (e.g., accuracy, precision, recall, f1-score, etc.) as the hyperparameter is varied, with a single dataset size used or see how the metric changes in response to changing dataset size. In Figure 5.4, the cross-validated metric (f1-score) is calculated as the dataset split (train & validate) is altered to determine the ideal split for further analysis. The datasets are incrementally varied in size, starting with one sample in the training dataset and adding one until only one sample remains in the validation set. The metric, say accuracy, is plotted for the model trained at each increment, producing a line with the spread of the metric indicated by the plotting of the cross-validation standard deviation. The two lines are thus produced, with the standard deviation shown in light shading around the lines (see Figure 5.4 A, C, & E).

The f1-score for the training data lines typically starts high, as it contains all but 1 sample, it should have ample data to determine which class the remaining sample in the test dataset belongs to. Conversely, the validation line should be relatively low compared to later models. In an ideal plot, the training data line drops as samples are transferred to the verification dataset, where the verification data line rises as more samples are added. Lines remaining at a consistent level are said to have converged, which is important as convergence indicates the probable best model that a dataset is expected to produce. Gaps between the training and verification data lines are said to be under-fitted and unrepresentative, with not enough training data supplied to demonstrate the model has found a suitable signal to make accurate classifications. If the training data line crosses the verification data line, the model is said to overfit. Overfitting suggests the model has begun to fit itself using noise, reducing its generalisability, and reducing prediction repeatability for the model due to low variance. Overfitting is also indicated when the standard deviation of the

training data line exceeds the verification line, as one of the cross-validation folds has been overfitted, and the researcher has no way of knowing which subset of the data has caused the overfitting, it is better to reduce the amount of data, removing the risk of overfitting.

In Figure 5.4, the first two principal components (1 and 2) were selected to train algorithms as they represented 83.25% of the explained variance 65.78 % in PC1 and 17.47% in PC2, including further principal components leading to overfitting. Learning curves were produced with 5-fold cross-validation for logistic regression, random forest, LDA, and support vector machine (C = 1 and liner kernel selected through grid search cross-validation), with underfitting shown in the learning curves excluding random forest and decision tree. F1-score was selected as the metric as it indicates changes in precision and recall, and as the application does not require an optimisation of one or the other, the f1-score provides a metric influenced by both. Logistic regression (A), LDA (C), and support vector machine (E) for PCA-reduced data. Similar learning curves were produced for the three models, converging in towards 80-83% f1-score, with the standard deviation of the cross-validation overlapping the verification data line in the 35-37 samples mark, indicating the possibility of model over-fitting. As 50 samples were used, the test-train split for models was therefore chosen to be 70% training (35 samples) and 30% test. Similar learning plots (A, C, & E) were followed by identical confusion matrices were produced (B, D, F), producing an f1-score of 79.99%. Slightly better than the 5-fold cross-validation scores (76.67% LR, 78.89% LDA, and 76.67%)

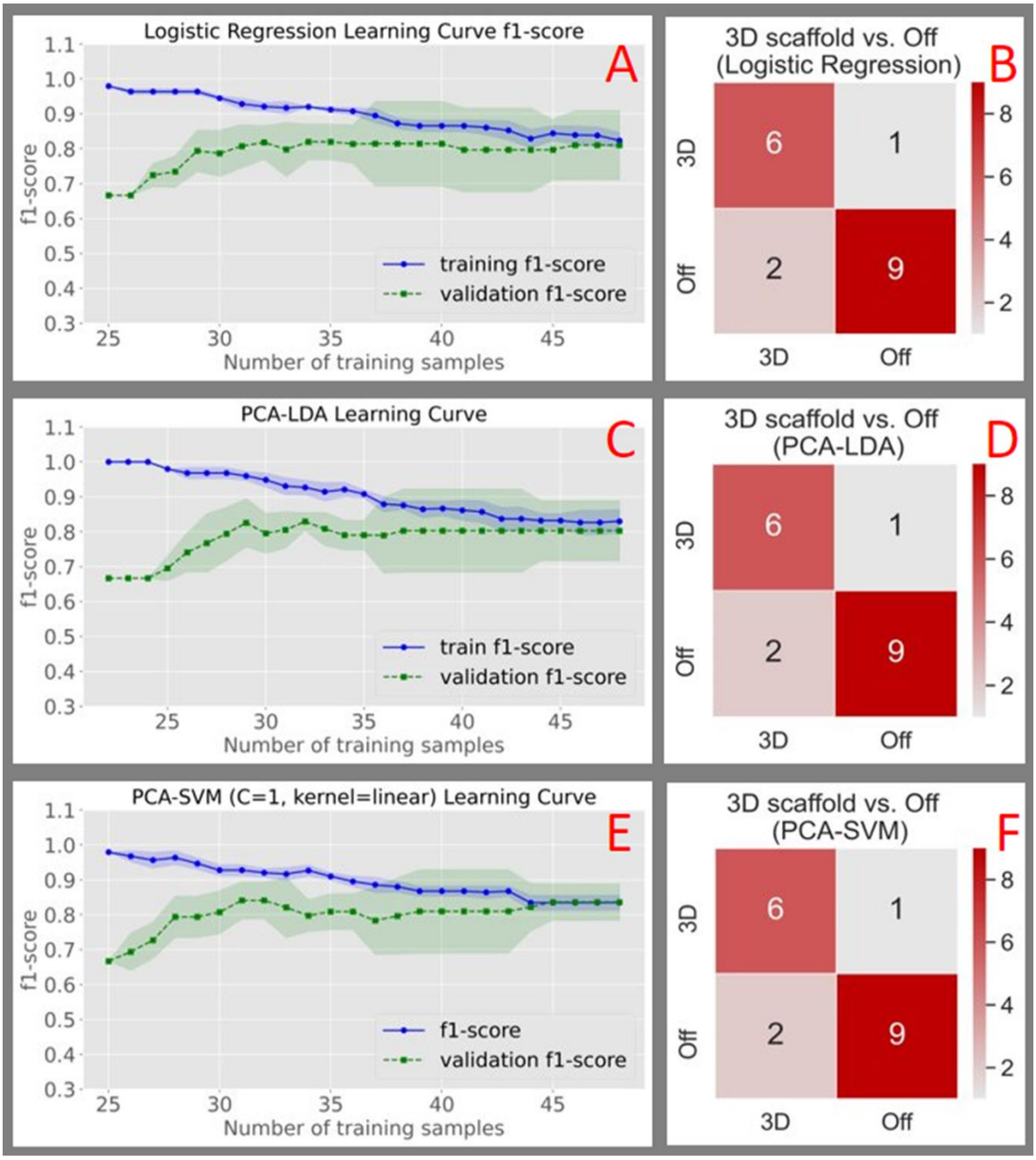

Figure 5.4 - Learning curves showing the 5-fold cross validation for different test-train splits: *Logistic regression (A), LDA (C), and SVM with hyperparameters C=1 and a linear kernel (E) models trained on PCA reduced data. Confusion matrices for the logistic regression (B), LDA (D), and SVM (F) trained using the learning curve indicated test-train split for cross-validation scores of 76.67% (logistic regression), 78.89% (LDA), and 76.67% (SVM).*

5.4. Mapping cell behaviour on cage scaffolds of varying pore size

Section 5.3 determined that Raman spectroscopy can distinguish cells cultured on simple 3D scaffolds providing a wall to support a 3D morphology. The disadvantage of simple scaffolds is the incapacity of VRM to map the entire scaffold in relation to the cell as a result of depth distortion. In Chapter 3, a cage design scaffold was mapped using VRM, showing that angled beams provide a method of circumventing depth distortion and increasing the range of scaffold designs available. Angled beams are especially useful for sample systems involving materials with two or more refractive indexes, where refractive index matching immersion media [7] is impossible. Angled beam scaffolds are therefore ideal for samples like single HaCaT cells cultured on an OrmoComp^{TM} scaffolds. The VRM avoided biological masking when a cell migrating through an angled beam (cage) scaffold pore in Chapter 3. By combing the findings from section 5.3, changes in cell behaviour and the cage scaffold design from Chapter 3, cell response to pore size can be explored. The increased insight made available through the analysis of individual slices (Chapters 3 and 4) can then be applied to objectively visualise the findings.

5.4.1. Initial visualisation of HaCaT cell on 5- and 10- beamed cage

Using the same data to visualise physical manifestations of altered cell behaviour, such as changed morphology, and carry out chemometric analysis is a key advantage of VRM. To provide higher resolution (than VRM) images for comparison, Figure 5.5 (A-C) provides SEM lateral views of the cages (5, 7, & 10-beamed), providing the view that a conventional Raman or microscopy image would provide. Figure 5.5 (D-F) provides an angled SEM view of the same cages, each below its lateral image above, providing an indication of the DLW prints axial accuracy (for comparison to the VRM below). Having confirmed the print accuracy of the more delicate cage scaffold designs, SEM conformation of scaffold dimensions is not required for future DLW printed scaffold during the project.

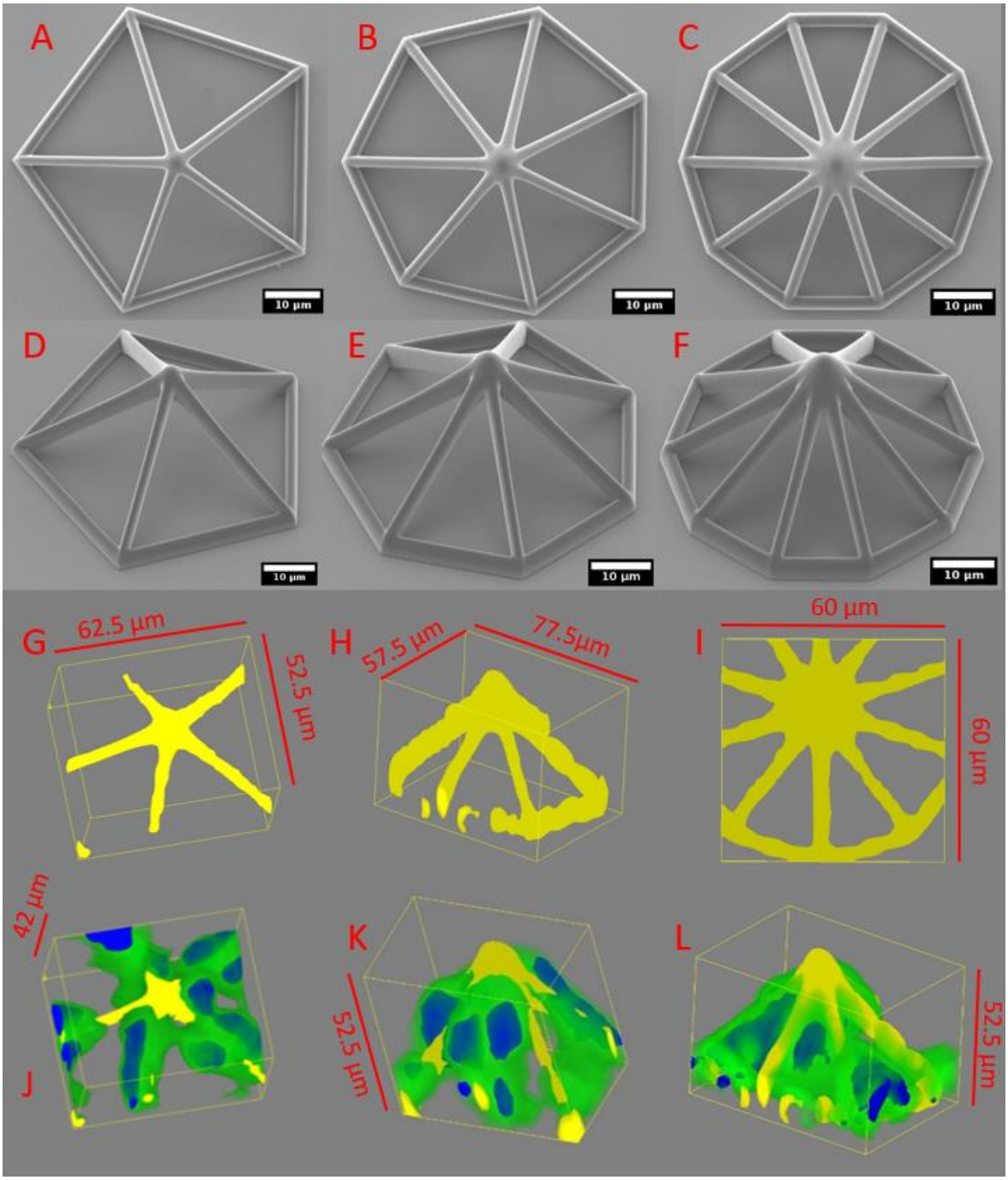

Figure 5.5 - ***SEM and Renishaw WiRE™ VRM images of cage constructs and cage cell-scaffolds****: Using standardised colouring (see methods), A-C) SEM images of a 5-beam (A), 7-beam (B), and 10-beam cage (C) cage constructs. D-E) Angled SEMs of the 5-beam (D), 7-beam (E), and 10-beam (F) cage constructs. G-I) WiRE™ VRMs of sections of the 5 (G), 7 (H), and 10-beam (I) cages. J-L) WiRE™ VRM of cells on different beamed cages.*

Another key advantage of Raman mapping is the ease with which a single spectral feature can be isolated. For example, Figure 5.5 (G-I) shows the VRM of the constructs only (cages), allowing the VRMs ability to map the construct to be determined (though comparison to the SEM) without the distraction of the biological section of the samples obscuring the view. It can be seen through comparison of Figure 5.5 A-F to the corresponding ta analytics and contains 100 batches with all available process and Raman spectroscopy measurements (~2.5 GB). This data is highly suitable for the development of big data analytics, machine learning (ML) or artificial intelligent scaffold VRMs (Figure 5.5 G-I) that the angled beams can be mapped without depth distortion. The lack of depth distortion with angled beamed scaffolds provides confidence going forward when the cell body (green) and nucleus (blue) are included in Figure 5.6.

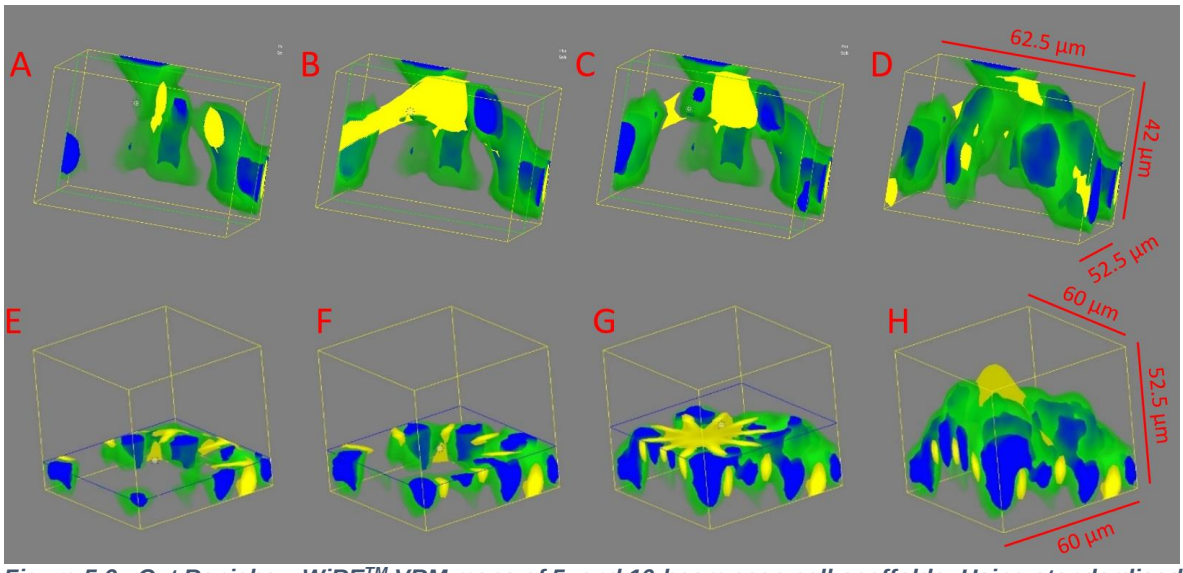

Figure 5.6 - Cut Renishaw WiRE™ VRM maps of 5- and 10-beam cage cell-scaffolds: Using standardised colouring (see methods): *In (A-D), axial cutting of a 5-beam construct VRM shows cross-sections through the cell-scaffold side from the scaffold rear (A), middle (B & C) and the whole VRM (D). In (E-H) a lateral cut shows the cross-sections of cells on a 10-beam cage from the bottom (E). Cells appear between beams through the middle cross-sections (F & G), with the entire VRM shown in (H).*

5.4.2. K-means directed vs. Renishaw WiRE™ comparison (5-beamed cage)

An initial visualisation of the cellular response to the different beam numbers (pore size) can be carried out using WiRE™, however, a rigorous analysis requires the objective shading of slices. The position of the cells is indicated in Figure 5.7 (J-L), where low-feature shading is used to false colour proteins (1330-1350 cm^{-1}) coloured green, nucleic acids (775-790 cm^{-1}) blue, and the OrmoComp™ scaffold material (1715-1750 cm^{-1}) yellow. The 5-beamed cage (Figure 5.7 – J) allows cells through the pore, with limited support for the cells between the beams resulting in an apparent elongation of the cell morphology, stretching along the cage beam. In Figure 5.7 (K), the 7-beamed cage (with the same diameter base) results in a tighter pore. The tighter pores in the 7-beamed cage look to provide the cells with the opportunity to spread across the pore and be supported by two beams, typically favouring the position between the beams. The 10-beamed cage in Figure 5.7 (L) has the tightest pores of the three options. The cells in Figure 5.7 (L) are shown in the pores, resting their higher nucleic acid regions (probably associated with the nucleus) on top of the pores and in some cases, across the beams.

The VRM in Figure 5.7 provides an external view of the cells cultured on the cage scaffolds. A feature of WiRE™ produced VRM is the ability to arbitrarily cut the map through a cross-section that provides a more detailed view of internal sections of the sample. The axial cross sections in Figure 5.7 (A-D) allow for the conformation that cells are only seen when attached to the beams, as opposed to sitting within the cage, using the same VRM as Figure 5.7 (J). Different views are provided starting with the cross-section showing the rear of the VRM view (A), steadily moving through the VRM to visualise more of the sample (B & C), until the entire VRM is shown (D). The different views (A-D) confirm the initial conclusion that the cells are exclusively seen along the cage beams for the five-beam cage. In Figure 5.7 (E-H), the same process is carried out for a 10-beam cage, selected to maximise the contrast in cell behaviours. The cross-section is lateral, providing a superior view of the cells resting their high nucleic acid (probable nuclei) between the cage beams. The lowest view (E) shows the bottom of the cells, with the cross-section moving higher in (F), with the blue region (nucleic acids) remaining between the beams. By (G), it can be seen

that the cells are resting on top of the beams as well as between them, with the cells appearing to coat the cage in (H). The WiRE™ produced VRM do provide a faster initial map, indicating the general location of the cell in relation to the scaffold.

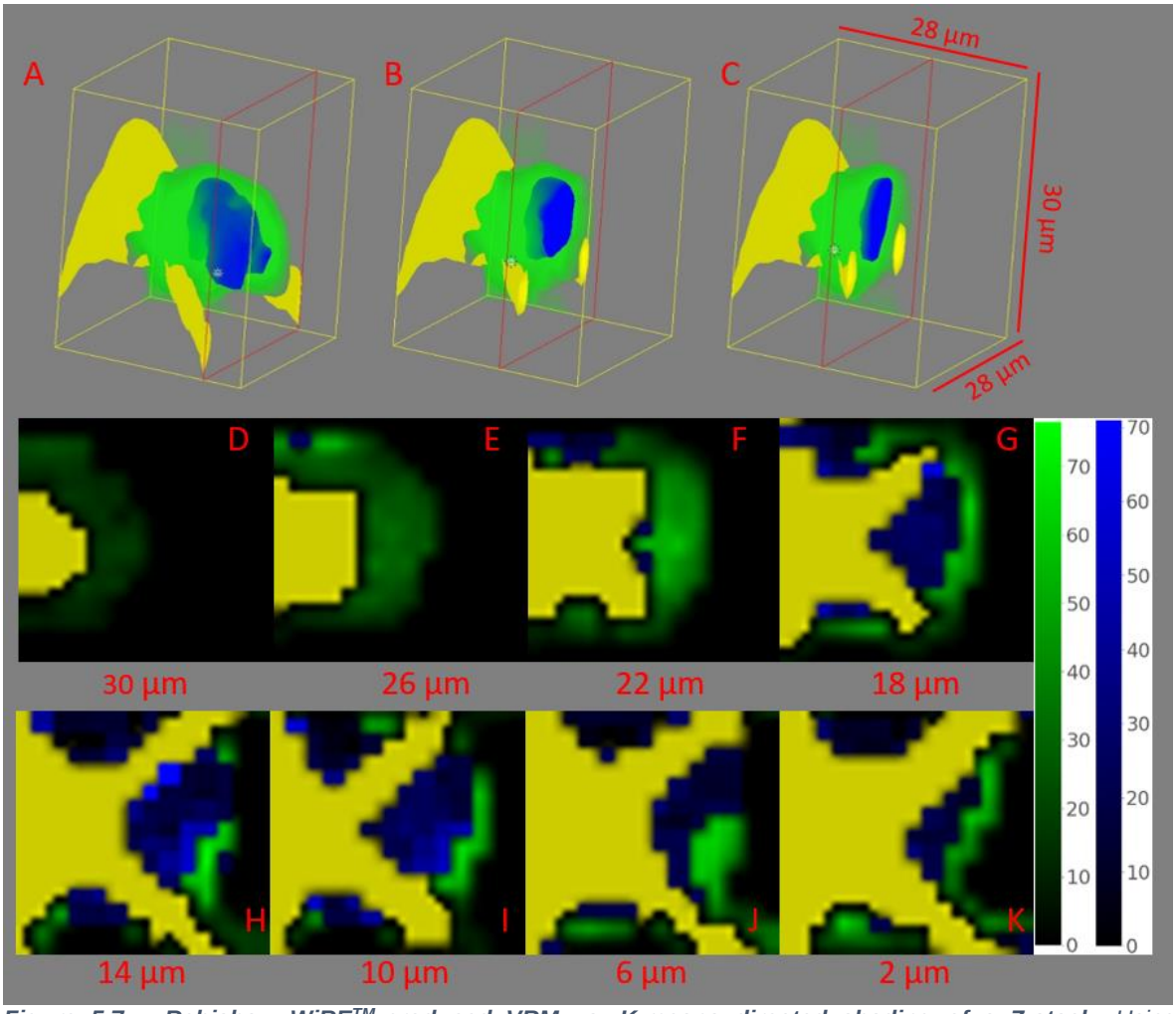

Figure 5.7 – Rehishaw WiRE™-produced VRM vs. K-means directed shading of a Z-stack: *Using standardised colouring (see methods). A 5-beamed cage & cell using a WiRE™-produced VRM in (A-C), with an axial cross-section moving through the HaCaT cell and scaffold, showing the whole cell, (A), cell centre (B), and rear (C). D-K) the separate slices of the VRM z-stack shaded using k-means directed shading (see Chapters 3 & 4 for cluster assignment method). Slices start at the top of the VRM stack (D), moving through the VRM at 4 µm intervals (z-steps) in (E-K), with the entire z-stack shading range in colour bars (right).*

Figures 5.5 and 5.6 demonstrate the advantages of viewing 3D views of VRMs, providing an intuitive overview of the sample. Viewing VRM as constituent slices provides the opportunity to apply objectively determined shading parameters (Chapter 4). Figures 5.7 & 5.8 compare two VRM in 3D and slice form for a 5-beamed cage (Figure 5.7) and a 10-beamed cage (Figure 5.8). The use of 5 and 10-beamed cages will be continued from Figure 5.6, as they provide the greatest contrast between cages. The shading convention for Figure 5.7 is consistent with the rest of the chapter, with the individual slices shaded using k-means directed shading, and the WiRE^{TM} produced VRM shaded using subjective shading, providing a quick overview image. Figure 5.7 shows a single HaCaT cell cultured on a 5-beamed cage, with a cell sitting on the connection between the beams, allowing it to form a spherical morphology. A-C shows a vertical cross-section moving through the cell, showing that the probable location of the nucleus, indicated through the mapping of the high nucleic acid region (775-790 cm^{-1}). The nucleus is centrally located, stretching between the two beams at the top of the scaffold and the thickness of the cell.

5.4.3. K-means directed vs. Renishaw WiRE^{TM} comparison (10-beamed cage)

The tendency to support the nucleus between beams is also observed in Figure 5.9, where the narrower pores allow for support closer to the base of the scaffold. The response of the cells to different positions on the scaffold is highlighted in the WiRE^{TM} VRM (Figure 5.8 A-D). Cells closer to the top of the scaffold supported between the scaffold beams, resulting in a more expended morphology compared to the cells closer to the slide surface. The advantage of using a WiRE^{TM}-produced VRM to visualise a large section of the scaffold, with several cells, is therefore highlighted by Figure 5.8 A-D. Although the k-means directed slices provide a more objective shading method for the analysis of specific molecular distributions, the WiRE^{TM} VRM provides a general impression of how the cells have responded to the scaffold. To provide the most consistent analysis, the collection of Raman maps or

spectra for datasets exploring differences between scaffolds may need to take the differences between the cells grown on different scaffold positions into account.

A difference between the 3D VRM in Figure 5.7 (A-C) and the slices (D-K) is that the slices show the top of the cell as higher (30 µm) in slice (A), the highest slice, with empty space shown in the 3D VRM, highlighting the danger of arbitrary shading for 3D (WiRE^{TM}) VRM. K-means directed shading provides strength to conclusions drawn from VRM, due to the increased objectivity of the shading method. The slices in Figure 5.8 (E-L) show the cells located between the beams from the maximum height at the cells detected (30 µm) in (F). The findings in Figure 5.7, where cells remain above the pores, are confirmed with the cells remaining between the beams until K/L (0-5 µm), where high nucleic acid regions are seen within the pore. The high nucleic acids regions in Figure 5.8 (K & L) suggest the cell is located within the pore, like the cell in Figure 5.5 and in Greiner et al [53], except closer to the bottom of the pore, suggesting a minimum width that the cell can migrate through. The cell in Figure 5.7 avoids the gap between the pores entirely, sitting in a position where the beams can support the spherical morphology shown in A-C, a conclusion reinforced when the slices are viewed in Figure 5.7 (D-K).

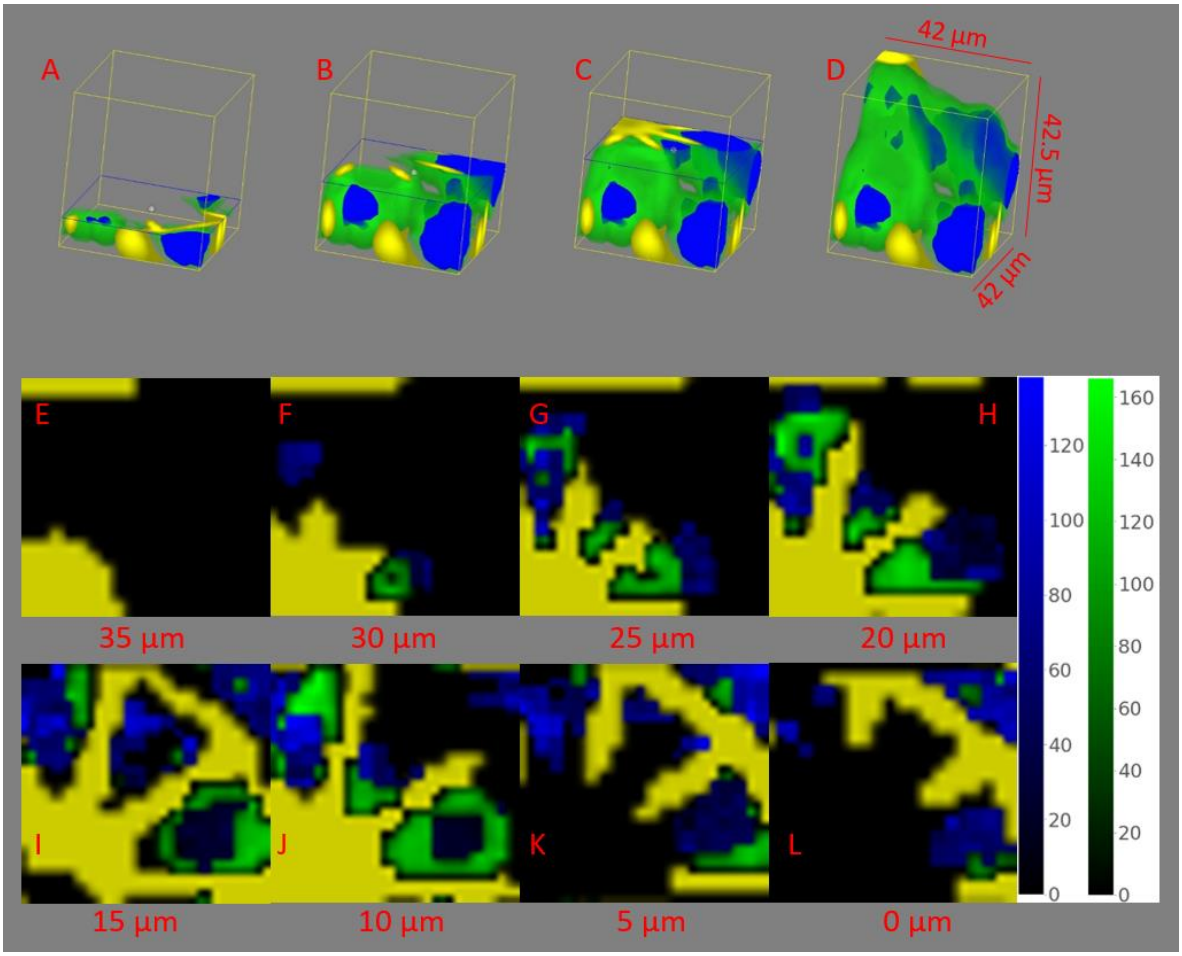

Figure 5.8 – Renishaw WiRE^{TM} VRM and slices of cell on a ten-beamed cage: Using standardised colouring (see methods): *A lateral cut shows a cross-section moving through cells on a ten-beamed cage in (A-D), showing cells appearing to coat the entire scaffold when the whole WiRE^{TM}-produced VRM is shown (D). In (E-L), the k-means directed shading of the z-stack is shown from the top slice (E), through each 5 µm z-step (F-k), to the bottom slice (L). The entire range within the related clusters for each cellular sub-section were used and are shown to the right of the slices.*

5.5. Distinguishing cells gown on scaffolds with different pore sizes

Having shown that VRM can visualise the morphological difference between cells grown on different cage scaffolds in section 5.4, a dataset was collected to establish whether the cage scaffold caused a molecular change in the cells.

5.5.1. PCA: Five-beam cages vs. Off

A dataset of 5-beamed cages (5BC) and off the scaffold (Off) was collected using the same method as that used in section 5.3, to see if the analysis was repeatable. Figure 5.9 shows the results from the PCA, using the first and second principal components that consist of 70.37% and 11.32% of the explained variance respectively. Figure 5.9 (A) shows the scores plot of PC1 and PC2, with clusters forming but overlapping. The loadings for PC1 (B) provide a wide range of molecules causing variance within the dataset. The positive loadings related to RNA 915 cm^{-1} [166], cytosine/guanine [166], or tyrosine/phenylalanine [110], [167], [175] shown in the (1171 cm^{-1}), where cytosine/guanine would link to the RNA seen in the 915 cm^{-1} peak. The PC1 negative loading peaks can be related to amide III [176] (1250 cm^{-1}), and 1338 cm^{-1} is in the 1330-11350 cm-1 protein region [6]. The benefit of including averaged spectra into the dataset is shown in PC1, where spectra that have all been randomly selected from the dataset may result in selection only from the nucleus by chance, producing spurious results. The negative loadings also highlight the CH_2 bending mode of proteins in the 1463 cm^{-1} peak [169], 1643 cm^{-1} (From Chapter 3), C=C, and amide I absorption [171]. Amide I is also linked to the 1671 cm^{-1} Raman peak [170]. The negative loadings, therefore, relate to the nucleic acids and proteins, previously associated with the change in morphology in section 5.3.1.

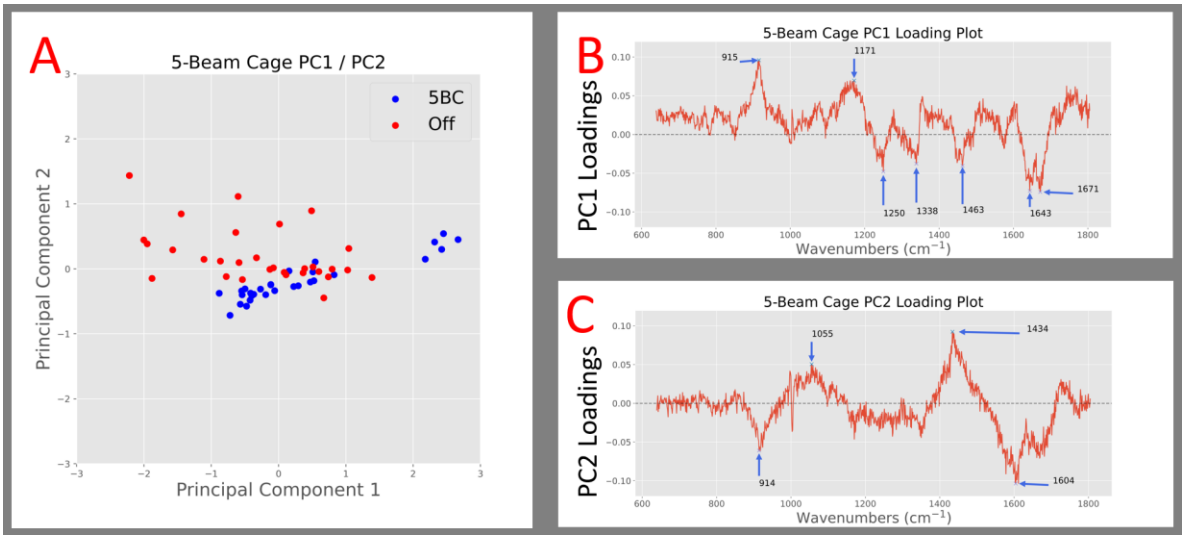

Figure 5.9 - PCA analysis of cells cultured in 3D morphologies supported by 5 beam cage (5BC) scaffolds and cultured off (Off) the scaffolds: *B) The explained variance plot, with the accumulated variance retained (y-axis) compared with the number of principal components (x-axis). The score plot for PC1 vs. PC2 is shown in (A), with s blue = 5-beamed cage (5BC) and red = cells cultured off the scaffold (Off). B) the loadings plot for PC1, with 915, 1171 & 1742 cm^{-1} positively loaded peaks, and 1250, 1338, 1463, 1643 & 1671 cm^{-1} negatively loaded peaks. C) The loading plot for PC2, with the 1055 cm^{-1} & 1434 cm^{-1} relating to the positive loading peaks and the 914 cm^{-1} & 1604 cm^{-1} negatively loaded.*

Due to the difficulty of determining a specific molecule that is independently responsible for the variance in PC1 and PC2, the off cells (red) generally favour the positive scores of PC2. The loading plot for PC2 (Figure 5.9 C) has fewer, but larger loadings peaks, with the positive loadings linked to lipids. The 1055 cm^{-1} could be protein C-O or C-N stretching (protein) [166], suggesting 1434 cm^{-1}, which can be linked to proteins or lipids [173], [177] is also related to proteins. The association with proteins is shown in Figure 5.10 through green highlighted in the 1055 cm^{-1} and 1434 cm^{-1} spectral regions in the average spectrum plot. The negative loadings are associated with RNA (914 cm^{-1}) [166] and the 1604 cm^{-1} C=O stretching in the amide I (proteins) [165], [166]. The negative loadings for PC2 similarly match the negative loadings of PC1, indicating a link to nucleic acids and proteins. The nucleus is an organelle high in both nucleic acids and proteins, as shown in low-feature mapping in Chapter 3. The negative loadings for both PC1 and PC2 may therefore be related to changes in the nucleus, or cytoplasm near the nucleus in response to the different support geometry.

To further investigate the spectral regions highlighted in the principal components, the average spectra of the two classes (top) and standard deviation of the entire dataset (bottom) are compared in Figure 5.10. The averaged spectra of the classes, 5-beamed scaffold (5BC – red) and the cells cultured off the scaffolds (Off – blue), show regions of the spectrum where the two classes diverge. Comparing averages provides a method of comparing the two classes at the cost of the data spread, which can be described by the standard deviation. Figure 5.10 (bottom) plots the standard deviation for each wavenumber for the entire dataset. The purpose of plotting the standard deviation for the entire dataset is to identify the wavenumbers with the greatest spread when looking at both classes. The standard deviation is a descriptive statistic, providing the spread of the data but missing a direct comparison between the classes. The two plots provide complementary information, with the averaged spectra providing a comparison between the two classes, with the limitation of averaging that the spread of the data is averaged out mitigated by the standard deviation plot.

Figure 5.10 shows the regions highlighted by the PCA by shading the background of the plot using colours associated with different molecules or combinations of molecules (blue = nucleic acids, green = proteins, & purple = lipids). The RNA 915 cm^{-1} Raman peak (blue background) indicated in PC1+ and PC2- is in a wider range of divergence between the two averaged spectra. The same region is associated with a broad peak when looking at the standard deviation in the entire dataset (bottom), centred on 915 cm^{-1} (black line). A change in the RNA peak may be linked to the changes in nuclear morphology discussed in section 5.3.3. The 1715-1750 cm^{-1} peak indicating potential OrmoComp™ contamination is not prominent in the average spectra or the standard deviation. The lack of a large spectral peak in the 1715-1750 cm^{-1} region (compared to that seen in section 5.4) demonstrates another advantage of partitioning Raman maps using k-means clustering, as the contamination that may influence the classification of cells grown on and off scaffolds can be removed or minimised, which will be continued in the next sections and chapter.

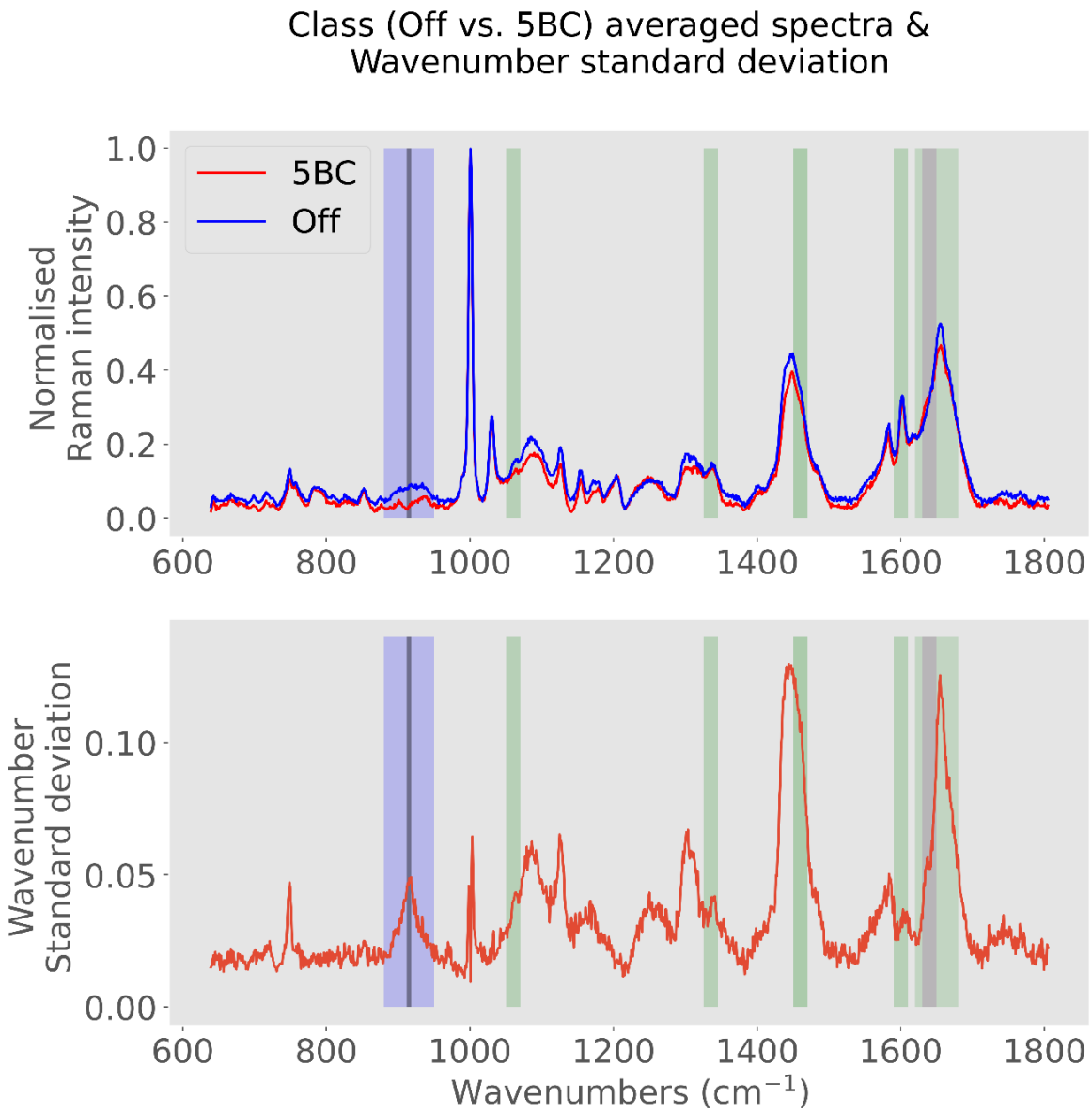

Figure 5.10 - Comparison of class average spectra (top) and dataset standard deviation (bottom): *Molecular assignments and a spectral peak are highlighting in both plots using background shading for nucleic acids (blue background), proteins (green background), lipids (purple background) and the 915 cm^{-1} spectral peak shown using the black line. Top) Showing the average spectrum for the 5BC (red) and Off (blue) classes, indicating specifically where the two classes deviate, but not the spread of the data. Bottom) The standard deviation for the entire dataset, showing the spread of the data.*

Proteins dominate the remainder of the spectral differences highlighted by the PCA, correlating with the findings in section 5.3. Changes in protein regions of the spectrum were hypothesised as relating to actin adaption in cells cultured in two- and three-dimensional morphologies. A shoulder (1050-1070 cm^{-1}) is highlighted as green on the broader 1050-1100 cm^{-1} spectral peak, associating the shoulder with

proteins in PC2+. The same peak is represented in the standard deviation peaks (bottom), with the 1050-1070 cm^{-1} shoulder apparent. 1330-1350 cm^{-1} region is associated with proteins [6], with 1338 cm^{-1} from PC1- therefore highlighted green for proteins. 1330-1350 cm^{-1} peak is shown on the standard deviation plot, showing that the collections of this wavenumber are spread further around the mean. Other protein-associated regions include 1440-1470 cm^{-1} shoulder relating to 1434 cm^{-1} (PC2+) & 1463 cm^{-1} protein (PC1-) assignments in the region. The 1590-1620 cm^{-1} Raman peak is highlighted green for the 1604 cm^{-1} Raman peak (PC2-) proteins. Highly loaded protein spectral peaks in the 1620-1680 cm^{-1} green region include the 1643 cm^{-1} peak in PC1- (assigned proteins or lipids for 1648 cm^{-1} in section 5.3.3) and 1652 cm^{-1} (proteins and lipids in PC1). The lipid assignment for 1630-1650 cm^{-1} is indicated with purple shading. The standard deviation for 1620-1680 cm^{-1} peak is one of the two highest, with a difference shown between the two classes also, resulting in a higher confidence that molecular changes are occurring in the protein and lipid composition in the cells due to being grown on the 5-beamed cage rather than a flat slide surface.

5.5.2. Supervised learning: Five-beam cages vs. Off

To replicate the analysis in section 5.3.4, learning curves were produced for the dataset using the same logistic regression (B), LDA (D), and SVM using hyperparameters C = 1 and linear kernel (F) in Figure 5.11. Initially, the algorithms failed to converge the training and validation lines whilst using the first and second principal components, suggesting under-sampling. To identify the principal components that distinguish the classes most effectively, a decision tree was trained (A) to indicate features (principal components) that distinguish the data most effectively, showing that the PCs with the greatest classification power were PCs 2, 5, and 6, which were selected as for further analysis, representing 14.34% of the explained variance combined. PC5 and PC6 represented 1.57 % and 1.45% of the explained variance respectively, potentially too small percentages to warrant selection. The use of PC5 and PC6 is justified by the production of learning curves

for all three algorithms shown in Figure 5.11, logistic regression (B), LDA (D), and SVM (F), converging. All three algorithms, using separate classification approaches, finding a cross-validated distinction between the classes supplies strength to the conclusion that those principal components retained signal rather than noise. All three models converge close to the 90% f1-score and similarly to the section 5.3.4 results, show 35 samples (70%) of the data as providing the highest f1-score for all three models without any overfitting occurring. Models were therefore trained using 70% training data, with the confusion matrices shown in Figure 5.11 C, E, & G respectively, with the models achieving F1-scores of 70.59% (LR), 93.33% (LDA), and 85.71% (SVM).

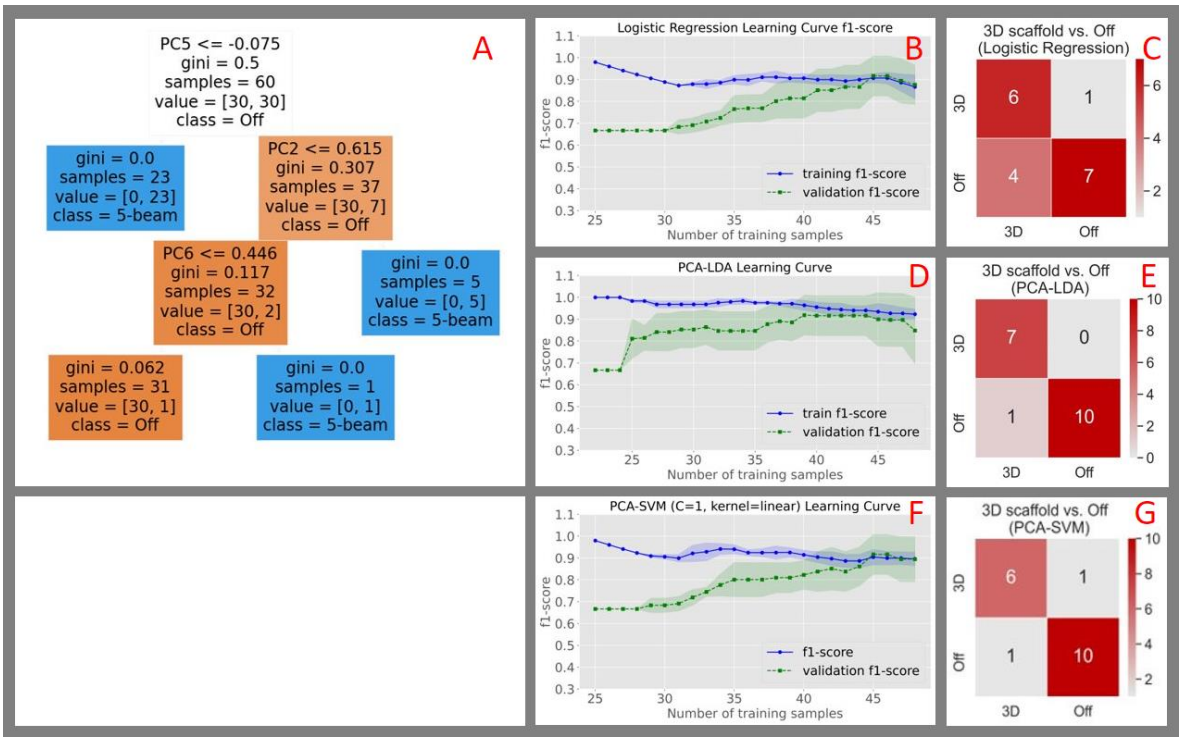

Figure 5.11 - Cross-validation and classification of cells cultured on a 5-beamed cage scaffold vs. cells cultured off the scaffold dataset: *A) Cross-validation results of five algorithms using 5-fold cross-validation. An average score of 76.66% for logistic regression, decision tree (85%), support vector machine (95%), random forest (93.34%), and linear discriminant analysis (81.68%). The highest average score (support vector machine) was selected and trained using training data (C = 0.1, kernel = poly, gamma = 1) and the test data used to produce predictions, with the results showing 100% sensitivity and 100% specificity.*

The 70.59% f1-score is the lowest, shown as a score at the lower edge of the range shown in the cross-validation standard deviation (green shading) in (B). Whereas the 93.33% and 85.71% f1-scores for the LDA and SVM algorithms are the higher scores for those algorithms. The high scores within the range indicated by the standard deviations for the LDA and SVM reveal that the training set data selection can produce the appearance of inflated model performance, showing the value of cross-validation and justifying excluding train-test splits producing standard deviations that cross the validation line whilst using learning curves. Conversely, an f1-score in the lower edge of the standard deviation range for the logistic regression reveals that if a different subset of samples were selected for the training dataset, the confusion matrix and f1-score would produce “better” looking results, which would not be seen when observed in isolation.

5.5.3. Supervised learning: Five-beam cages vs. 10-beam cages

Section 5.3 and 5.4 established that cells cultured on two-dimensional surfaces and three-dimensional scaffolds can be distinguished using Raman spectroscopy. Classification of cells grown on different 3D scaffold designs was the next phase of the investigation, to explore the effect of different scaffold geometries on cell morphology. Figure 5.12 shows the three-axis PCA plot for the first three principal components, relating to 89.62% of the explained variance. Clear clustering was not seen in the PCA between the five and ten beam cage samples for the combinations tested, including using a decision tree to identify the principal components that divide the classes most efficiently, which identified the fourth principal component as providing the most distinction between the classes. However, no greater separation was seen in the PCA plot, at the cost of variance. Figure 5.12 B, C & D show the learning curves for logistic regression, LDA, and SVM, repeating the analysis used in sections 5.3 and 5.4. The learning curves did not fully converge, with some meeting of the standard deviations but not a consistent meeting of the validation and training lines. The lines do seem to be moving together, suggesting they may converge with additional samples. The f1-score in the region where convergence

may occur is not high, shown as between 50-70% at the final points on the learning curves in (B, C, & D). However, the converged learning curves increase confidence in conclusions drawn from the models, providing a foundation for further investigation.

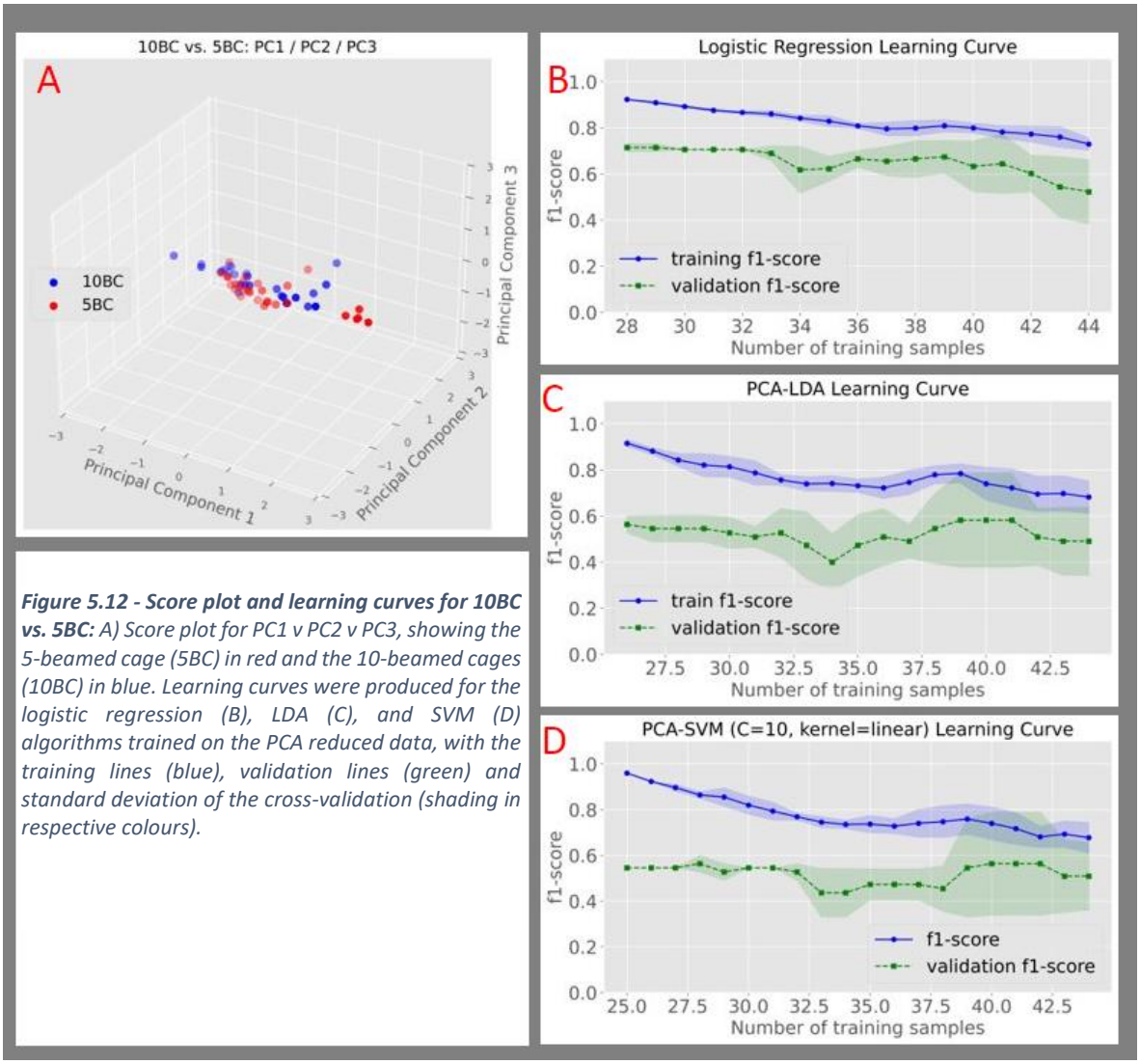

Figure 5.12 - Score plot and learning curves for 10BC vs. 5BC: *A) Score plot for PC1 v PC2 v PC3, showing the 5-beamed cage (5BC) in red and the 10-beamed cages (10BC) in blue. Learning curves were produced for the logistic regression (B), LDA (C), and SVM (D) algorithms trained on the PCA reduced data, with the training lines (blue), validation lines (green) and standard deviation of the cross-validation (shading in respective colours).*

5.6. Large, medium, and small square pores.

Having shown in section 5.3 that VRM can visualise changes in cell behaviour resulting in altered pore dimensions and established that Raman spectroscopy can classify cells depending on their morphology (2D vs. 3D). In section 5.4, cells grown on different pore dimensions, produced using different numbers of beamed cage scaffolds (5 vs. 10) resulted in the inconclusive distinction of the classes based on learning curves. The learning curves (Figure 5.12) suggested that convergence may be possible if a larger dataset is collected. Double the number of samples per class were therefore collected to study if a difference in square 18 μm deep pore dimension altered cell behaviour. Small (10μm^2), medium (20μm^2), and large (20×40μm^2) lateral dimension pores were produced, resulting in the shape remaining constant. The ability to determine any change simulating the response of a cellular population to a porous material, such as those found in bioengineered bone.

5.6.1. Renishaw WiRE^{TM} VRM of HaCaT cells in varied diameter pores

Figure 5.13 shows the WiRE^{TM} (3D) VRM of the cells in the small pore (A & B), the medium pore (C & D), and an example of the large pore (E & F). It can be seen in the axial view of the small pore (A), that the cell has fit itself within the pore, with the lateral view showing that it has provided support for itself on all four sides. As the pore grows in size, the medium pore stops the cell from being able to support itself on more than two sides (C & D). For the chemometric analysis, the decision was taken to focus on cells supported on two sides for the medium pores and one side for the large pores (with similar morphologies to the cell shown in Figure 5.2). By mapping cells supported by distinct wall numbers, the greater distinction between the cells in the medium pores and cells situated in the corner of a large pore (E & F) was aimed to be avoided.

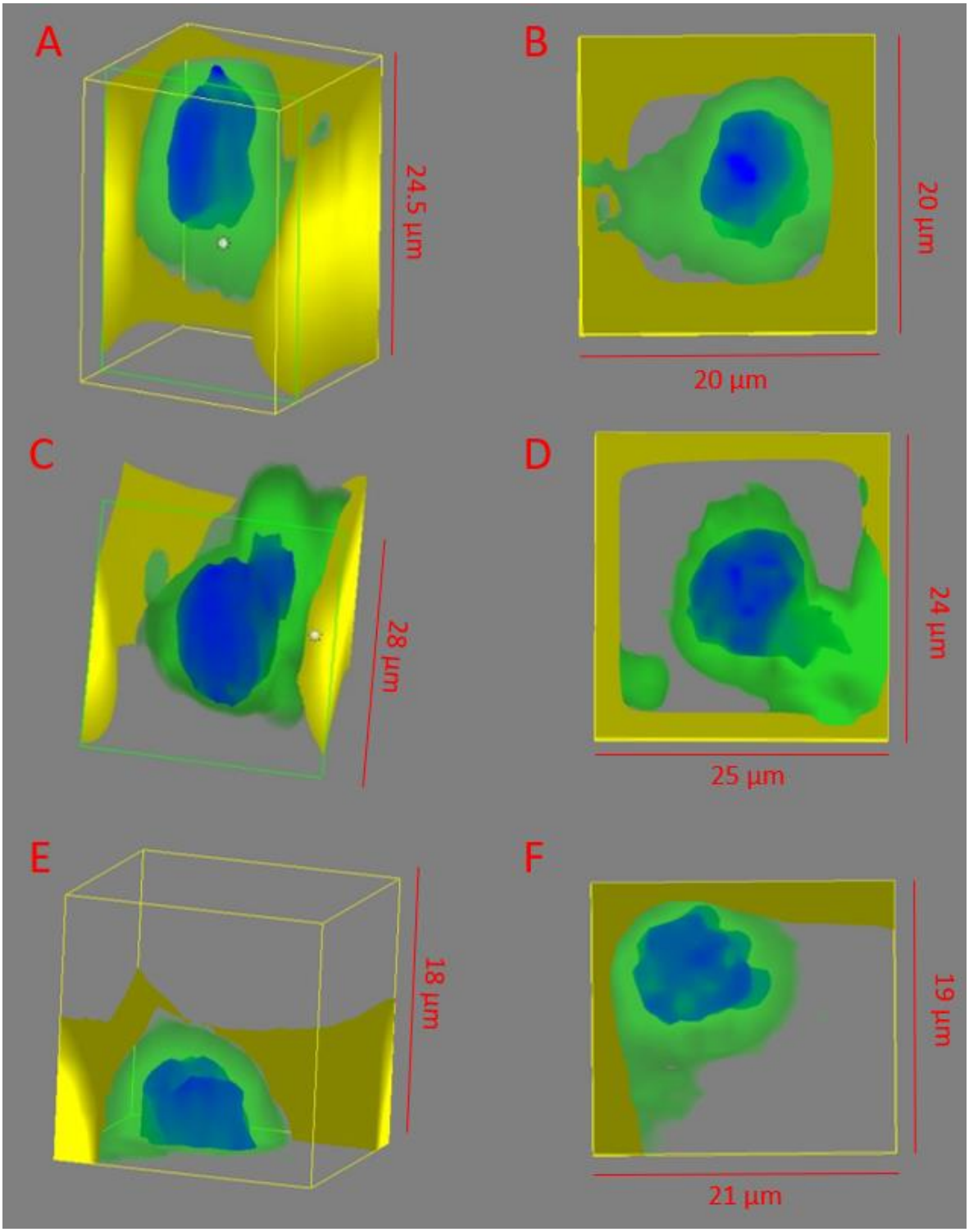

Figure 5.13 - WiRE™ VRM of cells in OrmoComp™ pores: *Using standardised colouring (see methods). The side (A) and top (B) views of a cell in the relatively small 10 × 10 µm lateral dimension pore. C & D) A cell entering the medium (20 × 20 µm lateral dimension) pore, supported by pore sides, and (D) showing the cell in a central location within the pore. E & F) Map a cell on the large pore (20 × 40 µm lateral dimension, where (E) shows the cell using the cell wall to support its 3D morphology and (F) shows the cells elongated morphology to stretch along the pore wall.*

5.6.2. Machine learning analysis of HaCaT cells in varied diameter pores

Figure 5.14 (A) shows a three principal component score plot for PC1, PC2, and PC3. The three principal components plotted in (A) represent 76% of the variance, as shown in the explained variance plot in (B). Distinct clusters are not produced in (A) with overlapping of cells cultured off scaffolds (Off-black), large (LgSq–blue), medium (MdSq-red), and small square pores (SmSq-green). The decision tree selection of principal components used in section 5.5.2. could not produce suitable class separation. To establish whether the principal components provided statistically significant relationships, Mann-Whitney U-tests were carried out on all pairs of principal components of over 1% explained variance, highlighting no statistical significance. The lack of clustering or statistical significance between the principal components leaves the conclusion that any molecular changes induced by different square pore dimensions cannot be identified using PCA. For applications where a Raman detectable change has been established, Raman spectroscopy could therefore be used to ascertain whether that change has occurred or not. The same method as 5.3.4 and 5.5.3. will be used for supervised learning to determine whether the use of class labels will provide improved performance.

4

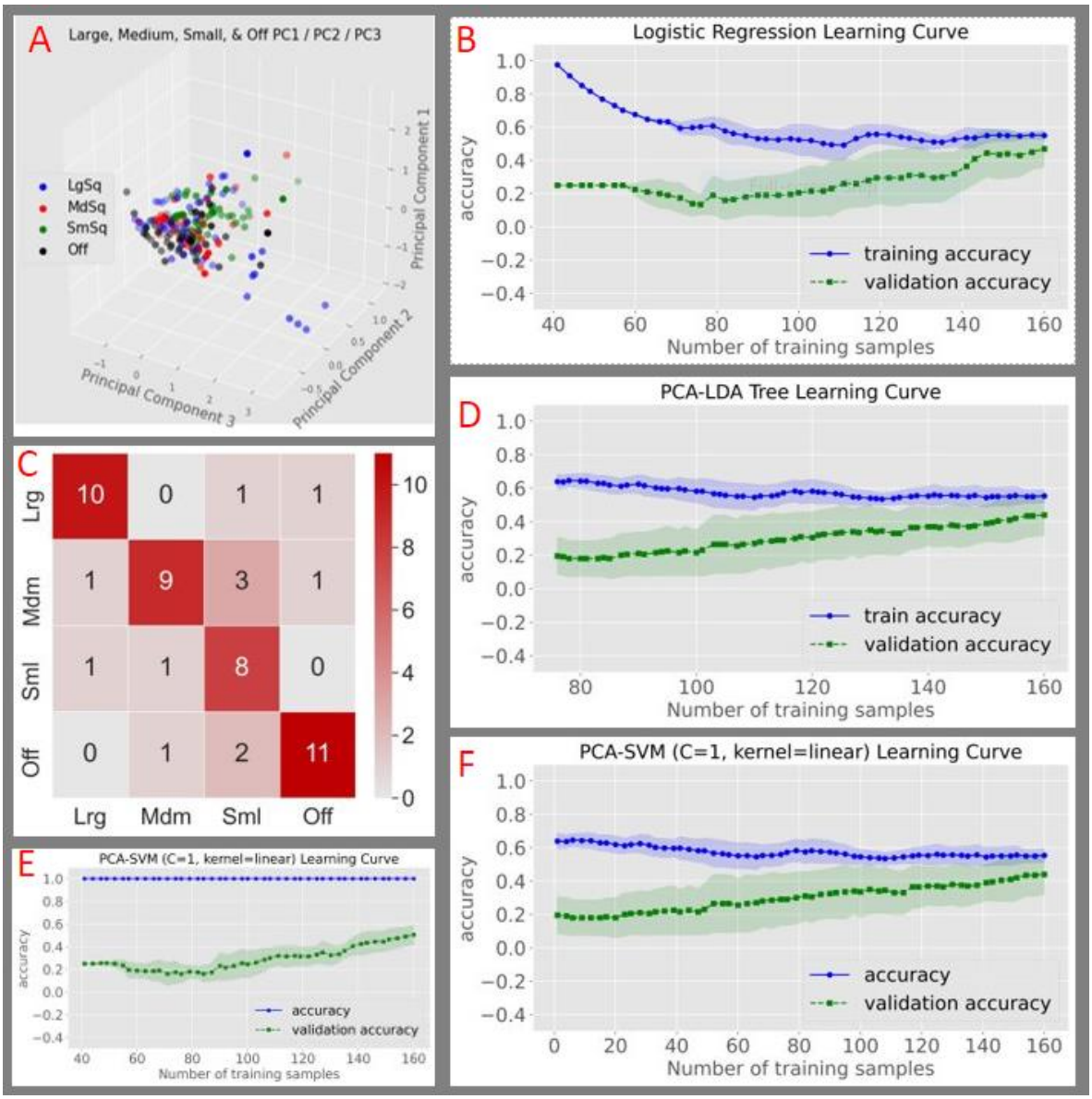

Figure 5.14 - PCA and classification of cells cultured in, small, medium, & large pores, and off the scaffold: *A) PCA score plot for PC1 v PC2 v PC3 (76% explained variance). C) The confusion matrix for a SVM trained on the entire dataset, learning curve (E). Learning curves for algorithms trained on PCA reduced data, with the logistic regression (B), LDA (D), and SVM (F) all converging closer to 50% f1-score.*

Initial investigation of supervised learning provided optimistic results using an SVM algorithm (C = 10 and polynomial kernel) that appeared to produce high-accuracy classification when trained on the entire spectrum. A model was initially trained on the entire spectrum, providing a starting point for the analysis, with accuracy chosen as the metric over the f1-score as it requires only correct and incorrect classification

for calculation. F1-score is calculated using false positives and false negatives, making a single learning curve incalculable for multiclass analysis. Figure 5.14 (C) shows the confusion matrix for the support vector machine (L = large pore, M = medium pore, S = small pore), trained on 75% of the data, resulting in an overall model accuracy of 84%. The learning curve for the full dataset (D) shows the improbability of this result generalising to new data (overfitting), with the validation accuracy raising no higher than 50%, indicating the ineffectiveness of the model. The 5-fold cross-validation of the training dataset produced an average score of 88.67%. Observed in isolation, these outputs provide significantly better model metrics than the learning curve (D) invalidated.

The training and validation line gap was reduced for logistic regression, LDA, and SVM (C=10 and linear kernel) models (B, D, & F) by following the previously outlined method for the larger dataset. The models were trained on a dataset of PCA-reduced dimensions (PC2, PC3, PC4, & PC6) selected by a decision tree. The three models (B, D, & E) produced similar learning curves, all close to convergence, indicating that the true maximum accuracy is close to 50%, which is unobservable using the confusion matrix in isolation. The lack of classification, using methods shown to distinguish cell cultures in two and three dimensions, results in the conclusion that Raman spectroscopy cannot distinguish molecular changes resulting from the changed pore dimension. A repeated result when looking at both the cage and square pore scaffold designs. An inability to distinguish cells grown on different pore dimensions could still be valuable when monitoring bioengineered constructs. In the case of an experiment looking at the effect of a biochemical stimulant, any classification seen could be isolated as resulting from the biochemical stimulus rather than the porous substrate/scaffold design. However, a control would be required for this to be stated with confidence.

5.7. Conclusions

The capacity to monitor cells using Raman spectroscopy, potentially as part of an automated cell culture system, initially requires two constraints to be met. The first is that the biological system is understood and the second is that a method of automating an output from that knowledge is carried forward. In this chapter, VRM and PCA were used to explore the biological system, both spatially (VRM) and biochemically (PCA). Analysis was carried out over three experiments, simple scaffolds, cage scaffolds, and small, medium, & large pores started with the simple scaffolds. Simple scaffolds were defined as such to note the block design of the scaffold, avoiding depth distortion by focusing on cells attached to the scaffold side. The VRM of a cell on the side of a scaffold (Figure 5.2) showed an altered morphology, elongated when compared to the VRM of cells sitting on the slide surface (Figure 4.3). An initial hypothesis asked if VRM could show morphological differences between cells grown on different scaffold dimensions, which was shown through the chapter in sections 5.3, 5.4, & 5.5.

Once SEM imaging had verified the scaffolds print quality, the next aim was to compare K-means directed shading to Renishaw WiRE^{TM} (Volume Viewer) produced VRM. WiRE^{TM}-produced VRM are quicker to produce and provide more intuitive images, especially when z-steps are chosen to minimise distortions (Chapter 4). WiRE^{TM}-produced VRM were previously used to indicate general changes in cell behaviour in response to scaffolds (sections 5.3.1, 5.4, & 5.5). However, it must be reiterated that shading parameters chosen by the researcher cannot constitute evidence towards conclusions on sample dimensions, due to lack of reputability. Z-stack was therefore used to map the simple scaffold (section 5.3.1) and cage scaffold (section 5.4) mapping, demonstrating the ability to repeatably separate the regions into key structures (scaffold, background, nucleus, & cytoplasm), solving the problem highlighted by Ashton et al [5] for VRM. Another hypothesis, which raised the research question asking if k-means directed shadings repeatability when mapping cells on different scaffold types, was established over

Figures 5.2, 5.8, & 5.9, showing cells on a simple scaffold (5.2) and cage scaffolds (5.8 & 5.9). K-means directed shaded VRM of cells on scaffolds will next be complemented with maps of cells without scaffolds to test the method in a different application (Chapter 6).

Having determined the repeatability of K-means directed shading, another advantage was used for further analysis, the removal or diminishment of unwanted regions such as the background, scaffold, or contamination. Having noticed some OrmoComp™ contamination in the averaged cluster spectra for the cell body in Figure 5.2, the k-means directed shading method was adapted to exclude scaffold material contamination from further analysis. PCA was then used to investigate molecular changes in the cells. Score plots established separation between cells grown on and off scaffolds (Figure 5.3), and loading plots were used to highlight protein (actin) and nucleic acid regions as responsible for the maximised variance in the principal components; suggesting their adaptations are linked to changes in morphology. The cage scaffolds followed the design of an angled beam scaffold in Chapter 4, the capacity of cage design scaffolds to alter cell behaviour compared to cells off scaffolds was tested (section 5.5). Average (mean) spectra for each class were plotted alongside the dataset standard deviation (Figure 5.10), strengthening the analysis by showing in which regions the classes deviated, repeating the spectral peaks highlighted in Figure 5.3. After Figure 5.9 repeated the separation shown in Figure 5.3, the next step was to test whether altered pore dimensions could influence the molecular composition of HaCaT cells.

For studies aiming to progress towards the automated monitoring of bioengineered constructs, it must also be established that the distinctions determined using unsupervised learning and Raman mapping can be transitioned onto techniques that can be trained for repeated use. One of the aims of this chapter was therefore to carry out machine learning classification, looking at repeatability in the analysis, over algorithms, and within the dataset. Justifying the investigation of the third hypothesis, that machine learning algorithms be trained to classify cells grown on two- and three-dimensional substrates. Using PCA for an initial investigation had an additional benefit, providing dimension reduction, with a decision tree used to streamline

feature (principal components) selection. Three algorithms were tested throughout the chapter (logistic regression, linear discriminant analysis, and support vector machine), which all rely on different statistical processes to carry out classification (Chapter 2). The repeatability of the classification using different algorithms was further reinforced using learning curves, which plotted the 5-fold cross-validation for the range of training dataset sizes. Training of the 3D vs. Off dataset resulted in learning curves that had an f1-score over 80%, indicating that the changes seen in the PCA could be translated into a supervised classification for more complex (cage) scaffolds. Repeating the same methods used to analyse the “simple” 3D scaffolds produced similar results with a wider spread of f1-scores, between 70 and 95% for the different algorithms.

The next step after separating cells on 2D and 3D substrates was to investigate the capacity of the method to separate cells on different variations of the scaffolds. Initially, 5 and 10 beamed scaffolds were selected, providing the greatest contrast in morphology as shown using VRM (section 5.4). Neither the PCA nor supervised learning methods were able to distinguish the two classes satisfactorily. Potentially resulting from the analysed cells being at different positions on the scaffold, with cells closer to the base of the pore being in a different morphology than those at the narrower pore region at the top. To counter the changing pore dimension, a final pore design was used alongside increasing the number of samples per class. As binary classification had already been completed in sections 5.3.4 and 5.5.3 (simple scaffolds and 5 beamed cages vs. Off), three pore dimensions were chosen, large (20×40), medium (20×20), and small (10×10), which with cells cultured off the scaffold included as a control. In Figure 5.13, the cells in/on the side of the scaffolds were visualised, showing the altered support structures provided to the cells by the different pores using VRM. PCA could not separate the four classes, followed by poor supervised classification.

The value of publishing learning curves was demonstrated in section 5.6.2. Initial inspection of the confusion matrix indicated impressive accuracy in distinguishing the ten samples/class. Inspection of the learning curve revealed overfitting, with subsequent feature selection resulting in model convergence for the three models,

but towards an unsuitable 50% accuracy. Potentially this indicates cells grown on different three-dimensional structures do not vary enough from one another for Raman spectroscopy to distinguish them, as two scaffold styles failed to produce suitable distinctions using unsupervised or supervised techniques. The capacity to determine when a culture system has not changed can be just as valuable as sensing altered behaviour when applied to monitoring a bioengineered construct. It is more difficult to assert with confidence that something has not changed, as opposed to cannot be detected, without the use of controls as a minimum and potentially statistical methods such as the calculation of p-values.

Chapter 6 - Flow chamber for in-situ Raman mapping

6.1. Introduction

Fluid flow provides a range of benefits to Raman spectroscopy. Thermal control of the fluid provides the opportunity to simulate *in vivo* temperatures, supporting live-cell Raman spectroscopy, or depending on the application, minimising thermal damage by cooling samples. A design aim (aim 1) for the flow chamber is therefore to include a method of controlling the fluid temperature, where the cooling may reduce thermal damage to the sample as highlighted in the Chapter 4 conclusions. For live or unfixed-cell Raman analysis, a target for the chapter is to warm the fluid to 37 $°C$. Fluid flow also provides a second aim (aim 2) for the chapter, to use the fluid to supply a drug, dithranol, as factors (nutrients, drugs, growth factors, etc.) are supplied in vivo, in a dynamic environment. A synergetic benefit when combined with the non-destructive monitoring that live-cell Raman provides.

The confocal Raman mapping of cells in a flow-immersion objective is unknown to the author. The use of enclosed flow chambers [178], [179] for Raman analysis of cells has resulted in the absence of Raman mapping and VRM (and the additional morphological detail) from previous Raman spectroscopy flow analyses. Testing of the flow chamber will follow a structured approach, first testing the capacity of Raman spectroscopy to collect a spectrum in the flow chamber from a direct laser written (DLW) construct, providing a well-defined structure for the initial test. Having established that Raman spectra can be collected, the testing will move onto Raman mapping, VRM, and repeats for single cell analysis; with the explicit objective of providing an open flow chamber that does not endanger the spectroscope through fluid spillage or flooding.

The development of an open flow chamber provides the opportunity to analyse cells in flow using an immersion objective, with the benefits of simpler refractive index matching, Raman mapping / VRM, or improved mapping resolution. The design, manufacture, and testing of such a flow chamber would determine the ability of Raman to analyse and visualise the effect of a drug (or another factor) supplied to cells within the Raman spectroscope, minimising disruption and avoiding the need for fixing [20]. Dithranol has previously been visualised within HaCaT cells [5], providing a key opportunity to observe the uptake and effect of the drug on cells. Dithranol provides the opportunity to map not only the response of the cell to the drug, which is feasible for many other drugs/factors but to visualise the location of the drug in the cell [5]. The advantage this provides is the increased confidence gained in assertions about the location of the drug that can then be linked to drug-affected regions of cells. Raman spectroscopy, as shown in Chapter 5, provides the capacity to link spectrally presented molecular insights to locations within 2D areas or 3D volumes with Raman mapping and VRM respectively. The use of dithranol also allows for the testing of a third aim (aim 3), to show an application of VRM to map a dithranol distribution through a cell.

Having expanded the visualisation of dithranol through a cell to three dimensions, spectra can be taken from the maps and used in chemometric algorithms to explore the cellular response to the drug alongside morphological insights. The value of an open flow chamber will therefore be demonstrated using Raman maps for the next aim (aim 4) of the chapter. Aim 4 is to verify the fluid flow supply of dithranol to unfixed cells using chemometric separation and Raman map visualisation of fluid-supplied dithranol exposed and unexposed cells. An initial investigation, as defined in Chapter 5, will use principal component analysis to investigate the biological response of the cell to dithranol. A controlled study will be carried out, using the same method used to supply the dithranol, except without the dithranol. Any subsequent change in the PCA score plots can therefore be linked to the addition of dithranol, with k-means directed shading adding confidence in morphological changes mapped, with findings then compared to previous sections and studies.

Hypotheses:

1) Dithranol distribution can be mapped using VRM.
2) Dithranol supplied by a flow chamber to unfixed HaCaT cells can be mapped using Raman spectroscopy.
3) Dithranol supplied by a flow chamber to unfixed HaCaT cells can be distinguished using Raman spectroscopy.

6.2. Flow chamber design, fabrication, & testing

The design of a flow chamber for use inside a Raman spectroscope with an immersion objective provides a range of challenges to overcome before flow Raman mapping is possible. Considerations can relate to the analysis of samples, ensuring the design supports cell survival for the duration of the experiment and that the sample will not move because of the flow. Alongside design considerations for Raman mapping, countering impediments relating to the additional weight or blocked movement of the flow chamber (and all supporting tubes, heaters, and the objective). To balance all the factors relating to the flow chamber design, the study challenges will be grouped into three design objectives: Spatial compatibility with the spectroscope.

- Slide stability for Raman mapping
- Biological support for the cells

6.2.1. Flow chamber design and fabrication

The first design objective, spatial compatibility with the spectroscope, required consideration of factors such as being able to fit inside the spectroscope hood. The Raman spectroscope stage had to be inspected to determine the size of the flow chamber it could accommodate and the weight it could predictably be able to move accurately enough for mapping in two and three dimensions. The spectroscope hood had a hole in the side for heating wires and thermostat cables for static liquid live-cell Raman spectroscopy, which were suitable for the tubes leading to a pump providing the flow (see Figure 6.5). The fluid tube is therefore fed through the hole and the tube is attached to either end of the flow chamber. The second consideration was designing the flow chamber in such a way that the slide could be kept as still as possible for mapping in the flow, to avoid distortion of the map. The flow chamber was therefore tailored to the slides being used in the Nanoscribe™, 25×25 mm square slides that are 0.5 mm deep. Both vertical and horizontal movements must be avoided for mapping to be successful. In Figure 6.1 the depth of the slide tray is 0.5 mm deep, the flow chamber top overlaps the slide at its sides providing a space for the fluid to flow through the centre of the flow chamber (over the sample) alongside a tightly fitting area for the slide (preventing vertical movement); however, the brittle slide could not be put under clamping forces, as the hard material of the flow chamber would probably result in damage to the slide in cases of miss alignment or over-tightening. Semi-circles (radius 2.5 mm) were added to aid the removal of the slide post-analysis. To stop horizontal movement or transit of the slide along the direction of the flow, a 1.25 mm lip was added to the flow chamber base, providing a stop to the slide.

A

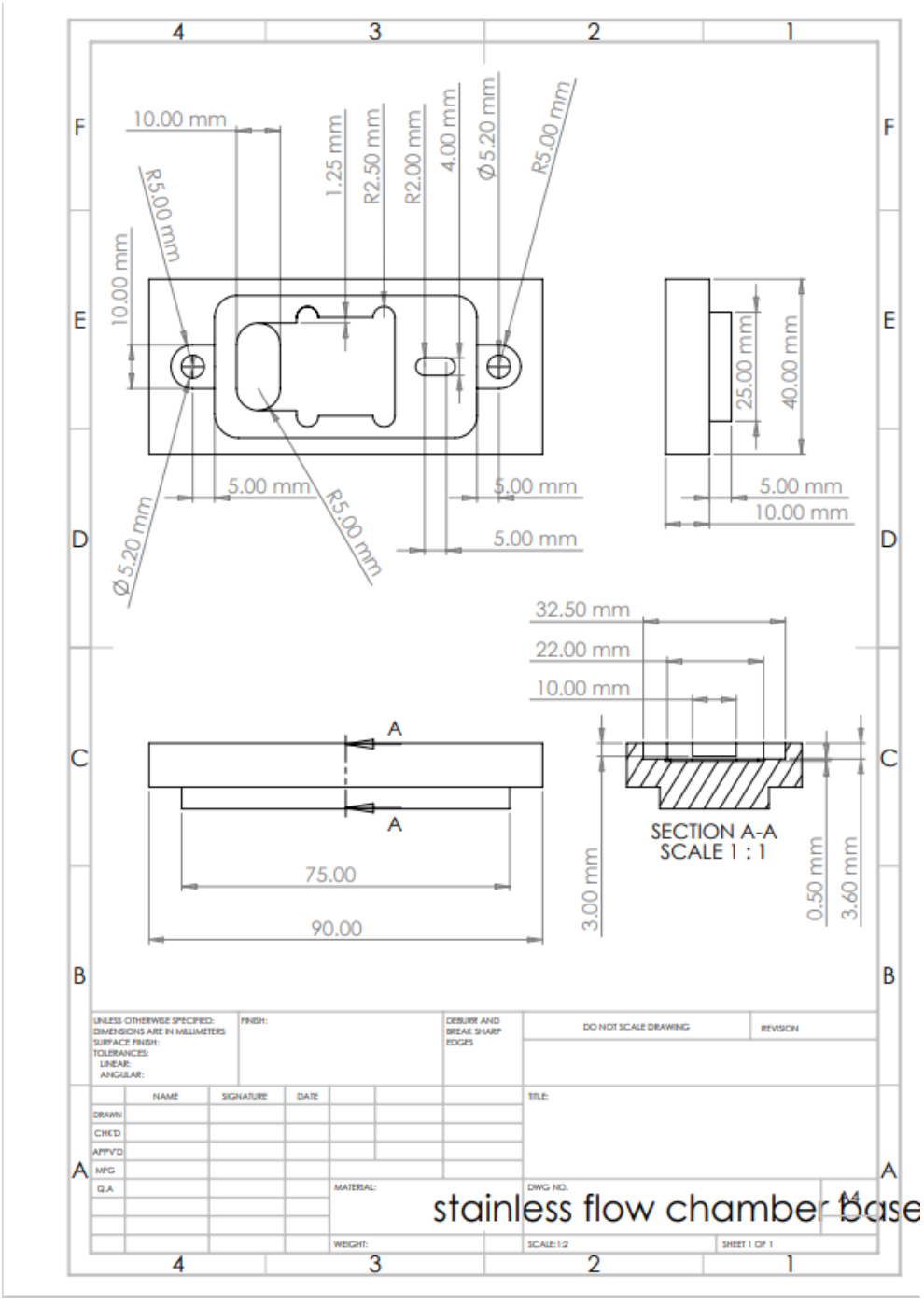
10.00 mm
R5.00 mm
10.00 mm
1.25 mm
R2.50 mm
R2.00 mm
4.00 mm
Ø5.20 mm
R5.00 mm
5.00 mm
R5.00 mm
Ø5.20 mm
5.00 mm
5.00 mm
25.00 mm
40.00 mm
5.00 mm
10.00 mm
32.50 mm
22.00 mm
10.00 mm
A
A
75.00
90.00
SECTION A-A
SCALE 1 : 1
3.00 mm
0.50 mm
3.60 mm
stainless flow chamber base

B

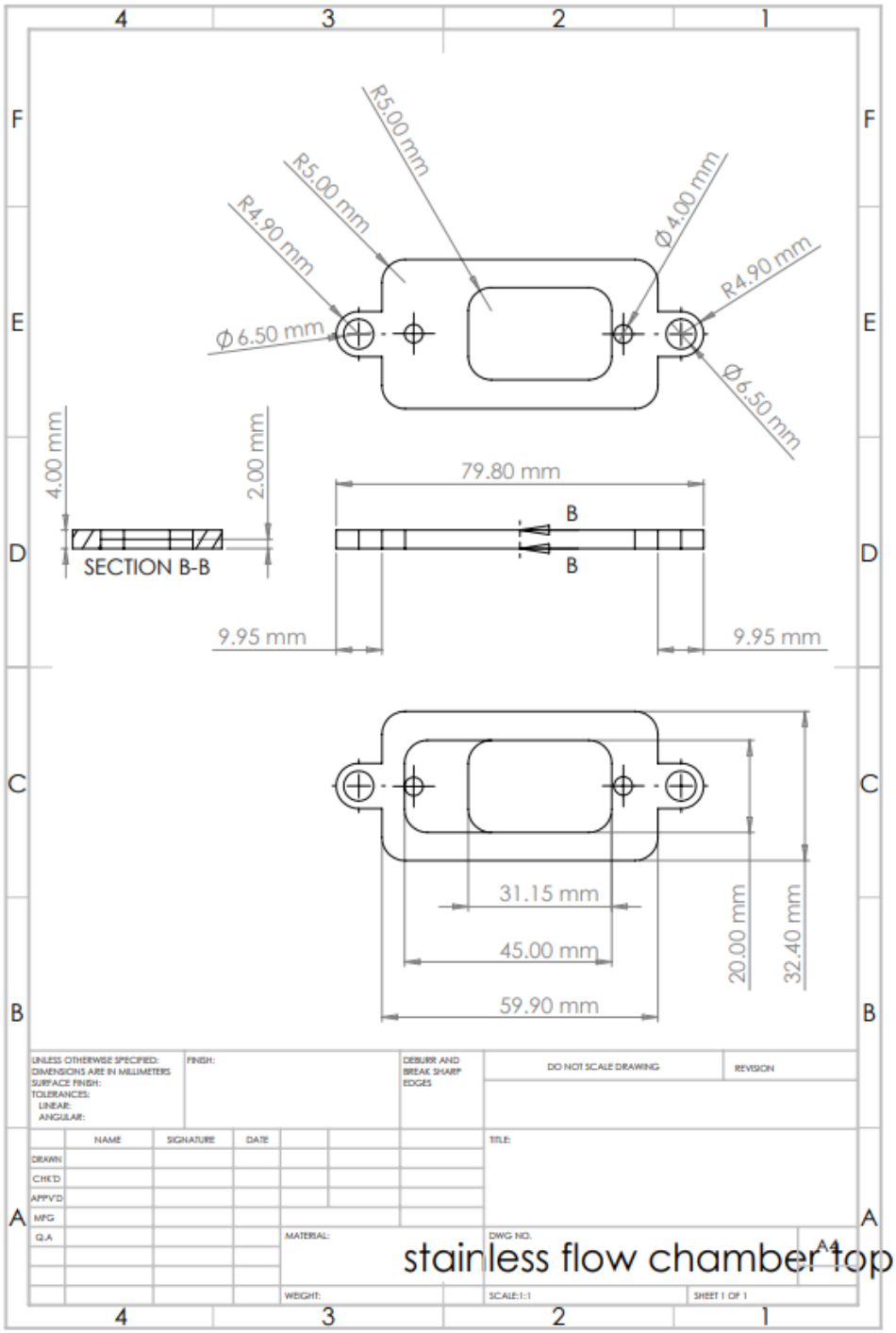

Figure 6.1 - Flow chamber engineering drawings: *Drawing of the flow chamber base (A) and top (B). The drawings were taken to the Lancaster University Engineering Department workshops and produced using precision milling to a tolerance of +/- 10 µm.*

As can be seen in Figure 6.2 the slide is clamped in the flow chamber by the flow chamber top being bolted to the flow chamber bottom (dashed lines showing bolt positions). Once secured, the slide is in a position for the flow to be pumped through a 5 mm diameter tube placed in the 4 mm diameter holes (producing an interference fit, holding the tubes in place) in the flow chamber top. The end providing the liquid has a small 4 mm wide trough (with 2 mm radius ends) in the flow chamber bottom (shown in Figure 6.1), this is to ensure that the end of the tube isn't crushed or pressed flush with the flow chamber bottom surface, potentially impeding the flow from the tube or providing pressure to eject it from the hole in the flow chamber top. The returning tube is then placed in the reservoir at the other end of the flow chamber base, a 9 mm wide and 8 mm deep trench that collects the fluid, providing a pool that ensures the tube is fully submerged when removing the fluid from the flow chamber, avoiding the production of bubbles within the flow. The flow provides an opportunity to regulate the temperature within the flow chamber, with the tubing being submerged in a heat bath, increasing the temperature to 37 °C, a key aspect of live-cell and unfixed Raman analysis. Another biological consideration for the cells in the maintenance of 5% CO_2 in the atmosphere, replicating the slightly higher CO_2 levels experienced *in vivo*, is critical to live-cell Raman. For proof-of-concept studies, a rudimentary plastic cover will be used to provide CO_2 to the flow chamber opening, however, the further development of CO_2 control will be an objective for the next stages of development, where unfixed analysis will be used for proof-of-concept. Unfixed Raman spectroscopy draws a distinction between the analysis of cells that are analysed within an incubation chamber (maintaining 37 °C and 5% CO_2) within the Raman spectroscope and those taken from an incubator and analysed without fixing prior to cell death. The studies will initially use unfixed Raman spectroscopy, as the CO_2 levels and temperature are not controlled with tight enough tolerances to constitute true live-cell Raman analysis. Sterilisation of the tubes will be carried out by pumping 70% alcohol through the tubes, followed by deionised water to remove the alcohol, and finally, culture media, which will be replaced with fresh culture media

for the cell experiments, to avoid dilution of the media. The flow chamber itself can be autoclaved or submerged in 70% alcohol.

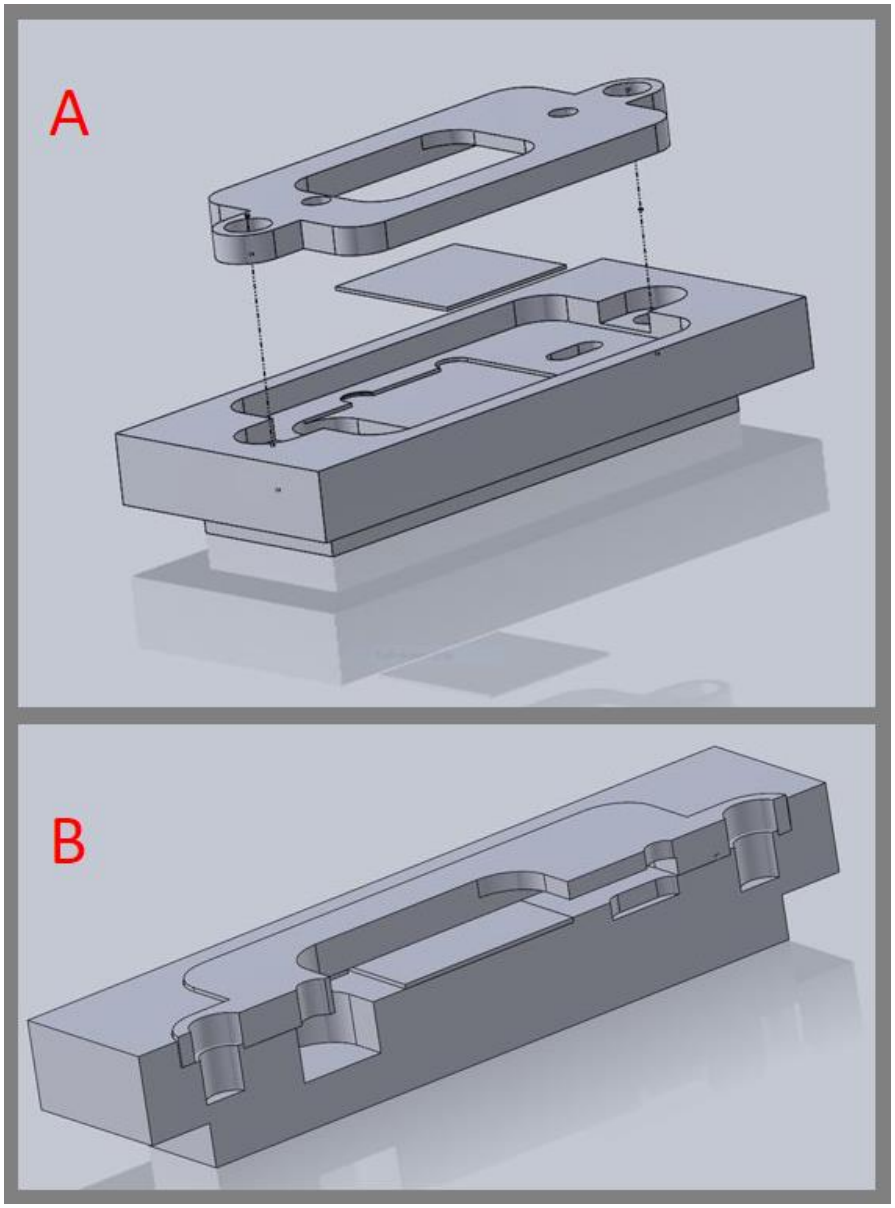

Figure 6.2 - Flow chamber 3D computer aided design images: *A) How the base, slide, and top fit together and the fluid path shown in a cut through image (B).*

The material selection for the flow chamber is reliant on factors already discussed, such as the ability to sterilise, using either alcohol or an autoclave. The weight of the flow chamber is also a key consideration, so the Raman stage can support the flow chamber without having movement inhibited for focusing and Raman mapping, or even damage to the stage through overloading. Stainless steel was chosen as a material resistant to corrosion and able to be sterilised in an autoclave and alcohol. Testing was required to ensure the weight of the flow chamber did not deteriorate the capacity of the spectroscope to produce maps, with aluminium an alternative if so. Stainless steel is resistant to oxidation or corrosion, which could contaminate the culture media and lead to flow chamber damage due to the fluid flowing through it. Design considerations for the fluid required enough depth to fully submerge the sample, and to provide enough fluid depth for the immersion objective to work at its correct depth of focus. The design had to make it impossible for the flow chamber, once set up correctly, to be unable to pump the fluid over the height of the chamber into the Raman stage and equipment. The design accounts for this by using a single tube for the supply and removal of the fluid, taking the fluid from the flow chamber, through a heat bath, through the pump, and back to the other end of the flow chamber. The use of a single tube means that if a pump malfunctions, the input of fluid is inherently stopped alongside the removal.

6.2.2. Flow chamber testing

Advantages of using a flow chamber include reduced thermal damage to samples and dynamic supply of biochemical factors to cells, more closely matching the in vivo environment were flow supplies cells with factors alongside physical stimulation. The experiments were broken into two phases. The first experiments determined if the flow chamber could successfully be used within the Raman equipment to collect Raman spectra, Raman maps, and volumetric Raman maps and if so, allow the next section to demonstrate the benefits of flow Raman analysis. The second phase determines if the flow chamber could successfully provide living cells with a

biochemical factor, with dithranol provided in the flow after an hour and mapped within the cell.

Test 1: Collecting a Raman spectrum and maps in two and three dimensions.

The first check was that the flow chamber did not introduce some unexpected contamination that would distort or destroy the collection of Raman spectra. Figure 6.3 (B) shows the first Raman spectrum of OrmoComp^{TM} collected in a flow chamber of this kind (after pre-processing). Next, potential problems resulting from the increased collection times for mapping and VRM were checked. Figure 6.3 (A) shows that flow does not move the sample during map collection by mapping an arrow designed OrmoComp^{TM} scaffold. Figure 6.3 (A) shows the arrow shape is retained when a 1×1µm resolution is used under flow conditions, demonstrating that the fluid flow does not destabilise this sample type during mapping. The next phase of the test checked the sample remained stable during VRM and that the flow chamber weight did not impede the VRM vertical movement. A 5 µm z-step and 2×2 µm lateral resolution were used to collect a VRM of a similar arrow scaffold shown in Figure 6.3 (C). The slice relating to the arrow is shown in Figure 6.3 (E) compared to a white light microscope image in Figure 6.3 (D). The arrow shape is again retained, with reduced image clarity, as expected from a reduced-resolution image. The ability of the Raman microscope to map polymer samples in two and three dimensions was determined by these initial tests. A key advantage for polymer samples would be to reduce thermal damage, especially for 3D Raman mapping with the inherently larger number of collections per area than conventional Raman mapping increasing the probability of thermal damage. Determining the capacity of the flow chamber to analyse 3D printed polymer samples justified the next phase of testing examining the suitability of the flow chamber for mapping single cells.

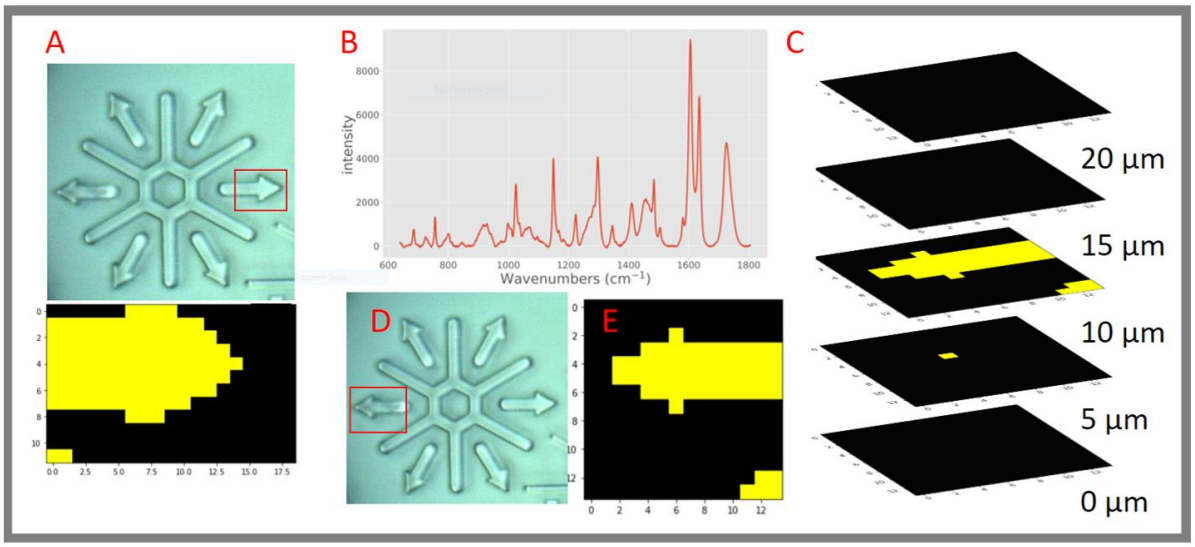

Figure 6.3 - Flow chamber initial testing: *Testing the flow chambers capacity to collect a Raman spectrum (B), a Raman map (red box showing 18 × 11 µm mapped area), and a VRM (C-E) under fluid flow conditions. Pixel counts (x and y axis) in A, C, & E, are in µm, with the mapped area shown in E (red box – D, showing a mapped area of 13 × 13 µm)*

Test 2: Collecting a Raman spectrum and maps of cells in two and three dimensions.

Having ensured the capacity of the flow chamber to map samples, the next test was to test whether the fluid flow did not wash fixed cells of the slide surface whilst producing two or three-dimensional Raman maps. In Figure 6.4 (B), a white light microscope image of a HaCaT cell and Raman maps (1×1 µm) the Raman intensity for each pixel for the 1330-1350 cm^{-1} protein region in green 6.4 (A) and 775-790 cm^{-1} nucleic acid in blue 6.4 (C) were initially produced in the test respectively. Figure 6.4 (D) shows a Raman map of two HaCaT cells, visualised using k-means cluster analysis qualitative shading. Three clusters relate to the cells, and one relates to the background, each shaded based on the average spectrum for each cluster. The averaged spectrum for each cluster is shown in Figure 6.4 (G) where the blue line relates to the blue cluster in Figure 6.4 (D), coloured blue in keeping with the shading

conventions in previous chapters, relating to nucleic acids (775-790 cm^{-1}). The high nucleic acid Raman peak shown on the average spectrum indicates the cluster is probably associated with the position of the nucleus.

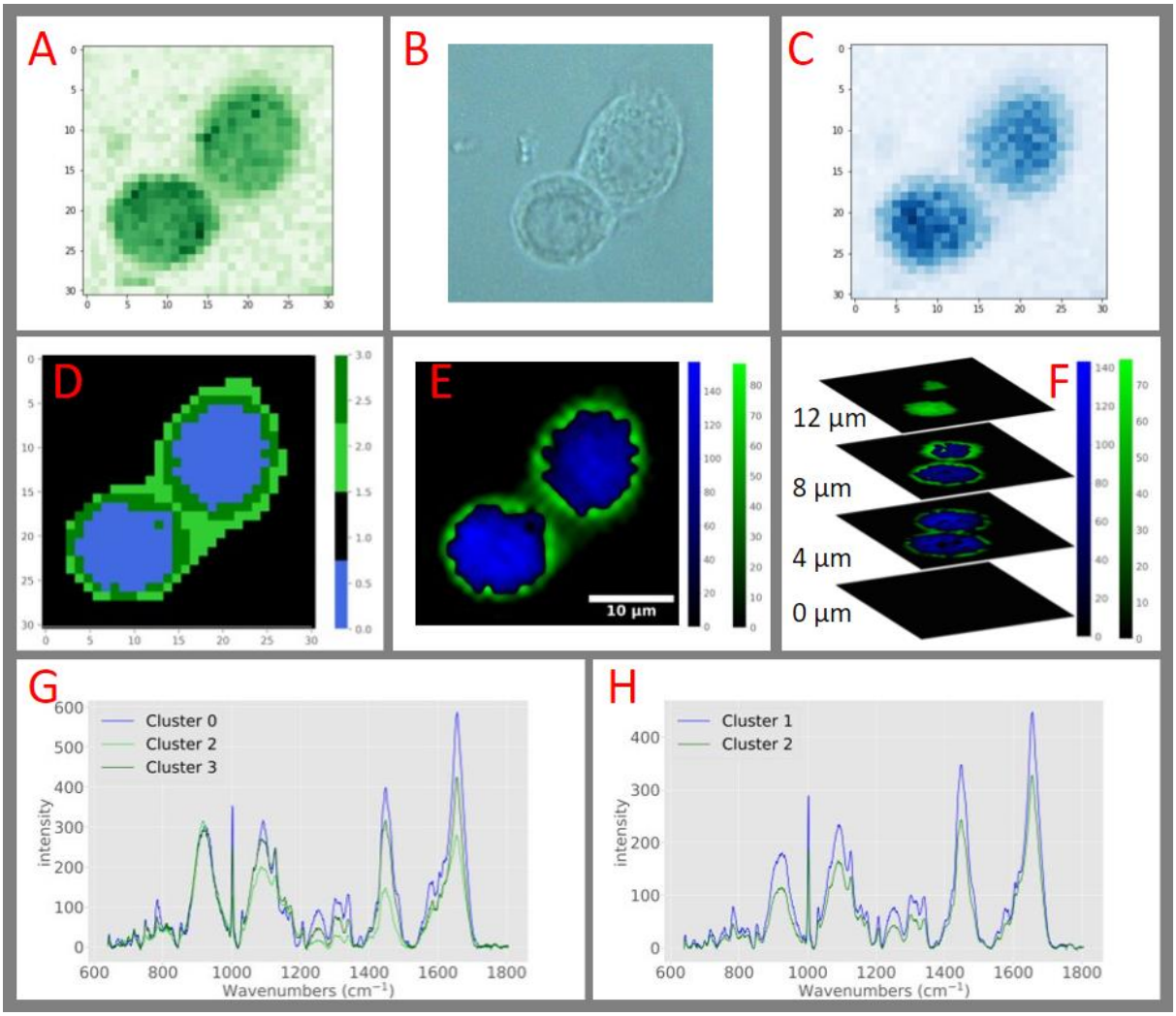

Figure 6.4 - Biological testing of the flow chamber: *A white light microscope image for Raman map verification(B), showing the mapped area (31 × 31 µm) in A and B. 1330-1350 cm^{-1} protein (Green - A), 775-790 cm^{-1} nucleic acid (Blue - C), k-means (D), and k-means directed shading (E) Raman maps. The average spectra for the k-means directed shaded Raman map (G). K-means directed shading of a VRM z-stack (F) alongside the averaged spectra for the VRM clusters (H). Pixel counts (x and y axis) in A, C, & D, are in µm*

Two clusters are associated with the cell body, where the nucleic acid peak is present but less prominent in the average spectra relating to the cell body, where the green spectrum relates to the dark green cluster and the red spectrum to the light green cluster, providing greater contrast in the plot. Figure 6.4 (E) therefore demonstrates that k-means directed shading from Chapters 3, 4, and 5, are possible within the flow chamber. The cell having not been washed off from the slide in the two-dimensional mapping (Figure 6.4 (E)) or when the mapping was repeated for the same two cells using VRM, the slices shown in Figure 6.4 (F). Repeating the mapping on the same two cells is important to show that they remained attached to the slide for a considerable amount of time and repeated maps. The repeatability research goal from Chapter 5 is also reinforced, achieving the goal stated in the conclusions to map cells off a scaffold using k-means directed shading of a z-stack, with the average spectra for the VRM clusters shown in 6.4 (H).

Test 3: Flow reduction in UV degradation

The third test explored the ability of the flow to reduce thermal damage in polymer samples. Figure 6.5 (A & B) shows the flow chamber set-up with polystyrene beads attached to a stainless-steel slide. A 244 nm ultraviolet laser, selected as the most damaging laser wavelength available, is focused on the bead, and ten collections were made in the same position, repeated five times for each analysis state. Figure 6.5 (C) shows the gradient of a Raman peak where the bond is breaking (the peak is reducing with greater laser exposure). The red line (still water) has the steepest gradient, showing that the bond breaks at the fastest rate without the flow. The blue line, showing the gradient for fluid flowing over the sample has the next steepest gradient, showing that the flow does reduce the rate at which the bond is broken through laser exposure. However, thermal degradation is only one potential cause of the bond breaking, for example, if the bond is breaking due to photodamage, the altered rate may result from the flow changing the laser focus. To control against photodamage, the flow analysis was repeated, except at a lower temperature. The black line relates to the set-up shown in Figure 6.5 (B), where the water tube is

placed in a box of ice as the water is pumped into the flow chamber. The temperature of the water was measured to drop from room temperature (22°C) to 10°C. The reduction in temperature further lowers the rate of degradation, with the lowest gradient relating to the black line. The reduced gradients in the blue (flow) and black (cooled flow) result in the conclusion that the degradation does relate to temperature and that the flow does reduce thermal damage. Figure 6.5 (C) shows that cross-linking can be reduced in the flow chamber, with the gradients showing the degradation of the 960-1040 cm^{-1} (benzine ring [180]) spectral peak, where this time the still water (red) results in the greatest rate of cross-linking, then flow (blue), and cooled flow (black) resulting in the slowest rate of cross-linking.

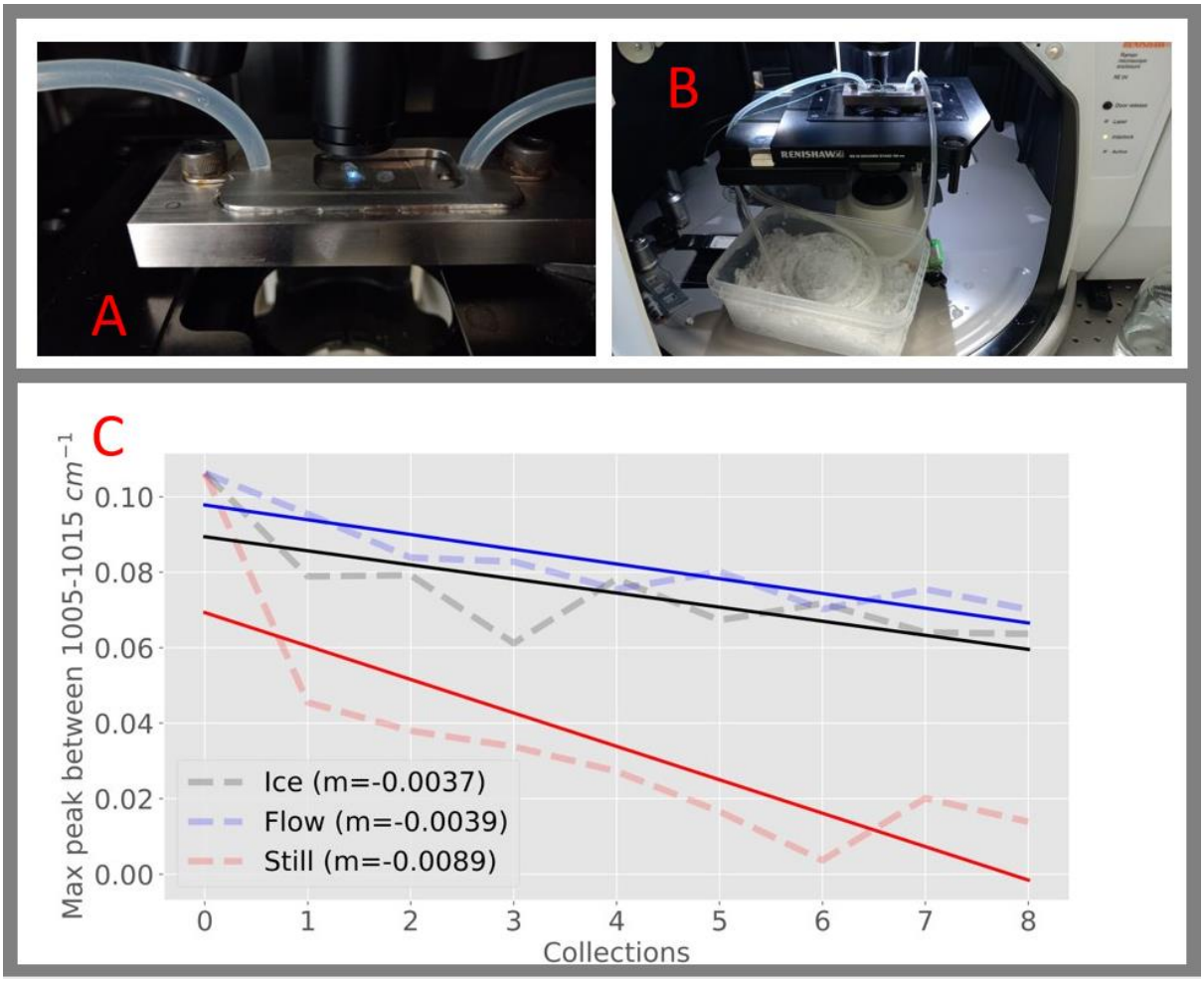

Figure 6.5 - Testing flow chamber cooling: *Focusing on the polystyrene bead in the flow chamber (A), using ice to cool the fluid, and the different cooling rates (C) for ice cooled fluid (Ice - black), uncooled fluid flow (Flow – blue) and still fluid (Still – red).*

6.3. Results and discussion (Part 1: Fixed cell verification)

Having tested the capacity of the flow chamber to map both polymer and cell samples in section 6.2, the ability of the flow chamber to provide drugs and factors to the cells within the flow chamber, and the ability of the Raman spectroscope to analyse and visualise the changes produced in the cell will be the focus of the remained of the chapter.

6.3.1. Fixed cell analysis of dithranol-exposed HaCaT cells

Dithranol has previously been mapped inside cells using the 598-615 cm^{-1} Raman peak [5], with the cellular response to the drug being shown over 22 hours. Being able to visualise the drug within the cell provides a key advantage to a study verifying the capacity of the flow chamber to deliver a drug, that by mapping the cell before and after flow drug exposure, the difference can be easily observed. To provide a baseline analysis, Figure 6.6 shows a VRM of a HaCaT cell that has been cultured for 3 hours in media with 2 µM dithranol and fixed, with a white light microscope image (Figure 6.6 - B) for comparison. The cell was cultured for two days before the dithranol exposure, a measure taken for the flow analysis to provide cells with the greatest opportunity to securely fix to the slide surface, providing continuity with the unfixed analysis (section 6.4). Figure 6. 6 (A) shows the dithranol (red) in the cellular matrix that the cell is sitting in, using the 598-653 cm^{-1} range reported by Aston et al [5]. However, dithranol is also visible within the cell. A narrower WiRE^{TM}-produced VRM is shown in Figure 6.6 - C), demonstrating that the presence of dithranol can be visualised through a cell without mapping the entire cell; a potential method of speeding VRM for unfixed or lice-cell Raman. The VRMs (Figure 6.6 – A & C) confirm the presence of dithranol inside the cell (and that it can be visualised), therefore justifying further exploration/stages and confirming the findings from [5].

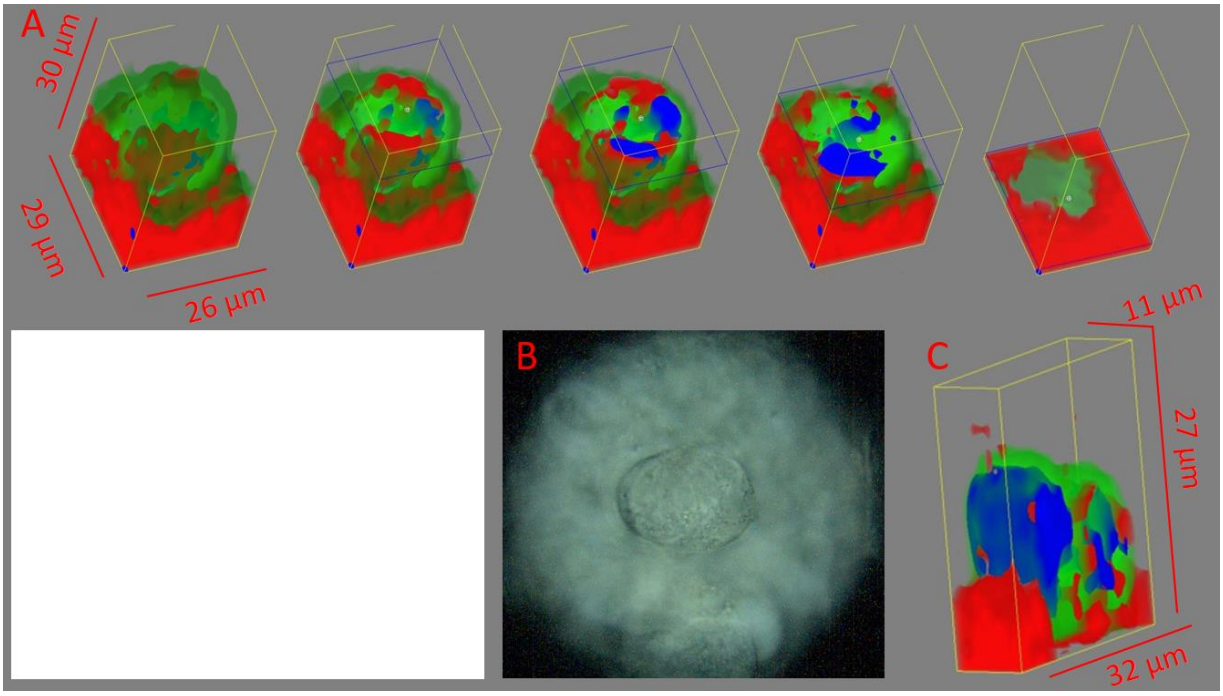

Figure 6.6 - VRM of dithranol exposed HaCaT cell: *Showing a lateral cut through cross-section through the height of the cell (A), a white light microscope image of the mapped cell (B), and a (laterally) thinner VRM of the cell (C).*

6.3.2. Fixed cell analysis score plots

In Figure 6.7 the principal component analysis (PCA) score plots provide an unsupervised method of visualising differences detected between the cells exposed to different dithranol concentrations, shown for principal components 1-5 relating to over 90% of the explained variance. The 2.2 µM (blue), 4.5 µM (green), and 9 µM (black) exposed cells are not separated in any of the score plots in Figure 6.7. However, the control cells (red), which relate to cells unexposed to dithranol, are seen as a separate cluster in PC3 vs. PC5 (A), PC3 vs. PC4 vs. PC5 (B), PC3 vs. PC4 (C), and PC1 vs. PC2 vs. PC3 (D). The control cells, which were not exposed to dithranol (red) are shown clustered separately in all the score plots. The clearest distinctions are seen in PC3-5, relating to 7% of the explained variance, indicating that further studies are required where separation is seen between the classes in principal components relating to a greater percentage of the variance; potentially suggesting fewer classes should be compared 9 (as was seen in Chapter 5).

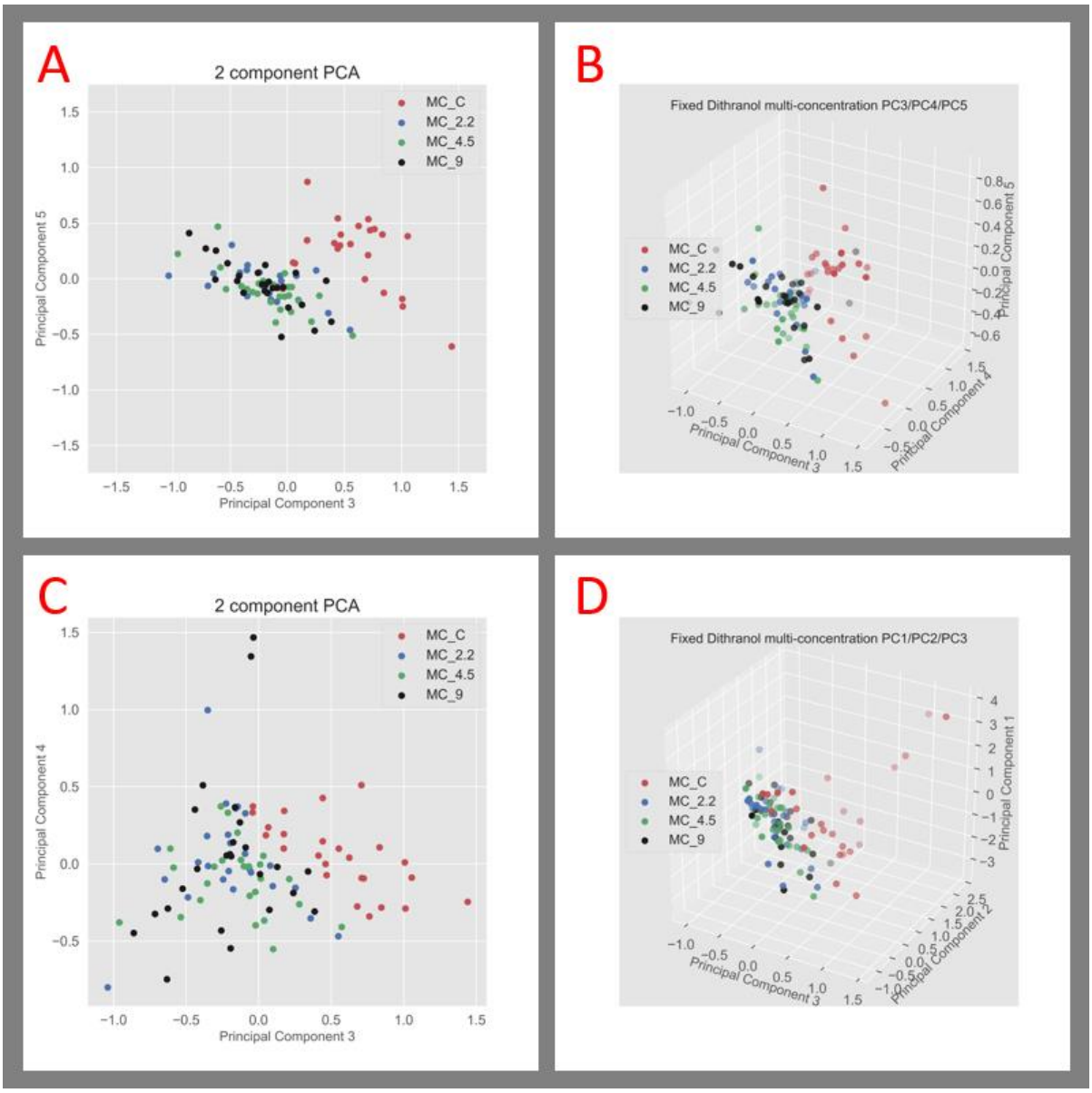

Figure 6.7 - PCA score plots for varied dithranol concentration: *Points coloured 2.2 µM (MC_2.2 - blue), 4.5 µM (MC_4.5 - green), 9 µM (MC_9 - black), and (0 µM) control (MC_C - red) for all score plots. PC3 vs. PC5 (A), PC3 vs. PC4 vs. PC5 (B), PC3 vs. PC4 (C), and PC1 vs. PC2 vs. PC3 (D). MC relating to multi-concentration.*

6.3.3. Fixed cell analysis loading plots

Figure 6.8 shows the loading plots for the three principal components used in Figure 6.8, showing the loading plots for PC1 (A), PC2 (B), and PC3 (C). Dithranol is shown

to have a significant influence on maximising the variance within the dataset, with the highest loading peaks in principal components 1 and 2 being the 589 cm^{-1} peak related to dithranol (red arrows). The high loadings for dithranol result from three of four classes are dithranol exposed. The dithranol concentration was also increased to 4 times that used in a previous study looking at Raman mapping of dithranol in cells [5] in the highest dithranol concentration class (MC_9). The other highly loaded 1178-1179 cm^{-1} and 1469-1471 cm^{-1} peaks are not only seen in more than one principal component but are also seen in the later PCA loading plots for unfixed cells (shown in blue arrows).

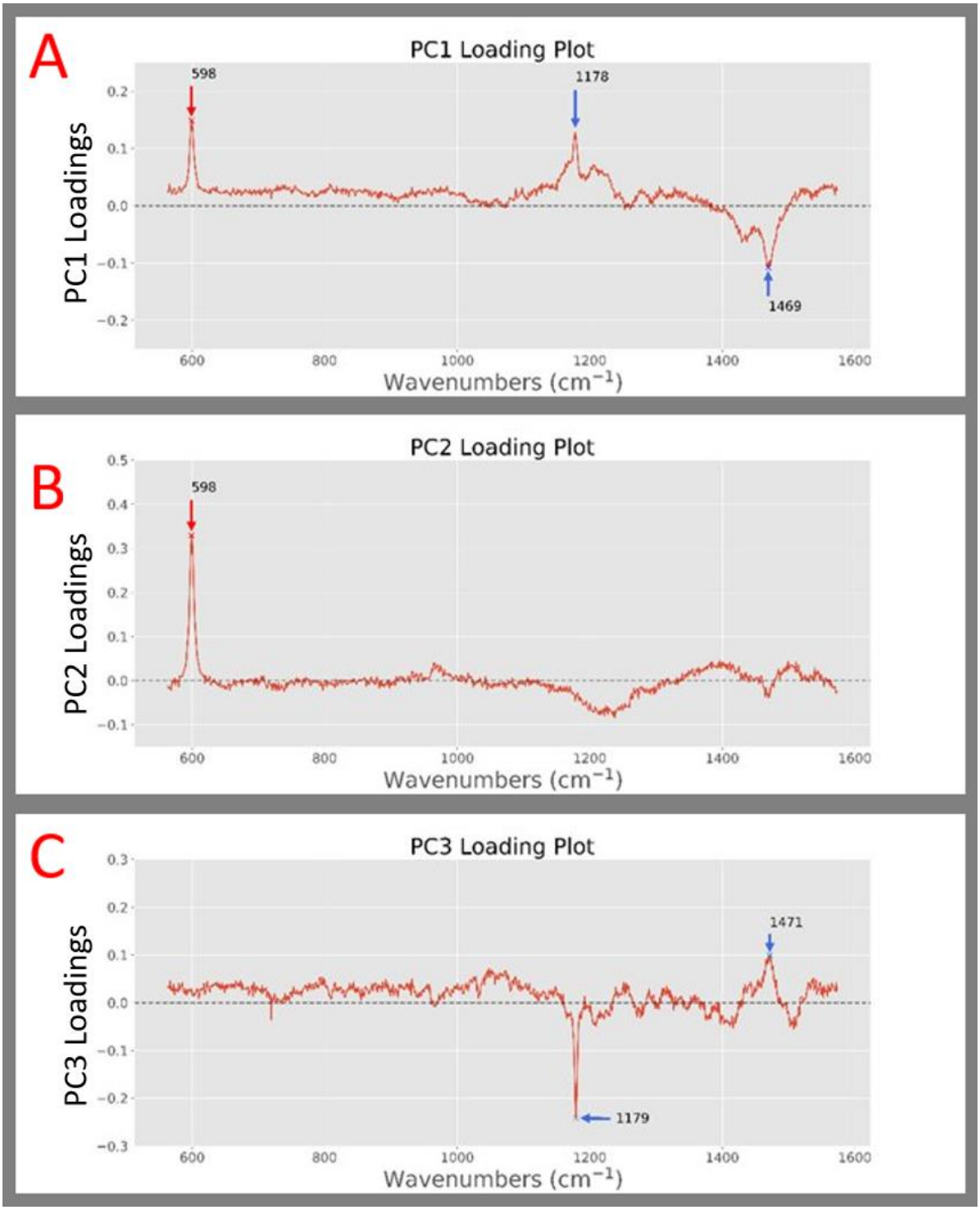

Figure 6.8 - Dithranol concentration loading plots: *Loading plots for PC1 (A), PC2 (B), & PC3 (C) from the principal component score plots in Figure 6.7, highlighting the 598 cm-1 (red arrow), and the 1178-1179 cm-1 and 1469-1471 cm^{-1} peaks (blue arrows).*

The 1178 cm^{-1} peak in the positive loadings of PC1 and 1179 cm^{-1} in the negative loadings of PC3. The 1160-1180 cm^{-1} region has many associations with proteins [110], with the 1161 cm^{-1} Raman peak identified as relating to proteins in Chapter 5 [172]. The 1175-1180 cm^{-1} region also has references linking it to nucleic acids [169], [181], Raman mapping of the distributions will be used in further investigation (Figure 6.9). The 1469 cm^{-1} peak has a high loading in the negative loading of principal component 1 and 1471 cm^{-1} the negative loading of principal component 3, the 1470 cm^{-1} region was associated with proteins and lipids in Chapter 5 [110], [170], which could indicate changes in the cell cytoplasm. In their study, Ashton et al [5] observed the dithranol initially (hours 0-6) located in the outer regions of the HaCaT cells they were mapping. The adaptation of lipids and proteins, molecules constituting large parts of the cytoplasm, would naturally be affected within the two-hour timeframe of this experiment, with the dithranol also seen in the cytoplasm in Figure 6.6.

6.3.4. Fixed cell univariate mapping comparison

Figure 6.9 compares the univariate maps of the wavelengths indicated by the PCA loadings in Figure 6.8. A univariate map of the 775-790 cm^{-1} Raman peak (Figure 6.9 - A) provides an indication of the nucleic acid distribution within the cell, a standard method used to locate the probable location of the nucleus throughout the thesis. Comparing the 775-790 cm^{-1} map with the 598 cm^{-1} map (Figure 6.9 - D) shows that the dithranol is outside of the high nucleic acid intensity region, matching the observation of Ashton et al [5] for this time point (2 hrs). the 1178-1179 cm^{-1} map (Figure 6.9 - B) has high-intensity regions more closely overlapping with the nucleic acid (775-790 cm^{-1}) high-intensity regions, suggesting that it may be linked to nucleic acids rather than proteins. The combination of the similar spatial distribution and Raman intensities for the 1178-1179 cm^{-1} (B) and 775-790 cm^{-1} (A) maps will result in 1178-1179 cm^{-1} Raman peak being assigned to Cytosine, guanine, and adenine [169] and coloured blue (Figure 6.9).

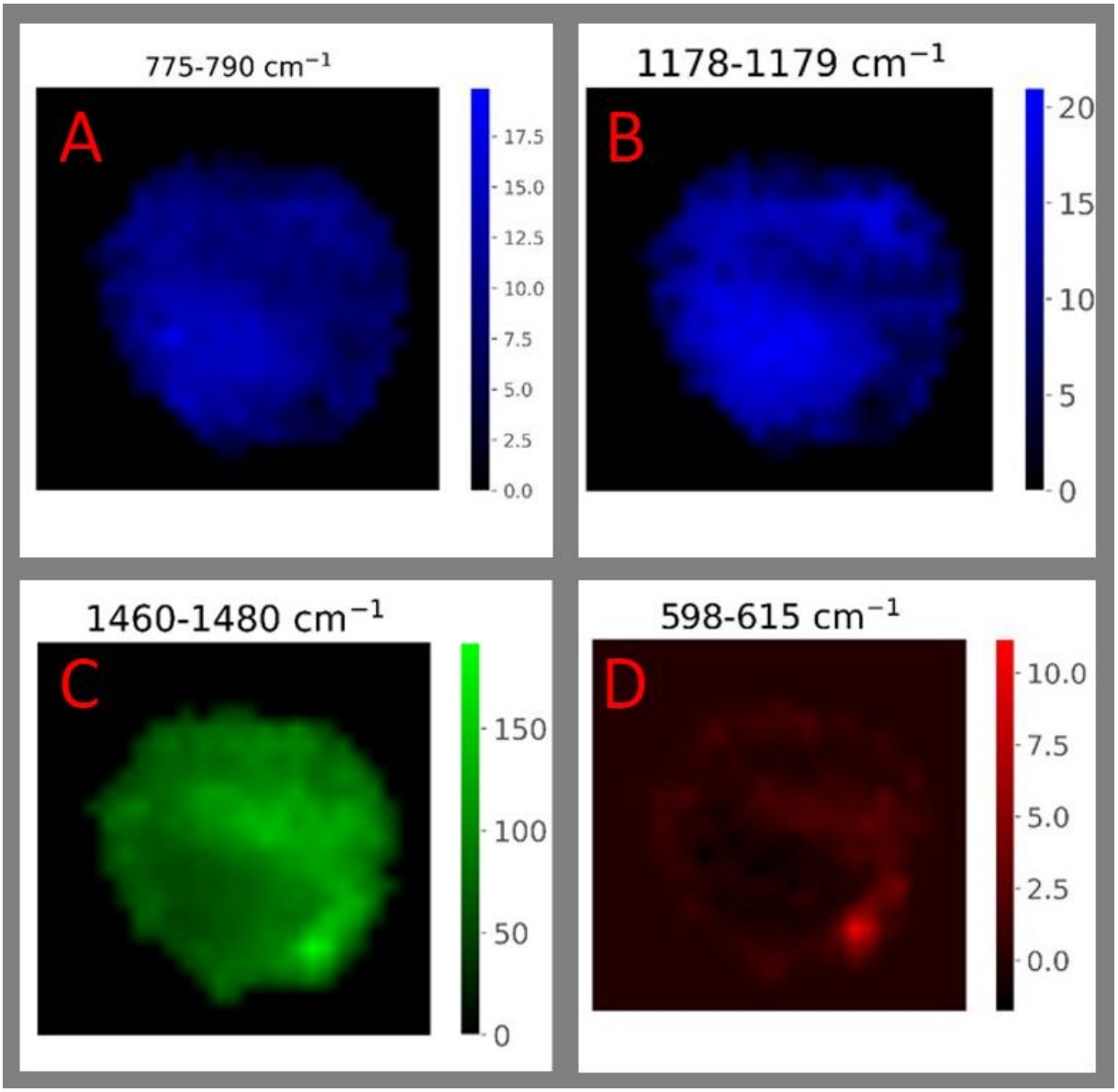

Figure 6.9 - Low(uni)-feature Raman maps of PCA highlighted Raman peaks: *Comparing the known nucleic acid 775-790 cm^{-1} region (A) map against the 1178-1179cm^{-1} Raman map and mapping the 1460-1480 cm^{-1} and 598-615 cm^{-1} loading plot highlighted peaks from Figure 6.8. Map dimensions: 26 × 29 µm*

Conversely, the 1460-1480 cm^{-1} region (Figure 6.9 - C) has significantly higher Raman intensities (over 150) than 1178-1179 cm^{-1} and 775-790 cm^{-1} (both near 20) regions, which matches the spatial distribution of the 598-615 cm^{-1} dithranol map (D). Lipids and proteins are linked to the cytoplasm and the high-scoring regions for the hyperspectral images – where we know that the high-intensity regions for the

hyperspectral images are linked to dithranol (as the most loaded peaks for the first two principal components were the 598 cm^{-1} peak). The 1460-1480 cm^{-1} will therefore be coloured green, which has been used throughout the thesis to indicate the cell body, although it should be noted that the spectral region is also associated with lipids. The different highly loaded peak regions being associated with different physical phenomena are shown in the direction of the loadings (Figure 6.8), with 1178-1179 cm^{-1} and 1469-1471 cm^{-1} peaks always loading in a different direction in principal components one and three respectively.

6.4. Results and discussion (Part B: Unfixed analysis)

Having established that Raman can distinguish fixed HaCaT cells that have been exposed to different concentrations of dithranol, the ability of the flow chamber to replicate the results relating to drug exposure or not can be carried out focusing on replicating the clearest results from the PCA (drug-exposed or not) within the flow chamber. Unfixed Raman spectroscopy will be used during proof-of-concept studies, where suitable results will justify the further development of the flow chamber to provide full live-cell analysis for further development towards an in-Raman environment for the monitoring of bioengineered constructs.

6.4.1. Controlling for cell death

As this is unfixed analysis, defined as analysing cells that are alive but unsupported in terms of 5% CO_2 levels, a control test was carried out to determine if any cell adaptions result from the dithranol exposure instead of cell death resulting from diminished culture conditions. The same procedure was carried out for the control analysis as the flow-supplied dithranol analysis in section 6.4.2. (minus the inclusion of the drug). Initial maps were collected of the cells using phenylalanine-free culture media, the cells were then cultured in the flow of phenylalanine-included media (providing the closest comparison to the experimental method used in section 6.3) for an hour, heated to 37 °C (dropping to 30 °C) through the hour. Phenylalanine-free culture media was then used for Raman mapping of the cells. PCA was used as a commonly used unsupervised method that allows for some interpretation through the loading plots. In Figure 6.10 B, more than 70% of the explained variance is captured in the first three principal components. Neither Figure 6.10 A, plotting PC1 VS. PC2, B (PC1 vs. PC3), nor C showing the three-dimensional plot looking at all three principal components revealed any separation, providing confidence that separation in these principal components in any further studies would result from the exposure of the drug.

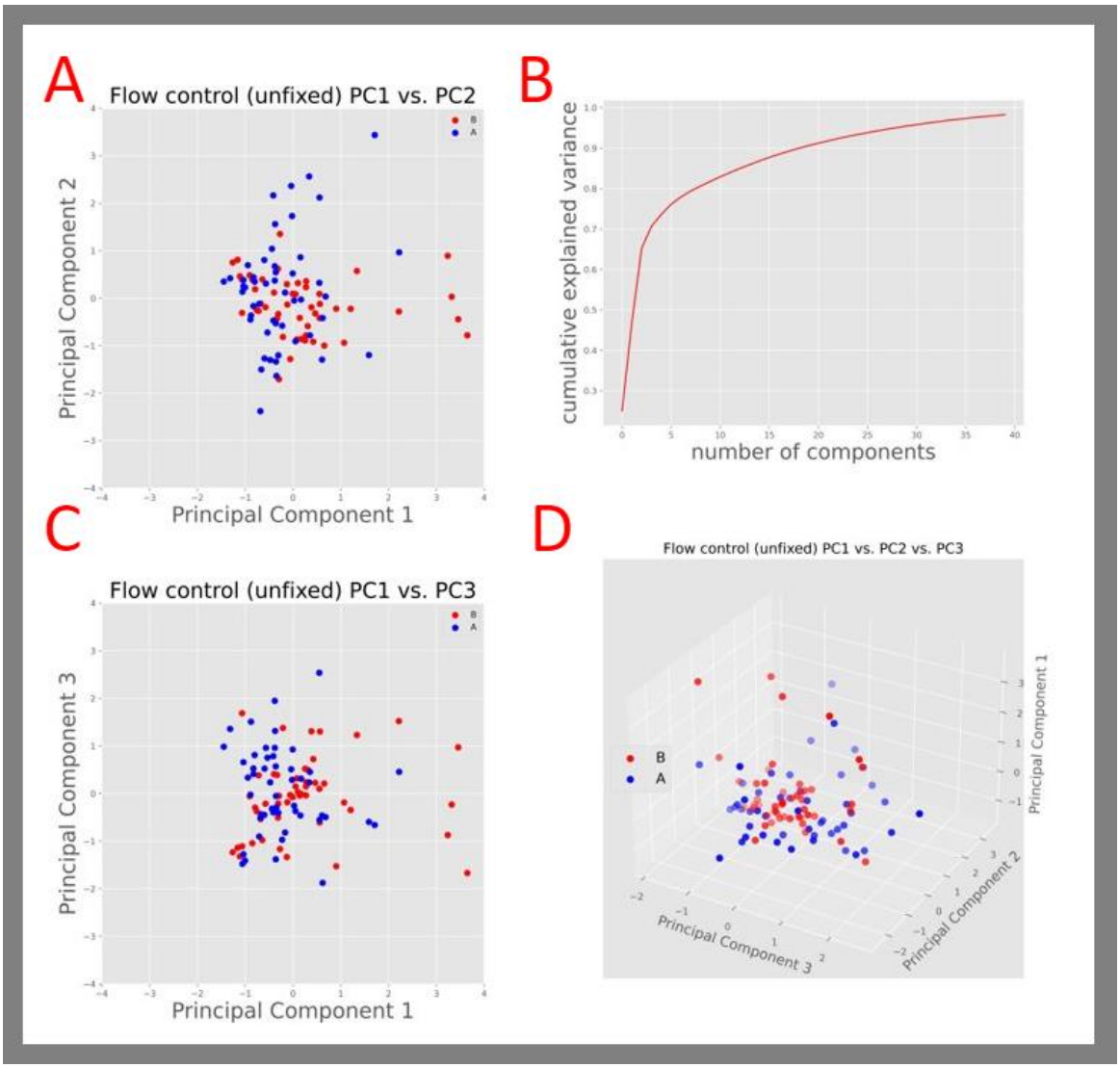

Figure 6.10 - PCA control study: *PCA explained variance chart showing the cumulative explained variance y-axis for each additional principal component (x-axis). Score plots for PC1 vs. PC2 (A), PC1 vs. PC3 (C), and PC1 vs. PC2 vs. PC3 (D), with red relating to collections before flow (B) and blue being collections after flow (A) for all three score plots.*

6.4.2. Flow supply to cell

The same process was carried out as described in section 6.4.1., except with the addition of 4.5 µM of dithranol with the phenylalanine-included media. The maps were again collected in the phenylalanine-free media. Figure 6.11 C shows the first three principal components of the dataset produced from the flow-supplied dithranol cells representing nearly 80% of the explained variance. Figure 6.11 A, B, and D show clear separation of the clusters for the same principal components used in section 6.4.1., where no separation can be seen. The concentration of Dithranol used in the experiment (2 µM) was shown to have a significant effect on cells in section 6.3. The separation between the drug-exposed and unexposed cells would therefore perhaps be expected, however, this study aims to show that the flow chamber can support unfixed cells well enough to take up drugs, it is strong evidence that the flow chamber has achieved that goal. Especially when paired with the control in section 6.4.1., where no such separation was achieved under the same conditions except for the presence of the drug. The swapping of the media provides another advantage, as the phenylalanine-free media is not contaminated by the drug, showing that any signal relating to the drug is that which the cell has retained.

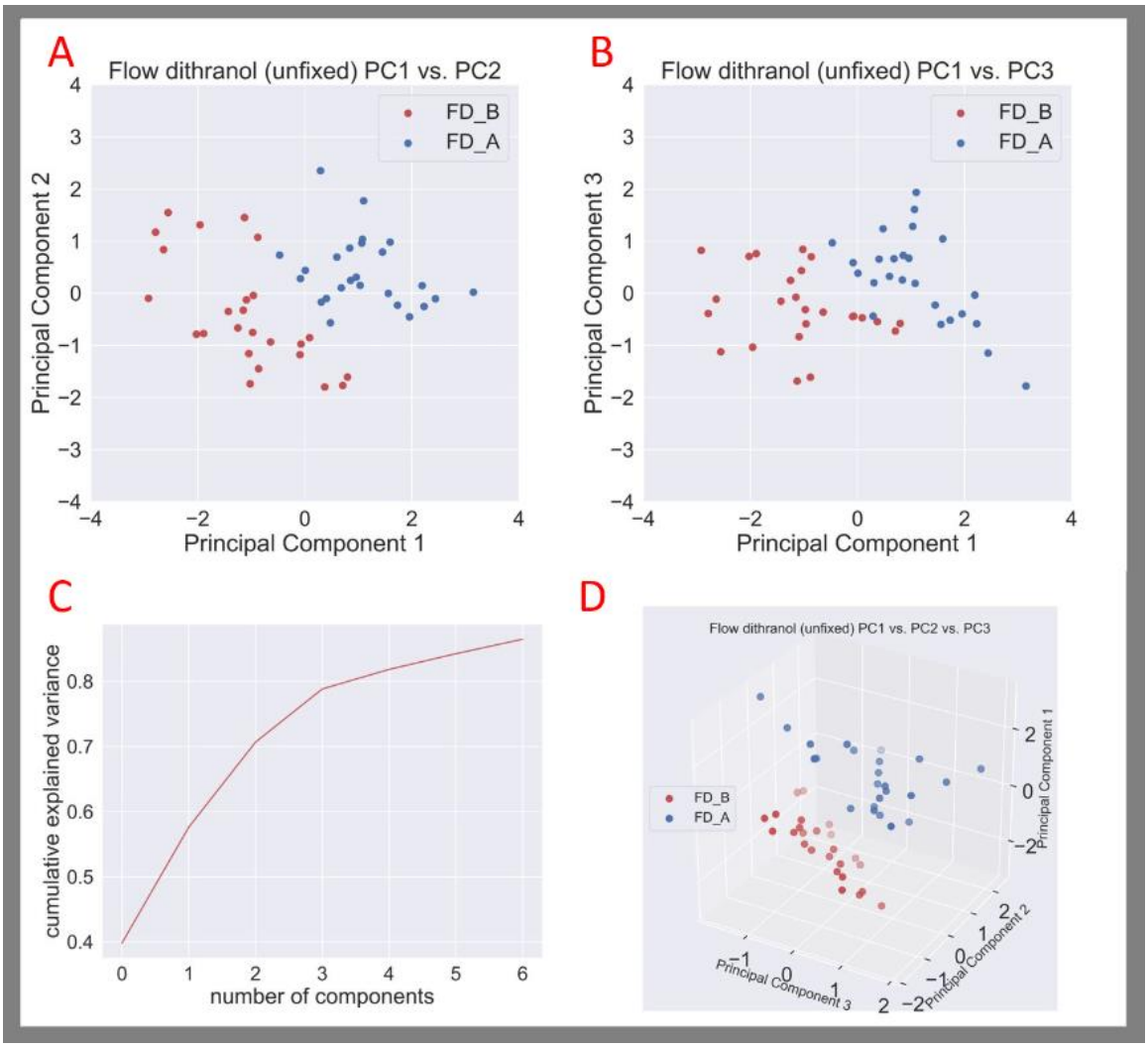

Figure 6.11 - Flow chamber supplied dithranol: *PCA explained variance plot (C). Score plots for PC1 vs. PC2 (A), PC1 vs. PC3 (B), and PC1 vs. PC2 vs. PC3 (D), where red = before flow supplied dithranol (FD_B) and blue = after flow supplied dithranol (FD_A).*

Figure 6.12 below shows the loading plots (PC1 – A, PC2 – B, & PC3 – C) for the PCA score plots in Figure 6.11 above. Key spectral peaks from section 6.4 (fixed cell analysis) are present in all three principal components, such as the 1178-1179 cm^{-1} region relating to nucleotides and 1462-1479 cm^{-1} region (proteins and lipids). Similar peaks occurring in the loading plots suggest that some of the same molecular adaptations are occurring in the unfixed cells. An absent peak from the loading plots for the unfixed cells is the 598 cm^{-1} Raman peak, which was a prominent positive loading in principal components one and two for the fixed cells. The loss of the dithranol Raman peak could be because only one class is dithranol exposed in the unfixed analysis (as opposed to three in the fixed), with higher concentrations also used in the fixed analysis. A range of other peaks is also observed in the unfixed loading plot, potentially showing the benefit of avoiding fixing.

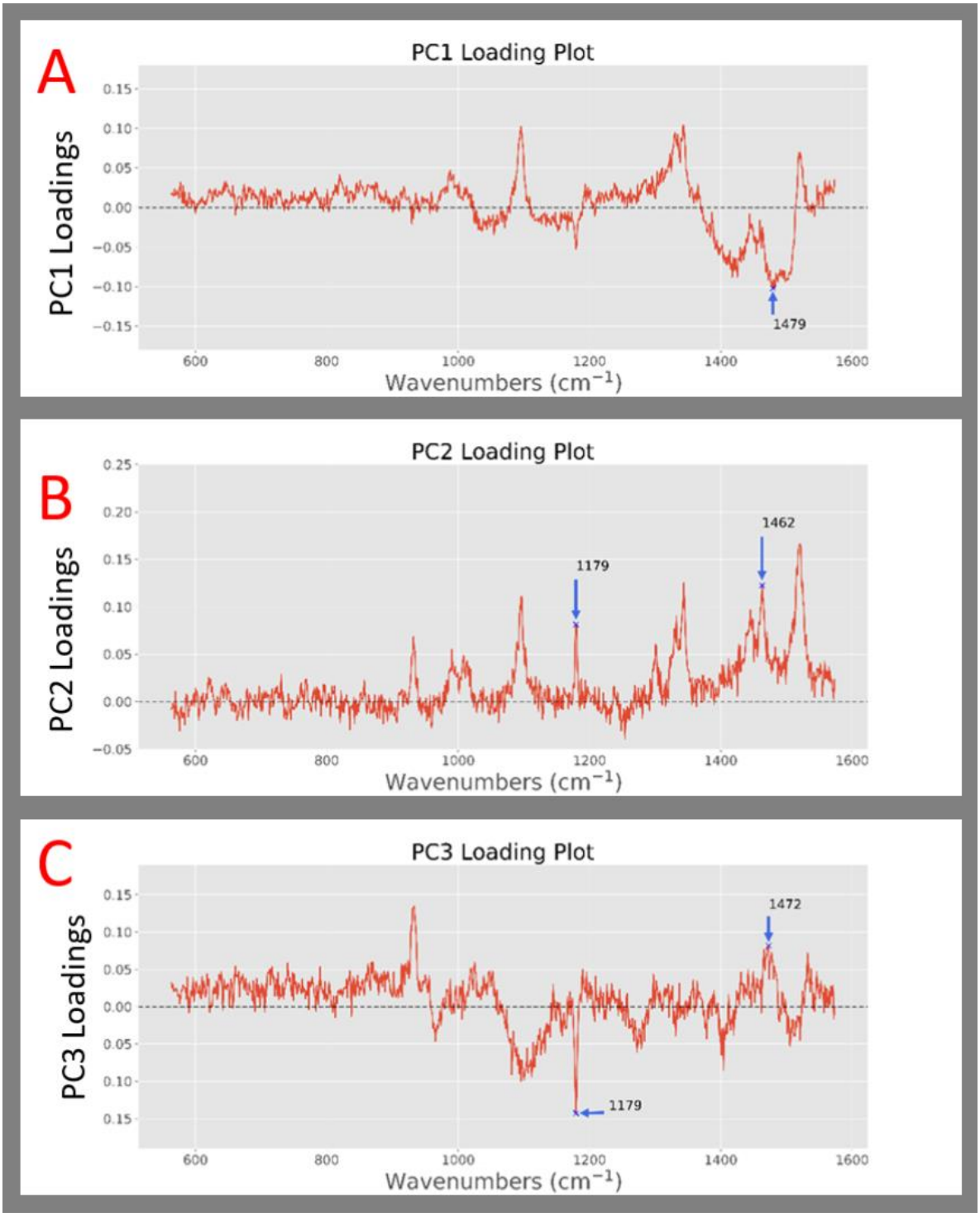

Figure 6.12 - Loading plots flow supplied dithranol (unfixed analysis): *Loading plots for the principal components in the score plots for Figure 6.11, with PC1 (A), PC2 (B), and PC3 (C). Repeated loading peaks from the dithranol concentration (Figure 6.8) highlighted with continued blue arrows on the 1179 cm^{-1} and 1462-1479 cm^{-1} loading peaks.*

6.4.3. Cell visual inspection before and after dithranol flow exposure.

Images provide a more intuitive method of inspection, having shown the response of the cells to flow-supplied dithranol in section 6.4.2., Raman mapping of cells before and after the exposure to dithranol allows for comparison to the images of fixed cells in section 6.3. Having used the WiRE^{TM} VRM for section 6.3.1., where the objective was to simply confirm the presence of dithranol in the cell, this section uses the k-means directed shading to visualise the difference in cell morphology and identify the regions where the dithranol has become concentrated inside the cell. to remove the background to make drawing conclusions easier (from the slices). Figure 6.13 A and B show the k-means clustering images, using qualitative shading and colours uncorrelated with a molecule to reduce the risk of confusion when molecules/colours are assigned to each region using the method described in Chapter 3 (see appendix). Figure 6.13 C and D show the k-means directed shading of each cell. The 598-653 cm^{-1} region relating to dithranol covers the entire cell (appendix), which shows no significant areas of concentration, with the cell only highlighted because the background has been removed. Therefore, no clusters are coloured red (dithranol) in C. C has a region of high nucleic acid which has correlating to the same region as the nucleus, as verified by fluorescence microscopy in Chapter 3. The yellow cluster in the K-means cluster image (A) is therefore coloured blue for nucleic acids in the k-means directed image. The pink cluster in the A relates to a high lipid region, resulting in it being coloured purple in the k-means directed image, with both placed on the 1330-1350 cm^{-1} protein spectral peak, which is high intensity throughout the cell, as has been seen through the project.

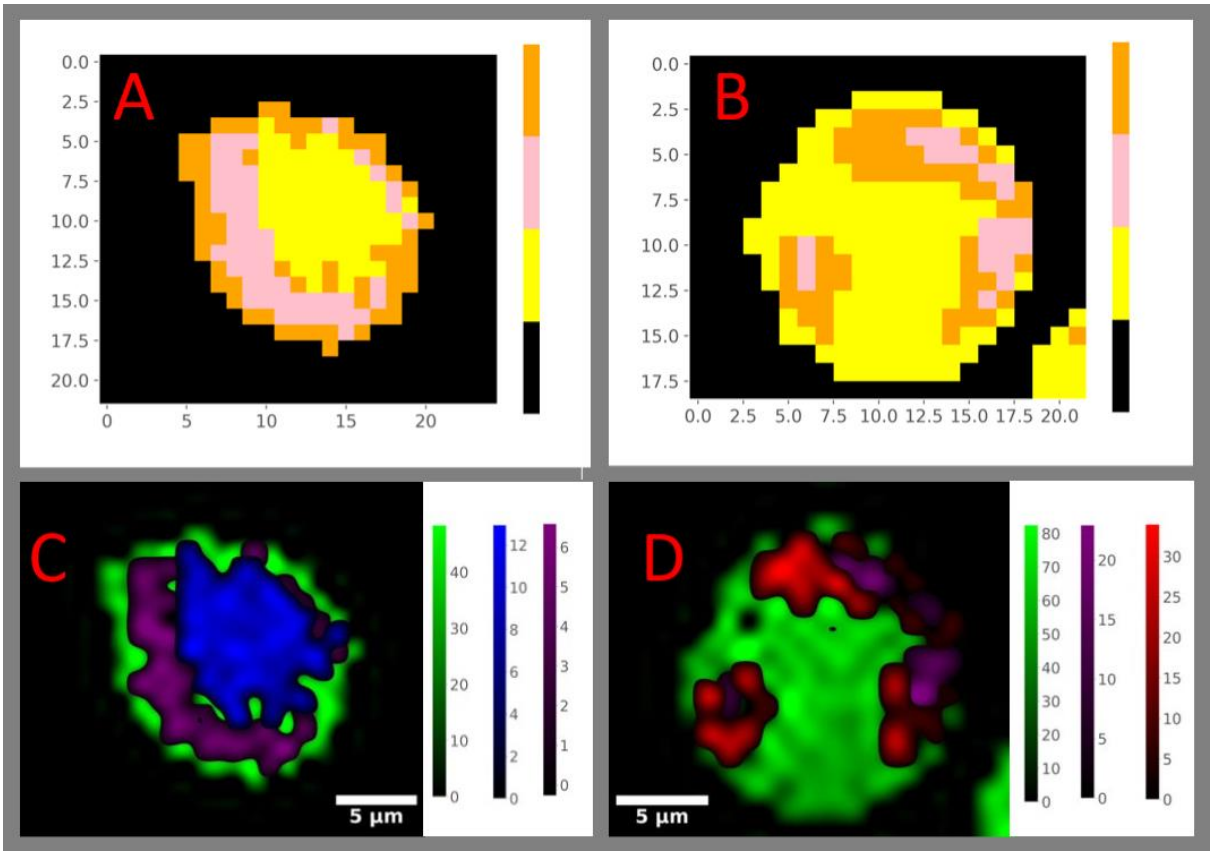

Figure 6.13 - Mapping unfixed cells pre- and post- flow chamber supplied dithranol: *Qualitative k-means shading of HaCaT cell before (A) and after (B) 2 µM flow supplied dithranol exposure and k-means directed shading of the same maps (C=before and D=after). Pixel counts (x and y axis) in A, & B are in µm*

D has a similarly high protein (1330-1350 cm^{-1}) region throughout the cell, although the nucleic acids are not as specifically packed into a region that could be the nucleus (as was seen in chapter 3), therefore no clusters are coloured blue. The orange and pink clusters in B relate to the high dithranol and lipid regions, when the entire cell is inspected (appendix), with a lower intensity region relating to the pink cluster in B. The Orange cluster was therefore assigned red, for dithranol, showing that the drug had concentrated in the lipid-rich region of the cytoplasm, the relatively low nucleic acid region within the image correlating with images in Ashton et al (Ref - 2015), which showed high-intensity regions for proteins and dithranol, with the nucleus becoming increasingly prominent over time (Ashton 2015). The visualisation of the maps proves further evidence that the cells have had the drug supplied to

them by the flow, in the Raman spectroscope, and responded in a similar fashion as to when the drug was supplied to them in an incubator. The clear demonstration justifies the further refinement of the flow chamber design, incentivising the development of a fully live-cell version for the investigation of factors used in the production of bioengineered constructs.

6.5. Conclusion

Supplying a drug (dithranol) in fluid flow more closely replicates in vivo conditions, incentivising the design, fabrication, and testing of a flow chamber that fits within a Raman spectroscope. Dithranol was selected as a drug capable of being Raman mapped within cells [5]. The ability of dithranol to Raman scatter enough to be discerned within the cell has the advantage of highlighting a key focus of this project, combining the morphological and molecular analysis provided by Raman spectroscopy. No flow chamber has previously been designed to facilitate two- and three-dimensional Raman mapping to the knowledge of the authors. Due to the novelty of the flow chamber design, the testing phase of the chapter started with the most basic feature of a spectroscope, to collect a spectrum. Further factors tested included the sample stability for Raman mapping in two and three dimensions, and the capacity of flow and cooled flow to reduce thermal damage in polystyrene beads.

Having tested the capacity of the flow chamber for mapping, fixed cells were initially analysed to ensure dithranol could not only be Raman mapped but could be distinguished from control cells using Raman spectroscopy and PCA. Looking at the dithranol provided an opportunity to clearly show how a molecular signal can be mapped (in 3D) alongside chemometric analysis. The first step of the dithranol analysis was to expand dithranol Raman mapping onto 3D from the previously published two-dimensional mapping [5], allowing the distribution of the drug to be observed through the cell (Figure 6.6); achieving the third chapter aims. Showing

that Raman spectroscopy can distinguish dithranol exposed and unexposed cells in section 6.3 increased confidence that moving onto unfixed cell analysis was possible for analysis of dithranol in HaCaT cells.

An initial study aimed to distinguish fixed cells exposed to different concentrations of dithranol, with score plots shown in Figure 6.7, showing cluster separation between the drug-exposed and unexposed, but not between the different dithranol concentrations. Loading plots were produced for Figure 6.8, and univariate mapping of highly loaded peaks is shown in Figure 6.9, showing the adaptability of the method described in Chapter 3. Inverting the method from using the observation of wavenumber intensity distribution over maps to allocate molecules (colours) to cellular regions, to instead using the method to verify molecular assignments to PCA loading plot peaks. The deeper analysis clarified which loaded peaks related to the drug-affected region of the cell (1460-1480 cm^{-1}). Map comparisons also established that although Chapter 5 assigned the 1161 cm^{-1} Raman peak to proteins, the 1178-1179 cm^{-1} peak was highlighted by the PCA loadings in Chapter 6 related to nucleotides. The fresh media also provided a washing effect for further verification using mapping.

After demonstrating that PCA can separate dithranol exposed from unexposed fixed HaCaT cells, the next step was to investigate unfixed cell analysis. A controlled study was carried out to check that the flow chamber maintains an environment stable enough to avoid altering the molecular composition of the cell. The same planned method to distinguish cells exposed to dithranol and not was employed, except the dithranol was withheld. Maps of cells were collected immediately on immersion in the flow chamber in Dulbecco's Modified Eagle Medium minus (phenylalanine red), followed by 2 hours of flow in full culture media, and finally, the full media was replaced, and the cells mapped again. PCA was then used on the selected spectra, with the aim of separating them into two classes (before and after). Figure 6.10 revealed a lack of separation in the score plot clusters. It is difficult to categorically state that the two classes could not be distinguished, but the lack of separation using this method provides strength to future analyses that see subsequent separation following the change of a single factor (the inclusion of dithranol in this case).

Clear separation of the before and after (drug exposure) classes is seen in Figure 6.11, which combined with the control study in section 6.4.1 provides clear evidence that Raman spectroscopy and PCA can distinguish cells exposed to dithranol in fluid flow; proving the second hypothesis correct. Importantly, once verified, it demonstrates the capacity of the flow to support cells and supply drugs/factors over two hours. The method used, replacing the dithranol-included culture media with fresh culture media before both analyses reduce the possibility that the dithranol influence is in response to the drug in the media. Loading plots were produced and showed continuity in some highly loaded peaks between the unfixed and fixed (Figures 6.8 & 6.12) cell PCA loadings.

Finally, the questions raised by Ashton et al [5] looking for a repeatable and objective shading method are addressed, by using k-means directed shading on the unfixed cells in section 6.4.2. A repeatable and objective mapping method allows for mapping to be used as verification, with increased confidence in the shading and boundaries between sub-cellular regions. The mapping in figure 6.13 provided a check that the HaCaT cells prior to and post dithranol flow exposure exhibit alterations. The mapping in Figure 6.13 also confirmed the drug is present in the post-exposure cell and the cellular response to the drug follows the pattern seen in previous sections and studies [5] and third chapter aims. The molecular adaptations localised around the location of the drug are significant enough that the k-means clustering identifies those regions before the nucleus (Figure 6.13 - D), which was also seen in the fixed cells (Figure 6.13 - C). The drug is again seen around the outer edge of the cell body, outside the region of higher intensity in the 775-790 cm^{-1} Raman map (Figure 6.13), comparable to the distribution seen for the fixed cell VRM (Figure 6.6). Two-dimensional mapping was used for the comparison of unfixed cells as VRM takes too long for cells that can move. Future studies may aim to determine the minimum VRM resolution that provides suitable morphological insight for the given experiment for unfixed or live-cell Raman VRM.

Another area of further investigation would be to see if cell behaviour changes as a result of fluid flow over the cells when they are cultured on different scaffold geometries. Using the VRM to map any change in morphology. Further research

could also focus on full live-cell Raman analysis, developing the flow chamber to control the environmental CO_2 levels, with refined control of the temperature, and automated fluid control. Automation could include varying the fluid flow rate, switching culture media for Raman mapping and extended cell culture, and drug/feature supply. Longer-term goals would be the further refinement of automation of culture conditions for streamlined experiments to include the collection of Raman spectra at given times, although this would require a direct interface with the Raman spectroscope.

Chapter 7 - Conclusions

7.1. Introduction

The purpose of this thesis was to build on research related to critical considerations for a method of monitoring bioengineered constructs or pharmaceutical testing of single cells. Low Raman scattering from water (H_2O) removes the dehydration necessity faced by infrared spectroscopy, providing the opportunity to analyse unfixed or living cells. Previous applications of Raman spectroscopy have previously monitored tissue-engineered constructs [156]–[158], cell stages, stem cells [182], and cell states [183]. The use of a flow chamber for Raman mapping has not been applied to mammalian cells previously. The final goal of the project was to develop an environment within a Raman spectroscope allowing the monitored culture of human cells, providing a platform to both spectrally and morphologically inspect the cellular response to environmental or pharmaceutical stimulation.

By strengthening both the Raman mapping and machine learning analysis, both could be applied in a dynamic environment of a Raman spectroscopy flow chamber, justifying the chamber design, fabrication, and testing. The application of both VRM and machine learning is a combination not previously seen by the author, potentially providing a platform for automated assessment of pharmaceuticals and possible production of immunologically matching organs. The versatility of a combined mapping-chemometric analysis approach was demonstrated through application to both bioengineering and pharmaceutical research questions within this thesis.

Any technique developed for the pharmaceutical industry demands repeatability and structured methods, easily transitioned into a fully calibratable standardised approach. Therefore, before the development of the flow chamber, several technical challenges needed addressing, relating to publications relating to Raman map/VRM collection [7], [40]–[42], shading [5], [6], and machine learning model training [3], [4]. The chapters were ordered to tackle iterative milestones simplifying subsequent

steps and moving toward the end goal of a Raman spectroscope platform for monitoring cell cultures. Working backward from the goal of applying machine learning and VRM to monitor cell cultures within a Raman spectroscope. Developing a platform to analyse cell cultures using Raman spectroscopy within a dynamic environment provides opportunities for temperature control, automated supply of pharmaceutical agents, and closer replication of *in vivo* conditions. But, before developing an entirely new device, bridging known Raman mapping/VRM/machine learning research gaps was critical.

A key outcome of the project was assessing the compatibility of VRM with machine learning classification to monitor cultured cells, requiring the collection of both VRM and machine learning train/test datasets. The need for deeper investigation of machine learning metrics was demonstrated, with the learning curve applied to reveal the training behaviour when different test-train spits are employed to increase confidence that the model is not over-trained. Assessing the repeatability of the machine learning analysis was chosen to be carried out using datasets collected from HaCaT cells cultured on different substrate dimensions (2D vs. 3D) and varied scaffold designs. Exploring cells cultured into different morphologies provided evidence that the method could be used to track changes in cell response to bioengineered scaffolds, alongside an ideal study to establish the computability of VRM and machine learning. The ability to map the altered cell morphologies being linked to PCA-determined biomarkers and then classified using machine learning.

However, to effectively assess the VRM and machine learning, key research questions relating to VRM first required addressing. Critical refinements for VRM of cell-scaffold constructs highlighted in the literature related to both shading [5], [6] and collection [7], [40]–[42] related distortions. Breaking the challenge into collection and data processing (shading) simplified the challenges. The design of accurately fabricated blocks, that could be used as a standard for calibrating VRM had been suggested by Baldock et al [6]. But representing the findings using a consistent approach throughout the chapter incentivised the first chapter to be focused on tackling challenges raised by Ashton et al [5], who questioned the current approaches to applying shading parameters to univariate Raman maps. The initial

focus on shading also provided another key simplification, the use of conventional (two-dimensional lateral) Raman mapping for the development of the method, for expansion to VRM in subsequent chapters.

7.2. Raman map shading

Ashton et al highlighted the need for a repeatable Raman map shading method, showing the disadvantages associated with automated (5-95%) Raman map shading, with the variability resulting from arbitrary selection of parameters demonstrated also in Chapter 3. A key research question for the project was the development of a shading method that could produce spectrally justified shading parameters. The benefit of tackling this research challenge for the thesis is to maximise confidence in morphological conclusions drawn from Raman maps throughout the project and in subsequent studies. To develop the shading justification suggested by Ashton et al, using violin plots [5], whilst employing the dithranol mapping, the thesis focused on single-cell analysis. A target of the shading method was to spectrally justify sub-cellular boundaries, highlighting key cellular regions like the nucleus and cytoplasm. Immortalised human keratinocytes (HaCaT) cells were selected for the development of the Raman mapping method, due to their use in a cell-dithranol psoriasis model [184]–[186]. The psoriasis model was a beneficial model to test Raman map shading on as Dithranol, the drug response being modelled, had previously been Raman mapped within HaCaT cells [5].

Different methods of shading Raman maps were highlighted with their benefits and limitations. The interpretability of univariate Raman mapping as contrasted with the reliability of clustering, inspired exploration of a shading method that could combine the two approaches. The first step of Chapter 3 was to select a clustering algorithm. Chapter 3 started with cluster images of HaCaT cells, using a standardised colour scheme for the thesis, which continued from a previous publication [6]. The limitation

of cluster shading is qualitative, removing the molecular fluctuation revealed within each cluster. Selecting k-means clustering instead of hierarchical cluster analysis achieved better HaCaT morphology correlation when verified fluorescence microscopy and principal component analysis hyperspectral images. K-means clustering also achieved quicker computation times, a beneficial property for a method designed to be applied to VRM datasets, which are inherently larger than conventional Raman maps of the same area and resolution. The chapter, therefore, aimed to combine the morphological accuracy and repeatability of k-means clustering with the molecularly interpretable (potentially quantitative) univariate Raman mapping.

Associating regions of Raman maps to clusters made achieving a critical goal of the thesis possible. By viewing the generalised (mean) cluster spectral distribution, assigning the cluster a colour (molecule) became spectrally informed when determining sub-sections within the Raman map to visualise the sample (cell). For example, the capacity to link the cluster to the nucleus or cytoplasm was demonstrated, providing a solution to the questions raised in previous studies [5], [6]. Another key outcome for the k-means directed method is the ability to isolate regions of interest (to the research question) or external to the cell (scaffold or background), also using spectral justification. Another key benefit of k-means-directed shading is increased objectivity, with subjectivity limited to the choices of the number and assignment of clusters.

The key finding of Chapter 3 was demonstrating the capacity of Raman spectroscopy to repeatably and objectively visualise morphological changes using mapping, a key objective in the monitoring method. By providing confidence in morphological analysis when monitoring changes in behaviour, the results are more effectively paired with machine learning. Outlining a robust Raman map shading method was an important first step in the project, reducing the effect of shading variability when investigating depth-related distortions in Chapter 4. [6][7], [30], [42]The choice of transparency settings [6] and opaqueness settings being further complicated by the need for consideration of sample refractive index published in a non-biological context [7], [30], [40]–[42]. Demonstrating k-means directed shading on conventional

Raman maps retained clarity before developing onto the opaqueness settings or z-stacking required in VRM. Comparison to PCA hyperspectral imaging provided both verification of the cluster boundaries and an indication of molecular signatures to investigate further using univariate mapping. The publication of spectrally justified shading is a key research outcome for the chapter and a significant step forward to the arbitrary choice of shading parameters highlighted by Ashton et al in 2015 [5].

7.3. VRM calibration

As with milestone 1, milestone 2 aimed to maximise confidence in morphological findings, this time focused on data collection. Bioengineered constructs are large enough to form tissues and eventually, organs are normally three-dimensional structures. A system designed to monitor cell-structure interactions for advanced constructs must therefore be capable of visualising the morphological response of the cells in 3D. In microscopy, the common method of determining the resolution is 0.5 × Airy disk, width for lateral resolution, and height for axial, a method previously shown ineffectual for axial resolution [7], [20], [40], [41]. Additional complexities compared to conventional Raman mapping include lateral and axial resolution asymmetry [20], [40], [41], and out-of-focus contributions [30], [42] justified a refined VRM method.

Direct laser writing (DLW) provided a method of determining VRM spatial accuracy, when investigating the influence of depth distortion, resolution asymmetry, and out-of-focus contributions [30], [42]. An important conclusion to draw from the DLW printed books (Figure 4.3) was that the apparent size of an object can be altered significantly by the z-step used in the VRM collection. DLW was found to provide suitable accuracy for calibrating VRM at a suitable scale for single-cell mapping, verified by scanning electron microscopy. The known size of the calibration block indicates the error level for a given VRM.

DLW is also a tool for fabricating three-dimensional cell culture environments, with high print accuracy providing the opportunity to investigate the effect of depth distortions on single-cell VRM. Developing the method specifically for the analysis of cells and scaffolds in the same map ensures the applicability of the method with a wide range of tissue engineering applications that use polymeric materials [187]–[190]. The challenge for Chapter 4, was therefore to produce a calibration method that uses material compatible with Raman mapping of cells, alongside accounting for optical considerations. OrmoComp™ was selected, with the previous publication of the bio-independent Raman peaks [6]. OrmoComp™ also has acceptable optical properties for single-cell VRM, especially when combined with effective design.

Designing scaffolds taking depth distortion and the diffraction limit was found to be useful when mapping tubes of staggered height, providing a starting point for iterative refinement of the method for analysing HaCaT cells with scaffolds. A couple of methods were used, initially looking at the differences between the mean and median of each Raman slice, using the violin plots suggested by Ashton et al (providing a linking analysis) to show the multiple of the slice median used as a threshold for the shading. Mapping varied scaffold depths that were hypothesised (section 4.3.3.) as within a range for the Raman system used 0.75 NA 50× objective in air, with a 532 nm laser, showed the need for an empirical calibration method, incentivising the design of calibration blocks in the next iteration. Comparing the results to scanning electron microscopy verified the shading method, allowing k-means directed shading (developed in parallel) to be applied to the calibrated VRM datasets.

An important outcome for the chapter was demonstrating that k-means directed shading developed in Chapter 3 could be applied to the shading of VRM z-stacks, visualising cells in different morphologies (Figures 4.10 & 4.11). The first experiment to combine the calibrated z-steps and k-means directed shading produced a VRM of a cell on a porous scaffold. The cell attachment to the scaffold, in a pore, meant the depth distortion and interference from the scaffold were avoided, informing the design of “simple” scaffolds in Chapter 5. The avoidance of scaffold axial depth also inspired the development of angled beam scaffolds, where thin sections (beams)

were angled at 45° and combined to produce a scaffold twenty times deeper than the calibration block defined maximum depth whilst avoiding depth distortion; tackling a chapter aim to advance scaffold design using the calibration findings (section 4.3.6). Defining z-steps and depth ranges provides a structured approach to VRM production, with the potential for expansion to larger applications than single-cell analysis.

The innovation of angled beam scaffolds provides a wider scope for influencing cell behaviour than simple scaffolds, and significantly more than calibration block depth scaffolds would. The final figure in Chapter 4 showed a hexagonal construct produced by joining angled beams together to form a cone, or cage structure. The avoidance of depth distortion for the cage scaffold provided the potential to alter the design to determine if the cellular response changes. Calibration block increases confidence in reported cell morphology changes, a key outcome for Chapter 5 comparing VRM visualised morphology to machine learning classification. The larger refractive index of the calibration block results in lower depth-related distortions within water-immersed cells, improving confidence in cellular VRM coordinates in calibrated maps. Scaffold designs that counter depth distortion and out-of-focus contributions when paired with suitable z-steps were next adapted to determine any influence on cell behaviour in Chapter 5. By combining the k-means directed shading with z-step calibrated VRM, the 3D morphologies can be investigated using dimension reduction and classified to demonstrate the capacity for cell-scaffold monitoring using supervised learning.

The key conclusion for the depth distortion section of the thesis is that DLW provides a fabrication method for constructs of known size, allowing for the calibration of VRM. The approach was shown to produce comparable results in VRM shaded using two different methods, including k-means-directed shading. By addressing gaps in the research relating to the collection and processing of Raman maps and VRM, the next stages of the thesis could focus on applying Raman mapping with machine learning for the monitoring of cell behaviour with maximised confidence in the findings. The additional findings of background removal and target region selection during the production of k-means directed Raman maps can be providing clearer

Raman map images and focus chemometric/machine learning analysis on regions within Raman maps.

7.4. Machine learning

To monitor a system, you must first understand it. Developing a monitoring method can therefore be broken into two stages. The first stage is to define an expected response from the system being monitored, allowing future behaviour to be compared to that standard. The second stage is to build a system that can carry out the comparison automatically and repeatably. In the context of a monitoring method of cells on a bioengineered construct, previous examples include tissue-engineered skin [18], [135], cartilage [136], single cells [137], and the extracellular matrix [138], with PCA also employed for drug response investigations [191]–[195]. A study exploring cell response to scaffold design provided an opportunity to combine the scaffold designs from Chapter 4, alongside developing the previous PCA analysis of cells in flow with VRM. The ability to view the cell response to porous scaffolds is advantageous in three dimensions. A previous publication by Greiner et al [8] previously showed altered invasiveness in response to the gene editing-induced nuclear stiffness reduction. Chapter 5 flipped this study, looking to detect molecular changes in cells changing their morphology in response to substrate geometry.

PCA provided an objective analysis ideal for initial data exploration, as the earlier introduction of subjectivity into a study may have a cascading effect through the analysis. The PCA loading plots increase interpretability by indicating the spectral regions maximising variance within the principal components. A broad analysis is provided by Raman spectroscopy through the linking of PCA-derived molecular information with VRM visualised morphological insight. Showing unsupervised separation in the PCA score plots increases confidence in subsequent supervised algorithm predictions, as the relationship being classified has a large enough

influence on the system to appear without the influence of labels. The addition of VRM allowed for the visualisation of altered cell morphology alongside any potential biomarkers or spectral regions of interest to the research question.

A key research question raised in Chapter 4 was: Is k-means directed shading of z-stacks generalisable/repeatable when mapping different scaffold designs scaffolds. The analysis was carried out over three scaffold design types “simple” scaffolds, cage scaffolds, and varied pore-size scaffolds. The findings from the previous chapters and phases into each subsequent experiment. PCA formed good cluster separation for the simple scaffold vs. Off and the 5-beamed cage scaffold vs. Off datasets but did not achieve separation for 5-beamed vs. 10-beamed cage scaffolds, or the varied pore sizes dataset. Combining VRM and PCA for an initial analysis, allowed the varied cellular responses to the scaffolds to be visualised, with the first figure showing the complexity of choosing transparency and opaqueness settings for WiRE^{TM}-produced VRM.

To determine the benefit of a more rigorous but complex shading method, the capabilities of different VRM approaches were initially compared. WiRE^{TM} VRM and k-means directed z-stacks were then produced to visualise the morphology of a cell on a scaffold, both showing an elongated morphology when compared to the VRM of cells on a flat surface in Chapter 4, Figure 4.3. However, WiRE^{TM}-produced VRM cannot be used in direct comparisons between subcellular regions in the way that you can for k-means directed shading of z-stacks. The use of k-means-directed shading allowed the averaged cluster spectra, showing the benefit of publishing this information through the detection of OrmoComp^{TM} contamination in the cell body cluster. The detection of spectral contamination incentivising the use of k-means clustering for region selection in subsequent sections of the thesis. The ability to map cells on different substrates and scaffolds (chapter 5 hypothesis 2) allowed another chapter hypothesis (1) to be tested, linking changed morphology to two and three-dimensional substrates.

The removal of scaffold-contaminated regions of the Raman maps was especially important when training machine learning models to demonstrate their capacity to

distinguish cells grown in different morphologies. Logistic regression, linear discriminant analysis (LDA), and support vector machine (SVM) were selected as supervised learning techniques capable of classifying datasets with under one hundred observations. The use of learning curves provided a more thorough illustration of the three models performance, with the 5-fold cross-validation behaving similarly for the three analyses. Learning curves show the researcher has not found the one subset within the dataset, or even one training dataset size, that has produced the correct metric. The suitable size of the training dataset is indicated alongside the spread of the results for each increment, if the lowest accuracy (or other metric) indicated by the standard deviation is suitable for the application, greater confidence in the model repeatability is provided.

A secondary purpose of the chapter relates to a thesis theme, standardisation, and repeatability, with the application of learning curves to increase confidence in the repeatability of the analysis. The publication of learning curves would increase the confidence in all machine learning models for vibrational spectroscopy. The convergence (or not) of all three trained models to similar scores, further increases confidence that a significant signal is detected to trust the class separation. Classification was achieved when distinguishing cells on simple scaffolds and the slide surface (off), and cells on the 5-beamed cage and off. Successful supervised classification of the cell on and off scaffolds was correlated with good separation in the PCA score plots, with poor classification produced for the 5-beam vs. 10-beam and the varied pore size datasets. The value of k-means removal of OrmoComp™ contaminated regions of the map, by increasing confidence that separation is a result of biological differences rather than contamination of scaffold materials, or not.

Determining whether dimension reduction (chapter 5 hypothesis 2) can separate, and achieve the chapter aim of supervised learning distinguishing cells grown on different geometry scaffolds provides a key research outcome towards monitoring cells on bioengineered constructs. The scaffold influence on the analysis is removed by the k-means removal of contaminated regions of the maps used. Further confidence is gained that OrmoComp™ contamination was avoided through its relatively high Raman intensity when compared to biological molecules. If

OrmoComp™ contamination remained, there would be a significant spectral difference, which could result in the separation of the Off class (which would not have any OrmoComp™). Reasons for the lack of separation could be not enough data, potentially the dataset is too unbalanced towards the porous scaffold cells. In a subsequent dataset with potential class imbalance, the control cells are isolated (Figure 6.7), where dithranol may result in more significant adaptations than size. However, it must also be said that pore dimension-induced adaptation in cells may be too small compared to the off cells. To try and counter the imbalanced dataset in section 5.3.4, random forest and decision tree classifiers were trained, as they are compatible with imbalanced datasets; failing to achieve suitable accuracies. Future studies looking to separate cells grown on different scaffold varieties (requiring unbalanced datasets) may target larger datasets for random forest algorithms.

The subtler differences between cells cultured in different 3D morphologies also provide potentially useful information moving forward. Although harder to demonstrate without controls, that a scaffold does not induce a significant difference in the cells is also useful information when monitoring a bioengineered construct. Beneficial results were repeatably shown to separate cells grown on two- and three-dimensional substrates. The morphological response of cells to being cultured in a three-dimensional morphology shown was shown using VRM. The molecular changes detected in response to being on or off a scaffold, typically relating to proteins and nucleic acids shown using PCA. It can therefore be concluded that cells on and off scaffolds could be monitored, with three trained models showing repeatability in proof-of-concept datasets. The key objective of Chapter 5 is the strengthened repeatability of machine learning systems for monitoring cell behaviour. The use of Raman spectroscopy to distinguish cells grown on different scaffold designs allowed the next experiments to develop the analysis from a static environment to a dynamic one.

7.5. Flow chamber

The last stage of the thesis looked to progress from static Raman analysis to dynamic, moving towards a platform for automated cell culture using full live-cell Raman with temperature and CO_2 control. Previous research had mapped cell-drug interactions [196]–[198] in static environments or limited to enclosed flow cytometry chambers [197]. Chapter 6 aimed to combine these approaches with the techniques developed in earlier chapters, developing an open design to allow for the use of an immersion objective. The use of an immersion objective provides an advantage over other flow mapping methods [196]–[198] in improving the optical properties between the objective and the sample, making VRM possible. The purpose of the chapter was to determine the flow chamber capabilities, iteratively increasing the complexity of analysis to build towards a platform, providing combined VRM-machine learning monitoring as seen in previous sections of the thesis.

The *in-situ* Raman flow chamber design aimed to build on the previous experiments, expanding the applications from monitoring substrate/scaffold influence on cell morphology to a pharmaceutical application (psoriasis model). No open flow chamber has been developed for dynamic VRM to the knowledge of the author. The novelty of the design demanded rigorous testing to ensure safety and data quality when bridging that gap. The testing ensured the flow chamber met the specified design aims, starting with simple spectral collection, moving onto conventional (lateral) Raman mapping, and VRM of DLW printed construct. The capacity of the flow chamber to influence sample temperature was demonstrated using both UV-laser analysis of polystyrene (cooling) and unfixed HaCaT cell analysis (warming). A Chapter 6 objective was exploring the versatility of the cell behaviour monitoring approach developed through the previous chapters (k-means directed shading, calibrated VRM z-steps, and chemometric approach. Collecting a VRM of a fixed HaCaT cell showed that VRM of a cell within the flow chamber is possible, even if some refinement is required for VRM to be quick enough for lice-cell Raman.

A VRM was collected within the flow chamber using a fixed HaCaT cell, justifying the continued investigation into an open flow chamber for Raman spectroscopy/VRM and justifying the dithranol-HaCaT cell investigation. The first dithranol experiments established a baseline for comparison in subsequent (more complex) analyses using fixed HaCaT cells. The malleability of the cell-scaffold experiments was tested by replicating the use of VRM and PCA to explore the system. A VRM of a HaCaT cell exposed to 2 μM of dithranol built on the analysis published by Ashton *et al* [5] visualising the dithranol within the cell in three dimensions. The dithranol distribution in the cytoplasm of the cell, as seen previously [5].

The VRM was then paired with PCA analysis, aiming to provide morphological and molecular standards for unfixed Raman analysis. PCA was selected for the unfixed analysis, to align with the exploratory method applied in Chapter 5 and previous publications exploring flow cytometry of cell drug exposure using Raman mapping [196], [197]. PCA score plots showed that the difference between dithranol-exposed and unexposed cells could be more easily distinguished than cells exposed to varied dithranol concentrations over two hours. The lack of separation in the score plot between the cells exposed to different dithranol concentrations may indicate the need for a larger dataset, the cellular response to the different concentrations not being significant enough, of the fixing process reducing the spectral information available.

The separation of the dithranol exposed and unexposed showed that the exposure to the drug could be detected with Raman spectroscopy and PCA, where PCA score plot separation of class clusters correlated with supervised learning classification success in Chapter 5. The loading plots for the principal components used also provided information as to the regions of the spectrum responsible for the separation of the drug-exposed from the drug-unexposed cells. The highly loaded peaks relating to the dithranol, proteins, and lipids regions, suggest that adaptions were occurring in the cytoplasm, concurring with the dithranol distribution seen in the VRM and the findings of previous research [5]. The main findings from the fixed analysis in Chapter 6 showed that mapping the three-dimensional dithranol distribution within

cells is possible and that PCA can separate dithranol exposed and unexposed HaCaT cells.

Alongside providing an opportunity to explore the adaptability of the VRM-chemometric analysis for monitoring cell behaviour, a dynamic environment was desirable for replicating *in vivo* conditions more closely. The flow chamber was shown to provide an approach for controlling cell culture variables (temperature, factors, culture media type) to be altered without disturbing the sample position, critical for a system designed for Raman mapping. The control of temperature was valuable when investigating unfixed cell Raman analysis, where a key Chapter 6 aim, supporting cell life through an extended (1-2 hour) study. Being able to support cell life in a stable enough condition to be undetectable in a control study incentivised the study of unfixed cells, increasing the complexity of the analysis, and moving towards monitoring of cells using true live-cell Raman spectroscopy.

The unfixed analysis is the more accurate term for the initial flow chamber analysis, with control of the CO_2 concentration limited and the temperature inconsistent compared to true live-cell Raman. The flow chamber did provide predictable survival of the cells over the two hours of the previous fixed cell analysis. A control study found that the flow chamber did not cause detectable changes in the cells using Raman spectroscopy and PCA. Following the control study, the same experiment was carried out, using the same method except for including the dithranol. Raman maps were collected before and after the two hours in the flow chamber using phenylalanine-free culture media. The PCA score plot results showed no separation of the cells before and after the flow chamber, suggesting that any subsequent cluster separation would result from any change in the culture conditions. The PCA results for the before and after maps subsequently showed clear separation when the drug was included in the two-hour flow exposure resulting from the dithranol. Inspection of the loading plots showed some concurrent peaks from the fixed cell analysis previously relating to proteins and lipids, relating to the cytoplasm, highlighting the value of the fixed cell analysis and a standard moving forward. Unfixed mapping of the cells before and after the dithranol flow exposure, shaded

using k-means directed shading, showed similar dithranol distribution to the VRM carried out on a fixed cell, showing further concurrency in the analyses.

A key research outcome for Chapter 6 was establishing that cells could be supplied a drug (dithranol) inside a Raman spectroscope and that Raman mapping and chemometrics were able to verify the presence of the drug (Figures 6.10-13). Successfully supplying a drug to cells in a flow chamber justifies the development of the flow chamber to true live cell Raman spectroscopy, potentially with the addition of automated temperature, fluid, and CO_2 control. The automation of the live-cell environment would allow for longer-term experiments and incentivise the further development of automated Raman spectra and map collections. A wider range of drug and cell combinations could be monitored, providing simpler studies to refine the technology upon, building towards tissue or bioengineered constructs. The loss of the dithranol Raman peak in the loadings between the fixed and unfixed dithranol supply provides an area of research for future studies, understanding whether it relates to an unbalanced dataset (75% varied dithranol – 25% control), or whether the flow provided a better means of supplying the drug; more closely replicating the human bodies environment. An important outcome from Chapter 6 is the testing of a flow chamber for Raman spectroscopy, which now tested is a platform that significantly expands the cell stimulation within a Raman spectroscope that can be Raman mapped.

7.6. Future research

The goal of the project was to develop methods of monitoring cells for the further development of an automated method of monitoring bioengineered constructs. Chapters 3 and 4 looked at the production and processing of Raman maps in two- and three-dimensions. The potential of Raman spectroscopy for the visualisation and monitoring of altered cell behaviour was explored in Chapter 5 and the findings from the previous three chapters were applied within the novel *in situ* Raman spectroscope flow chamber in Chapter 6. The flow chamber provides a platform for single cells to be monitored in a dynamic environment, allowing the cells to be visualised and analysed using the mapping techniques developed in the previous chapters. A potential area of further investigation would be to see if cell behaviour changes result from fluid flow over the cells when they are cultured on different scaffold geometries. Using the VRM to map any change in morphology through exploration of methods to speed VRM collection times [199]–[201].

The focus of this thesis has been single HaCaT cells, future research would ideally identify a wider range of target cells (e.g. different disease models, stem cells, or primary cells). Investigating different cell types and research questions would further demonstrate the versatility of the approach. Different cell types would also stimulate further scaffold designs, with different bioengineering research goals, such as cell attachment, deeper scaffold invasion, or cell migration, to be explored. Different and varied cell behaviours may necessitate increasingly complex monitoring requirements, requiring the training of more complex machine learning models. The collection of larger datasets would therefore be a key focus of future research to provide greater strength to the monitoring capacity of Raman spectroscopy. The production of larger datasets may provide the opportunity to train robust multi-class machine learning models, providing the opportunity to monitor a wider range of behaviours with a single model.

Visualising (Chapter 4) and classifying (Chapter 5) altered cell morphology in response to scaffold design using VRM (Chapters 4 and 5) invites questions about other adaptations it can reveal. Potential areas of research could include molecular

variation in response to substrate material properties, like changes in nuclear stiffness in response to higher scaffold Young's modulus. The tools developed in Chapters 3 and 4, facilitate the linking of changes in a specific location/organelle within a cell to a desirable outcome that can subsequently be used to train machine learning models, potentially exploring larger biological systems.

Bridging gaps in Raman spectroscopy and machine learning to monitor bioengineered constructs provides rigorous methods for testing cells for tissue engineering and pharmaceutical research. The thesis focused on single-cell analysis, reducing the collection times, and maintaining a link to research that guided key research outcomes for the project [6]. Reduction of VRM collection times is important for research with the goal of developments towards live-cell VRM. However, larger systems have been mapped using VRM, like whole Zebrafish [84]. A longer-term goal for the research could be the monitoring of tissues or tissue-engineered constructs. Goals that require quicker VRM collection or a targeted analysis to indicate the health of the entire system through inspection of key regions. Improving collection time would also increase testing time, providing medical devices to surgeons sooner.

References

[1] M. C. McCorry *et al.*, “Sensor technologies for quality control in engineered tissue manufacturing,” *Biofabrication*, vol. 15, no. 1. Institute of Physics, Jan. 01, 2023. doi: 10.1088/1758-5090/ac94a1.

[2] D. Zuncheddu *et al.*, “Quality control methods in musculoskeletal tissue engineering: from imaging to biosensors,” *Bone Research*, vol. 9, no. 1. Springer Nature, Dec. 01, 2021. doi: 10.1038/s41413-021-00167-9.

[3] H. J. Byrne *et al.*, “Spectropathology for the next generation: Quo vadis?,” *Analyst*, vol. 140, no. 7. Royal Society of Chemistry, pp. 2066–2073, Apr. 07, 2015. doi: 10.1039/c4an02036g.

[4] M. J. Baker *et al.*, “Clinical applications of infrared and Raman spectroscopy: State of play and future challenges,” *Analyst*, vol. 143, no. 8. Royal Society of Chemistry, pp. 1735–1757, Apr. 21, 2018. doi: 10.1039/c7an01871a.

[5] L. Ashton, K. A. Hollywood, and R. Goodacre, “Making colourful sense of Raman images of single cells,” *Analyst*, vol. 140, no. 6, pp. 1852–1858, Mar. 2015, doi: 10.1039/c4an02298j.

[6] S. J. Baldock, A. C. S. Talari, R. Smith, K. L. Wright, and L. Ashton, “Single-cell Raman microscopy of microengineered cell scaffolds,” *Journal of Raman Spectroscopy*, vol. 50, no. 3, pp. 371–379, Mar. 2019, doi: 10.1002/jrs.5525.

[7] N. Everall, “Optimising image quality in 2D and 3D confocal Raman mapping,” *Journal of Raman Spectroscopy*, vol. 45, no. 1, pp. 133–138, 2014, doi: 10.1002/jrs.4430.

[8] A. M. Greiner, B. Richter, and M. Bastmeyer, “Micro-Engineered 3D Scaffolds for Cell Culture Studies,” *Macromol Biosci*, vol. 12, no. 10, pp. 1301–1314, Oct. 2012, doi: 10.1002/mabi.201200132.

[9] A. O. Paggiaro, R. Bastianelli, V. F. Carvalho, C. Isaac, and R. Gemperli, “Is allograft skin, the gold-standard for burn skin substitute? A systematic literature review and meta-analysis,” *Journal of Plastic, Reconstructive and Aesthetic Surgery*, vol. 72, no. 8. Churchill Livingstone, pp. 1245–1253, Aug. 01, 2019. doi: 10.1016/j.bjps.2019.04.013.

[10] R. Gibbs, “Selected internet viewings,” *Ann R Coll Surg Engl*, vol. 89, no. 6, pp. 649–652, Aug. 2007, doi: 10.1308/003588407x205558.

[11] M. J. Wilhelm, “Long-term outcome following heart transplantation: Current perspective,” *J Thorac Dis*, vol. 7, no. 3, pp. 549–551, 2015, doi: 10.3978/j.issn.2072-1439.2015.01.46.

[12] R. Dimitriou, G. I. Mataliotakis, A. G. Angoules, N. K. Kanakaris, and P. V. Giannoudis, “Complications following autologous bone graft harvesting from the iliac crest and using the RIA: A systematic review,” *Injury*, vol. 42, no. SUPPL. 2, 2011, doi: 10.1016/j.injury.2011.06.015.

[13] M. S. Katz *et al.*, “Postoperative morbidity and complications in elderly patients after harvesting of iliac crest bone grafts,” *Medicina (Lithuania)*, vol. 57, no. 8, Aug. 2021, doi: 10.3390/medicina57080759.

[14] R. M. Delaine-Smith, A. Sittichokechaiwut, and G. C. Reilly, “Primary cilia respond to fluid shear stress and mediate flow-induced calcium deposition in osteoblasts,” *FASEB Journal*, vol. 28, no. 1, pp. 430–439, 2014, doi: 10.1096/fj.13-231894.

[15] K. A. Esmonde-White, M. Cuellar, C. Uerpmann, B. Lenain, and I. R. Lewis, “Raman spectroscopy as a process analytical technology for pharmaceutical manufacturing and bioprocessing,” *Analytical and Bioanalytical Chemistry*, vol. 409, no. 3. Springer Verlag, pp. 637–649, Jan. 01, 2017. doi: 10.1007/s00216-016-9824-1.

[16] G. Kalisz *et al.*, “Application of raman spectroscopic imaging to assess the structural changes at cell-scaffold interface,” *Int J Mol Sci*, vol. 22, no. 2, pp. 1–16, Jan. 2021, doi: 10.3390/ijms22020485.

[17] L. J. Power *et al.*, “Sensing tissue engineered cartilage quality with Raman spectroscopy and statistical learning for the development of advanced characterization assays,” *Biosens Bioelectron*, vol. 166, Oct. 2020, doi: 10.1016/j.bios.2020.112467.

[18] A. J. Bullock, M. Garcia, J. Shepherd, I. Rehman, and M. Sheila, “Bacteria induced pH changes in tissue-engineered human skin detected non-invasively using Raman confocal spectroscopy,” *Applied Spectroscopy Reviews*, vol. 55, no. 2. Taylor and Francis Inc., pp. 158–171, Feb. 07, 2020. doi: 10.1080/05704928.2018.1558232.

[19] M. J. McIvor *et al.*, “Direct monitoring of single-cell response to biomaterials by Raman spectroscopy,” *J Mater Sci Mater Med*, vol. 32, no. 12, Dec. 2021, doi: 10.1007/s10856-021-06624-5.

[20] R. Boitor, F. Sinjab, S. Strohbuecker, V. Sottile, and I. Notingher, “Towards quantitative molecular mapping of cells by Raman microscopy: Using AFM for decoupling molecular concentration and cell topography,” *Faraday Discuss*, vol. 187, pp. 199–212, 2016, doi: 10.1039/c5fd00172b.

[21] H. J. Butler *et al.*, “Using Raman spectroscopy to characterize biological materials,” *Nat Protoc*, vol. 11, no. 4, pp. 664–687, Apr. 2016, doi: 10.1038/nprot.2016.036.

[22] O. A. Maslova *et al.*, “Raman imaging and principal component analysis-based data processing on uranium oxide ceramics,” *Mater Charact*, vol. 129, pp. 260–269, Jul. 2017, doi: 10.1016/j.matchar.2017.05.015.

[23] M. Bourbousson, I. Soomro, D. Baldwin, and I. Notingher, “Ex vivo Raman spectroscopy mapping of lung tissue: label-free molecular characterization of nontumorous and cancerous tissues,” *Journal of Medical Imaging*, vol. 6, no. 03, p. 1, Aug. 2019, doi: 10.1117/1.jmi.6.3.036001.

[24] N. Moshkov, B. Mathe, A. Kertesz-Farkas, R. Hollandi, and P. Horvath, “Test-time augmentation for deep learning-based cell segmentation on microscopy

images," *Sci Rep*, vol. 10, no. 1, Dec. 2020, doi: 10.1038/s41598-020-61808-3.

[25] A. A. Shah, H. A. M. Malik, A. H. Muhammad, A. Alourani, and Z. A. Butt, "Deep learning ensemble 2D CNN approach towards the detection of lung cancer," *Sci Rep*, vol. 13, no. 1, Dec. 2023, doi: 10.1038/s41598-023-29656-z.

[26] Gerhard Herzberg, *Molecular Spectra and Molecular Structure: Infrared and Raman spectra of polyatomic molecules*, vol. 2, New Jersey, Princeton Hall, 1939, p. 7

[27] B. Campanella, V. Palleschi, and S. Legnaioli, "Introduction to vibrational spectroscopies," *ChemTexts*, vol. 7, no. 1, Mar. 2021, doi: 10.1007/s40828-020-00129-4.

[28] H. P. P. and P. Burrows, *Chemistry3: Introducing inorganic, organic and physical chemistry (3rd Ed.) - Chapter 10.*, 2nd Ed., Oxford, Oxford University Press, 2013, pp. 476-491

[29] A. Syed and E. A. Smith, "Raman Imaging in Cell Membranes, Lipid-Rich Organelles, and Lipid Bilayers," 2017, doi: 10.1146/annurev-anchem.

[30] N. J. Everall, "Confocal Raman Microscopy: Performance, Pitfalls, and Best Practice", Applied Spectroscopy, vol. 63, no. 9, pp. 245-262, 2009, doi.org/10.1366/000370209789379196

[31] R. Slipets, O. Ilchenko, C. Mazzoni, F. Tentor, L. H. Nielsen, and A. Boisen, "Volumetric Raman chemical imaging of drug delivery systems," *Journal of Raman Spectroscopy*, vol. 51, no. 7, pp. 1153–1159, Jul. 2020, doi: 10.1002/jrs.5869.

[32] C. Kallepitis *et al.*, "Quantitative volumetric Raman imaging of three dimensional cell cultures," *Nat Commun*, vol. 8, Mar. 2017, doi: 10.1038/ncomms14843.

[33] B. Ramamurthy, S. Cohen, M. Canales, and F. D. Coffman, "Three-dimensional cellular raman analysis: Evidence of highly ordered lipids within

cell nuclei," *Journal of Histochemistry and Cytochemistry*, vol. 66, no. 12, pp. 889–902, Jan. 2018, doi: 10.1369/0022155418794125.

[34] M. Uematsu and T. Shimizu, "Raman microscopy-based quantification of the physical properties of intracellular lipids," *Commun Biol*, vol. 4, no. 1, Dec. 2021, doi: 10.1038/s42003-021-02679-w.

[35] A. B. Zoladek *et al.*, "Label-free molecular imaging of immunological synapses between dendritic and T cells by Raman micro-spectroscopy," in *Analyst*, Royal Society of Chemistry, 2010, pp. 3205–3212. doi: 10.1039/c0an00508h.

[36] J. Gala de Pablo *et al.*, "Biochemical fingerprint of colorectal cancer cell lines using label-free live single-cell Raman spectroscopy," *Journal of Raman Spectroscopy*, vol. 49, no. 8, pp. 1323–1332, Aug. 2018, doi: 10.1002/jrs.5389.

[37] J. M. Surmacki, B. J. Woodhams, A. Haslehurst, B. A. J. Ponder, and S. E. Bohndiek, "Raman micro-spectroscopy for accurate identification of primary human bronchial epithelial cells," *Sci Rep*, vol. 8, no. 1, Dec. 2018, doi: 10.1038/s41598-018-30407-8.

[38] R. Daum, E. M. Brauchle, D. A. C. Berrio, T. P. Jurkowski, and K. Schenke-Layland, "Non-invasive detection of DNA methylation states in carcinoma and pluripotent stem cells using Raman microspectroscopy and imaging," *Sci Rep*, vol. 9, no. 1, Dec. 2019, doi: 10.1038/s41598-019-43520-z.

[39] R. Smith, K. L. Wright, and L. Ashton, "Raman spectroscopy: An evolving technique for live cell studies," *Analyst*, vol. 141, no. 12. Royal Society of Chemistry, pp. 3590–3600, Jun. 21, 2016. doi: 10.1039/c6an00152a.

[40] N. J. Everall, "Modeling and Measuring the Effect of Refraction on the Depth Resolution of Confocal Raman Microscopy," *Applied Spectroscopy*, vol. 54, no. 6, 2000. doi.org/10.1366/00037020019503

[41] N. J. Everall, "Confocal Raman Microscopy: Why the Depth Resolution and Spatial Accuracy Can Be Much Worse than You Think," *Applied spectroscopy*, vol. 54, no. 10, pp. 1515-1520, 2000. doi.org/10.1366/0003702001948

[42] N. J. Everall, “Confocal Raman microscopy: Common errors and artefacts,” *Analyst*, vol. 135, no. 10. Royal Society of Chemistry, pp. 2512–2522, 2010. doi: 10.1039/c0an00371a.

[43] D. Lambert, C. Muehlethaler, L. Gueissaz, and G. Massonnet, “Raman analysis of multilayer automotive paints in forensic science: Measurement variability and depth profile,” *Journal of Raman Spectroscopy*, vol. 45, no. 11–12, pp. 1285–1292, 2014, doi: 10.1002/jrs.4490.

[44] H. Wang, N. Huang, J. Zhao, H. Lui, M. Korbelik, and H. Zeng, “Depth-resolved in vivo micro-Raman spectroscopy of a murine skin tumor model reveals cancer-specific spectral biomarkers,” *Journal of Raman Spectroscopy*, vol. 42, no. 2, pp. 160–166, 2011, doi: 10.1002/jrs.2677.

[45] S. Duraipandian, M. M. Knopp, M. R. Pollard, H. Kerdoncuff, J. C. Petersen, and A. Müllertz, “A fast and novel internal calibration method for quantitative Raman measurements on aqueous solutions,” *Analytical Methods*, vol. 10, no. 29, pp. 3589–3593, Aug. 2018, doi: 10.1039/c8ay00753e.

[46] E. Simone, A. N. Saleemi, and Z. K. Nagy, “Application of quantitative Raman spectroscopy for the monitoring of polymorphic transformation in crystallization processes using a good calibration practice procedure,” *Chemical Engineering Research and Design*, vol. 92, no. 4, pp. 594–611, 2014, doi: 10.1016/j.cherd.2013.11.004.

[47] C. L. M. Morais, K. M. G. Lima, M. Singh, and F. L. Martin, “Tutorial: multivariate classification for vibrational spectroscopy in biological samples,” *Nature Protocols*, vol. 15, no. 7. Nature Research, pp. 2143–2162, Jul. 01, 2020. doi: 10.1038/s41596-020-0322-8.

[48] M. Farsari, M. Vamvakaki, and B. N. Chichkov, “Multiphoton polymerization of hybrid materials,” *Journal of Optics*, vol. 12, no. 12. IOP Publishing Ltd, 2010. doi: 10.1088/2040-8978/12/12/124001.

[49] K. Sugioka and Y. Cheng, “Femtosecond laser three-dimensional micro-and nanofabrication,” *Applied Physics Reviews*, vol. 1, no. 4. American Institute of Physics Inc., Dec. 01, 2014. doi: 10.1063/1.4904320.

[50] D. Cheng, R. K. Jayne, A. Tamborini, J. Eyckmans, A. E. White, and C. S. Chen, “Studies of 3D directed cell migration enabled by direct laser writing of curved wave topography,” *Biofabrication*, vol. 11, no. 2, 2019, doi: 10.1088/1758-5090/ab047f.

[51] J. H. Campbell, N. Nicole, O. Stein, Y. Liu, Y. Lu, and L. Jiang, “Three-dimensional printing and deformation behavior of low-density target structures by two-photon polymerization,” SPIE-Intl Soc Optical Eng, Aug. 2017, p. 66. doi: 10.1117/12.2274193.

[52] A. I. Son *et al.*, “An Implantable Micro-Caged Device for Direct Local Delivery of Agents,” *Sci Rep*, vol. 7, no. 1, Dec. 2017, doi: 10.1038/s41598-017-17912-y.

[53] Alexandra M Greiner *et al*, “Cell type-specific adaptation of cellular and nuclear volume in micro-engineered 3D environments”, *Biomaterials*, vol. 69, pp. 121-132, 2015, doi.org/10.1016/j.biomaterials.2015.08.016

[54] F. Klein *et al.*, “Two-component polymer scaffolds for controlled three-dimensional cell culture,” *Advanced Materials*, vol. 23, no. 11, pp. 1341–1345, Mar. 2011, doi: 10.1002/adma.201004060.

[55] E. Kim, S. J. Yoo, C. Moon, B. J. Nelson, and H. Choi, “SU-8-based nanoporous substrate for migration of neuronal cells,” *Microelectron Eng*, vol. 141, pp. 173–177, Jun. 2015, doi: 10.1016/j.mee.2015.03.016.

[56] S. Turunen, E. Käpylä, M. Lähteenmäki, L. Ylä-Outinen, S. Narkilahti, and M. Kellomäki, “Direct laser writing of microstructures for the growth guidance of human pluripotent stem cell derived neuronal cells,” *Opt Lasers Eng*, vol. 55, pp. 197–204, 2014, doi: 10.1016/j.optlaseng.2013.11.003.

[57] T. Gissibl, S. Wagner, J. Sykora, M. Schmid, and H. Giessen, “Refractive index measurements of photo-resists for three-dimensional direct laser writing,” *Opt Mater Express*, vol. 7, no. 7, p. 2293, Jul. 2017, doi: 10.1364/ome.7.002293.

[58] Anika Trautmann *et al*, “Two-photon polymerization based large scaffolds for adhesion and proliferation studies of human primary fibroblasts”. *Optics and Laser Technology*, vol. 106, pp. 474–480, 2018, doi.org/10.1016/j.optlastec.2018.05.008

[59] S. Turunen, T. Joki, M. L. Hiltunen, T. O. Ihalainen, S. Narkilahti, and M. Kellomäki, “Direct Laser Writing of Tubular Microtowers for 3D Culture of Human Pluripotent Stem Cell-Derived Neuronal Cells,” *ACS Appl Mater Interfaces*, vol. 9, no. 31, pp. 25717–25730, Aug. 2017, doi: 10.1021/acsami.7b05536.

[60] B. Spagnolo *et al.*, “Three-dimensional cage-like microscaffolds for cell invasion studies,” *Sci Rep*, vol. 5, May 2015, doi: 10.1038/srep10531.

[61] S. Rehman, Z. Movasaghi, J. A. Darr, and I. U. Rehman, “Fourier transform infrared spectroscopic analysis of breast cancer tissues; Identifying differences between normal breast, invasive ductal carcinoma, and ductal carcinoma in situ of the breast,” *Appl Spectrosc Rev*, vol. 45, no. 5, pp. 355–368, Sep. 2010, doi: 10.1080/05704928.2010.483674.

[62] Alexandra M. Greiner *et al*, “Multifunctional polymer scaffolds with adjustable pore size and chemoattractant gradients for studying cell matrix invasion”, *Biomaterials*, vol. 35, no. 2, pp. 611-619, 2014, https://doi.org/10.1016/j.biomaterials.2013.09.095

[63] H. Abdi and L. J. Williams, “Principal component analysis,” *Wiley Interdisciplinary Reviews: Computational Statistics*, vol. 2, no. 4. pp. 433–459, Jul. 2010. doi: 10.1002/wics.101.

[64] Christophe B.Y. Cordella., “PCA: The Basic Building Block of Chemometrics,” in *Analytical Chemistry*, InTech, 2012. doi: 10.5772/51429.

[65] M. J. Baker *et al.*, “Using Fourier transform IR spectroscopy to analyze biological materials,” *Nat Protoc*, vol. 9, no. 8, pp. 1771–1791, 2014, doi: 10.1038/nprot.2014.110.

[66] H. Zou, T. Hastie, and R. Tibshirani, “Sparse principal component analysis,” *Journal of Computational and Graphical Statistics*, vol. 15, no. 2, pp. 265–286, Jun. 2006, doi: 10.1198/106186006X113430.

[67] B. Scholkopf, Alex Smola, and K. Müller, “Kernel Principal Component Analysis.”, *International Conference on Artificial Neural Networks*, 1997, pp. 1-6, DOI:10.1007/BFb0020217

[68] J. Dorney, F. Bonnier, A. Garcia, A. Casey, G. Chambers, and H. J. Byrne, “Identifying and localizing intracellular nanoparticles using Raman spectroscopy,” *Analyst*, vol. 137, no. 5, pp. 1111–1119, Mar. 2012, doi: 10.1039/c2an15977e.

[69] S. Hugelier *et al.*, “Weighted fuzzy clustering for (Fuzzy) constraints in multivariate image analysis– Alternating least square of hyperspectral images,” *Journal of Spectral Imaging*, vol. 5, 2016, doi: 10.1255/jsi.2016.a7.

[70] C. Lima *et al*, “K-means and Hierarchical Cluster Analysis as segmentation algorithms of FTIR hyperspectral images collected from cutaneous tissue,” *SBFoton International Optics and Photonics Conference*, pp. 1-4, 2018, DOI: 10.1109/SBFoton-IOPC.2018.8610920

[71] M. Z. Naser and A. H. Alavi, “Error Metrics and Performance Fitness Indicators for Artificial Intelligence and Machine Learning in Engineering and Sciences,” *Architecture, Structures and Construction*, Nov. 2021, doi: 10.1007/s44150-021-00015-8.

[72] M. Sokolova and G. Lapalme, “A systematic analysis of performance measures for classification tasks,” *Inf Process Manag*, vol. 45, no. 4, pp. 427–437, Jul. 2009, doi: 10.1016/j.ipm.2009.03.002.

[73] A. Humphrey *et al.*, “Machine-learning classification of astronomical sources: estimating F1-score in the absence of ground truth,” Sep. 2022, doi: 10.1093/mnrasl/slac120.

[74] A. Tharwat, T. Gaber, A. Ibrahim, and A. E. Hassanien, “Linear discriminant analysis: A detailed tutorial,” *AI Communications*, vol. 30, no. 2, pp. 169–190, 2017, doi: 10.3233/AIC-170729.

[75] A. Ben-Hur and J. Weston, “A user’s guide to support vector machines.,” *Methods Mol Biol*, vol. 609, pp. 223–239, 2010, doi: 10.1007/978-1-60327-241-4_13.

[76] V. Jakkula, “Tutorial on Support Vector Machine (SVM).”, *Jakkula2011TutorialOS*, pp. 1-13, 2011, CorpusID:1511540

[77] C. A. Meza Ramirez, M. Greenop, Y. A. Almoshawah, P. L. Martin Hirsch, and I. U. Rehman, “Advancing cervical cancer diagnosis and screening with spectroscopy and machine learning,” *Expert Review of Molecular Diagnostics*, vol. 23, no. 5. Taylor and Francis Ltd., pp. 375–390, 2023. doi: 10.1080/14737159.2023.2203816.

[78] J. Liu, M. Osadchy, L. Ashton, M. Foster, C. J. Solomon, and S. J. Gibson, “Deep convolutional neural networks for Raman spectrum recognition: A unified solution,” *Analyst*, vol. 142, no. 21, pp. 4067–4074, Nov. 2017, doi: 10.1039/c7an01371j.

[79] A. J. Myles, R. N. Feudale, Y. Liu, N. A. Woody, and S. D. Brown, “An introduction to decision tree modeling,” *Journal of Chemometrics*, vol. 18, no. 6. pp. 275–285, Jun. 2004. doi: 10.1002/cem.873.

[80] G. Biau and E. Scornet, “A Random Forest Guided Tour,” Nov. 2015, [Online]. Available: http://arxiv.org/abs/1511.05741

[81] B. Gregorutti, B. Michel, and P. Saint-Pierre, “Correlation and variable importance in random forests,” *Stat Comput*, vol. 27, no. 3, pp. 659–678, May 2017, doi: 10.1007/s11222-016-9646-1.

[82] Michael Greenop, “K-means_directed_shading,” https://github.com/MichaelGreenop/K-means_directed_shading. Accessed: 01/08/2023

[83] Michael Greenop, “RIP_wdf,” https://github.com/MichaelGreenop/RIP_wdf. Accessed: 01/08/2023

[84] H. Høgset *et al.*, “In vivo biomolecular imaging of zebrafish embryos using confocal Raman spectroscopy,” *Nat Commun*, vol. 11, no. 1, Dec. 2020, doi: 10.1038/s41467-020-19827-1.

[85] J. P. Smith *et al.*, “Raman hyperspectral imaging with multivariate analysis for investigating enzyme immobilization,” *Analyst*, vol. 145, no. 23, pp. 7571–7581, Dec. 2020, doi: 10.1039/d0an01244k.

[86] Y. Luo, F. Qi, C. T. Gibson, Y. Lei, and C. Fang, “Investigating kitchen sponge-derived microplastics and nanoplastics with Raman imaging and multivariate analysis,” *Science of the Total Environment*, vol. 824, Jun. 2022, doi: 10.1016/j.scitotenv.2022.153963.

[87] M. A. S. de Oliveira, M. Campbell, A. M. Afify, E. C. Huang, and J. W. Chan, “Hyperspectral Raman microscopy can accurately differentiate single cells of different human thyroid nodules,” *Biomed Opt Express*, vol. 10, no. 9, p. 4411, Sep. 2019, doi: 10.1364/boe.10.004411.

[88] A. Surkova and A. Bogomolov, “Analysis of Milk Microstructure Using Raman Hyperspectral Imaging,” *Molecules*, vol. 28, no. 6, Mar. 2023, doi: 10.3390/molecules28062770.

[89] S. Wang *et al.*, “Studying the pathological and biochemical features in breast cancer progression by confocal Raman microspectral imaging of excised tissue samples,” *J Photochem Photobiol B*, vol. 222, Sep. 2021, doi: 10.1016/j.jphotobiol.2021.112280.

[90] J. Li *et al.*, “Unveiling osteosarcoma responses to DAPT combined with cisplatin by using confocal Raman microscopy,” *Biomed Opt Express*, vol. 12, no. 9, p. 5514, Sep. 2021, doi: 10.1364/boe.432933.

[91] B. Zhang *et al.*, “Raman microspectroscopy based TNM staging and grading of breast cancer,” *Spectrochim Acta A Mol Biomol Spectrosc*, vol. 285, Jan. 2023, doi: 10.1016/j.saa.2022.121937.

[92] J. Li *et al.*, “Confocal raman spectral imaging study of DAPT, a γ-secretase inhibitor, induced physiological and biochemical reponses in osteosarcoma cells,” *Int J Med Sci*, vol. 17, no. 5, pp. 577–590, 2020, doi: 10.7150/ijms.43506.

[93] H. Wang *et al.*, “Confocal Raman microspectral analysis and imaging of the drug response of osteosarcoma to cisplatin,” *Analytical Methods*, vol. 13, no. 22, pp. 2527–2536, Jun. 2021, doi: 10.1039/d1ay00626f.

[94] J. Li *et al.*, “Microscopic Raman illustrating antitumor enhancement effects by the combination drugs of γ-secretase inhibitor and cisplatin on osteosarcoma cells,” *J Biophotonics*, vol. 15, no. 12, Dec. 2022, doi: 10.1002/jbio.202200189.

[95] S. Ŝaŝić, D. A. Clark, J. C. Mitchell, and M. J. Snowden, “A comparison of Raman chemical images produced by univariate and multivariate data processing - A simulation with an example from pharmaceutical practice,” *Analyst*, vol. 129, no. 11, pp. 1001–1007, 2004, doi: 10.1039/b409879j.

[96] T. Adão *et al.*, “Hyperspectral imaging: A review on UAV-based sensors, data processing and applications for agriculture and forestry,” *Remote Sens (Basel)*, vol. 9, no. 11, Nov. 2017, doi: 10.3390/rs9111110.

[97] A. Daniel *et al.*, “Raman mapping of oral tissues for cancer diagnosis,” in *Journal of Raman Spectroscopy*, John Wiley and Sons Ltd, 2014, pp. 541–549. doi: 10.1002/jrs.4493.

[98] L. Rodrigues e Brito, A. B. Chaves, A. Braz, and M. F. Pimentel, “Raman hyperspectral imaging and a novel approach for objective determination of the order of crossing ink lines,” *Spectrochim Acta A Mol Biomol Spectrosc*, vol. 223, Dec. 2019, doi: 10.1016/j.saa.2019.117287.

[99] W. Liu, C. Jing, X. Liu, and J. Du, “3D imaging of single bacterial cells using surface-enhanced Raman spectroscopy with a multivariate curve resolution

model," *Analyst*, vol. 147, no. 2, pp. 223–229, Jan. 2022, doi: 10.1039/d1an01879e.

[100] H. Wang *et al.*, "Investigating the cellular responses of osteosarcoma to cisplatin by confocal Raman microspectroscopy," *J Photochem Photobiol B*, vol. 226, Jan. 2022, doi: 10.1016/j.jphotobiol.2021.112366.

[101] Florian Spörl *et al*, "A Circadian Clock in HaCaT Keratinocytes". *Journal of Investigative Dermatology*, vol. 131, no. 2, pp. 338-348, Feb 2011, doi: 10.1038/jid.2010.315. Epub 2010 Oct 21

[102] Christoph Krafft *et al*, "Identification of organelles and vesicles in single cells". *Vibrational Spectroscopy*, vol. 38, no. 1-2, pp. 85-93, 2005, doi.org/10.1016/j.vibspec.2005.02.008

[103] Kentaro Mera *et al*, "ER signaling is activated to protect human HaCaT keratinocytes from ER stress induced by environmental doses of UVB", *Biochemical and Biophysical Research Communications*, vol. 397, no. 2, pp. 350-354, 2010, doi.org/10.1016/j.bbrc.2010.05.128

[104] A. F. Deyrieux and V. G. Wilson, "In vitro culture conditions to study keratinocyte differentiation using the HaCaT cell line," *Cytotechnology*, vol. 54, no. 2, pp. 77–83, Jun. 2007, doi: 10.1007/s10616-007-9076-1.

[105] N. A. Petushkova *et al.*, "Proteomic characterization of HaCaT keratinocytes provides new insights into changes associated with SDS exposure," *Biomedical Dermatology*, vol. 4, no. 1, Dec. 2020, doi: 10.1186/s41702-019-0054-y.

[106] I. Colombo *et al.*, "HaCaT Cells as a Reliable in Vitro Differentiation Model to Dissect the Inflammatory/Repair Response of Human Keratinocytes," *Mediators Inflamm*, vol. 2017, 2017, doi: 10.1155/2017/7435621.

[107] A. Zamarrón *et al.*, "Extract of deschampsia antarctica (EDA) prevents dermal cell damage induced by uv radiation and 2,3,7,8-tetrachlorodibenzo-p-dioxin," *Int J Mol Sci*, vol. 20, no. 6, Mar. 2019, doi: 10.3390/ijms20061356.

[108] J. Lever, M. Krzywinski, and N. Altman, “Points of Significance: Principal component analysis,” *Nature Methods*, vol. 14, no. 7. Nature Publishing Group, pp. 641–642, Jun. 29, 2017. doi: 10.1038/nmeth.4346.

[109] Jake Lever, Martin Krzywinski & Naomi Altman, “Principal component analysis,” *Nature Methods*, vol. 14, no. 7, pp. 641-642, 2017, doi.org/10.1038/nmeth.4346

[110] A. C. S. Talari, Z. Movasaghi, S. Rehman, and I. U. Rehman, “Raman spectroscopy of biological tissues,” *Applied Spectroscopy Reviews*, vol. 50, no. 1. Taylor and Francis Inc., pp. 46–111, Jan. 02, 2015. doi: 10.1080/05704928.2014.923902.

[111] E. Perevedentseva, A. Krivokharchenko, A. V. Karmenyan, H. H. Chang, and C. L. Cheng, “Raman spectroscopy on live mouse early embryo while it continues to develop into blastocyst in vitro,” *Sci Rep*, vol. 9, no. 1, Dec. 2019, doi: 10.1038/s41598-019-42958-5.

[112] M. Kopec, A. Imiela, and H. Abramczyk, “Monitoring glycosylation metabolism in brain and breast cancer by Raman imaging,” *Sci Rep*, vol. 9, no. 1, Dec. 2019, doi: 10.1038/s41598-018-36622-7.

[113] G. Koutentaki, P. Krýsa, D. Trunov, T. Pekárek, M. Pišlová, and M. Šoóš, “3D Raman mapping as an analytical tool for investigating the coatings of coated drug particles,” *J Pharm Anal*, vol. 13, no. 3, pp. 276–286, Mar. 2023, doi: 10.1016/j.jpha.2023.02.004.

[114] S. McAughtrie, K. Lau, K. Faulds, and D. Graham, “3D optical imaging of multiple SERS nanotags in cells,” *Chem Sci*, vol. 4, no. 9, pp. 3566–3572, Jul. 2013, doi: 10.1039/c3sc51437d.

[115] C. C. Horgan *et al.*, “Molecular imaging of extracellular vesiclesin vitro viaRaman metabolic labelling,” *J Mater Chem B*, vol. 8, no. 20, pp. 4447–4459, May 2020, doi: 10.1039/d0tb00620c.

[116] M. Jiao, S. Cao, L. Ren, and R. Li, “Analysis of composite microplastics in sediment using 3D Raman spectroscopy and imaging method,” *Journal of*

Hazardous Materials Advances, vol. 3, p. 100016, Nov. 2021, doi: 10.1016/j.hazadv.2021.100016.

[117] P. Meksiarun *et al.*, “Comparison of multivariate analysis methods for extracting the paraffin component from the paraffin-embedded cancer tissue spectra for Raman imaging,” *Sci Rep*, vol. 7, Mar. 2017, doi: 10.1038/srep44890.

[118] T. Kümmel *et al.*, “Rapid brain structure and tumour margin detection on whole frozen tissue sections by fast multiphotometric mid-infrared scanning,” *Sci Rep*, vol. 11, no. 1, Dec. 2021, doi: 10.1038/s41598-021-90777-4.

[119] P. Lasch, A. Hermelink, and D. Naumann, “Correction of axial chromatic aberrations in confocal Raman microspectroscopic measurements of a single microbial spore,” *Analyst*, vol. 134, no. 6, pp. 1162–1170, 2009, doi: 10.1039/b822553b.

[120] S. Schrof, P. Varga, L. Galvis, K. Raum, and A. Masic, “3D Raman mapping of the collagen fibril orientation in human osteonal lamellae,” *J Struct Biol*, vol. 187, no. 3, pp. 266–275, Sep. 2014, doi: 10.1016/j.jsb.2014.07.001.

[121] F. Foucher, G. Guimbretière, N. Bost, and F. Westall, “Petrographical and Mineralogical Applications of Raman Mapping,” in *Raman Spectroscopy and Applications*, InTech, 2017. doi: 10.5772/65112.

[122] V. T. Hoang *et al.*, “Optical properties of buffers and cell culture media for optofluidic and sensing applications,” *Applied Sciences (Switzerland)*, vol. 9, no. 6, 2019, doi: 10.3390/app9061145.

[123] X. J. Liang, A. Q. Liu, C. S. Lim, T. C. Ayi, and P. H. Yap, “Determining refractive index of single living cell using an integrated microchip,” *Sens Actuators A Phys*, vol. 133, no. 2 SPEC. ISS., pp. 349–354, Feb. 2007, doi: 10.1016/j.sna.2006.06.045.

[124] K. Majzner, A. Kaczor, N. Kachamakova-Trojanowska, A. Fedorowicz, S. Chlopicki, and M. Baranska, “3D confocal Raman imaging of endothelial cells and vascular wall: Perspectives in analytical spectroscopy of biomedical

research," *Analyst*, vol. 138, no. 2. Royal Society of Chemistry, pp. 603–610, Jan. 21, 2013. doi: 10.1039/c2an36222h.

[125] K. Czamara, K. Majzner, A. Selmi, M. Baranska, Y. Ozaki, and A. Kaczor, "Unsaturated lipid bodies as a hallmark of inflammation studied by Raman 2D and 3D microscopy," *Sci Rep*, vol. 7, Jan. 2017, doi: 10.1038/srep40889.

[126] N. J. Everall, "Confocal Raman Microscopy: Performance, Pitfalls, and Best Practice," *Appl Spectrosc*, vol. 63, no. 9, pp. 245A-262A, 2009, doi: 10.1366/000370209789379196.

[127] H. Carruthers, D. Clark, F. C. Clarke, K. Faulds, and D. Graham, "Three-dimensional imaging of pharmaceutical tablets using serial sectioning and Raman chemical mapping," *Journal of Raman Spectroscopy*, vol. 53, no. 6, pp. 1115–1125, Jun. 2022, doi: 10.1002/jrs.6337.

[128] K. L. Elcock *et al.*, "Total knee arthroplasty in patients with severe obesity provides value for money despite increased complications," *Bone and Joint Journal*, vol. 104, no. 4, pp. 452–463, Apr. 2022, doi: 10.1302/0301-620X.104B4.BJJ-2021-0353.R3.

[129] A. Kaneko, Y. Eto, and M. Tsukamoto, "Survival after total joint arthroplasty in patients with rheumatoid arthritis. Comparison of the postoperative life expectancies and survival by initial operative years: 1970s and 1980s group versus 1990s group," *Mod Rheumatol*, vol. 14, no. 6, pp. 466–469, Dec. 2004, doi: 10.1007/s10165-004-0348-8.

[130] M. Palazzuolo, A. Antoniadis, J. Mahlouly, and J. Wegrzyn, "Total knee arthroplasty improves the quality-adjusted life years in patients who exceeded their estimated life expectancy", doi: 10.1007/s00264-020-04917-y/Published.

[131] S. M. Kurtz *et al.*, "International survey of primary and revision total knee replacement," *Int Orthop*, vol. 35, no. 12, pp. 1783–1789, Dec. 2011, doi: 10.1007/s00264-011-1235-5.

[132] S. Sundaram *et al.*, “Esophageal regeneration following surgical implantation of a tissue engineered esophageal implant in a pediatric model,” *NPJ Regen Med*, vol. 7, no. 1, Dec. 2022, doi: 10.1038/s41536-021-00200-9.

[133] R. S. Magalhaes, J. K. Williams, K. W. Yoo, J. J. Yoo, and A. Atala, “A tissue-engineered uterus supports live births in rabbits,” *Nat Biotechnol*, vol. 38, no. 11, pp. 1280–1287, Nov. 2020, doi: 10.1038/s41587-020-0547-7.

[134] E. A. Gubareva, E. V. Kuevda, A. A. Basov, A. S. Sotnichenko, S. N. Bolotin, and S. S. Dzhimak, “Biophysical methods for quality evaluation of decellularized and recellularized tissue-engineered constructs of organs and tissues,” *J Biosci*, vol. 44, no. 6, Dec. 2019, doi: 10.1007/s12038-019-9953-8.

[135] P. Gault *et al.*, “Tissue-engineered ligament: Implant constructs for tooth replacement,” *J Clin Periodontol*, vol. 37, no. 8, pp. 750–758, Aug. 2010, doi: 10.1111/j.1600-051X.2010.01588.x.

[136] Mads S. Bergholt, Michael B. Albro, and Molly M. Stevens “Online quantitative monitoring of live cell engineered cartilage growth using diffuse fiber-optic Raman spectroscopy”. *Biomaterials*, vol. 140, pp. 128-137, 2017, doi.org/10.1016/j.biomaterials.2017.06.015

[137] A. R. Boyd, G. A. Burke, and B. J. Meenan, “Monitoring cellular behaviour using Raman spectroscopy for tissue engineering and regenerative medicine applications.,” *J Mater Sci Mater Med*, vol. 21, no. 8, pp. 2317–2324, 2010, doi: 10.1007/s10856-009-3965-0.

[138] M. S. Bergholt, A. Serio, and M. B. Albro, “Raman Spectroscopy: Guiding Light for the Extracellular Matrix,” *Frontiers in Bioengineering and Biotechnology*, vol. 7. Frontiers Media S.A., Nov. 01, 2019. doi: 10.3389/fbioe.2019.00303.

[139] C. Jensen and Y. Teng, “Is It Time to Start Transitioning From 2D to 3D Cell Culture?,” *Frontiers in Molecular Biosciences*, vol. 7. Frontiers Media S.A., Mar. 06, 2020. doi: 10.3389/fmolb.2020.00033.

[140] M. Kapałczyńska *et al.*, “2D and 3D cell cultures – a comparison of different types of cancer cell cultures,” *Archives of Medical Science*, vol. 14, no. 4, pp. 910–919, 2018, doi: 10.5114/aoms.2016.63743.

[141] N. P. Damayanti, Y. Fang, M. R. Parikh, A. P. Craig, J. Kirshner, and J. Irudayaraj, “Differentiation of cancer cells in two-dimensional and three-dimensional breast cancer models by Raman spectroscopy,” *J Biomed Opt*, vol. 18, no. 11, p. 117008, Nov. 2013, doi: 10.1117/1.jbo.18.11.117008.

[142] J. R. Jones, D. S. Brauer, L. Hupa, and D. C. Greenspan, “Bioglass and Bioactive Glasses and Their Impact on Healthcare,” *Int J Appl Glass Sci*, vol. 7, no. 4, pp. 423–434, Dec. 2016, doi: 10.1111/ijag.12252.

[143] C. Go´mez *et al*, “Use of an autologous bioengineered composite skin in extensive burns_ Clinical and functional outcomes. A multicentric study”, *Burns*, vol. 37, pp. 580–589, 2011, doi:10.1016/j.burns.2010.10.005

[144] X. Li, G. Xu, and J. Chen, “Tissue engineered skin for diabetic foot ulcers: a meta-analysis”, *Int J Clin Exp Med*, vol. 8, no. 10, pp. 18191-18196, 2015, ISSN:1940-5901/IJCEM0014309

[145] Á. Sierra-Sánchez, K. H. Kim, G. Blasco-Morente, and S. Arias-Santiago, “Cellular human tissue-engineered skin substitutes investigated for deep and difficult to heal injuries,” *npj Regenerative Medicine*, vol. 6, no. 1. Nature Research, Dec. 01, 2021. doi: 10.1038/s41536-021-00144-0.

[146] S. Haeusner *et al.*, “From Single Batch to Mass Production–Automated Platform Design Concept for a Phase II Clinical Trial Tissue Engineered Cartilage Product,” *Front Med (Lausanne)*, vol. 8, Aug. 2021, doi: 10.3389/fmed.2021.712917.

[147] Theofanis Stampoultzis, Peyman Karami, and Dominique P. Pioletti, “Thoughts on cartilage tissue engineering_ A 21st century perspective”. *Current Research in Translational Medicine*, vol. 69, no. 3, July. 2021, https://doi.org/10.1016/j.retram.2021.103299

[148] Brian J Huang, Jerry C Hu, and Kyriacos A Athanasiou, “Cell-based tissue engineering strategies used in the clinical repair of articular cartilage”, *Biomaterials*, vol. 98, pp. 1-22, 2016, https://doi.org/10.1016/j.biomaterials.2016.04.018

[149] Saurabh Bhargava *et al*, “Tissue-Engineered Buccal Mucosa Urethroplasty—Clinical Outcomes”. *European Urology*, vol. 53, no. 6, pp. 1263-1271, 2008, doi.org/10.1016/j.eururo.2008.01.061

[150] P. Pagella, A. Cordiale, G. D. Marconi, O. Trubiani, M. Rasponi, and T. A. Mitsiadis, “Bi oengi neered tooth emulati on systems for regenerati ve and pharmacologi cal purposes,” *Eur Cell Mater*, vol. 41, pp. 502–516, 2021, doi: 10.22203/eCM.v041a32.

[151] S. W. F. R. Waqanivavalagi, S. Bhat, M. B. Ground, P. F. Milsom, and J. Cornish, “Clinical performance of decellularized heart valves versus standard tissue conduits: a systematic review and meta-analysis,” *Journal of Cardiothoracic Surgery*, vol. 15, no. 1. BioMed Central Ltd, Sep. 18, 2020. doi: 10.1186/s13019-020-01292-y.

[152] L. Huang *et al.*, “Rapid, label-free histopathological diagnosis of liver cancer based on Raman spectroscopy and deep learning,” *Nat Commun*, vol. 14, no. 1, Dec. 2023, doi: 10.1038/s41467-022-35696-2.

[153] A. Baliyan, H. Imai, A. Dager, O. Milikofu, and T. Akiba, “Automated Hyperspectral 2D/3D Raman Analysis Using the Learner-Predictor Strategy: Machine Learning-Based Inline Raman Data Analytics,” *Anal Chem*, vol. 94, no. 2, pp. 637–649, Jan. 2022, doi: 10.1021/acs.analchem.1c01966.

[154] E. Lipiec *et al.*, “Monitoring uvr induced damage in single cells and isolated nuclei using sr-ftir microspectroscopy and 3d confocal raman imaging,” *Analyst*, vol. 139, no. 17, pp. 4200–4209, Jul. 2014, doi: 10.1039/c4an00838c.

[155] C. Salzlechner *et al.*, “Complementary techniques to analyse pericellular matrix formation by human MSC within hyaluronic acid hydrogels,” *Mater Adv*, vol. 1, no. 8, pp. 2888–2896, 2020, doi: 10.1039/d0ma00472c.

[156] A. R. Boyd, G. A. Burke, and B. J. Meenan, “Monitoring cellular behaviour using Raman spectroscopy for tissue engineering and regenerative medicine applications.,” *J Mater Sci Mater Med*, vol. 21, no. 8, pp. 2317–2324, 2010, doi: 10.1007/s10856-009-3965-0.

[157] A. R. Walther, N. Ditzel, M. Kassem, M. Ø. Andersen, and M. A. B. Hedegaard, “In vivo non-invasive monitoring of tissue development in 3D printed subcutaneous bone scaffolds using fibre-optic Raman spectroscopy,” *Biomaterials and Biosystems*, vol. 7, Aug. 2022, doi: 10.1016/j.bbiosy.2022.100059.

[158] W. L. Lo *et al.*, “Raman spectroscopy monitoring of the cellular activities of a tissue-engineered ex vivo produced oral mucosal equivalent,” *Journal of Raman Spectroscopy*, vol. 42, no. 2, pp. 174–178, 2011, doi: 10.1002/jrs.2688.

[159] M. Gargotti, U. Lopez-Gonzalez, H. J. Byrne, and A. Casey, “Comparative studies of cellular viability levels on 2D and 3D in vitro culture matrices,” *Cytotechnology*, vol. 70, no. 1, pp. 261–273, Feb. 2018, doi: 10.1007/s10616-017-0139-7.

[160] R. J. Swain, G. Jell, and M. M. Stevens, “Non-invasive analysis of cell cycle dynamics in single living cells with Raman micro-spectroscopy,” *J Cell Biochem*, vol. 104, no. 4, pp. 1427–1438, Jul. 2008, doi: 10.1002/jcb.21720.

[161] E. R. Pavlova, D. V. Bagrov, Y. V. Khramova, D. V. Klinov, and K. V. Shaitan, “Nuclei deformation in HaCaT keratinocytes cultivated on aligned fibrous substrates,” *Moscow Univ Biol Sci Bull*, vol. 72, no. 2, pp. 85–90, Apr. 2017, doi: 10.3103/S0096392517020043.

[162] F. V. Almeida *et al.*, “The cytolinker plectin regulates nuclear mechanotransduction in keratinocytes,” *J Cell Sci*, vol. 128, no. 24, pp. 4475–4486, 2015, doi: 10.1242/jcs.173435.

[163] Michael Greenop, “Random_SpecSelect,” https://github.com/MichaelGreenop/Random_SpecSelect. Accessed: 01/08/2023

[164] M. Versaevel, T. Grevesse, and S. Gabriele, “Spatial coordination between cell and nuclear shape within micropatterned endothelial cells,” *Nat Commun*, vol. 3, 2012, doi: 10.1038/ncomms1668.

[165] S. Sigurdsson, P. A. Philipsen, L. K. Hansen, J. Larsen, M. Gniadecka, and H. Christian Wulf, “Detection of skin cancer by classification of Raman spectra,” *IEEE Trans Biomed Eng*, vol. 51, no. 10, pp. 1784–1793, Oct. 2004, doi: 10.1109/TBME.2004.831538.

[166] James W Chan *et al*, “Micro-Raman Spectroscopy Detects Individual Neoplastic and Normal Hematopoietic Cells”, *Biophysical Journal*, vol. 90, no. 2, pp. 648-656, 2006, DOI: 10.1529/biophysj.105.066761

[167] Z. Huang, A. McWilliams, H. Lui, D. I. McLean, S. Lam, and H. Zeng, “Near-infrared Raman spectroscopy for optical diagnosis of lung cancer,” *Int J Cancer*, vol. 107, no. 6, pp. 1047–1052, Dec. 2003, doi: 10.1002/ijc.11500.

[168] N. Stone, C. Kendall, N. Shepherd, P. Crow, and H. Barr, “Near-infrared Raman spectroscopy for the classification of epithelial pre-cancers and cancers,” *Journal of Raman Spectroscopy*, vol. 33, no. 7, pp. 564–573, 2002, doi: 10.1002/jrs.882.

[169] N. Stone, C. Kendall, J. Smith, P. Crow, and H. Barr, “Raman spectroscopy for identification of epithelial cancers,” *Faraday Discuss*, vol. 126, no. 1, pp. 141–157, 2004, doi: 10.1039/b304992b.

[170] Eoghan O´ Faola´in *et al*, “A study examining the effects of tissue processing on human tissue sections using vibrational spectroscopy”. *Vibrational Spectroscopy*, vol. 38, pp. 121-127, 2005, doi:10.1016/j.vibspec.2005.02.013

[171] R. Malini *et al.*, “Discrimination of normal, inflammatory, premalignant, and malignant oral tissue: A Raman spectroscopy study,” *Biopolymers*, vol. 81, no. 3, pp. 179–193, Feb. 2006, doi: 10.1002/bip.20398.

[172] Naiyan Huang *et al.*, “Full range characterization of the Raman spectra of organs in a murine model cancers”, *Optics Express*, vol. 19, no. 23, pp. 22892-22909, 2011, doi.org/10.1364/OE.19.022892

[173] D. P. Lau *et al.*, “Raman spectroscopy for optical diagnosis in normal and cancerous tissue of the nasopharynx - Preliminary findings,” *Lasers Surg Med*, vol. 32, no. 3, pp. 210–214, 2003, doi: 10.1002/lsm.10084.

[174] W. T. Cheng, M. T. Liu, H. N. Liu, and S. Y. Lin, “Micro-Raman spectroscopy used to identify and grade human skin pilomatrixoma,” *Microsc Res Tech*, vol. 68, no. 2, pp. 75–79, Oct. 2005, doi: 10.1002/jemt.20229.

[175] R. Jyothi Lakshmi, V. B. Kartha, C. Murali Krishna, J. G. R Solomon, G. Ullas, and P. Uma Devi, “Tissue Raman Spectroscopy for the Study of Radiation Damage: Brain Irradiation of Mice,” *Radiation Research*, vol. 157, no. 2, pp. 175-182, 2002, doi.org/10.1667/0033-7587(2002)157[0175:TRSFTS]2.0.CO;2

[176] L. E. Kamemoto *et al.*, “Near-infrared micro-raman spectroscopy for in vitro detection of cervical cancer,” *Appl Spectrosc*, vol. 64, no. 3, pp. 255–261, 2010, doi: 10.1366/000370210790918364.

[177] Zhuang Liu, Corrine Davis, Weibo Cai, Lina He, Xiaoyuan Chen, and Hongjie Dai, “Circulation and long-term fate of functionalized, biocompatible single-walled carbon nanotubes in mice probed by Raman spectroscopy”, *Applied Biological Sciences*, vol. 105, no. 5, pp.1410-145, 2008, doi.org/10.1073/pnas.0707654105

[178] C. Zhang *et al.*, “Stimulated Raman scattering flow cytometry for label-free single-particle analysis,” *Optica*, vol. 4, no. 1, p. 103, Jan. 2017, doi: 10.1364/optica.4.000103.

[179] B. Hansson *et al.*, “Development of a flow cell based Raman spectroscopy technique to overcome photodegradation in human blood,” *Biomed Opt Express*, vol. 10, no. 5, p. 2275, May 2019, doi: 10.1364/boe.10.002275.

[180] Leslie Howlett, “Raman Spectra of Benzene and Toluene,” *Nature*, vol. 128, p. 796, 1931.

[181] A. J. Ruiz-Chica, M. A. Medina, F. Sánchez-Jiménez, and F. J. Ramírez, “Characterization by Raman spectroscopy of conformational changes on guanine-cytosine and adenine-thymine oligonucleotides induced by aminooxy analogues of spermidine,” *Journal of Raman Spectroscopy*, vol. 35, no. 2, pp. 93–100, 2004, doi: 10.1002/jrs.1107.

[182] F. Ravera, E. Efeoglu, and H. J. Byrne, “Monitoring stem cell differentiation using Raman microspectroscopy: Chondrogenic differentiation, towards cartilage formation,” *Analyst*, vol. 146, no. 1, pp. 322–337, Jan. 2021, doi: 10.1039/d0an01983f.

[183] T. Ichimura *et al.*, “Visualizing cell state transition using raman spectroscopy,” *PLoS One*, vol. 9, no. 1, Jan. 2014, doi: 10.1371/journal.pone.0084478.

[184] S. E. George, R. J. Anderson, M. Haswell, and P. W. Groundwater, “An investigation of the effects of dithranol-induced apoptosis in a human keratinocyte cell line,” *Journal of Pharmacy and Pharmacology*, vol. 65, no. 4, pp. 552–560, Apr. 2013, doi: 10.1111/jphp.12019.

[185] Á. Farkas *et al.*, “Dithranol upregulates IL-10 receptors on the cultured human keratinocyte cell line HaCaT,” *Inflammation Research*, vol. 50, pp. 44–49, 2001.

[186] K. A. Hollywood *et al.*, “Exploring the mode of action of dithranol therapy for psoriasis: A metabolomic analysis using HaCaT cells,” *Mol Biosyst*, vol. 11, no. 8, pp. 2198–2209, May 2015, doi: 10.1039/c4mb00739e.

[187] M. C. Socci *et al.*, “Polymeric Materials, Advances and Applications in Tissue Engineering: A Review,” *Bioengineering*, vol. 10, no. 2. MDPI, Feb. 01, 2023. doi: 10.3390/bioengineering10020218.

[188] G. L. Koons, M. Diba, and A. G. Mikos, “Materials design for bone-tissue engineering,” *Nature Reviews Materials*, vol. 5, no. 8. Nature Research, pp. 584–603, Aug. 01, 2020. doi: 10.1038/s41578-020-0204-2.

[189] F. Doberenz, K. Zeng, C. Willems, K. Zhang, and T. Groth, “Thermoresponsive polymers and their biomedical application in tissue engineering-A review,” *Journal of Materials Chemistry B*, vol. 8, no. 4. Royal Society of Chemistry, pp. 607–628, 2020. doi: 10.1039/c9tb02052g.

[190] T. Biswal, “Biopolymers for tissue engineering applications: A review,” in *Materials Today: Proceedings*, Elsevier Ltd, 2019, pp. 397–402. doi: 10.1016/j.matpr.2020.09.628.

[191] Q. Matthews, A. Jirasek, J. Lum, X. Duan, and A. G. Brolo, “Variability in Raman Spectra of Single Human Tumor Cells Cultured in Vitro: Correlation with Cell Cycle and Culture Confluency.”

[192] M. Gargotti, E. Efeoglu, H. J. Byrne, and M. Gargotti, “Raman spectroscopy detects biochemical changes due to Raman spectroscopy detects biochemical changes due to different cell culture environments in live cells in vitro different cell culture environments in live cells in vitro Recommended Citation Recommended Citation Recommended Citation,” 2018. [Online]. Available: https://arrow.tudublin.ie/nanolart/78

[193] H. Moradi *et al.*, “Raman micro-spectroscopy applied to treatment resistant and sensitive human ovarian cancer cells,” *J Biophotonics*, vol. 10, no. 10, pp. 1327–1334, Oct. 2017, doi: 10.1002/jbio.201600211.

[194] Z. Farhane, F. Bonnier, M. A. Maher, J. Bryant, A. Casey, and H. J. Byrne, “Differentiating responses of lung cancer cell lines to Doxorubicin exposure: in vitro Raman micro spectroscopy, oxidative stress and bcl-2 protein expression,” *J Biophotonics*, vol. 10, no. 1, pp. 151–165, Jan. 2017, doi: 10.1002/jbio.201600019.

[195] Z. Farhane, F. Bonnier, A. Casey, and H. J. Byrne, “Raman micro spectroscopy for in vitro drug screening: Subcellular localisation and interactions of doxorubicin,” *Analyst*, vol. 140, no. 12, pp. 4212–4223, Jun. 2015, doi: 10.1039/c5an00256g.

[196] M. Li, J. Xu, M. Romero-Gonzalez, S. A. Banwart, and W. E. Huang, “Single cell Raman spectroscopy for cell sorting and imaging,” *Current Opinion in Biotechnology*, vol. 23, no. 1. pp. 56–63, Feb. 2012. doi: 10.1016/j.copbio.2011.11.019.

[197] J. Gala De Pablo, M. Lindley, K. Hiramatsu, and K. Goda, “High-Throughput Raman Flow Cytometry and beyond,” *Acc Chem Res*, vol. 54, no. 9, pp. 2132–2143, May 2021, doi: 10.1021/acs.accounts.1c00001.

[198] M. Knauer, N. P. Ivleva, R. Niessner, and C. Haisch, “A flow-through microarray cell for the online SERS detection of antibody-captured E. coli bacteria,” *Anal Bioanal Chem*, vol. 402, no. 8, pp. 2663–2667, Mar. 2012, doi: 10.1007/s00216-011-5398-0.

[199] M. Lotfi Choobbari *et al.*, “Studying the concentration of polymers in blended microplastics using 2D and 3D Raman mapping,” *Sci Rep*, vol. 13, no. 1, Dec. 2023, doi: 10.1038/s41598-023-35010-0.

[200] Z. Liao, F. Sinjab, H. M. Elsheikha, and I. Notingher, “Optical sectioning in multifoci Raman hyperspectral imaging,” *Journal of Raman Spectroscopy*, vol. 49, no. 10, pp. 1660–1667, Oct. 2018, doi: 10.1002/jrs.5450.

[201] W. Hauswald, R. Förster, J. Popp, and R. Heintzmann, “Thermal illumination limits in 3D Raman microscopy: A comparison of different sample illumination strategies to obtain maximum imaging speed,” *PLoS One*, vol. 14, no. 8, Aug. 2019, doi: 10.1371/journal.pone.0220824.